Development and characterization of a portable NMR probe for the monitoring of water quality and for the study of the kinetics of chemical reactions

Guilherme Baumgarten

UNIVERSITÉ DE STRASBOURG & FHNW

ÉCOLE DOCTORALE MATHÉMATIQUES, SCIENCES DE L'INFORMATION ET DE L'INGÉNIEUR

Laboratoire des sciences de l'ingénieur, de l'informatique et de l'imagerie (ICube) & Institut pour l'ingénierie médicale et l'informatique médicale (IM^2)

THÈSE présentée par :

Guilherme BAUMGARTEN

Soutenue le : **17 juillet 2024**

pour obtenir le grade de : **Docteur de l'université de Strasbourg**

Discipline / Spécialité : **Sciences de l'ingénieur / Circuits et systèmes**

Développement et caractérisation d'une sonde RMN portable appliquée au suivi de la qualité de l'eau et à l'étude de la cinétique des réactions chimiques

DIRECTEURS DE THÈSE :

M. MADEC Morgan	Maître de conférences, Université de Strasbourg
M. HÉBRARD Luc	Professeur des Universités, Université de Strasbourg

CO-ENCADRANT DE THÈSE :

M. PASCAL Joris	Professeur, Haute Ecole Spécialisée de la Suisse du nord-ouest

RAPPORTEURS :

M^{me} DELTIMPLE Nathalie	Professeur des Universités, Université de Bordeaux
M. FERUGLIO Sylvain	Maître de conférences, Sorbonne Université

EXAMINATEURS :

M. WEBER Serge	Professeur des universités, Université de Lorraine
M. BERTANI Philippe	Maître de conférences, Université de Strasbourg

UNIVERSITY OF STRASBOURG & FHNW

DOCTORAL SCHOOL IN MATHEMATICS, INFORMATION SCIENCES AND ENGINEERING

Engineering science, computer science and imaging laboratory (ICube) & Institute for medical engineering and medical informatics (IM^2)

PHD THESIS by:

Guilherme BAUMGARTEN

Defended on: **17 July 2024**

to obtain the degree: **PhD, Doctor of the University of Strasbourg**

Discipline / Speciality: **Engineering sciences / Circuits and systems**

Development and characterization of a portable NMR probe for the monitoring of water quality and for the study of the kinetics of chemical reactions

SUPERVISORS:

Mr. MADEC Morgan	Associate professor, University of Strasbourg
Mr. HÉBRARD Luc	Professor, University of Strasbourg
Mr. PASCAL Joris	Professor, University of Applied Sciences and Arts Northwestern Switzerland

RAPPORTEURS:

Ms. DELTIMPLE Nathalie	Professor, University of Bordeaux
Mr. FERUGLIO Sylvain	Associate professor, Sorbonne University

REVIEWERS:

Mr. WEBER Serge	Professor, University of Lorraine
Mr. BERTANI Philippe	Associate professor, University of Strasbourg

Table of contents

Acknowledgment

First, I would like to thank my family, friends and colleagues for the support, understanding and encouragement during this work.

Successively, I would like to thank my supervisors for all the accomplished work and guidance. Specifically, I thank Morgan Madec for all the cooperation and interesting scientific insights, Luc Hebrárd for the availability and valuable suggestions, and Joris Pascal for organizing the many project and academic activities in which I could participate, including lectures and the supervision of students.

Of the greatest importance were as well the colleagues that started working on the topic prior to me and laid down the basis of the developed work, while effectively transmitting the acquired knowledge: Duc-Vinh Nguyen, Lucas Werling and Chunchesh Malangi Gajendramurthy. I am as well grateful for the support of my fellows Céline Vergne, Thomas Quirin, Hugo Nicolas, Corentin Féry, Frédéric Bourgeois, Dominic Jeker and Sara Bieri.

During my time at the FHNW, I had the pleasure of meeting and exchanging with great people, among whom Erik Schkommodau, that was there since my application process, Markus Degen, from whom I was able to learn a lot concerning teaching and how to handle different conflict situations, David Hradetzky that was always available for an exchange on the most different topics, Enkelejda Miho, whose sympathy and way of being were always accompanied by an smile, and Christelle Jablonski, who was of great assistance during the practical work. I also would like to thank Sebastian Wendeborn, Clément Javerzac, Simone Hemm-Ode and Michael de Wild for the occasional exchanges that we had during this time.

At the Unistra, I was as well in contact with great people who participated in my doctoral studies one way or another: Philippe Bertani, with whom I always had a pleasure to work and who always answered my questions in a simple yet very smart way, Jean-Pierre Djukic, whose valuable experience helped us progress, and Wilfried Uhring, who always responded promptly to my questions.

I had much exposure to different companies and their quick reaction were key to the fast understanding of the faced difficulties and the posterior work progression. In this sense, I would like to thank Stefan Wintzheimer, Michael Distler and Markus Mützel from the company Pure Devices, Miha Gjura from Red Pitaya, as well as the team from the company Caylar.

Some interesting and useful exchanges were as well done together with external fellows, among which John Beausire Wyatt Webber, Pavel Demin, Kazuyuki Takeda and Allen Devaney Elster, for whom I would like to show my deepest appreciation.

Finally, I would like to thank the students with whom I had the opportunity to work during my doctoral studies: Laurent Gloor, Nevio Paganini, Dorina Hacksteiner, Tom Lanz and Benedetto Berardi.

List of abbreviations

Abbreviation	Meaning
1D	1 Dimension
2D	2 Dimension
3D	3 Dimension
ADC	Analog-to-Digital Converter
AMS	Ambient Mass Spectrometry
ANR	National Agency for Research, Agence Nationale de la Recherche
APIs	Application Programming Interface
ASIC	Application-Specific Integrated Circuit
CL-MIS	ChemiLuminescence–Molecular Imprinting Sensor
COTS	Commercial Off-The-Shelf
DAC	Digital-to-Analog Converter
DC	Direct Current
DFT	Discrete Fourier Transform
EC	European Commission
ELISA	Enzyme-Linked ImmunoSorbent Assay
ESD	Energy Spectral Density
EU	European Union
FEM	Finite Element Method
FFT	Fast Fourier Transform
FHNW	University of Applied Sciences and Arts Northwestern Switzerland, Fachhochschule Nordwestschweiz
FID	Free Induction Decay
FT	Fourier Transform
FWHM	Full Width at Half Maximum
GC	Gas Chromatography
GC–MS	Gas Chromatography–Mass Spectrometry
GUIs	Graphical User Interface
HPLC/Fluo	High-Performance Liquid Chromatography/FLUOrescence
HWHM	Half Width at Half Maximum
IARC	International Agency for Research on Cancer
IC	Integrated Circuit
ICF	Inhomogeneity Convolution Function

Abbreviation	Meaning
IC–MS	Ion Chromatography–Mass Spectrometry
IC–MS/MS	Ion Chromatography–Mass Spectrometry/Mass Spectrometry
ISFET	Ion-Sensitive Field-Effect Transistor
LAN	Local Area Network
LC–MS	Liquid Chromatography–Mass Spectrometry
LC/MS–MS	Liquid Chromatography/Mass Spectrometry–Mass Spectrometry
LGR	Loop-Gap Resonator
LNA	Low-Noise Amplifier
LoD	Limit of Detection
MF	Methyl Formate
MRI	Magnetic Resonance Imaging
Msps	MegaSamples Per Second
NMR	Nuclear Magnetic Resonance
OS	Operating System
PA	Precision Agriculture
PC	Personal Computer
PFASs	Per- and polyFluoroAlkyl Substances
pH	Potential of Hydrogen
PL	Programmable Logic
ppb	Parts Per Billion
ppm	Parts Per Million
PPPs	Plant Protection Products
PS	Processing System
PSD	Power Spectral Density
RAFT	Reversible Addition−Fragmentation Chain-Transfer
R&D	Research and Development
RF	Radio Frequency
RMS	Root Mean Square
SCPI	Standard Commands for Programmable Instruments
SDR	Software Defined Radio
SERS	Surface-Enhanced Raman Scattering
SMA	SubMiniature version A
SmCo	Samarium–Cobalt
SNR	Signal-to-Noise Ratio

Abbreviation	Meaning
SoC	System-on-a-Chip
SPR	Surface Plasmon Resonance
sps	Samples Per Seconds
UHF	Ultra-High-Field
ULF	Ultra-Low-Field
Unistra	University of Strasbourg, Université de Strasbourg
US	United States
UV	UltraViolet
VNA	Vector Network Analyzer
WPS	Water Pollution Sensor
ZULF	Zero-to-Ultra-Low-Field

Introduction

The work presented in this manuscript was performed within the University of Strasbourg (Unistra, France) and the University of Applied Sciences and Arts Northwestern Switzerland (FHNW, Switzerland) affiliations, and within the framework of the Interreg WPS (Water Pollution Sensor) and the ANR Dip-NMR (Dip NMR Spectroscope on Chip for in situ Catalysis Monitoring) projects. Hereupon we intend to provide the reader with a short overview of the work that was performed during these doctoral studies and the contributions we were able to provide to our Fellows and to the institutions that participated in it.

These doctoral studies were accomplished within the theme of low-field NMR (Nuclear Magnetic Resonance) and around the assumption that a portable miniaturized NMR spectrometer would bring valuable application possibilities as well as that any breakthrough in this research field would contribute to the state of the art of portable miniaturized NMR spectrometers. Although NMR techniques are mainly used by chemistry professionals for the analysis and identification of substances withing a solution, the development of an NMR spectrometer is *per se* a multidisciplinary field topic, where as many science fields as chemistry, physics and quantum physics, mathematics, electronics, programming (to name a few) come into play, therefore requiring the concurrent understanding of some of their aspects to different degrees. The successful design and implementation of such systems and its correct functioning are thus dependent on many different aspects that require a broad multidisciplinary understanding.

This work was therefore accomplished pursuing the idea that a portable miniaturized NMR device intended to monitor water quality and various chemical reactions would be of great interest for research and commercial intents. Moreover, our assumption was that developing the device with low-cost off-the-shelf hardware components would make such implementation of a higher quality-cost ratio compared to available low-field NMR devices on the market. This should be possible because the requirements, in terms of signal quality, and particularly in terms of spectral resolution, are allegedly lower for our targeted applications, when compared to other typical applications that need conventional NMR spectrometry instead. The use of off-the-shelf electronics also means that the production process of such developed system would be at least partially simplified.

NMR is a useful tool widely used in the identification and quantification of chemical compounds. Making NMR portable means bringing the lab to the field by enabling *in situ* analysis and therefore expanding greatly the employment possibilities of this technology within modern organic chemistry, catalysis, biology, medicine, and industry [1]. Within our research groups at Unistra and the FHNW, research efforts on portable miniaturized NMR technologies

from previous work of Duc-Vinh Nguyen [2] and Lucas Werling [3] bore fruit and allowed this follow-up work. We therefore looked forward to bringing together already existing knowledge by applying it to different application scenarios, so that we could transform our first results into a proof of concept and determine the way forward.

In order to pursue the achievement of such objective, different R&D (Research and Development) activities were performed during these studies, which for formalization purposes can be divided into 3 main topics: (1) the development of simulation tools intended for the understanding and the prediction of the performance of such low-field NMR systems, (2) the development of an NMR spectrometer prototype to reach a proof of concept on the aforementioned projects, and (3) the determination of supplementary specifications for the further development of this prototype in order to reach the performance required by those projects.

The first main topic, which proposes different and complementary simulation tools that model an NMR spectrometer electronic chain and different aspects of the NMR experiment, is subdivided according to the different developed tools:

1. A simulator tool that can deform a given spectrum following the inhomogeneity of the static magnetic field $\overrightarrow{B_0}$.
2. A parametrizable software application that is able to simulate the whole electronic chain of an NMR spectrometer (in what concerns its transmission and reception composing elements), providing the expected signals for each of the different steps of the electronic processing. This piece of software can provide us with all expected waveforms within the NMR spectrometer aforementioned electronic parts.
3. A software script that enables measurement accumulations by means of Time-shifting and Time-dilatation, provided that their amplitudes are above the noise floor.

This whole software toolchain is consequently able to provide valuable insights on the electronic toolchain, therefore being capable of assessing some of its aspects, and nonetheless being able to operate as a requirement provider for the NMR system design process.

The second work package is about the development of an NMR spectrometer prototype. A complete NMR system is composed of a very stable and homogeneous magnetic field generator (permanent magnet or electromagnet), a coil and electronic circuits for conditioning and acquisition. Within the scope of this PhD, the focus was put on the electronic circuit, which is composed of:

1. The excitation of the sample, *i.e.*, the generation of an RF (Radio Frequency) signal at the desired Larmor frequency.

2. The reception and analogue preprocessing of the induced sample response up to its sampling.
3. The digital postprocessing and formatting to extract the information of interest.

The present version of our NMR spectrometer is therefore composed of the following self-developed and adapted pieces:

- Excitation path:
    - Generation of the RF excitation at the Larmor's frequency.
    - Amplification and direction of this signal towards the receiving coil.
- Receiving path:
    - Collection and preamplification of the measured FID (Free Induction Decay) signal.
    - Further filtering and amplification.
    - Generation of the oscillator signal for frequency down-conversion purposes.
    - Mixing of the signal for implementing the frequency down-conversion.
    - Sampling of the frequency down-converted signal.
    - Signal processing and output formatting.

The command of the electronic chain was implemented by means of a commercial SDR (Software Defined Radio) board from the company Red Pitaya, which runs on a Linux-based OS (Operating System) and which can be remotely configured and controlled by a MATLAB interface communicating with the board over the SCPI (Standard Commands for Programmable Instruments) protocol. Thus, the natural choice for the baseline software platform as well as for the signal and data processing environment was MATLAB itself.

Furthermore, we used hereunto as a support and reference system a Benchtop NMR spectrometer from the company Pure Devices [4], which provided us with the static magnetic field B_0 and its necessary shimming correction, in addition to the receiving coil, although a design process for the receiving coils was as well developed within this work. Some measurements of strong signal substances were performed in order to exemplify the way of employment of the prototype and to characterize its performance. Moreover, measurement campaigns were also performed with samples corresponding to the targeted applications.

The third and final section is about summing up and putting together of additional requirements that must be respected in order to further developed a fully functional low field portable miniaturized NMR spectrometer, this being done from the obtained results in this work as well as from our developed tools. Included in this section are timing related aspects of the employed processing system and electronics, estimations of the allowed inhomogeneity of the

static magnetic field $\overrightarrow{B_0}$, evaluation of the current state of the prototype, appreciation of temperature related issues, among other aspects.

Therefore, a natural sequential chapter structure was adopted for this manuscript, where, at first, we give the big picture concerning the state of the art on both low-field NMR and the targeted applications. In the second chapter, some basics of NMR theory and related topics are presented to the reader along with an overview of NMR spectrometers and their composing elements. The third chapter is a description of our simulation toolchain together with the related validation results. The fourth chapter describes the different parts of our current NMR Spectrometer Prototype. The fifth chapter presents experimental results obtained from measurements for the targeted applications. To finish, we proceed with discussions on the additional requirements that must be respected in order to further develop our prototype, while putting forward future perspectives and listing further concise suggestions. Design material and extended analyses are attached under the Appendix section in the end of these writings.

Chapter 1 - Context and state of the art

This chapter aims at providing the reader with the necessary context on the state of the art of the involved applications and trend topics: on the one hand, as presented in the first section, pollutants detection on potable water and more general PA (Precision Agriculture) applications with a focus on the detection of glyphosate, and in the other hand, as in the second section, monitoring of chemical reactions. Additionally, the third section contemplates the subject of portable miniaturized NMR spectroscopy as a mean for achieving such application demands, taking into account the already laid down work within our research teams.

3.1. Pollutants detection on potable water as a precision agriculture trend

Because the general objective of PA is the maximization of agricultural output (food and ingestible goods) with regards to agricultural input (all kinds of agricultural resources employed in the production of agricultural outputs including pesticide and fertiliser use) taking into consideration social and environmental aspects, there is a permanent trend within PA branches to optimize resource usage by exploring new technologies, while keeping an eye on related sustainability aspects [5]. Miniaturization trends and miniaturized technologies to the point of the nanoscale are being currently pursued within PA and its branches. Figure 1 provides an overview of such nanoscale trends within sustainable PA, putting forward the most common ways that these novel technologies are impacting the field, by providing farmers with field tools for (1) precise delivering of fertilizers, (2) early detection of plant diseases and pests, (3) precision breeding, (4) monitoring and analyzing soil and water contaminants, (5) enhancing crop protection and reducing chemical usage, and (6) real-time monitoring of soil conditions. Such tools pursue ultimately a positive economically sustainable output: a healthy growth by increasing productivity, *i.e.*, producing more while consuming and impacting less the surrounding environment.

Among these various topics, our focus is on environmental water quality control, which seems to be one of the most critical insofar, as it is a public health issue of worldwide concern [6]. Water sources and its ramifications are multiple and the possibilities of polluting these waters are manifold as well. Several industrial and societal actors can play a role in degrading water quality and consequently further state structures are put into place in order to supervise, mitigate and foresee the impact of water pollution. These regulatory bodies have an overall objective of protecting and enhancing the status of aquatic systems and promoting sustainable water use within their jurisdictions. Figure 2 depicts a classic local water system where the

different types of water resources and actors interact with each other. Clean water is usually available from groundwater and surface water sources, and these can be contaminated by agricultural, industrial and sewage residues. Spatial protections are put in place in order to prevent the generalized contamination of the available water resources. Furthermore, water quality monitoring is typically enforced as a mean of controlling the effectiveness of the water quality protection associated public policies.

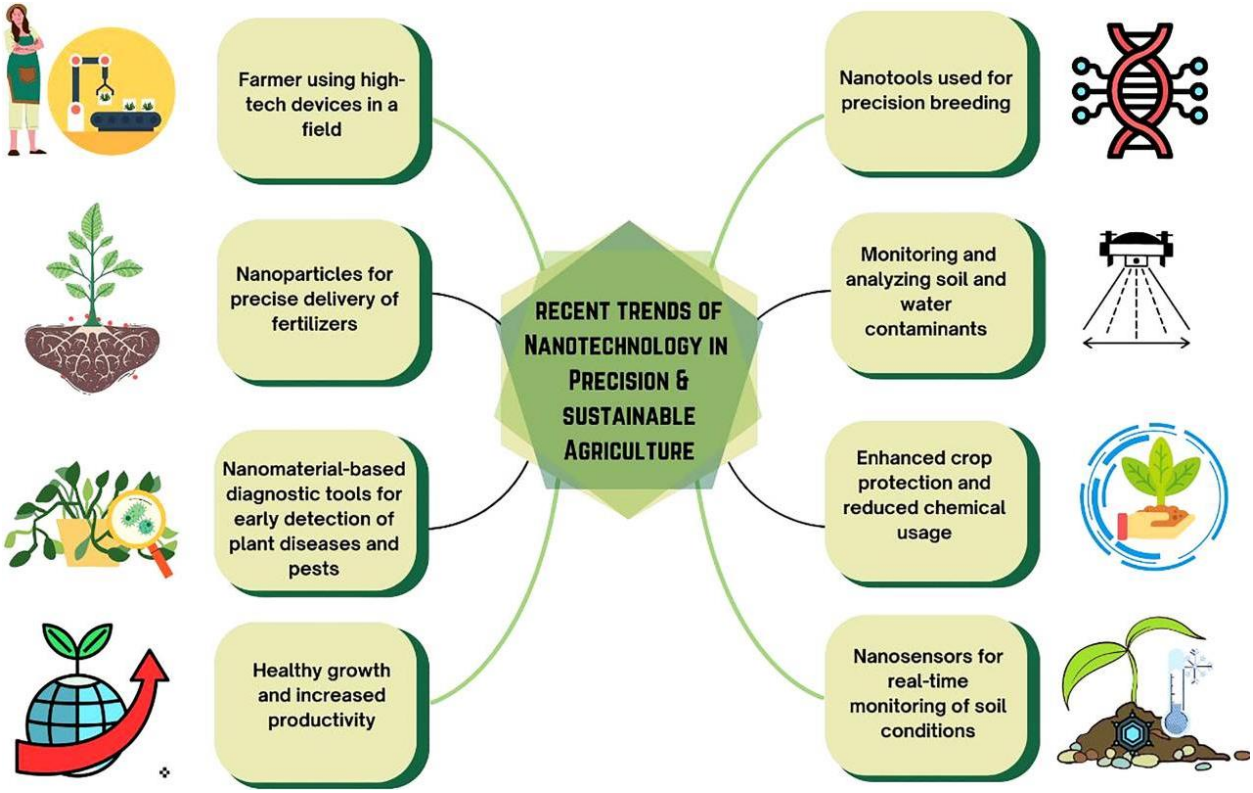

Figure 1 - Recent trends of nanotechnology in precision agriculture. [5]

From the latest data available, a significant number of European countries present deteriorated and deficient chemical and ecological statuses for their water bodies [7], as it can be seen in Figure 3 for the surface water. The current water quality situation is so far from the ideal scenario that even citizen effort is being arrogated to try to improve the situation [8], since current existing frameworks still fail grandly in identifying contaminations risks [9].

Usual monitoring targets within water quality control are pesticides, pharmaceuticals, heavy metals, personal care products as sunscreen lotions, PFASs (Per- and polyFluoroAlkyl Substances), and microplastic. The concentrations of such elements are usually measured ranging from µg/L to ng/L and can be indirectly determined through many physicochemical parameters such as the identification of the presence of a number of nutrients and the amount of dissolved oxygen, or the determination of the sample temperature, salinity, conductivity, pH (potential of Hydrogen), etc. Novel water quality control approaches propose continuous biomarker monitoring with single molecule resolution (1) by particle mobility sensing [10] and (2)

by measuring free particle motion [11]. Monitoring rates of recurrence can vary depending on the severity of the substance impact on the human health and on the environment and are usually within the range of once a week up to once every decade, being therefore classified as surveillance, operational or investigative monitoring types following their practical intents. Anyways, it is currently sought that the overall monitoring improves in order to provide sufficient spatial and temporal resolution and in some cases to make it more cost-effective [12].

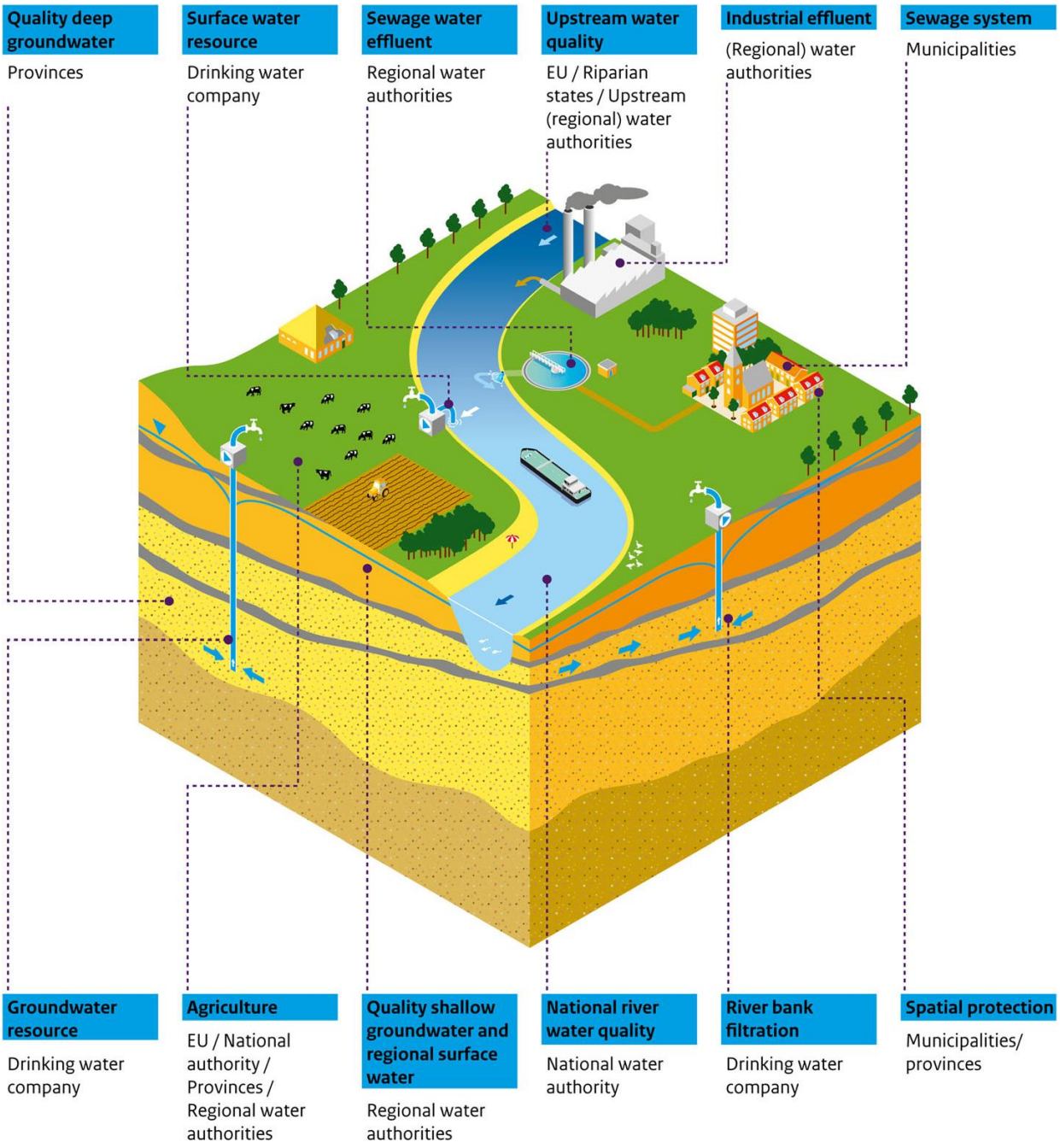

Figure 2 - Schematic view of water system, the types of resources analysed and the actors involved. Modified. [13]

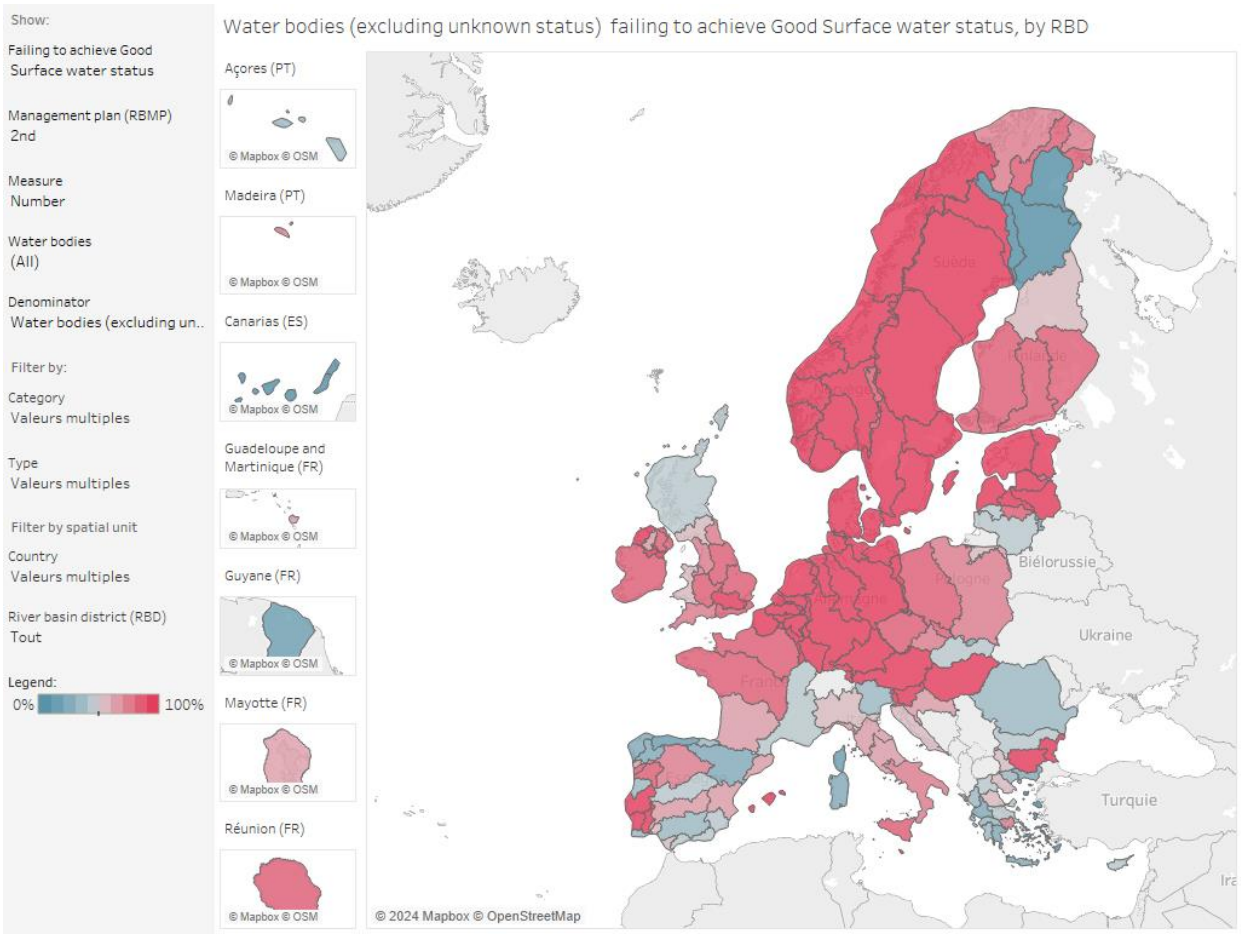

Figure 3 - Surface water status in the European Union as of May 2024. Modified. [7]

Bieroza et al. [14] stated that the topmost significant causes of failure in surface water bodies are Hydromorphological pressures (40%) and diffuse pollution from agriculture (38%), with point sources (18%) and water abstraction (7%) following up. These causes may overlap for given water bodies, so that they are not mutually exclusive.

Regarding crops, pesticides are largely employed on agriculture in order to accomplish pest management and increase productivity. Nowadays, due to intensive agriculture, they end up being present on a variety of different water bodies [15]. Specific techniques are put forward in order to enhance their usage [16]. To name a few, the United States Environmental Protection Agency [17], the EC (European Commission) [18] and the Swiss Federal Office for the Environment [19] provides lists of pesticides and regulates their use. Among the types of pesticides that PA aims at minimizing, we can cite the following ones – and what they are intended to combat:

The employment of such chemicals, among which the ones presented in Table 1, is usually strongly regulated within the different worldwide jurisdictions because the human exposure to such substances can cause acute health effects as stinging eyes, rashes, blisters, blindness, nausea, dizziness, diarrhoea and ultimately death. Furthermore, many chronic effects are known to be caused by the contact with such pesticides: cancers, birth defects,

reproductive harm, immunotoxicity, neurological and developmental toxicity, and disruption of the endocrine system.

Pesticide	Effective against	Example of commercial product
Insecticides	Insects	Asana® [20]
Herbicides	Plants	Roundup® [21]
Rodenticides	Rodents (rats & mice)	Harmonix® [22]
Bactericides	Bacteria	SaniDate® [23]
Fungicides	Fungi	Aliette® [24]
Larvicides	Larvae	Abate® [25]

Table 1 - Kinds of pesticides, what are they effective against, and an example of a commercial product for each cited pesticide category.

Pathak et al. [26] have performed a comprehensive review on the status of pesticide effects on human health and other aspects. Figure 4 shows the current percentual distribution of pesticides and their primary impact on the human body.

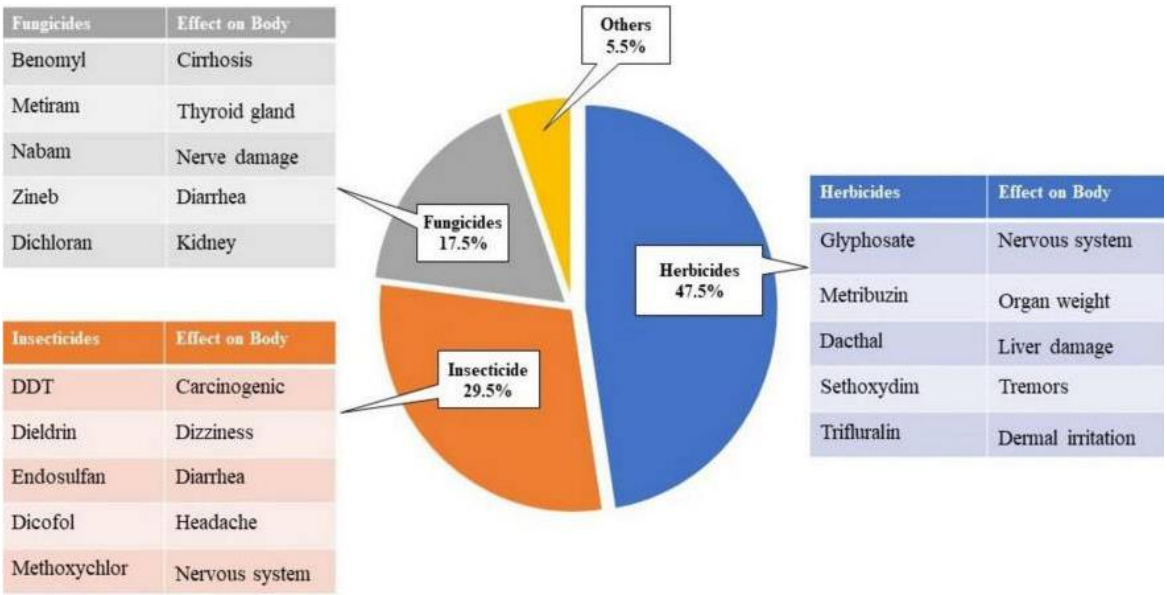

Figure 4 - Percentage distribution of pesticides. [26]

Runoff and pesticide drift are known as central loss processes through which pesticides are disseminated into the environment [27]. Pesticide loss causes water field contamination and many other forms of environmental harming. This is as well the main way of glyphosate into the

core available drinking water sources, which is a primary potable water contaminant and is a common herbicide used for agriculture, lawn, and garden care. In the human case, it can be mainly ingested from eating foods treated with glyphosate-based products or from drinking contaminated water. It causes developmental effects, including reduced infant body weight and skeletal changes, minor gastrointestinal effects, including changes to the salivary gland and there are suspicions of it being the root cause of various cancers. The International Agency for Research on Cancer (IARC) classifies it as probably carcinogenic to humans [28]. Different institutions officially determine to their jurisdictions the safe amount of glyphosate and other pesticides contamination to be allowed so that its inherent risks to human health can be diminished. Others, as is the case of the Department of Health of the American State of Minnesota through its Health Risk Assessment Unit, state discretionary safety values based on local experience and evidence, being for the aforementioned actor currently considered a non-cancer water guidance value of $500\ ppb$ (parts per billion) to be protective [29]. Panis et al. [30] have summarized to a great extent these different advised levels, which can vary greatly among considered jurisdictions, as shown in Figure 5.

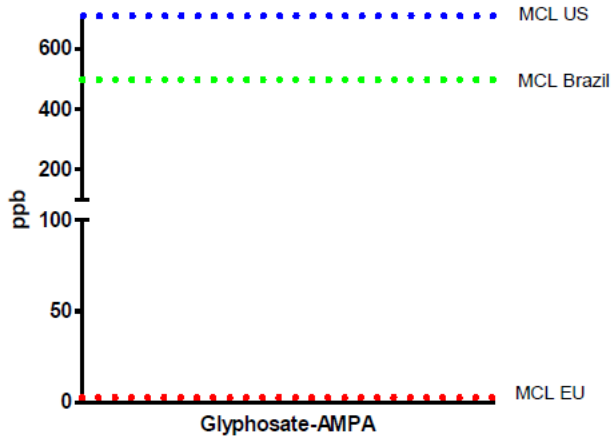

Figure 5 - Pesticide levels (in ppb) in drinking water. The lines indicate the maximum concentration allowed for each pesticide in Brazil (green line), US (blue line) and Europe (red line). Modified. [30]

Hundreds of thousands of chemicals and their mixtures are currently registered worldwide for production and use [31], and they are to a great extent employed on European soil as well. In response to the danger that the usage of such substances represents to the health of the exposed people, the European decision-making bodies have made research on the topic water a topmost priority by setting the so called water policy, with current activities intending to tackle water pollution and safeguard water quality for an expected success implementation horizon aiming at 2030 [32]. In this sense, several EC directives have been issued with the objective of improving the situation regarding the quality of water and the related safety issues within EU (European Union) jurisdiction: (1) on establishing a framework for Community action in the field of water policy [33], (2) on the protection of groundwater against

pollution and deterioration [34] and (3) on environmental quality standards in the field of water policy [35]. Therefore, it is currently the will of the EU political instances that further advanced monitoring of water quality be enforced in the near future [36].

Pollutants are typically challenging to be detected, especially when in relatively small concentrations and dissolved in drinking water. Usually, contaminants in water supply can be detected by a range of different techniques and technologies that are grouped in discontinuous (sample-based) methods and in-line sensor-based monitoring methods [37]. Current available alternatives are typically expensive and require high qualified, trained staff to operate the analysis apparatus. For instance, biosensors are put forward for the detection of arsenic in groundwater as a valid alternative for this specific water pollutant [38]. In Italy, existing monitoring methods were employed in the analysis of 40 plastics bottled and tap water samples from many parts of the country, appointing to the occurrence of different organic pollutants and heavy metals in the considered samples, providing evidence that more frequent surveillance practices are required [39].

Glyphosate is arguably the world dominant herbicide worldwide [40]. As from the 13th of October 2023, there was no European parliamentary qualified majority on the renewal of approval of the employment of glyphosate in agriculture as an active substance in PPPs (Plant Protection Products) on European soil, so that on the 28th of November 2023, the European Commission was obliged to renew the authorization of use of glyphosate for another 10 years. The related implementing regulation dates from 29th of November 2023 [41]. For the time being, it seems obvious due to economic and food safety reasons that the use of pesticides in general and glyphosate in particular cannot be totally avoided nor greatly reduced, and even less can it be abruptly stopped without severe social consequences, so that pesticide monitoring must be further improved in order to guarantee a sustained safe use. Indeed, even in a hypothetical scenario where we could all of a sudden abolish using such chemicals, there is actually so much of them already within our farming soils and downstream compartments, that the long-term impacts of their presence in the current levels would be guaranteed to resurface. Figure 6 depicts the long-term characteristics of the pesticide employment problematic within water circuits. Its essential message is that the already existing pollution within our water circuits is an acute latent legacy problem that might resurface at any moment within a timespan from years to centuries, so to continue to impact our lives and health for as long as this very same duration.

Regardless of current legislation in force, the dangers related to the ingestion of and exposure to glyphosate and other pesticides are known and there is presently no kind of commercially available system on the market that meets practical utility needs in consonance to European requirements [42], let alone commercially available portable miniaturized NMR spectrometers for the assessment of water quality.

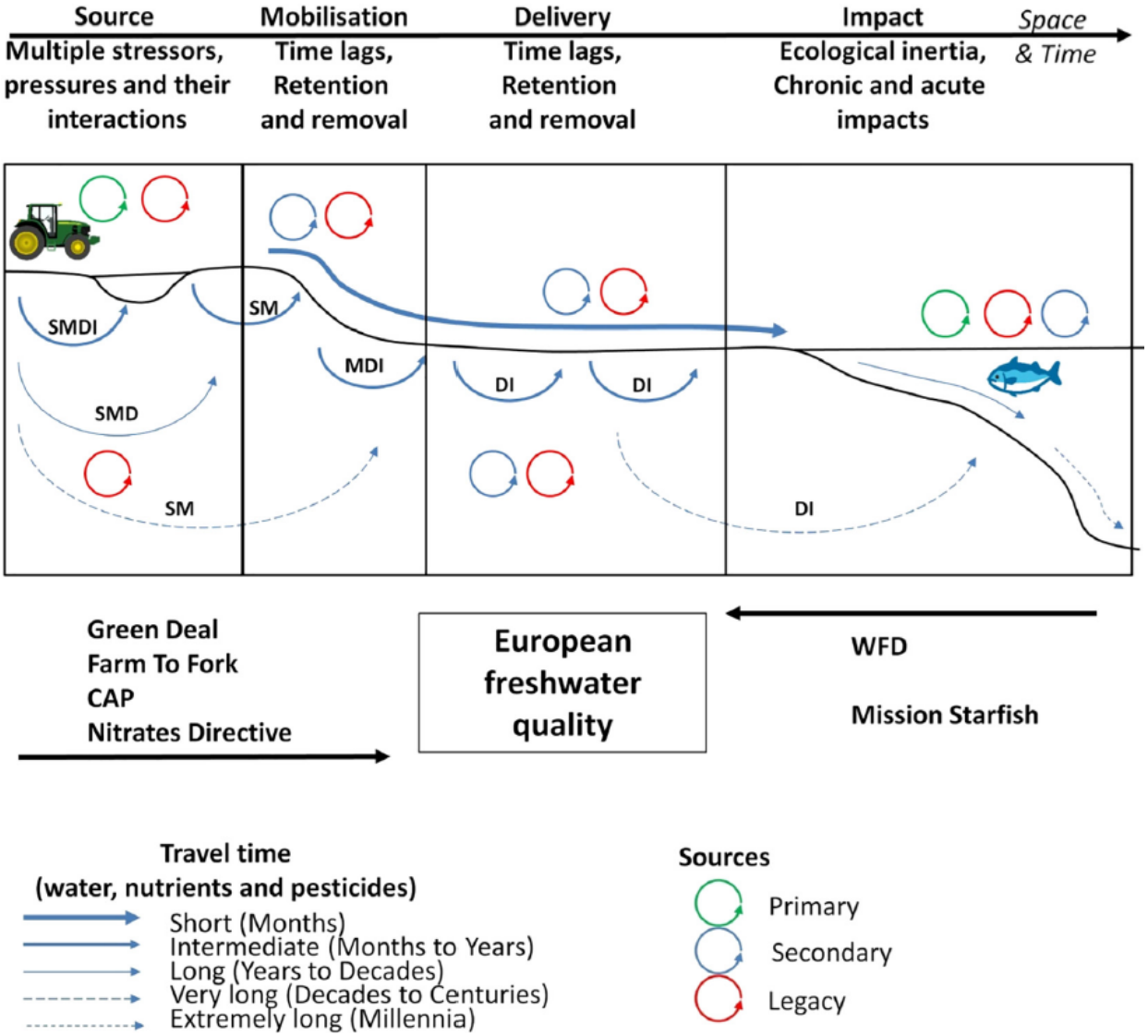

Figure 6 - Complexity of the water pollution continuum and European strategies to improving freshwater quality. A conceptual representation of terrestrial water cycle and pollution trajectories of different travel times (denoted by weight of arrows) and extent (denoted by letters indicating S (Source), M (Mobilisation), D (Delivery) and I (Impact)). Each continuum step involves complex processes controlling diffuse pollution mobilisation, retention and transfer to the downstream compartment. European freshwater quality is regulated by the WFD (Water Framework Directive - focus on impact) while the new Green Deal, Farm to Fork, CAP (Common Agricultural Policy) and Nitrates Directive are focussed on sources and their mobilisation. Mission Starfish focuses on reducing pollution point sources and restoring ocean ecosystems. Modified. [14]

There are currently many bioanalytical and biomonitoring methods that can be used in glyphosate detection when dissolved in water-based fluids, as drinking water, blood, plasma, serum, gastric content, breast milk or urine [43], for instance (1) ELISA (Enzyme-Linked ImmunoSorbent Assay) for both water and urine, (2) LC–MS (Liquid Chromatography–Mass Spectrometry) or LC/MS–MS (Liquid Chromatography coupled to tandem Mass Spectrometry) for urine, and (3) HPLC/Fluo (High-Performance Liquid Chromatography coupled to FLUOrescence detection) for water. Further methods [44] include (4) HPLC coupled with UV

(UltraViolet) detection, (5) ion chromatography, IC–MS (Ion Chromatography–Mass Spectrometry) or IC–MS/MS (Ion Chromatography tandem Mass Spectrometry) [45], (6) GC (Gas Chromatography) or GC–MS (Gas Chromatography–Mass Spectrometry).

Valle et al. made an extensive review on methods used in glyphosate detection [46]. They went through the above quoted chromatography techniques, which are most employed in clinic scenarios but not only, however going further on electrochemical sensors and spectroscopic methods. Sensory methods based on the electrochemical characteristics of glyphosate within a given sample explore mainly electric properties to be measured, as for instance for the (7) amperometry and for the (8) voltametric methods or for the (9) capillary electrophoresis method, which employs a capacitively coupled tactless conductivity system. The electromagnetic based absorption and emission techniques, in the other hand, are particularly effective in identifying nuclei of interest. Examples of existing spectrometry techniques that can be employed for glyphosate detection include (10) SERS (Surface-Enhanced Raman Scattering), which magnify the sample molecular vibrations allowing single-molecule detection, SPR (Surface Plasmon Resonance), that can be used as an optical biosensor for monitoring interactions between an analyte in a solution and an immobilized bioelement on the SPR sensor surface by means of electromagnetic waves / surface plasmon polaritons, (11) CL-MIS (ChemiLuminescence–Molecular Imprinting Sensor), by using small dimension microspheres as a molecular printer synthesizing onto a molecularly imprinted polymer base using precipitation polymerization with glyphosate as template, and (12) NMR.

NMR is a particularly convenient method to be employed in pesticide detection because it is not sample-specific, meaning that it is versatile, and it can be both qualitatively and quantitatively employed. The detection of glyphosate through NMR was already demonstrated a long time ago by employing NMR spectroscopy [47]. The executed NMR experiment required D_2O (called heavy water or deuterium oxide: ^2H_2O) for providing the necessary NMR lock signal within a ^{31}P (phosphorus NMR spectroscopy). The setup employed an excitation frequency of 81 MHz from a Varian XL-200 superconducting Fourier transform NMR spectrometer. The NMR analysis used signal processing and acquisition techniques such as NMR signal accumulation, zero filling and quadrature detection, so to improve SNR (Signal-to-Noise Ratio) and the overall quality of the analysis outcome.

Further studies are as well available, where ^1H (proton) and ^{31}P NMR spectroscopies were used in combination to detect glyphosate in biological fluids, with respective Larmor frequencies of 300.09 MHz and 121.48 MHz generated by an Avance 300 NMR spectrometer from Bruker [48]. On plant related use cases analysis concerning glyphosate, Thelen et al. [49] evaluated interactions of 2,4-D dimethylamine and 2,4-D butoxyethylester formulations with glyphosate in solution using ^1H NMR technology concerning activity on grass weed and broadleaf species, while Ge, d'Avignon et al. investigated this herbicide activity in glyphosate-

resistant horseweed leaf tissue from ^{31}P NMR experiments [50] as well as its impact on plant metabolism through phosphorus NMR spectroscopy [51]. Further NMR analysis studies comprise the determination of glyphosate in dried wheat by means of ^{1}H NMR spectroscopy employing a Bruker Avance 600 MHz spectrometer equipped with a 5-mm z-gradient TXI (H/C/N) cryoprobe [52], and solid-state NMR determination of glyphosate metabolism in bacteria employing low-field ^{15}N and ^{13}C NMR spectroscopy [53].

The common characteristic among all these application approaches to the detection of glyphosate, and more specifically when employing NMR, is that they are laboratory-based procedures, engendering elevated analysis costs due to personnel and logistics aspects. The bottom line of utilizing portable miniaturized NMR for glyphosate detection in drinking water is to minimize these associated analysis costs by taking the lab to the field.

3.2. Monitoring of chemical reaction kinetics

Beyond water quality monitoring, NMR can also be a very noteworthy tool for chemical reaction monitoring. There are many reasons why one would like to monitor the kinetics of chemical processes: from fundamental research in chemistry aiming at understanding the elementary mechanisms actuating within chemical reactions in order to support the elaboration of new chemical processes to the evaluation and optimization of already existing industrial processes and applications within chemical synthesis of pharmaceutical compounds and environmental protection.

Monitoring of chemical reaction kinetics falls into the scope of the redefinition of industrial processing design, which is also a major concern of EU political and decision-making instances. In Europe, the Horizon 2020 framework [54] [55] of the EU, which was then succeeded by the Horizon Europe research and innovation funding programme [56], set the ground for the creation of a general roadmap on that purpose. Among the declared objectives of these initiatives, one can cite the progressive abandonment of the employment of fossil resources as well as the rationalization of the usage of natural resources and the optimization of production processes, always taking into account the associated ecological impact. At national level, countries as France [57] and the Netherlands [58] [59] are actively incorporating such European goals into their respective domestic research strategies. Among the currently pursued goals within the catalysis domain, there is the explicit intention of developing sophisticated characterization tools for the continuous reaction monitoring and acquisition of reaction kinetic information.

Today, even smartphones [60] and micro-reaction devices [61] are being used to attain such objective. Catalytic systems [62] are natural targeted systems when talking about kinetics monitoring. Existing reaction monitoring methods include for instance colorimetry by applying

spectrophotometry techniques, mass spectrometry sometimes allied to forms of chromatography techniques, pH-metry, gas pressure measurement and other gas sensing techniques, and NMR.

Colorimetry quantifies human color perceptions. Spectrophotometry reduces its scope by strictly studying the physical correlates of color perception by means of spectral analysis. Since different chemical components present different radiation frequencies and their emitted spectral radiation changes during a chemical reaction, the formation of chemical products and reactants in forward and reverse directions can be therefore monitored by spectrophotometry. Such shifts allow for the characterization of the observed compounds and their respective concentrations. Fernandes et al. [63] put forward a review on novel approaches for colorimetric measurements in order to provide the necessary background for the wise choosing of the most appropriate colorimetric detector given the targeted application. An example of colorimetry-based system was presented by Wang et al. [64], where a microfluidic-colorimetric approach was developed to monitor air pollution. Doane et al. [65] used the photoluminescence color change in cesium lead iodide nanoparticles to monitor the kinetics of an external organohalide chemical reaction by halide exchange, while Lin et al. [66] were able to develop gradient-based colorimetric sensors for continuous gas monitoring.

Mass spectrometry allied or not with some variant of chromatography, as in GC–MS or in LC–MS, is another spectral-driven technique that can be employed in the monitoring of chemical reactions. This analytical technique measures the mass-to-charge ratio of ions, *i.e.*, a relation between a mass as a quantity of matter and a given particle electric charge – the ion in this case. The measurement outcomes using mass spectrometry are presented as mass spectrum plots, which are plots of the intensity of ion signals as function of the mass-to-charge ratios that provide determining information about chemical identities and structures of compounds, isotopic signatures and more generally, metrics about the masses of molecules and particles. One example of such mass spectrum plots for the toluene can be seen in Figure 7. Ray et al. [67] published an extensive review on modern approaches for analyzing chemical reactions employing mass spectrometry focusing on on-line methods, therefore excluding monitoring using off-line chromatography interfaced to mass spectrometry or other off-line techniques. In the other hand, Sun et al. [68] made a global review of AMS (Ambient Mass Spectrometry) methods for monitoring chemical reactions, including both on-line and off-line methodologies for a large range of reaction types.

PH-meters are employed in the measurement of the acidity / basicity of solutions. PH-metric measurements are a reflect of the hydrogen-ion activities in water-based solutions and therefore can be used as a technique for evaluating chemical reactions taking place in water, being therefore an indirect way of chemical reaction monitoring. The principles of ion-sensitive solid-state devices, *i.e.*, pH-metry capable sensors, were posed by Bergveld in 1970 [69]. Since

then, ISFET (Ion-Sensitive Field-Effect Transistor) technology was understood to be capable to be employed in pH-based reaction monitoring because its response to the variation of the solution pH [70], as seen in Figure 8. Although classic pH-meters are stablished equipment, there are efforts to design low-power, compact sensors to overcome known undesirable factors of classic technologies, which can be at the same time employed in chemical reaction monitoring, for example one which produces a pH change such as that of DNA base incorporation [71]. Moreover, since lots of pH-sensitive dyes exist [72] (we have all used pH test strips at least once in our lives), colorimetry is also a very nice tool to monitor reactions during which pH changes can be measured.

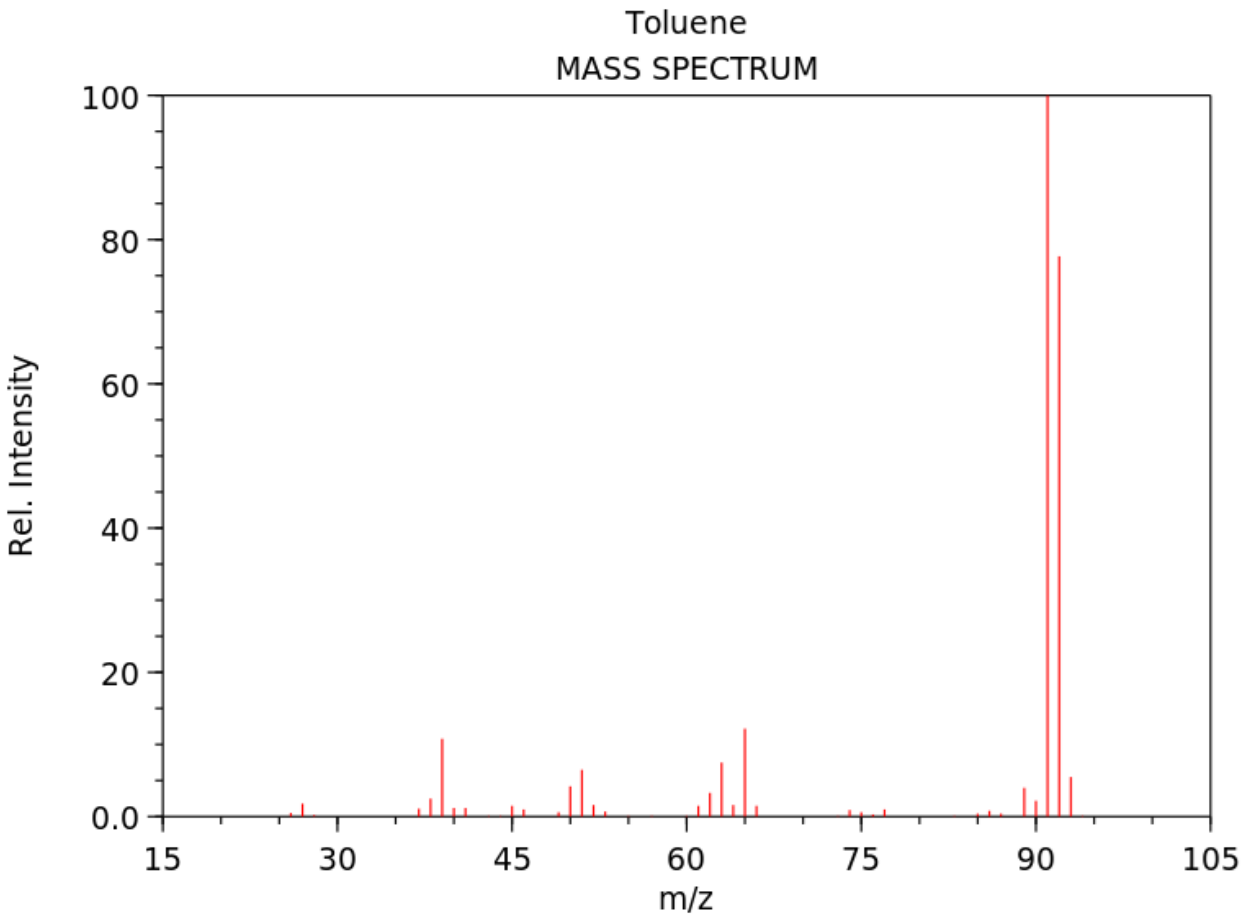

Figure 7 - One possible mass spectrum representation for the toluene: the relative intensity showing the isotopic distribution as function of mass-to-charge ratio values (m/z). Modified. [73]

On gas-based reactions, the measurement of the absolute or relative gas pressures and the analysis of their variations on time can be another way of reaction monitoring. For the case that the chemical reaction produces or consumes gas, therefore altering the overall gas pressure, the measure of the absolute gas pressure can be used as an indirect indicator of the reaction kinetics. For such scenario, a simple gas pressure sensor suffices. In the other hand, when the overall gas pressure stays the same although there are changes in the concentrations of the specific gas components of the reaction, a partial gas pressure measurement is

necessary, meaning that a particular gas pressure sensor specifically sensible to one or more of the involved gas components is mandatory. The second variant is clearly more complex and expensive to implement than the first one, especially when talking about integrated solutions. These scenarios, although less explored and only applicable with relatively low sensitivity to a range of chemical reactions, illustrate how reaction monitoring through gas pressure measurement is viable. The direct sensing of given types of gases is also used in chemical reaction studies, *e.g.*, for measuring ammonia evolution [74].

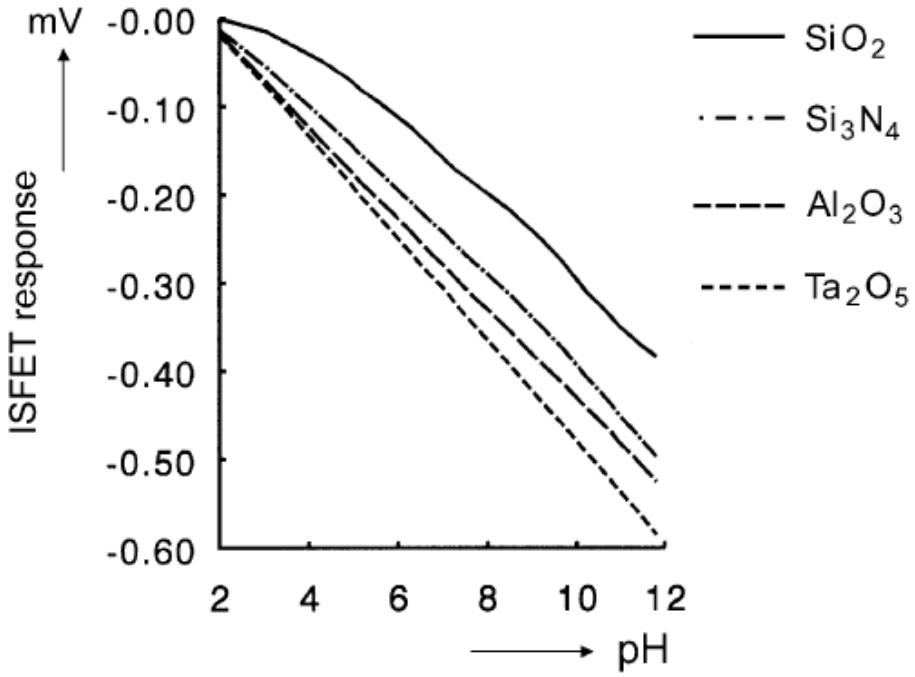

Figure 8 - ISFET response as function of the pH: this allows ISFET to be employed as a pH sensor. Modified. [70]

Finally, there is NMR spectroscopy, which is in the catalysis domain scope a suitable technology to be used within reaction monitoring [1] since it has already been used for years in the detection and quantification of molecules within solutions, it is non-specific, and therefore it is in this sense quite adaptable to different application scenarios. This technique is even more efficient for kinetics monitoring because it provides matched measurements on multiple molecules at once.

Usually, the reaction occurs within a small reactor with the standard NMR tube used to measure static solutions being replaced by a flow cell, allowing for the continuous solution transfer from the reactor to the measuring spot. During the reaction, acquisitions are performed periodically to follow the resulting spectral variations. Khajeh et al. [75] have employed such method in order to measure reaction kinetics, with resulting measured spectral lines looking like the ones in Figure 9.

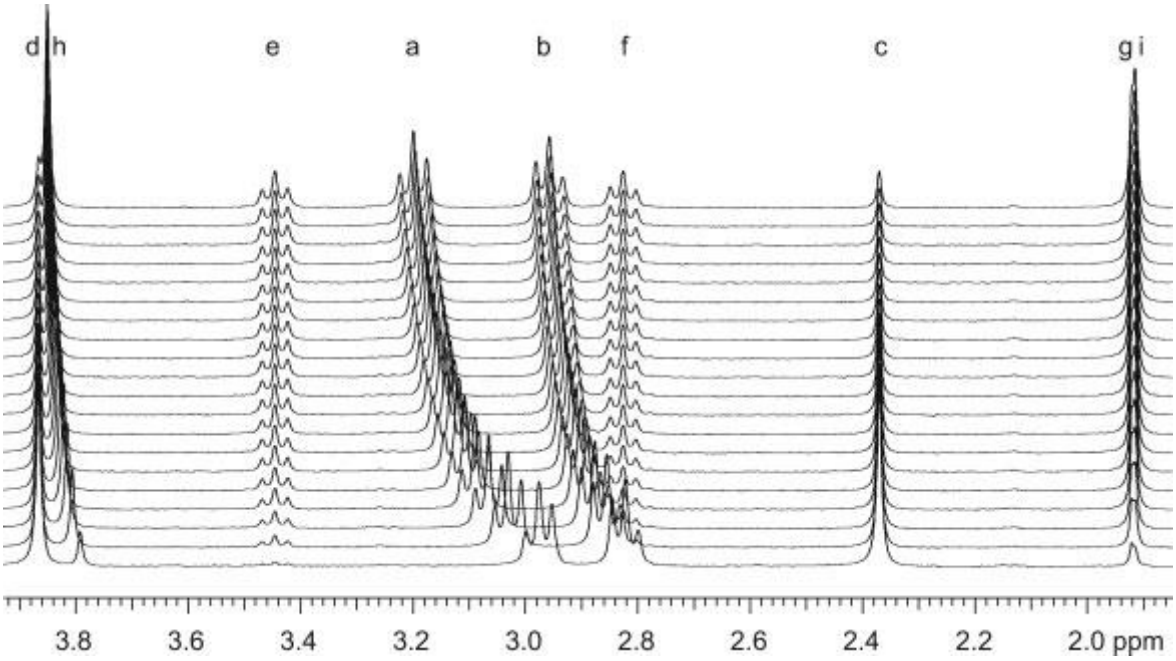

Figure 9 - Time course array for the solution of phenylethylamine and 2-methoxyphenyl acetate in D_2O, with every 35th spectrum from the first (bottom) to the last (top) shown, from 0 to 4 h reaction time. The lower-case letters from 'a' to 'i' correspond to the methyl and methylene signals. During the course of the reaction, the chemical shifts of signals 'a', 'b' and 'h' change as a result of the change in pH as hydrolysis proceeds. Modified. [75]

The method consisting in transferring the sample from the reactor to the flow cell is however problematic. If the solution transfer occurs too fast, the measurement quality decreases because a fraction of the excited nuclei within it will have already left the flow cell by the acquisition of the acquisition. In the other hand, if the transfer happens too slow, the reaction continues within the flow cell under uncontrolled conditions such as differing temperature and pressure, possibly resulting in inaccurate kinetic measurements. Additionally, the fact of having to transfer the solution after the reaction effectively starts induces a delay between the effective reaction occurrence and the measurement moment, which is inversely proportional to the flow rate. Consequently, the monitoring of the initial moments of the reaction are lost, fact that is problematic when talking about chemical kinetics, because these early measurements are of the utmost importance for this kind of analysis [76]. Continuous plug-like flow techniques [77] that act as real time measurement systems are a mean of latency mitigation, although distortions are still present in the analysis results.

Alternatively, there is the possibility of building micro-reactors inside the spectrometer itself, as explored by Brächer et al. [78]. They put in place a controlled micro-reactor for pressure and temperature in form of a so-called probe head inside the NMR spectrometer, which provided measurement results analogous to the ones presented on Figure 10.

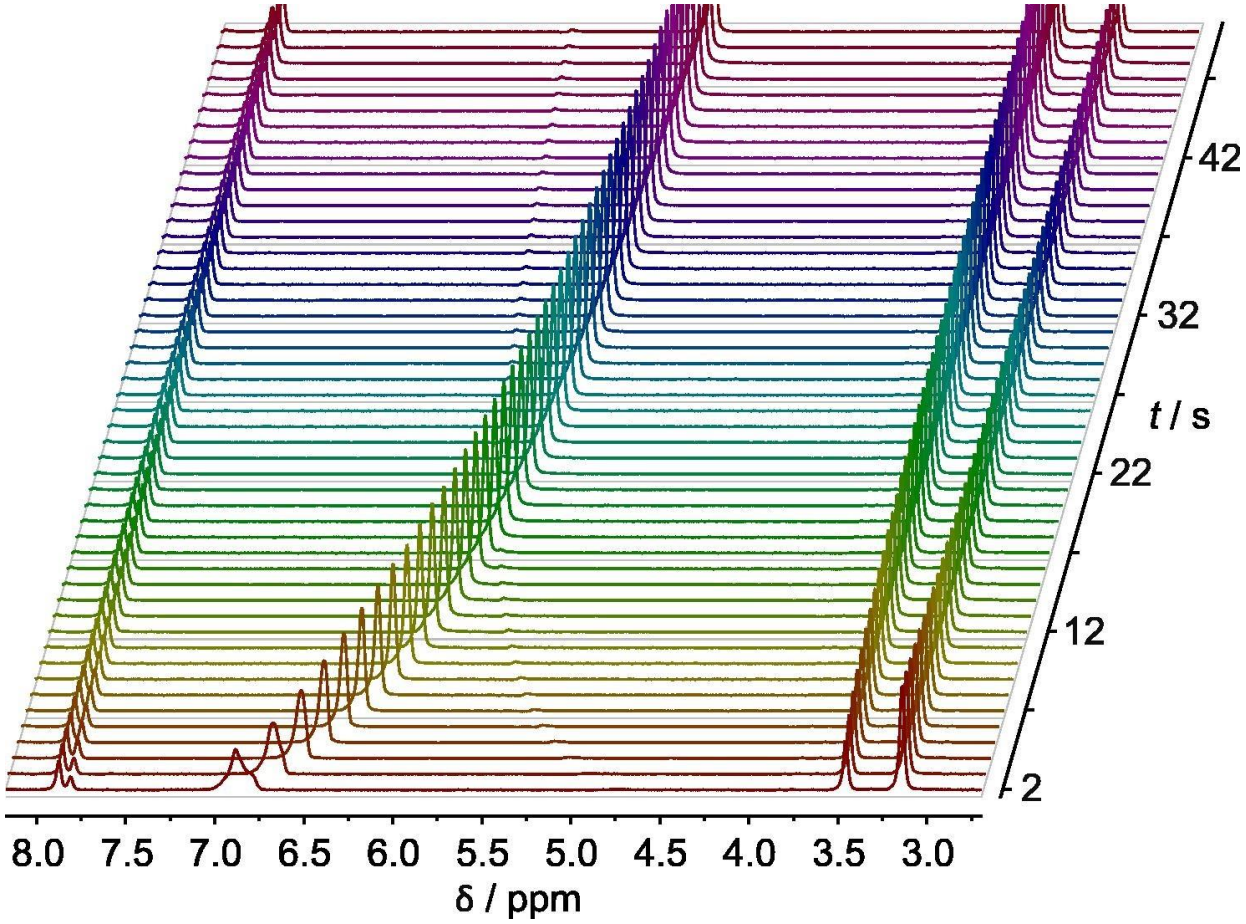

Figure 10 - Stacked plot of ^{1}H NMR spectra as a function of the reaction time. The spectra are acquired during the kinetic experiment of the MF (Methyl Formate) formation using 2 mass-% of sulfuric acid at 333 K. Modified. [78]

It is not without saying that such method is complex to implement and requires expensive, non-transportable equipment. Furthermore, the control of the experiment conditions within the micro-reactor is not straightforward and requires all the more complex construction processes as the complexity of the reaction itself increases.

Nonetheless, the use of low-field NMR spectroscopy is an important asset in what concerns process and reaction monitoring [79].

Within the reaction monitoring topic, many research papers exploring NMR spectroscopy as a mean of chemical reaction and process investigation are already available, as for instance on: (1) employing online low-field NMR spectroscopy for process control of an industrial lithiation reaction [80], (2) using benchtop NMR spectroscopy as an online non-invasive in vivo lipid sensor for microalgae cultivated in photobioreactors [81], (3) online process monitoring of a batch distillation by medium field NMR spectroscopy [82], (4) employing benchtop NMR for online reaction monitoring of the biocatalytic synthesis of aromatic amino alcohols [83], (5) on using benchtop flow-NMR for rapid online monitoring of RAFT (Reversible Addition−Fragmentation chain-Transfer) and free radical polymerisation in batch and continuous reactors [84], and on (6) optimising reaction performance in the pharmaceutical industry by

monitoring with NMR [85]. Many other industrial application notes can be currently found online, as for example on: (7) benchtop NMR reaction monitoring for kinetic profiling [86], (8) online monitoring of the formation of a diimine [87], (9) online monitoring of the N-acetylation reaction of L-phenylalanine [88], (10) online reaction monitoring of a nucleophilic aromatic substitution (S_NAr) reaction by ^{1}H and ^{19}F NMR [89], (11) quantifying the formation of stereoisomers by benchtop NMR spectroscopy [90], and on (12) monitoring a Claisen-Schmidt condensation reaction by NMR [91]. And although companies as Magritek [92] and Bruker [93] have reaction monitoring solutions based on NMR systems, currently they are definitively not yet miniaturized to a degree that could be considered as portable, as to bring the NMR to the field.

3.3. Towards portable miniaturized nuclear magnetic resonance spectroscopy

The previous sections showcased applications for which there is a natural trend or will to employ NMR spectroscopy. And although there is much available content on related scenarios where NMR can be already successfully used, the fully portable miniaturized solution is still lacking. Indeed, a portable miniaturized low-field NMR spectrometer would facilitate the analysis process in many cases due to its intrinsic flexibility and overall production cost, therefore being a valuable development within the NMR spectroscopy domain as well as a commercial competitive alternative regarding the currently available systems, which for most application areas are still tendentially both [94] high field fixed NMR spectrometers [95] [96] and medium to low field benchtop NMR spectrometers [97] [98] [99].

ZULF (Zero-to-Ultra-Low-Field) or ULF (Ultra-Low-Field) NMR is a promising spectrometry method, although currently highly experimental, as Buckenmaier et al. demonstrated for ^{1}H and ^{19}F NMR spectroscopy [100] and Zhukov et al. for ^{13}C NMR spectroscopy [101]. In the other hand, UHF (Ultra-High-Field) NMR spectroscopy is in the practice unviable for field analysis scenarios, even if, on NMR experiments, the SNR depends strongly on the strength of the static magnetic field $\overrightarrow{B_0}$. This was showcased by Moser et al. on their review of UHF NMR and MRI (Magnetic Resonance Imaging) use cases [102] and by Yanagisawa et al. on their own survey for the Asia region [103]. Indeed, the use of medium- to low-field more compact NMR systems *in lieu of* high field spectrometers seems to be possible and currently the most adapted technologies, being predicted for use within diverse applications where portability, size and weight, and overall costs play an important role.

Since at least a couple decades, the miniaturization of NMR systems is an intense investigation subject. Known portable miniaturized NMR spectrometer design bottlenecks are the miniaturization of the magnet responsible for generating the $\overrightarrow{B_0}$ magnetic field, the

integration of the measurement probe, among other specific design challenges. Concerning the size decrease of the permanent magnet, it is possible by replacing for instance a helium-cooled superconductor magnet by a small rare-earth permanent magnet. The counterpart to such magnet size decrease is however the reduction of the magnetic field strength and of its overall homogeneity, specially within the measurement area. This homogeneity decrease contributes straightforwardly to a loss of measurement sensitivity and resolution. Nevertheless, small magnet constructions based on Halbach [104] structures have already presented suitable performances [105]. One such Halbach magnet can be seen in Figure 11.

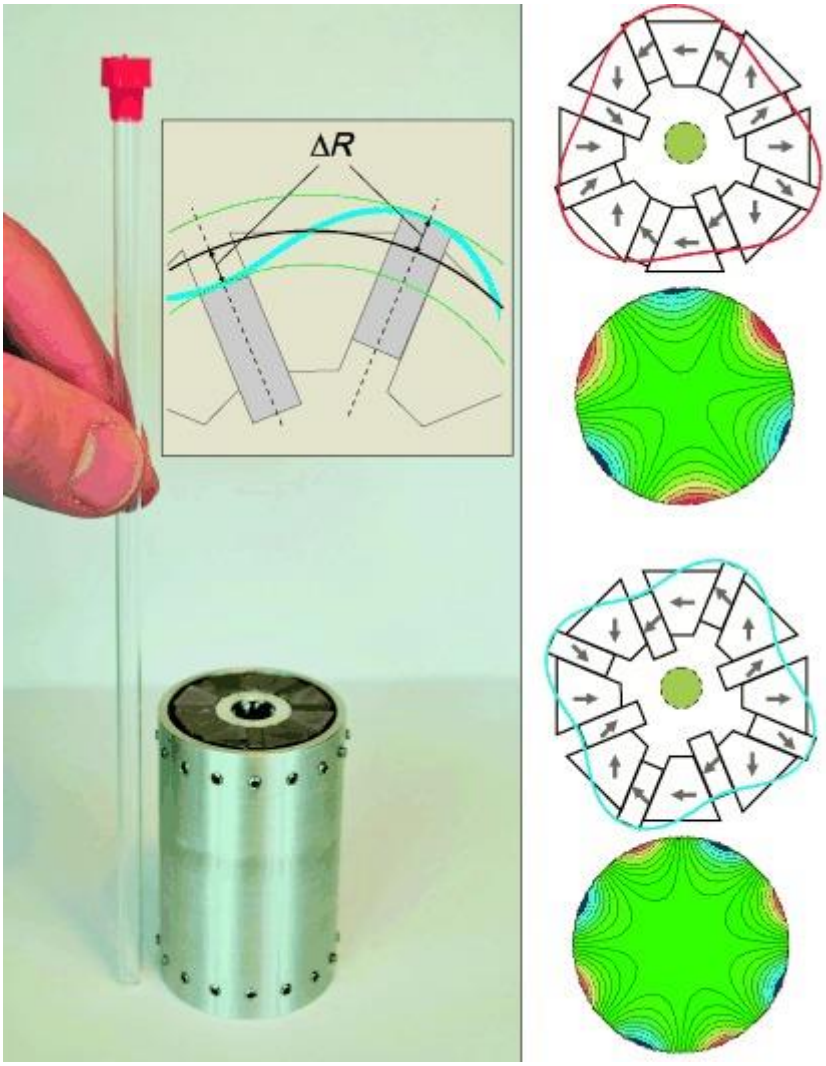

Figure 11 - Example of a Halbach magnet composed of rectangular and trapezoidal pieces of SmCo (Samarium–Cobalt) which generate a field of 0.7 T. Modified. [105]

In what concerns NMR measurement probes, the first work on planar micro-coils on gallium arsenide substrates for NMR use was published 30 years ago [106]. An example of the coil geometry produced back then is shown in Figure 12.

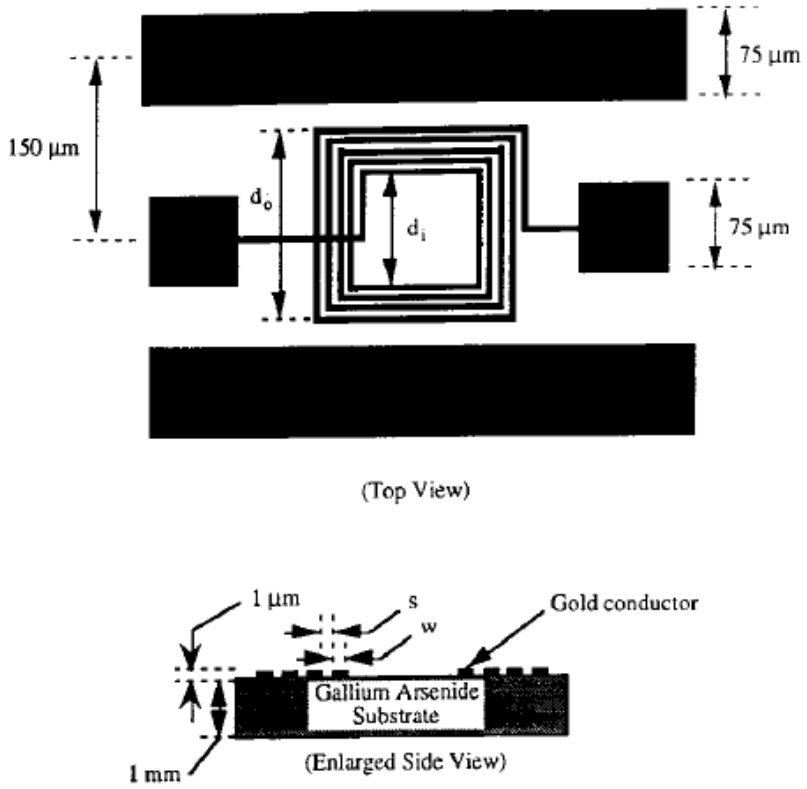

Figure 12 - Multiturn, planar microcoil configuration. [106]

Further developments comprise the improved design of such devices, where in many cases the integration of the micro-coil and the emission and reception electronic circuitry within the same IC (Integrated Circuit) unit is pursued. An example of such advancements applied to chemical reaction monitoring was published by Wensink et al [107]. Moreover, Sun et al. demonstrated that the genuine miniaturization of an NMR spectroscopy system towards real portability is possible [108]. To accomplish such great miniaturization, the authors employed a small commercial magnet and realized a remarkable integration of their electronic circuitry, utilizing in their setup as well as receiving coil a planar micro-coil, as shown in Figure 13. These advancements are inscribed in an evolutive design process, where at first in-house fabricated micro-coils with discrete electronics were used to prove the authors' innovative concepts [109].

On the topic of sanitary regulation, as it is also the case for safety related matters on the control of drinking water quality, Liu et al. [110] experimented the detection of avidin in given samples, employing for that their CMOS mini-NMR system from Figure 13 as well.

Another example of compact NMR spectroscopy system was provided by McDowell and Fukushima [111], where they employed a 1-T magnet weighting 685 g with an achieved line width of 0.24 ppm (parts per million).

Furthermore, within the NMR spectroscopy field and related ones, some alternative system designs already existed, and many others have since then followed: integration of microfabricated fluidic systems within NMR spectroscopy [112], use of microscale NMR probe technology [113], and employment of massive parallel MRI detector arrays [114] – to cite a few.

Finally, in what concerns the preferred design of the NMR system electronic circuitry, there are mainly two adopted approaches among researchers: the one preferring everything done from scratch and the one maximizing the use of COTS (Commercial Off-The-Shelf) components.

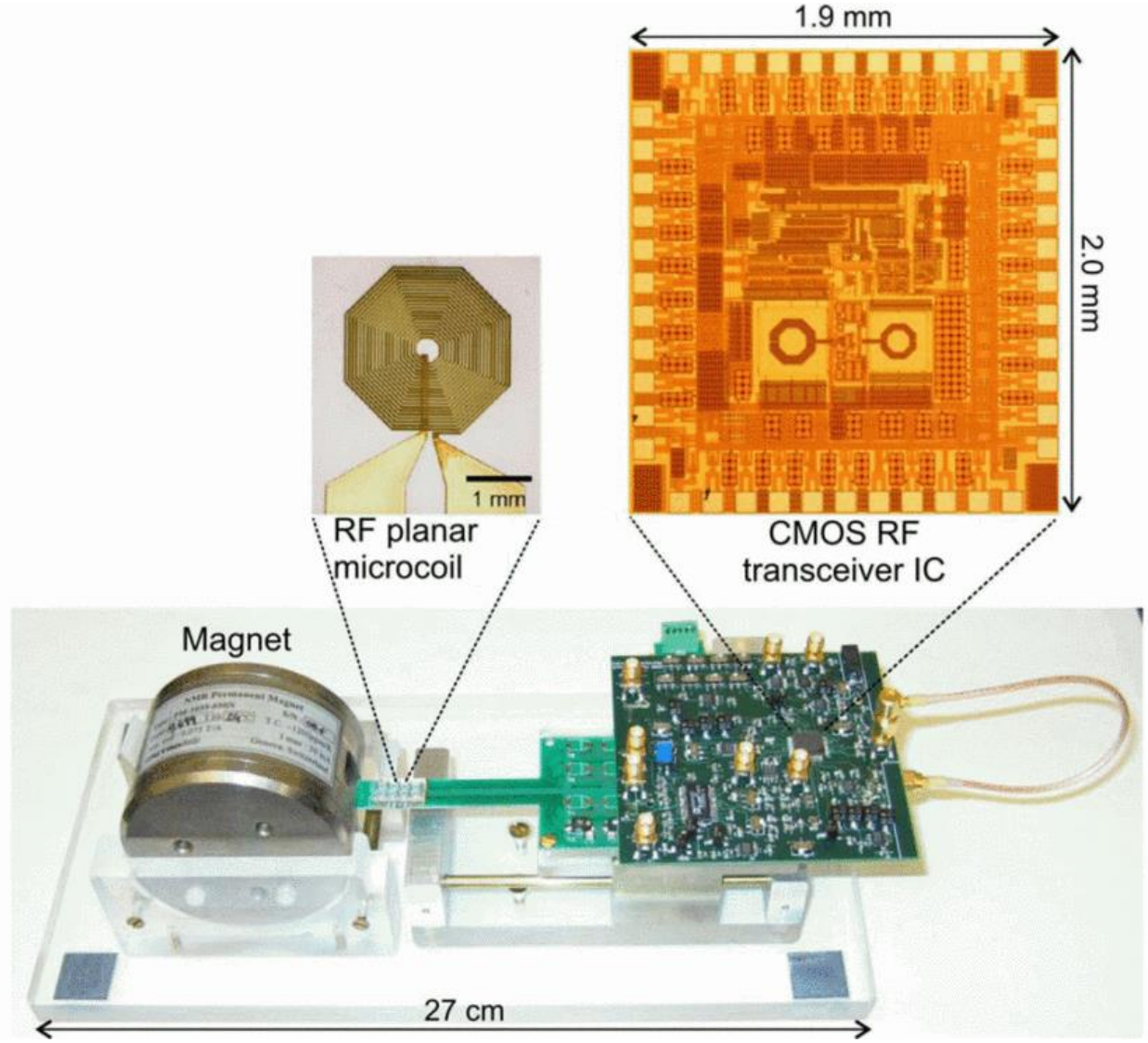

Figure 13 - CMOS RF biosensor utilizing NMR. The entire system weighs 2 kg, where the commercial magnet dominates the weight. Modified. ([108], [110])

Takeda et al. chose the first design philosophy and focused on developing the electronic circuitry for their NMR spectrometers basically from scratch. In a series of publications on: (1) a highly integrated FPGA-based nuclear magnetic resonance spectrometer [115], (2) open-source core modules for implementing an integrated FPGA-based NMR spectrometer [116], (3) annual reports on NMR spectroscopy [117], and on (4) an electro-mechano-optical NMR probe for ^{1}H-^{13}C double resonance in a superconducting magnet [118], they showcased the evolution of their OPENCORE NMR spectrometer shown in Figure 14. Kachkachi et al. also opted for this approach with their own (5) design and experimental validation of a SoC-FPGA-based compact NQR spectrometer [119].

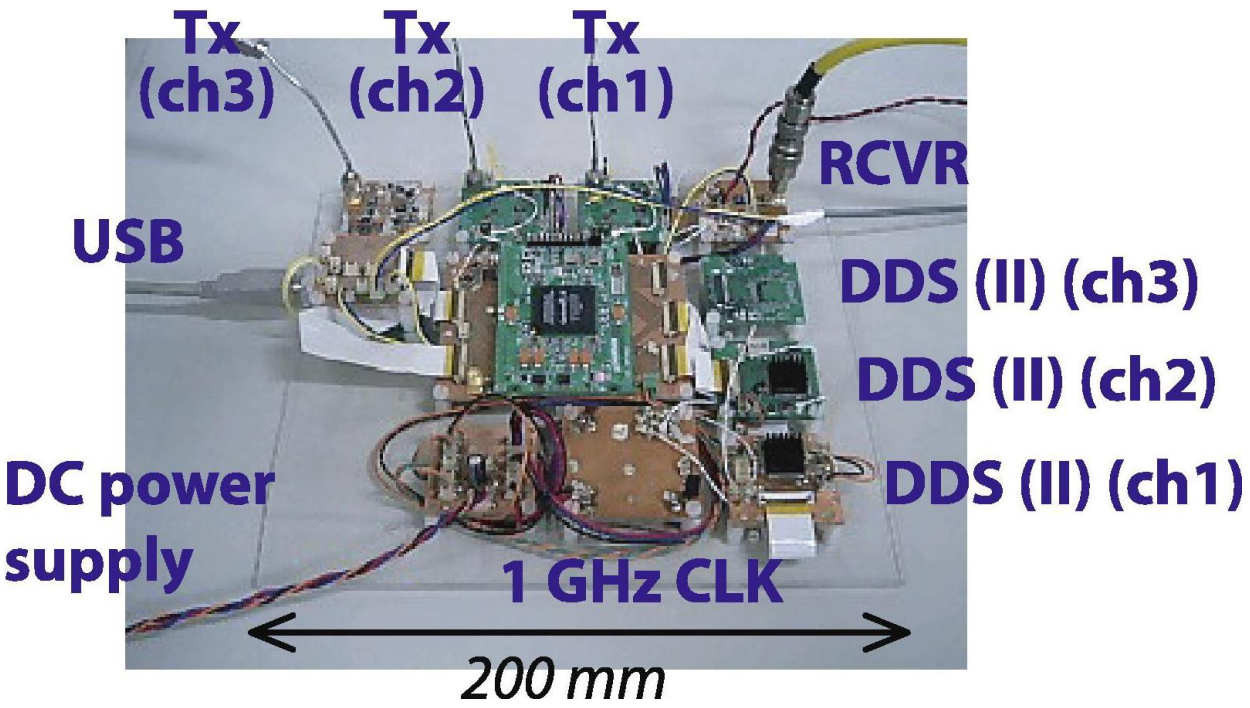

Figure 14 - A snapshot of an OPENCORE NMR spectrometer with home-built circuitry. Modified. [116]

Figure 15 - Lab-Tools Mk3 NMR Relaxation Spectrometer with a Red Pitaya STEMLab 125-14. Modified. ([120], [121])

In the other hand, Webber et al. opted for building NMR systems out of COTS (Commercial Off-The-Shelf) available hardware alternatives. They produced a series of publications mainly – but not only – on the suitable applications for their developed NMR system, *e.g.*, on: (6) a digitally based precision time-domain spectrometer for NMR relaxation and NMR cryoporometry [120], (7) the implementation of an easy-to-apply NMR cryoporometric instrument for porous materials [122], (8) credit-card sized field and benchtop NMR relaxometers using field programmable gate arrays [123], (9) a review of the use of simple time-domain NMR / MRI for material-science [121], and finally, on (10) some applications of a field programmable gate array based time-domain spectrometer for NMR relaxation and NMR cryoporometry [124], where their system Lab-Tools Mk3 NMR Relaxation Spectrometer, that can be seen in Figure 15, and his successor, the Lab-Tools Mk4 NMR Relaxation Spectrometer [125], were put forward.

NMR

This chapter illustrated the existing challenges and current advancements in what concern pollutants detection in drinking water and chemical reaction monitoring, two declared objectives to be addressed by our team research efforts. We demonstrated what is the state of the art within these two application fields and exposed alternative measurement methods used for those same purposes. Among all shown measurement methods, NMR fits both application fields requirements. With the application context available, we moved to show the state of the art of existing NMR-based measurement systems that somehow matched with aspects of our intended application areas. In this regard, we could disclosure work of some fellow researchers that, although not working explicitly towards the same goals and application scenarios, are as well exploring low-field NMR setups, which are tendentially low-cost and intrinsically low-resolution.

We are convinced that, for the applications targeted within this thesis, exploratory knowledge concerning the contents of the samples to be analysed will generate system performance expectancies, which in turn will impose certain technological constraints onto the manufacturing of portable miniaturized NMR systems. Our aim is therefore not to match the performance of current available commercial systems, but rather produce a low-cost and integrable device, whose intrinsic performance will forcibly be lower than that of commercial systems, however high enough for the targeted applications.

The next chapter will provide the reader with a targeted theoretical basis on the NMR effect from the perspective of a system designer and illustrate what are the necessary physical, chemical, and mathematical basic foundations for starting with the development of an NMR

spectrometer. An overview of the technological composing bricks of such systems are provided for a better understanding of how the NMR experiment happens within them.

Chapter 2 - Theoretical background

Nuclear Magnetic Resonance (NMR) is based on the principle of magnetic resonance, and it was first described in 1938 by Isidor Rabi et al. [126] based on the previous work of the duo Stern–Gerlach in 1921 and 1922 on the quantized aspect of the spatial orientation of angular momentum by providing experimental evidence of directional quantization in magnetic fields [127].

An NMR system is typically composed of a permanent magnet, a coil for the excitation of the sample and another for the measurement of the incoming NMR signal, and the necessary electronics to provide the excitation signal and process the measured NMR signal. In most systems, the excitation and the measurement coil are in fact the same physical coil, and it is addressed by the name *receiving coil* [128]. This is made possible by the use of an electronic switch that connects the receiving coil alternately to the excitation electronic circuit and to the readout circuit, as necessary. We therefore always refer to the NMR coil as the receiving coil, even when talking about it in the excitation context.

The next sections of this chapter propose a rationalisation of the NMR phenomenon focusing on the most important aspects when considering portable miniaturized NMR spectrometer devices.

2.1. Physical principle

Each considered chemical element taking part in the NMR experiment can present a magnetic moment which is an intrinsic form of angular moment of elementary particles, and it is called spin or more generally referred as spin quantum number of the particle. The spin itself is a result from the quarks composing the particle and are subject of study in relativistic quantum mechanics and quantum field theory. Having nuclear spins is a requirement for nuclei to undergo magnetic resonance. An unconstrained representation of these concepts can be seen in Figure 16. The atoms that are composed by an odd number of protons (^{1}H, ^{2}H, ^{14}N, ^{19}F, ^{31}P, etc.) or neutrons (^{13}C, etc.) participate in the NMR experiment, while the ones presenting an even number of both protons and neutrons (^{12}C, ^{16}O, etc.) are not able to.

Although other elementary particles present spin angular moments, as it is the case for the electron, NMR experiments take advantage of effects concerning nuclear magnetic moments only.

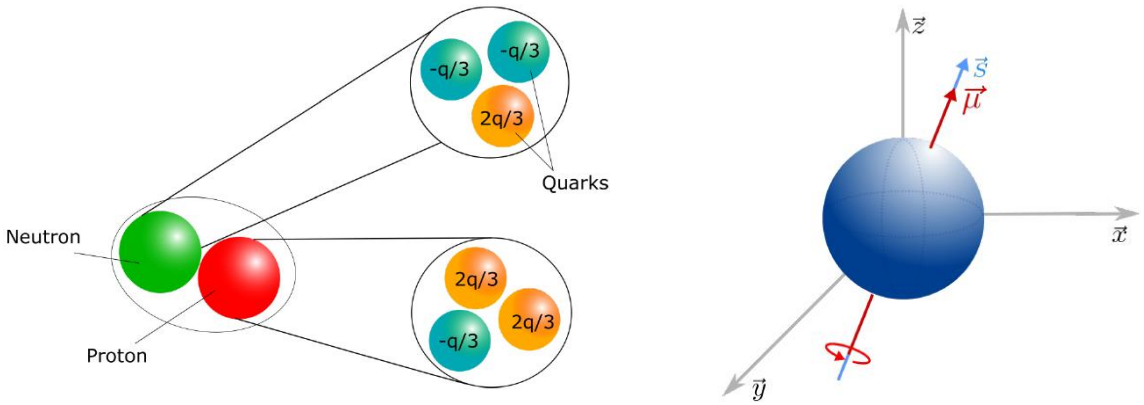

Figure 16 - Left side: quarks composing nuclei. Right side: it results in the existence of nuclear angular momentum $\vec{s}$ and magnetic moment $\vec{\mu}$. Modified. [2]

When considering a particle not immersed in any magnetic field, its magnetic moment is aleatorily directed and do not present any particular pointing bias. The same principle applies as well to a sample containing many molecules within a given considered volume under no magnetic field. Thus, at the macroscopic scale, no notable effect can be observed emanating from this sample because the average orientation of all single magnetic moments from each particle combined is zero. However, the fact of inserting the sample into a relatively strong static magnetic field orders the spins of the nuclei along its direction. This static magnetic field is called $\overrightarrow{B_0}$ in NMR. This is the stationary condition of the sample when inserted into an idle NMR spectrometer. Furthermore, under these conditions, the single ordered magnetic moments $\vec{\mu}$ of the particles within the sample can be perceived, at the macroscopic scale, as a single magnetization vector $\vec{M}$ with magnitude M_0 pointing towards $\overrightarrow{B_0}$. Figure 17 depicts the effect of inserting particles with existing spin quantum numbers into a static magnetic field $\overrightarrow{B_0}$.

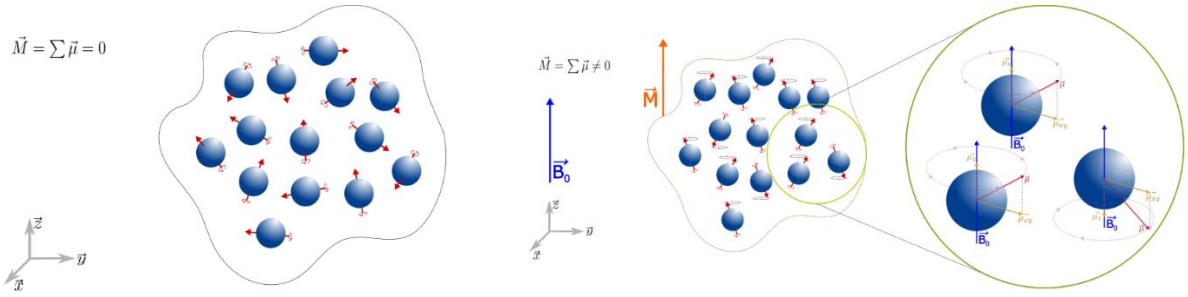

Figure 17 - Left side: in the absence of a static magnetic field, single magnetic moments are random. Right side: the presence of $\overrightarrow{B_0}$ tends to align these magnetic moments along its own direction. Modified. [2]

When aligning itself towards the static magnetic field $\overrightarrow{B_0}$, a single magnetic moment $\vec{\mu}$ does it in a well-defined manner called Larmor precession, and so does the magnetization vector $\vec{M}$. It is said that the single magnetic moments precess about the external magnetic field in which they are enclosed. Being the precession a 3D rotational movement, it happens at a

specific angular frequency called Larmor frequency, which depends on the strength of $\overrightarrow{B_0}$ and on the considered nucleus through its gyromagnetic ratio γ:

$$\omega_0 = \gamma B_0 \tag{1}$$

The Larmor frequency in terms of Hz is denoted f_0, and it is related to the Larmor angular frequency ω_0, that is expressed in terms of rad/s, as follows:

$$f_0 = \frac{\omega_0}{2\pi} \tag{2}$$

Therefore, for a given particle, f_0 is linearly related to the strength of $\overrightarrow{B_0}$ and to its gyromagnetic ratio γ as following:

$$f_0 = \frac{\gamma\, B_0}{2\pi} \tag{3}$$

With the sample enclosed in $\overrightarrow{B_0}$, by targeting it during the right time with an orthogonal RF signal at the material Larmor's frequency through a receiving coil, one can tip the magnetization vector perpendicularly to $\overrightarrow{B_0}$. This finite RF signal is called $\overrightarrow{B_1}$ in NMR. Immediately after $\overrightarrow{B_1}$ ceases to exist, the spins of the molecules start precessing back about $\overrightarrow{B_0}$ in a characteristic form that can be measured by the same receiving coil. Figure 18 shows these vectorial movements in detail.

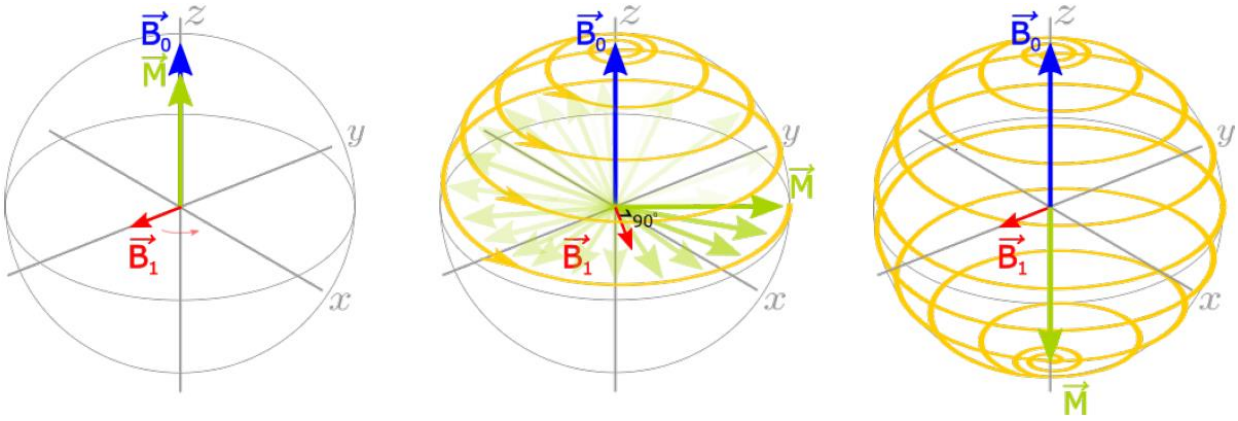

Figure 18 - Effect of applying a RF signal $\overrightarrow{B_1}$ to the sample already within $\overrightarrow{B_0}$. Left side: this is the exact moment where $\overrightarrow{B_1}$ is applied to the sample. At this moment, $\vec{M}$ is aligned towards $\overrightarrow{B_0}$. Middle: the duration of $\overrightarrow{B_1}$ was exact the necessary so that $\vec{M}$ is perpendicular to $\overrightarrow{B_0}$. If $\overrightarrow{B_1}$ ceases to exist exactly at this moment, $\vec{M}$ will precess from this position directly back about $\overrightarrow{B_0}$. Right side: the duration of $\overrightarrow{B_1}$ was so long that $\vec{M}$ is now opposite to $\overrightarrow{B_0}$. Modified. [2]

While in the considered volume, the precession about $\overrightarrow{B_0}$ has a helical form, and its projection in the Euclidean $(\vec{x},\vec{y})$ plane presents a decreasing radius tending to zero with the passing of the time. Moreover, if at the end of the excitation, *i.e.*, when $\overrightarrow{B_1}$ ceases, $\vec{M}$ is perpendicular to $\overrightarrow{B_0}$, its projection in the $(\vec{x},\vec{y})$ plane is at the maximal amplitude, which is of great practical interest.

During the reception process, the receiving coil senses $\vec{M}$ in this same $(\vec{x},\vec{y})$ plane. The precession of $\vec{M}$ about $\overrightarrow{B_0}$ takes thus the form of an amortized-on-time sinewave, as shown in Figure 19. In NMR, this characteristic signal is called an FID (Free Induction Decay) waveform. From a temporal perspective, an FID can be typically described by means of three main parameters [129]:

- the longitudinal or T_1-relaxation time, which is the time that the vectorial component of $\vec{M}$ aligned to $\overrightarrow{B_0}$ needs to attain $(1-1/e)M_0$, *e.g.*, about 63% of its maximal stationary value;
- the ideal transverse or T_2-relaxation time, which is the theoretical time that the vectorial components of $\vec{M}$ that are transversal to $\overrightarrow{B_0}$ would need to attain $1/e$ of its initial value, or about 37%, if $\overrightarrow{B_0}$ were perfectly homogeneous (this parameter depends primarily on atomic and molecular interactions);
- the actual transverse or T_2^*-relaxation time, which is the observed time that the vectorial components of $\vec{M}$ that are transversal to $\overrightarrow{B_0}$ need to attain $1/e$ of its initial value, or about 37%.

In practice, the T_2^* parameter is always shorter than T_2 and mainly depends on the inhomogeneity of $\overrightarrow{B_0}$: the more inhomogeneous $\overrightarrow{B_0}$ is, the shorter the observable FID will be.

At the macroscopic scale, it can be demonstrated that both time constants T_2 and T_2^* can be related to each other and to the average inhomogeneity of the static field σ_{B_0} within the sample volume as follows:

$$\frac{1}{T_2^*} = \frac{1}{T_2} + \frac{1}{T_{inhomogeneity}} = \frac{1}{T_2} + \gamma\sigma_{B_0} \tag{4}$$

where γ is the gyromagnetic ratio of a given nucleus and σ_{B_0} is a metric (*e.g.*, the standard deviation) of the inhomogeneity of the static magnetic field $\overrightarrow{B_0}$ within the sample volume.

The frequency of the FID, here denoted f_{FID}, is almost equal to the through $\overrightarrow{B_1}$ applied Larmor frequency f_0, but not quite. Intramolecular interactions change it slightly, acting like a kind of signature. These small changes in frequency are most often referred as chemical shifts δ, which are usually given in ppm, *i.e.*, 10^{-6} of the Larmor frequency, as follows:

$$f_{FID} = f_0\,(1+\delta), \qquad \delta = \frac{f_{FID} - f_0}{f_0} \tag{5}$$

It is worth noting that the difference $f_{FID} - f_0$ reflects the fact that historical conventions on chemical shift definition and nomenclature portrayed the measured resonating frequency as higher than the excitation frequency, what provides than positive values for the chemical shifts [130].

From these chemical shifts, NMR analysts can screen for and identify specific substances within the analysed sample. These chemical shifts of course affect the FID, but

because they are quite close to the Larmor frequency, it is difficult to perceive their temporal impact. Therefore, chemists always consider the FT (Fourier Transform) of the FID instead, which is called the NMR spectrum.

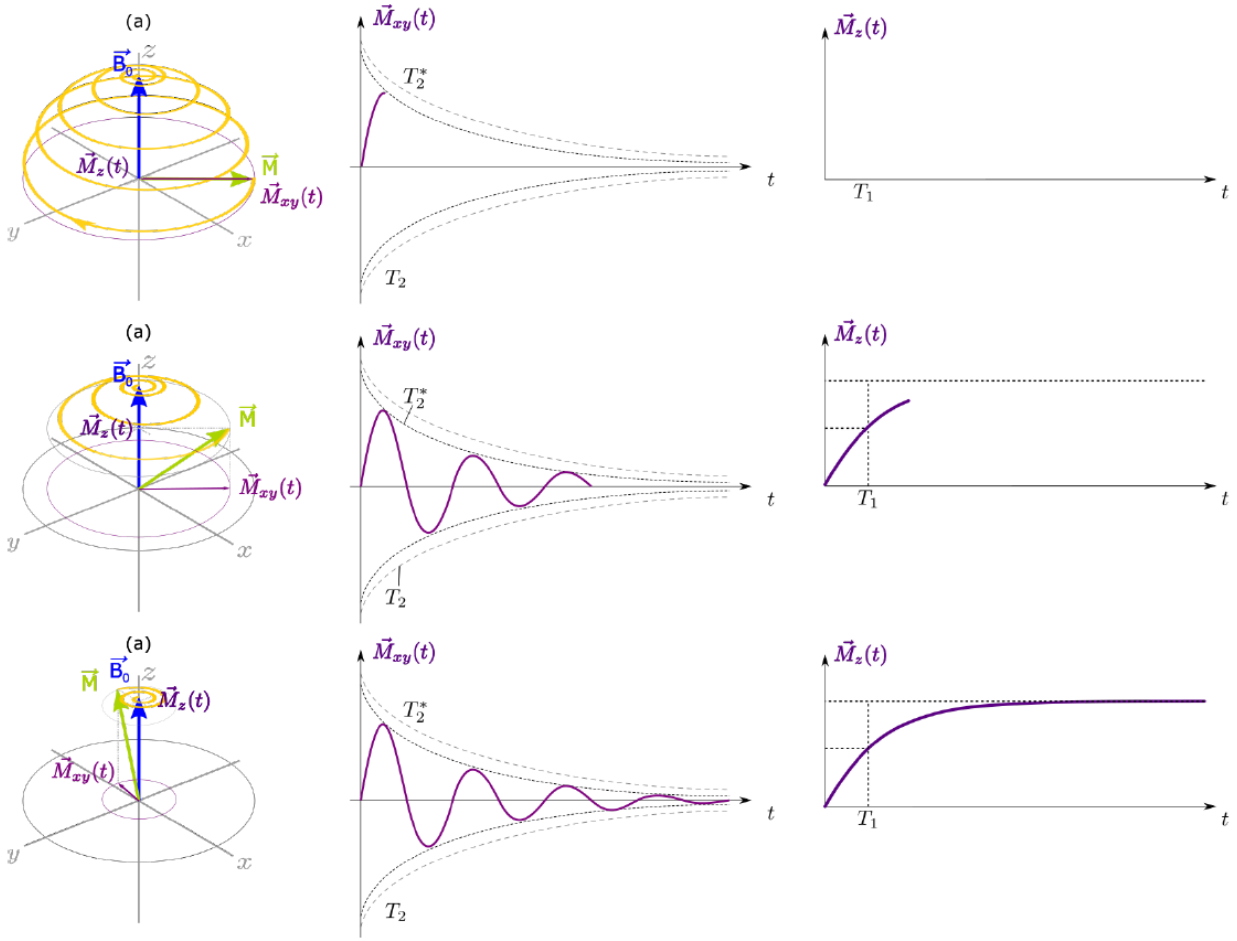

Figure 19 - Magnetization vector $\overrightarrow{\mathrm{M}}$ from the perspective of the receiving coil: the enclosing helix is perceived as an FID electrical signal by the coil. Top side: $\overrightarrow{\mathrm{B}_1}$ just ceased to exist and the precessing of $\overrightarrow{\mathrm{M}}$ about $\overrightarrow{\mathrm{B}_0}$ has just started. Middle: the precession has lasted a bit more than T_1, meaning that the vectorial component of $\overrightarrow{\mathrm{M}}$ which points towards the direction of $\overrightarrow{\mathrm{B}_0}$ has passed the mark of about 63% of its maximum stationary value M_0. Bottom side: the amplitude of the FID is practically 0, and up to this point the precession of $\overrightarrow{\mathrm{M}}$ about $\overrightarrow{\mathrm{B}_0}$ has already lasted more than T_2^*. Modified. [2]

Now, let the Dirac delta function be heuristically defined as:

$$\mathfrak{D}(x) \cong \begin{cases} +\infty, & x = 0 \\ 0, & x \neq 0 \end{cases}, \qquad \int_{-\infty}^{\infty} \mathfrak{D}(x)dx = 1 \tag{6}$$

Strictly theoretically, a single chemical shift δ, which is nothing else then a shift in frequency, would appear on the spectral representation as a Dirac delta function at this very shifted frequency providing that the nuclear magnetic resonance would last forever. However, as a same kind of atom, for instance ^{1}H, can be part of several different functional groups within

a studied sample, the resulting spectrum would therefore be a sum of Dirac-like impulses, each of them corresponding to a particular chemical shift reflecting the influence of a particular functional group where the observed kind of atom participates.

Moreover, due to the relaxation time depicted in Figure 19, the peaks are more Lorentzian-shaped than Dirac-like. As stated above, in practice, the relaxation time is always dominated by T_2^*. Thus, the width of the Lorentzian-like peaks increases as T_2^* decreases, up to the point where the peaks start overlapping.

As T_2^* depends on $\overrightarrow{B_0}$ field inhomogeneity according to equation (4), we emphasize that field homogeneity is a critical factor when aiming at keeping a high spectral resolution. Depending on the shape of $\overrightarrow{B_0}$ inhomogeneity, the deformation of the spectral peaks can take far more complex shapes than simple Lorentzian-like ones, as we will see in the next chapter. A high-homogeneous field is much more challenging to obtain on low-field NMR than on high-field NMR devices. In order to illustrate this purpose, Figure 20 contrasts the low- and high-resolution NMR spectra for ethanol, where we can see the overlapping of some spectral peaks.

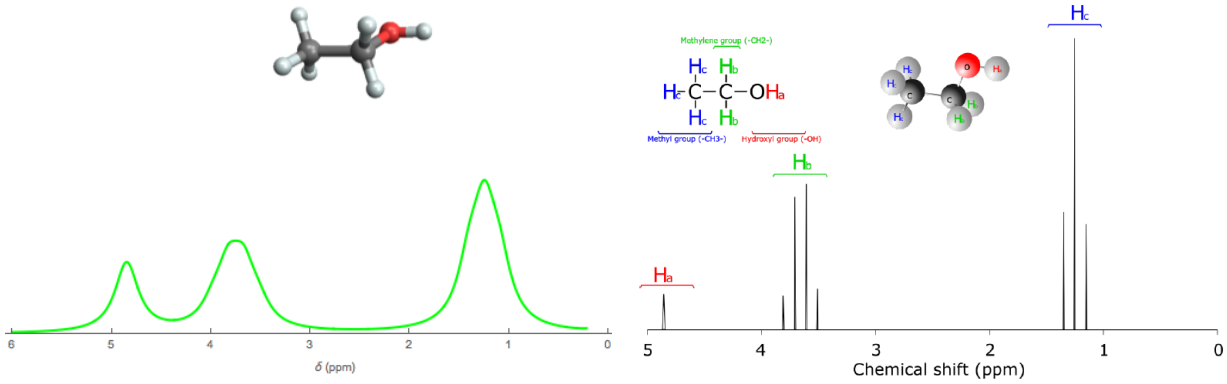

Figure 20 - NMR chemical shift representation of ethanol. Left side: a representation of the earliest detection of the chemical shift, obtained at Stanford University in 1951; the three peaks in ethanol have approximate δ values of 4.85, 3.75 and 1.25, with relative intensities identifying these with the OH, C^{H_2}, and C^{H_3} protons, respectively. Right side: at higher resolution, spin-spin splittings can be observed for this typical ^{1}H NMR ethanol spectrum. Modified. [131] and [2]

^{1}H NMR, also called proton NMR, for which the atom of interest is the hydrogen, exhibit spectra whose line intensity for a given molecule with nuclei having proton spins ($s = 1/2$) respect a multiplicity criterion due to J-couplings (also called spin-spin coupling) that are in the form of a Pascal's triangle, as the one that can be seen in Table 2. By means of apportion, it is possible to categorize the spectral outcome following Table 2 by estimating the ESD (Energy Spectral Density) and relating it to the possible NMR spectral forms, so to estimate how much energy belongs to each peak and therefore which multiplicity applies. Nuclei with other spin quantum numbers present different line intensity ratio distributions [132].

Multiplicity	Intensity ratio	Number of hydrogens on the neighbouring carbon (N)	Number of lines per peak (N+1)
Singlet	1	0	1
Doublet	1:1	1	2
Triplet	1:2:1	2	3
Quartet	1:3:3:1	3	4
Quintet	1:4:6:4:1	4	5
Sextet	1:5:10:10:5:1	5	6
Septet	1:6:15:20:15:6:1	6	7
Octet	1:7:21:35:35:21:7:1	7	8
Nonet	1:8:28:56:70:56:28:8:1	8	9

Table 2 - Multiplicities (N+1) and line intensity ratios for a nucleus that is split by N identical nuclei of spin $1/2$. Partially extracted from [133].

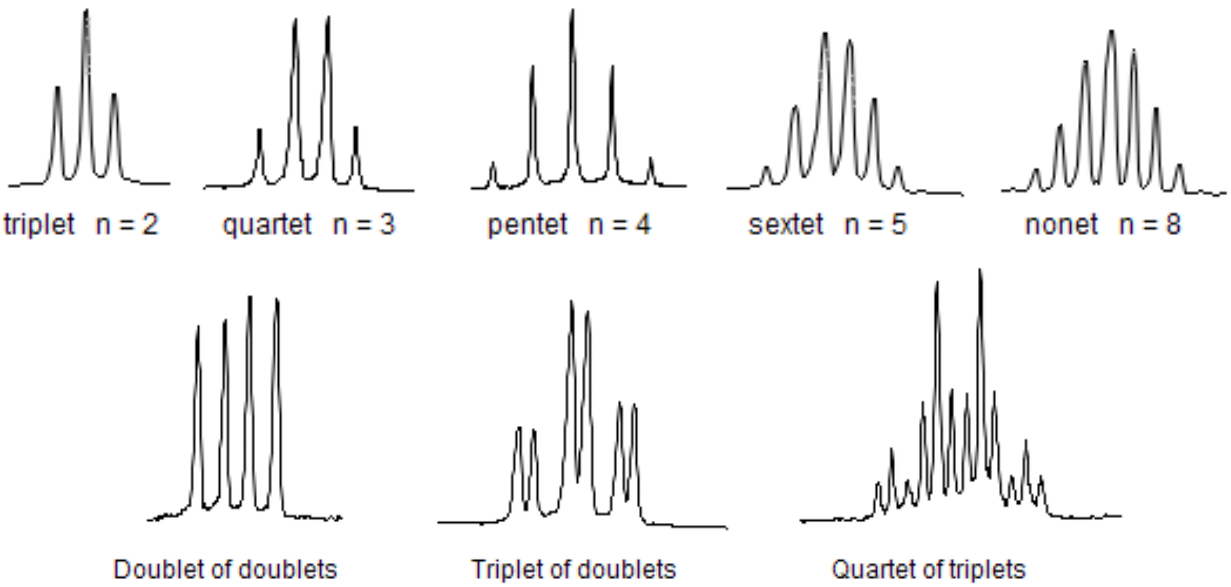

Figure 21 - Top side: single peaks with different line multiplicities. Bottom side: multiple peaks and their line multiplicities. Modified. [134]

Theoretically, NMR spectra present well-known peak and line intensity ratios. From the characteristic frequency response of an NMR spectrum, it is possible, after estimating the

amplitude of one single peak, to determine the remaining peaks amplitudes by calculating them. An artistical representation of lines per peak as well as some peaks with different line multiplicities are shown in Figure 21.

2.2. Mathematical outline

After this general overview of the physical principle of the NMR phenomenon, we proceed by detailing how the involved electrical quantities can be mathematically formalized. For the sake of simplicity, we consider under this section an NMR signal presenting a single chemical shift. The generalization of this mathematical framework for samples where molecules present several distinct chemical shifts can be easily accomplished by means of the mathematical principle of superposition. Indeed, an FID presenting several chemical shifts is in fact the sum-on-time of single corresponding chemical-shifted FIDs. The same mathematical principle of superposition applies as well to the corresponding Fourier transforms because of the linearity property of this mathematical operation.

In ideal conditions, the mathematical description of an FID measured by the receiving coil is the following:

$$\mathcal{s}_{FID}(t) = \mathcal{s}_0 \cos(\omega_{FID} t) e^{\frac{-t}{T_2^*}} \qquad \forall\, t \geq 0 \tag{7}$$

where ω_{FID} is the angular frequency of the FID in rad/s. This equation is in fact the real part of the quadrature form of the FID, which is given by:

$$\mathcal{s}_{FID}^{Q}(t) = \mathcal{s}_0 [\cos(\omega_{FID} t) + i \sin(\omega_{FID} t)] e^{\frac{-t}{T_2^*}} \qquad \forall\, t \geq 0 \tag{8}$$

In both cases, the envelope of the FID, *i.e.*, the external shape containing the FID is:

$$\varepsilon_{\mathcal{s}_{FID}}(t) = \varepsilon_{\mathcal{s}_{FID}}^{Q} = \pm \mathcal{s}_0 e^{\frac{-t}{T_2^*}} \qquad \forall\, t \geq 0 \tag{9}$$

At $t = 0$, which from now on is meant to be the exact moment where the sample excitation through $\overrightarrow{B_1}$ ceases and the FID itself begins, the maximum amplitude value for these functions happens, namely:

$$\mathcal{s}_0 = \omega_0 M_0 V B_u \tag{10}$$

where ω_0 is the Larmor angular frequency in rad/s, M_0 is the magnitude of the magnetization vector of the sample in the direction of the static magnetic field in A/m at $t = 0$, V is the considered volume in m^3 and B_u is the unitary field of the coil in T/A. Therefore, $\mathcal{s}_0$ is the maximum amplitude of the NMR signal for a given volume V, while $\mathcal{s}_{FID}(t)$ or $\mathcal{s}_{FID}^{Q}(t)$ represent the temporal behavior of this FID signal for this given volume V, and are measured in volts.

The magnitude of the magnetization vector $\vec{M}\big|_{t=0}$ is dependent on many physical factors, including the considered sample temperature T and the static magnetic field $\overrightarrow{B_0}$, which

itself is highly dependent on the temperature T. This means that variations of these variables engender variations of the magnitude of the magnetization vector, however to different degrees:

$$M_0 = B_0 \frac{N_s(\gamma\hbar)^2 s(s+1)}{3kT} \tag{11}$$

where:

$$N_s = n_h \frac{P_{ab}}{100} c_i N_a \tag{12}$$

being [135]:

- N_s the number of spins per unit volume.
- γ the gyromagnetic ratio.
- $\hbar$ the reduced Planck constant *i.e.*, $\hbar = \frac{h}{2\pi} = 1.05\ldots \times 10^{-34}$ Js.
- s the spin quantum number associated with the spin angular momentum, which can assume the values of $[0, \frac{1}{2}, \frac{3}{2}, 2, \ldots]$.
- k the Boltzmann constant, which is 1.380649×10^{-23} J/K.
- T the sample temperature in K.
- n_h the number of nuclei participating in the NMR.
- P_{ab} the abundance of the observed chemical element, usually given as a percentage.
- c_i the molecular concentration in mol/kg.
- N_a the Avogadro constant, which is $6.02214076 \times 10^{23}$ mol^{-1}.

Indeed, the impact of temperature variation on the strength of magnetic fields is known [136]. In NMR, it means that by changing the temperature, we engender a change of the experiment Larmor frequency f_0 following equation (3). It follows that changes in temperature during a measurement lead to a corresponding change of the experiment Larmor frequency while the experiment is taking place, as well as dynamically changing the magnetization vector $\overrightarrow{M_0}$ and thus the very amplitude of the NMR signal following equation (10). All these temporal changes that lead to the change of f_0 as an end effect fall under the term of *temperature drifting*, which is a close synonym of the term *field drifting* in NMR. This is because the primary impact of the change in temperature is the change of the strength of the magnetic field. However, NMR chemical shifts are *per se* already temperature dependent [137], and this can lead to further unexpected changes of the NMR analysis outcome [138]. These effects will be rediscussed later in the experimental-related part of the manuscript.

Still concerning the mathematical description of the NMR signal, it is important to notice that we directly employ T_2^* instead of T_2 in equations (7) and (8), because it gives us the mathematical representation of the realistic perceived FID that one is going to measure with an ideal receiving coil, therefore already taking into consideration field inhomogeneity. The real relaxation time is always shorter than the theoretical one, meaning that the less homogeneous

the static magnetic field $\overrightarrow{B_0}$ is, the faster the FID amplitude decreases into the existing electronic noise floor of the employed measurement channel.

The frequency information of the FID can be extracted by means of the FT operand, where the FT of a given function in the time domain provides us with a corresponding function in the frequency domain. This resulting function reflects the frequency components composing the time domain original signal. The FT $\mathfrak{F}(f)$ of any given time-domain signal $f(t)$ is defined as:

$$\mathfrak{F}(f) = \int_{-\infty}^{\infty} f(t) e^{-i2\pi f t} dt \tag{13}$$

Since the considered NMR signal $\mathcal{s}_{FID}^{Q}(t)$ starts by definition at $t = 0$, we limit the lower limit of the integration to zero, and therefore, its FT is:

$$\begin{aligned} S_{FID}^{Q}(f) &= \int_{0}^{\infty} \mathcal{s}_{FID}^{Q}(t) e^{-i2\pi f t} dt = \mathcal{s}_0 \int_{0}^{\infty} [\cos(\omega_{FID} t) + i\sin(\omega_{FID} t)] e^{\frac{-t}{T_2^*}} e^{-i2\pi f t} dt \\ &= \mathcal{s}_0 \int_{0}^{\infty} e^{i\omega_{FID} t} e^{\frac{-t}{T_2^*}} e^{-i2\pi f t} dt = \mathcal{s}_0 \int_{0}^{\infty} e^{i\omega_{FID} t - \frac{t}{T_2^*} - i2\pi f t} dt \\ &= \mathcal{s}_0 \int_{0}^{\infty} e^{t(i\omega_{FID} - \frac{1}{T_2^*} - i2\pi f)} dt \end{aligned} \tag{14}$$

following the application of Euler's formula:

$$e^{ix} = \cos(x) + i\sin(x), \qquad \forall x \in \mathbb{R} \tag{15}$$

For an NMR signal, analogously to equation (2), its angular frequency relates to its frequency in terms of Hz as follows:

$$\omega_{\mathrm{FID}} = 2\pi f_{\mathrm{FID}} \tag{16}$$

By solving the integral in equation (14), and then substituting the Larmor angular frequency by its equivalent in Hz, we have as result:

$$S_{FID}^{Q}(f) = \frac{\mathcal{s}_0}{2\pi} \left[\frac{e^{t(i\omega_{FID} - \frac{1}{T_2^*} - i2\pi f)}}{i\omega_{FID} - \frac{1}{T_2^*} - i2\pi f} \right]_0^{+\infty} = \frac{\mathcal{s}_0}{2\pi \left(i2\pi (f_{FID} - f) - \frac{1}{T_2^*} \right)} \tag{17}$$

The corresponding ESD (Energy Spectral Density) is provided by calculating $|S_{FID}^{Q}(f)|^2$ and is given in V^2/Hz when no normalization on impedance is performed. Therefore:

$$\left| S_{FID}^{Q}(f) \right|^2 = \frac{{\mathcal{s}_0}^2}{\left(\frac{1}{T_2^*} \right)^2 + (2\pi (f_{FID} - f))^2} \tag{18}$$

The whole ESD amount calculated from (18) is split among all occurring Lorentzian-like spectral peaks for molecules with a spin $1/2$ following the schema from Table 2:

- For a singlet, the whole ESD belongs to the single peak.

- Doublets share the half of the total ESD, *i.e.*, each peak accounts for $\frac{|S_{FID}^{Q}(f)|^2}{2}$.
- Triplets present a split ratio of 1:2:1, *i.e.*, $\frac{|S_{FID}^{Q}(f)|^2}{4}$, $\frac{|S_{FID}^{Q}(f)|^2}{2}$ and $\frac{|S_{FID}^{Q}(f)|^2}{4}$.
- And so on for the further cases of multiple spectral peaks.

In order to define the related SNR, one has to move from the transient scenario where the ESD is the suitable measuring unit and consider the process as stationary, therefore considering the concept of PSD (Power Spectral Density). For this however, we first introduce the DFT (Discrete Fourier Transform) $\mathfrak{X}_k$, since we typically evaluate the sampled FID, instead of its analogue counterpart:

$$\mathfrak{X}_k = \sum_{n=0}^{N-1} x_n e^{-i2\pi\frac{k}{N}n} \tag{19}$$

where a sequence of N discretized time-domain points $\{x_n\} := x_0, x_1, \dots, x_{N-1}$ is transformed in a frequency-domain sequence given by $\{\mathfrak{X}_k\} := \mathfrak{X}_0, \mathfrak{X}_1, \dots, \mathfrak{X}_{N-1}$.

Now, one of Parseval's theorem understandings is that the total energy of a signal, *i.e.*, the ESD, can be calculated by summing power-per-sample across time or spectral power across frequency. It means that PSD is in fact the ESD normalized by the number of samples N composing the frequency spectrum, being the average power P_{signal} of the measured FID:

$$P_{signal} = \frac{1}{N}\sum_{k=0}^{N-1} |\mathfrak{X}_k|^2 \tag{20}$$

In the same way, it is interesting to look at the PSD from the perspective of the receiving coil so to take into consideration its thermal noise P_{noise}^{coil}:

$$P_{noise}^{coil} = 4kTR_{coil} \tag{21}$$

where R_{coil} is the receiving coil resistance.

For a given bandwidth Δf, the corresponding noise level on the receiving coil $V_{RMS_{noise}}^{coil}$ given in V/√Hz is:

$$V_{RMS_{noise}}^{coil} = \sqrt{4kTR_{coil}\Delta f} \tag{22}$$

The SNR is commonly defined as the ratio of the average power of a given signal to the average power of the existing and not desired noise P_{noise}, which encompasses not only the thermal noise of the coil P_{noise}^{coil}, but also noise from the electronics and further noise from any additional noise sources:

$$\mathrm{SNR} = \frac{P_{signal}}{P_{noise}} \tag{23}$$

As signal and noise must be evaluated at the same underlying conditions, including considered impedance, the SNR can also be seen as the ratio between the squared RMS (Root

Mean Square) amplitudes $V_{RMS_{signal}}$ (corresponding to P_{signal}) and $V_{RMS_{noise}}$ (corresponding to P_{noise} and comprising $V_{RMS_{noise}}^{coil}$ as well as noise from the electronics and further noise sources):

$$\mathrm{SNR} = \left(\frac{V_{RMS_{signal}}}{V_{RMS_{noise}}}\right)^2 \tag{24}$$

At this point, for instance, one can estimate the theoretical existent noise level in the receiving coil and its impact on the measured NMR signal by calculating the SNR from the PSD values of the FID signal and of the thermal noise of the receiving coil:

$$\mathrm{SNR} = \frac{1}{4kTNR_{coil}} \sum_{k=0}^{N-1} |\mathfrak{X}_k|^2 \tag{25}$$

In case there is an estimation of the PSD due to the system electronics or from the whole acquisition channel including external noise sources, it must be incorporated into (25) as well, undoubtedly bringing the resulting value of the SNR down. Rated values [2] in RMS terms for the overall input referred noise of the acquisition channels are in the range 1 to 3.5 nV/√Hz for portable miniaturized NMR systems working with static magnetic fields in the range 0.5 to 5 T.

In a general note, it is worth pointing out that the SNR level can be improved by either increasing signal level or decreasing noise level. Decreasing noise levels can be attained in a classic fashion by improving the electronics and the receiving coil design, and by better isolating the system against external noise sources. In what concerns the improvement of the measured signal level, the way forward is by optimizing the terms composing $\mathcal{S}_0$ in equation (10) and therefore in the equations (3) and (11): the increase of the strength of the static magnetic field $\overrightarrow{B_0}$, *i.e.*, of the Larmor frequency f_0, the increase in the considered experiment volume V, the increase of the receiving coil sensitivity, and the decrease of the experiment temperature all favor the increase of the measured signal level.

2.3. Hardware for miniaturization.

According to the hereabove considerations, the minimum set of conditions for the NMR phenomenon to happen is:

- a so homogenous as possible static magnetic field $\overrightarrow{B_0}$,
- an RF varying magnetic field $\overrightarrow{B_1}$ at Larmor's frequency,
- and a so stable as possible measuring temperature.

On top of that, the system has to be able to measure the resulting NMR signal with enough sensitivity in order to overpass the intrinsic noise of the receiving part of the system, process it, and provide the results in due form to the NMR analyst. An NMR spectrometer has

therefore to provide all these necessary elements such that the NMR experiment can take place within an acceptable quality of measurement for the desired analysis.

When considering portable miniaturized NMR systems, we already delineate some of the systems technical and working characteristics, although the physical principles of the NMR are the same taking place. The portability and the miniaturization of NMR systems engender some design constraints of the system hardware composing pieces that are mainly related to the facts that such systems should (1) weight as less as possible – therefore limiting the size of the magnet producing the static magnetic field $\overrightarrow{B_0}$, (2) not need complex and resource consuming stabilization mechanisms to work – avoiding hence the extreme refrigeration and temperature stabilization of the sample measuring mechanism, (3) consume as less as possible energy while being able to autonomously work as long as possible on the field, (4) and generally try to optimize all system engineering characteristics usually relevant for portable miniaturized systems.

Point (1) limits therefore the strength of $\overrightarrow{B_0}$ that usually is stronger the more magnetic material we are able to put together, placing us forcibly in low to medium field NMR, where the Larmor frequency is in the MHz range, usually not going over a hundred megahertz. Point (2) engenders the impossibility of working with too low stabilized temperatures – in opposition to other laboratory NMR systems that can incorporate such feature – and also makes more difficult the stabilization when working within ambient to high temperatures whatsoever, imposing the system operation under temperature drifting conditions. Points (3) and (4) impose classic engineering requirements when talking about portability and miniaturization of systems – as having to consider what kind of power source will be deployed, how will be the provided autonomy in terms of energy requirements as well as in terms of operational requirements, how such systems will work under harsh conditions when on the field, etc.

The different hardware parts of an NMR spectrometer can generally be categorized within the following main building blocks:

(a) permanent magnet unit or other form of magnetic field generation (to provide $\overrightarrow{B_0}$).
(b) temperature control system to stabilize the temperature within the measuring volume (to best possibly avoid temperature drifting).
(c) shimming coils (to improve the homogeneity of $\overrightarrow{B_0}$).
(d) shimming coils current control system (to apply the correct electric current intensity into the shimming coils).
(e) receiving coil (for measuring the NMR signal and emitting $\overrightarrow{B_1}$).
(f) receiving coil 50 Ω tuning, if applicable (so that signal travels at its best from and to the receiving coil), and the necessary electronic switch to automatically alternate between the transmission and the reception modes.
(g) excitation electronics (to bring $\overrightarrow{B_1}$ from its generation source to the receiving coil).

(h) reception electronics (to bring the NMR signal to the sampling unit).

(i) processing unit usually integrating many functional bricks (for controlling the shimming coils, for generating $\overrightarrow{B_1}$ at the desired shape, amplitude, duration, and frequency, and for sampling the NMR signal at an appropriate rate – typically getting instructions from and sending measured data to an external computer / system through a standardized communication protocol).

These hardware elements can be seen together in a possible NMR spectrometer design in Figure 22.

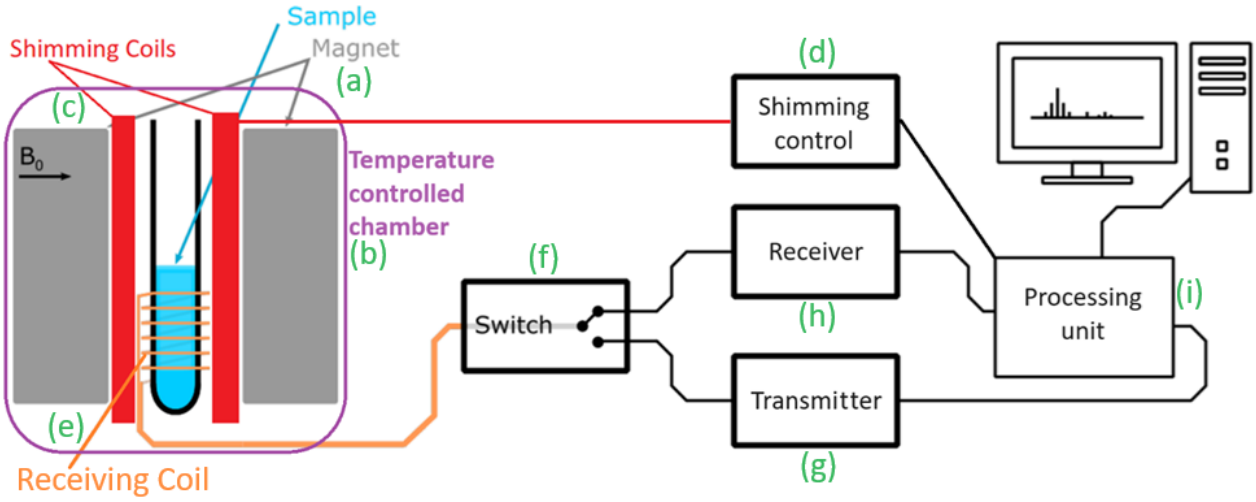

Figure 22 - A possible setup representation of an NMR spectrometer, depicting its main functional blocks and controlling elements, where the receiving coil is both used for transmission and reception of the involved signals. Modified. [2]

While the processing unit is usually a single digital micro-controlled / micro-processed and / or FPGA based processing board responsible for the control of all further electronic modules, the shimming control is basically a controlled current source and depends on the complexity of the shimming design architecture, *e.g.*, intended shimming order corrections, geometry and spatial positioning of the shimming coils, etc. In the other hand, the receiver and transmitter functional electronic blocks can present various design flavours, being nevertheless based on a classic signal path workflow. The typical signal path between the signal processing unit and the receiving coil for both the receiver and the transmitter blocks and the electronic components used in within are depicted in Figure 23.

For this hardware to operate properly, a corresponding set of software bricks are necessary, that can be either embedded within the spectrometer or run on the host computer connected to the spectrometer:

(j) the configuration and trigger setting of $\overrightarrow{B_1}$.

(k) the configuration and activation setting of the shimming coils current.

(l) the automation of the optimization process of $\overrightarrow{B_0}$ correction, *i.e.*, of the shimming, if applicable.

(m) the configuration and trigger setting of the sampling mechanism.
(n) filtering and signal processing of the sampled NMR signal.
(o) output formatting (usually to present the acquired data as spectra in terms of chemical shifts).
(p) accumulation algorithm (so that weak NMR signals can be measured), if applicable.
(q) unit calibration (to fine tune chemical shift values of acquired data), if applicable.
(r) lock system (to implement the locking, *i.e.*, the field drifting compensation by monitoring one specific frequency peak of reference – typically from ^{2}H as in D_2O – and actuating accordingly to correct the remaining ones), if applicable.

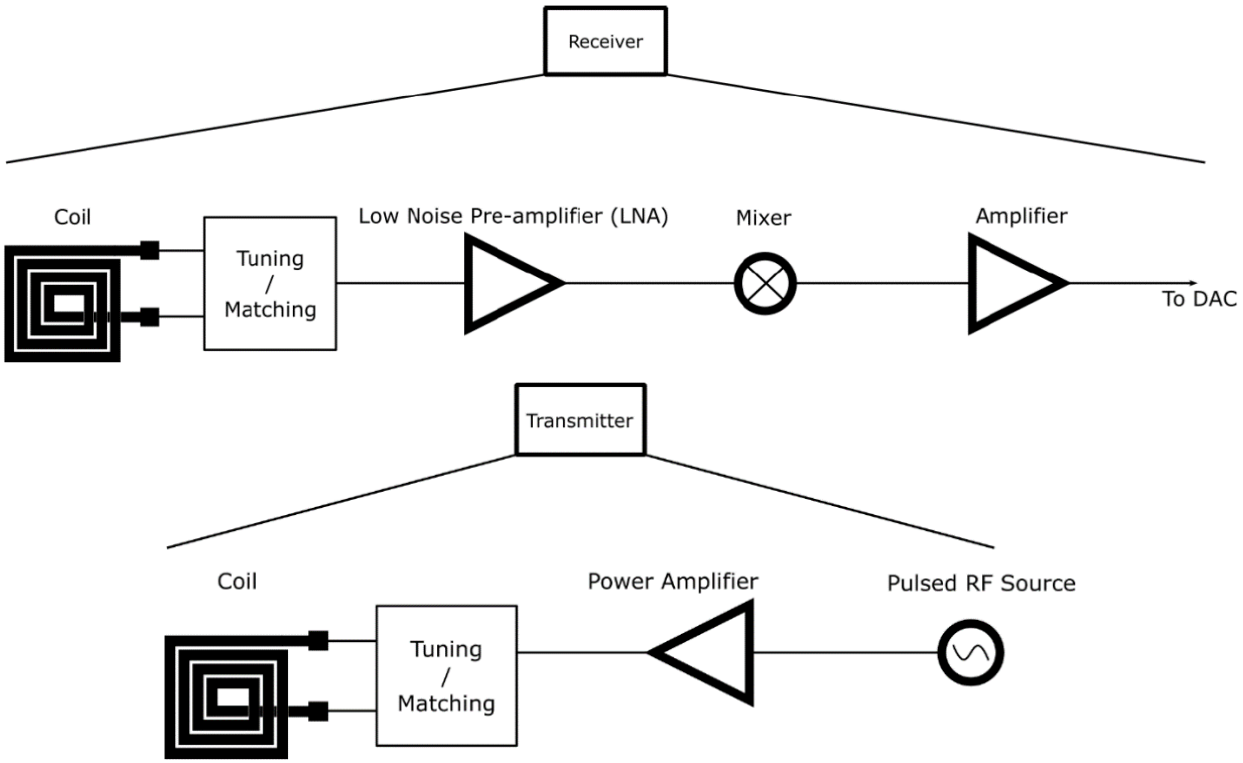

Figure 23 - Top side: the classic signal path within an NMR apparatus receiver, from the receiving coil up to the processing unit. Bottom side: the classic signal path within an NMR apparatus transmitter, logically in the opposite direction as for the receiver, i.e., from the processing unit up to the receiving coil. Modified. [2]

NMR

In this chapter, the way the NMR phenomenon happens from a quantum perspective and the way it is perceived from an electromagnetic perspective was depicted: quantum spins in an aligned manner result to be equivalent to a magnetic vectorization abstraction that, after

ceased the excitation at the Larmor Frequency, takes the form of an electric FID-shaped signal at our NMR receiving coil. The frequency components of this measured NMR signal represent the molecular structure of the sample and are a kind of signature of the different chemical compounds. The better the homogeneity of the static magnetic field $\overrightarrow{B_0}$ is, *e.g.*, by having a good quality magnet and an effective shim system, the better is the signal that is available at the NMR receiving coil. By means of, at first, electronic amplification and analogic signal processing culminating in an electronic mixer, we down-convert the high-frequency NMR signal to a low-frequency equivalent one, which allows us then to sample and digitally process it. The processing unit can then provide us with the acquired NMR spectra.

In order to better understand the entire NMR experiment process from the NMR spectrometer perspective and also as a mean of design support and assessment, we came up with a whole set of simulation tools that provide valuable insights within the functioning of the different technological elements composing such spectrometers. The next chapter presents this simulation tool chain, which encompasses (1) the mathematical ground upon which the simulations were built, (2) the simulation of the electronic elements of the NMR spectrometer, (3) a simulation tool for temporal FID shifting correction due to sampling imprecisions, and (4) a simulator of spectral degradation due to magnetic field inhomogeneity.

Chapter 3 - NMR Simulator Toolchain

One of the major challenges when considering the use of NMR for a given application is to determine the LoD (Limit of Detection) of the measurement device. The quantification of the LoD is required to determine whether the existing spins in the considered volume are enough to enable the detection of the substances within the analysed sample or, conversely, to estimate the minimum concentration of the molecule of interest that makes the detection possible. From a hardware perspective, among other factors, the LoD is strongly dependent on the noise-related PSD, *i.e.*, P_{noise} (see previous chapter), and on the strength and especially on the inhomogeneity of the static magnetic field $\overrightarrow{B_0}$ reflected on the signal-related PSD, *i.e.*, P_{signal}, both affecting the system overall SNR as given in equation (23).

The understanding of the impact of the electronic noise on the LoD is straightforward. Since the amplitude of the resulting NMR spectral peaks depends on the density of spins of the chemical compound of interest, one can easily define, for this compound, a single-measurement threshold concentration below which peaks are drowned in noise and cannot be detected. In the same way, the strength of $\overrightarrow{B_0}$ directly determines the strength of the measured FID according to equations (10) and (11).

On the other hand, the static magnetic field inhomogeneity always induces a characteristic broadening of the NMR peaks. For the accurate determination of the LoD, the knowledge of how peaks are degraded is a prerequisite. However, this degradation prediction is not straightforward. As first-order approach, we can consider that distortion leads to Lorentzian-shaped peaks and characterize the deformation by the FWHM (Full Width at Half Maximum) of these Lorentzian curves. FWHM is also commonly applied as its declension HWHM (Half Width at Half Maximum) in spectroscopy.

Basically, the broadening of the NMR peaks has two mainly negative effects. The first one is that it provokes an overlap of contiguous spectral peaks, worsening our capabilities of identifying the analysed molecules by its characteristic NMR signature. The consequences of this effect are however less important for applications in which the targeted molecule is already known, since the NMR analysist already expects a spectral signature in a certain form, ultimately not definitively preventing the detection and the quantification of the concentration of the targeted molecules. Secondly, as the energy contained in the measured NMR signal, which is quantified as the area below the corresponding spectral peaks, is approximatively the same for a not so prominent field inhomogeneity, as a rule of thumb, if a spectral peak widens, its spectral amplitude decreases, leading ultimately to its vanishing under the combined electronic and coil thermal noise levels.

In order to support the design and the assessment of NMR spectrometers, we developed and propose hereunder an NMR Simulator Toolchain. Indeed, being able to evaluate field inhomogeneity and the impact of the existing SNR is of the utmost importance for NMR spectrometers design and application assessment, up to the point where the system designer can be able to determine the impact of the employment of non-optimal hardware and magnets that can lead to spectral deterioration and ultimately to the completely uselessness of a given NMR spectrometer device for its original intended targeted application.

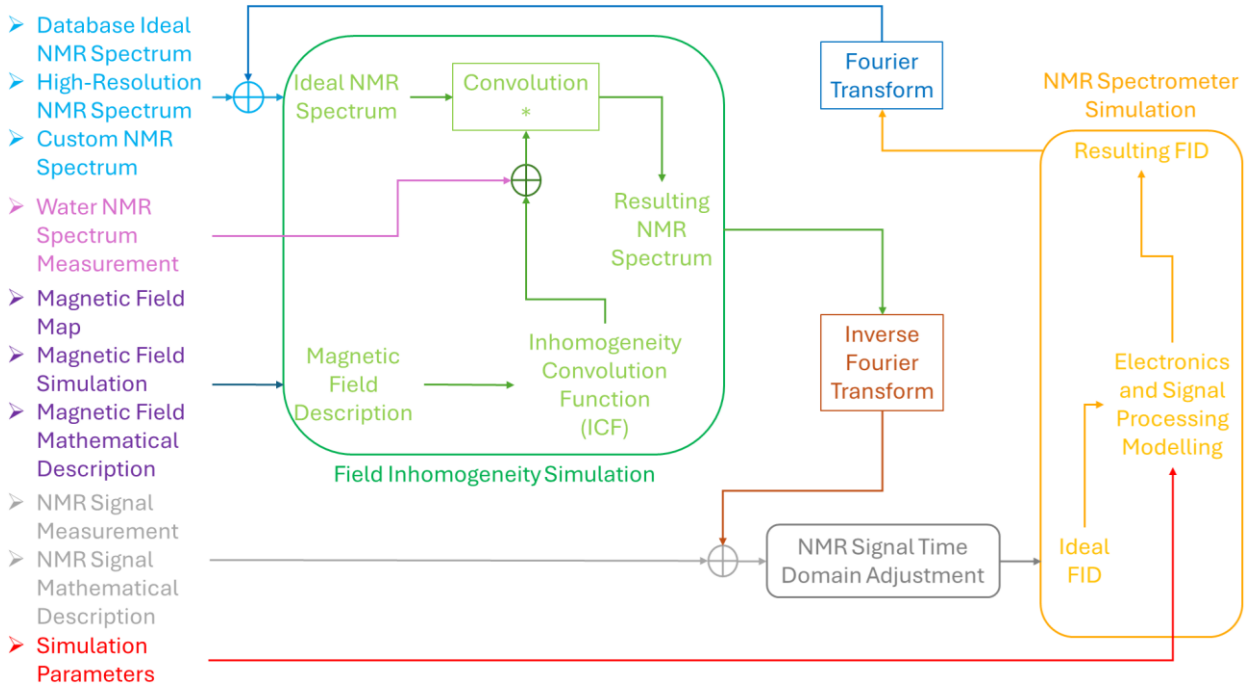

Figure 24 - The NMR Simulator toll chain is composed of its 3 functional distinct interconnected main building blocks: the static magnetic field inhomogeneity assessment (green), the NMR signal time domain adjustment (gray), and the NMR spectrometer simulation (yellow) modules. Aligned to the left are the different supported data input categories.

Our simulator is a software tool chain providing simulations of the system electronic elements, corrections of measured NMR signals, as well as evaluations of spectral degradation following field inhomogeneity, as illustrated in Figure 24. The possible inputs of the NMR Simulator Toolchain are described on the left side of the picture, and items that share the same colour are interchangeable. The toolchain is composed of three blocs: the Field Inhomogeneity Simulation, the NMR Spectrometer Simulation and the NMR Signal Time Domain Adjustment module. They can interoperate in different ways. For instance, the green tool can provide the orange one with free-of-noise-and-disturbance FID signals, however taking into account the impact of field inhomogeneity. Conversely, the orange tool can provide the green one with NMR spectra that already integrates perturbations due to the electronics, however corresponding to signals obtained within a homogeneous magnetic field. Finally, the grey bloc can timely adjust FIDs which were imprecisely obtained by the acquisition system. The symbol ⊕ in Figure 24

denotes the XOR (EXCLUSIVE-OR, *i.e.*, $IN_1 \oplus IN_2$) operator, meaning that only one of both incoming inputs is required for the simulation.

The following subsections depict each of these software modules and provide intermediate results for each one, including associated evaluations and discussions, when applicable. We start by introducing the mathematical framework employed in the simulations, particularly demonstrating how the impact of field inhomogeneity is incorporated into the spectral analysis. We then proceed with the single software modules, first going through the field inhomogeneity assessment one, secondly demonstrating the associated contents of the NMR spectrometer electronics and signal processing simulations, and finally showing how the FID adjustment for time-domain signal accumulation works.

3.1. Field inhomogeneity simulation

The first developed simulation tool aims at assessing the impact of $\overrightarrow{B_0}$ inhomogeneity on the resulting quality of the NMR spectra. Figure 25 illustrates its general framework.

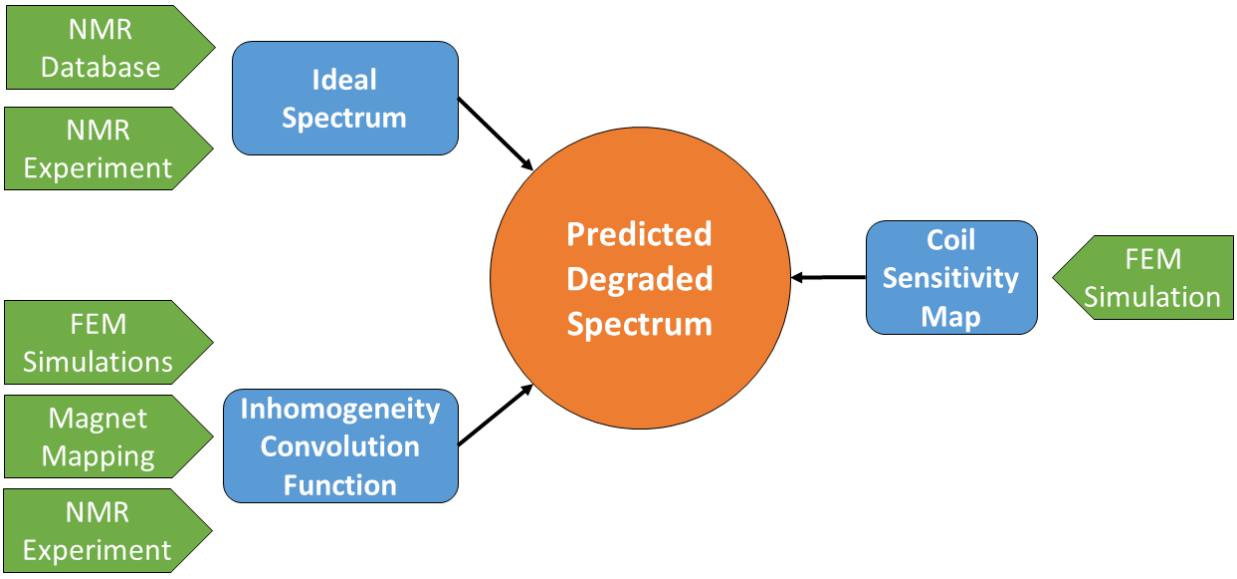

Figure 25 - For the prediction of the degradation of an NMR spectrum, three variables are taken into consideration: an NMR spectrum, the ICF derived from the description of a static magnetic field, and the coil sensitivity. Here, FEM stands for finite element method. Modified. [139]

Three inputs are expected from this simulation tool: an NMR spectrum, the description of a magnetic field, and information about the receiving coil sensitivity. As opposed to the magnetic field inhomogeneity, the receiving coil sensitivity does not degrade a frequency spectra *per se*, attenuating however the amplitude of the measured temporal NMR signal and consequently attenuating spectral magnitude. This attenuation factor can be mathematically modelled as a simple multiplication by a constant, if we consider that the sensitivity map of the

receiving coil is perfectly homogeneous or if we consider $\overrightarrow{B_0}$ to be perfectly homogeneous. More complex scenarios arise when taking into consideration the real sensitivity map of the receiving coil and assuming that there are local fluctuations of $\overrightarrow{B_0}$ within the sensible volume of the coil. Indeed, the resulting attenuation would become a weighted sum of the different local temporal signal components composing the NMR signal.

For the sake of simplicity, while explaining how this tool works and the mathematical ground it is based on, we consider an ideal receiving coil with an overall homogeneous sensitivity equal to unity, and no noise whatsoever. The mathematical basis from the previous chapter extended by the theoretical addendum presented below allows us therefore to put forward a model upon which the spectral degradation due to field inhomogeneity can be estimated. FID signals and their corresponding frequency components are composite and, in practice, $\overrightarrow{B_0}$ can never be perfectly homogeneous. Therefore, we start by a hypothetical ideal scenario and gradually introduce complexity to it.

3.1.1. Mathematical background

This section presents the mathematical background related to the field inhomogeneity simulation.

FID and spectrum in a homogeneous field – Case of the sample containing only one functional group

Henceforth, it is considered that a functional group presents a distinct chemical shift. We start therefore by studying a sample that contains only one molecular group, which itself contains only one functional group P, *e.g.*, water, immersed into a perfectly homogeneous static magnetic field $\overrightarrow{B_0}$. The corresponding real part of the FID signal $\mathcal{s}_{FID_P}$ for this single functional group P, where $\mathcal{s}_{0_P}$ is the FID initial amplitude, f_{FID_P} is the FID frequency corresponding to its single chemical shift δ_P, and T_{2P} is the relaxation time constant for this particular functional group P and reflects the perfect homogeneity of $\overrightarrow{B_0}$, is given by:

$$\mathcal{s}_{FID_P}(t) = \mathcal{s}_{0_P}\cos\left(2\pi f_{FID_P} t\right) e^{-\frac{t}{T_{2P}}}, \qquad \forall t \geq 0 \tag{26}$$

However, our preferred FID mathematical representation, from which the friendliest Fourier transform solution can be deduced, is the one written in its quadrature form, here denoted by $\mathcal{s}^{Q}_{FID_P}$, where i is the imaginary unit, as follows:

$$\mathcal{s}^{Q}_{FID_P}(t) = \mathcal{s}_{0_P}\left[\cos\left(2\pi\, f_{FID_P} t\right) + i\,\sin\left(2\pi f_{FID_P} t\right)\right] e^{-\frac{t}{T_{2P}}}, \qquad \forall t \geq 0 \tag{27}$$

The corresponding frequency spectrum $S^{Q}_{FID_P}$ is simply the application to the previous equation of the Fourier transform definition as in equation (13), and presents a Lorentzian-like distribution shaped curve given by:

$$\left|S^{Q}_{FID_P}(f)\right| = \frac{\mathcal{s}_{0_P}}{2\pi} \frac{1}{\sqrt{\left(\frac{1}{2\pi T_{2_P}}\right)^2 + (f_{FID_P} - f)^2}} \tag{28}$$

Analogously to equation (5), in equations (26), (27) and (28), the frequency of the FID f_{FID_P} is related to the Larmor frequency f_0 by the chemical shift δ_P according to the relationship:

$$f_{FID_P} = f_0\,(1 + \delta_P) \tag{29}$$

FID and spectrum in a homogenous field – Case of the sample containing several functional groups

For a sample presenting K distinct chemical shifts due to different k functional groups subjected to a perfectly homogeneous static magnetic field $\overrightarrow{B_0}$, where $k \in [1, K]$ denotes the existing single distinct chemical shifts of this sample, the resulting perceived NMR signal is nothing else than the superposition of the different FIDs originated from these different functional groups. This NMR signal can be formalized as $\mathcal{s}_{FID_K}$, where $\mathcal{s}_{0_k}$ is the single FID initial amplitudes corresponding to each functional group, f_{FID_k} is the single FID frequencies corresponding to the single chemical shifts δ_k, and T_{2_k} is the single relaxation time constants for each single functional group, reflecting the perfect homogeneity of $\overrightarrow{B_0}$:

$$\mathcal{s}_{FID_K}(t) = \sum_{k=1}^{K} \mathcal{s}_{0_k} \cos\left(2\pi f_{FID_k} t\right) e^{-\frac{t}{T_{2_k}}}, \qquad \forall t \geq 0 \tag{30}$$

However, once again, we prefer instead to consider its quadrature representation, as follows:

$$\mathcal{s}^{Q}_{FID_K}(t) = \sum_{k=1}^{K} \mathcal{s}_{0_k}\left[\cos\left(2\pi f_{FID_k} t\right) + i\,\sin\left(2\pi f_{FID_k} t\right)\right] e^{-\frac{t}{T_{2_k}}}, \qquad \forall t \geq 0 \tag{31}$$

The Fourier transform of the sum of these K functions being the sum of the Fourier transform of those same K functions, the resulting frequency spectrum $S^{Q}_{FID_K}$ including the K distinct Lorentzian-like curves corresponding to the K considered functional groups is in the form:

$$\left|S_{FID_K}^{Q}(f)\right| = \sum_{k=1}^{K} \frac{\mathcal{s}_{0_k}}{2\pi} \frac{1}{\sqrt{\left(\frac{1}{2\pi T_{2_k}}\right)^2 + (f_{FID_k} - f)^2}} \tag{32}$$

Taking into account equations (5) and (29), the frequency of each single FID f_{FID_k} is related to the Larmor frequency f_0 by its specific chemical shift δ_k as follows:

$$f_{FID_k} = f_0\,(1 + \delta_k) \tag{33}$$

FID and spectrum in a homogeneous however shifted field

We now consider the situation where the static field is still homogeneous in the measurement volume, however its intensity is slightly shifted from the ideal static magnetic field $\overrightarrow{B_0}$. Let us note ΔB_0 – the uppercase Greek letter delta is not to be confounded with the Laplace operator – as being this intensity shift. Such shift of the magnetic field intensity leads to a corresponding proportional shift of the Larmor frequency Δf_0 according to the following equation:

$$\Delta f_0 = \frac{\gamma \Delta B_0}{2\pi} \tag{34}$$

Considering equation (33), a shift in the Larmor frequency Δf_0 induces in turn a shift on the FID frequency Δf_{FID_k} as follows:

$$\Delta f_{FID_k} = \frac{\gamma \Delta B_0}{2\pi}(1 + \delta_k) \tag{35}$$

Estimation of the FID and spectrum in an inhomogeneous field by spatial discretization

One way of estimating the FID and the spectrum measured from a sample in an inhomogeneous $\overrightarrow{B_0}$ field is by dividing the whole measurement volume into sub-volumes (voxels, *i.e.*, pixeled volume units) that are small enough so that we can consider the static magnetic field within each voxel as homogeneous. At the first order, the FID or the spectrum acquired by the receiving coil are the sum of the FIDs or spectra originating from within each of these voxels. By considering the size of these voxels tending to be infinitely small, we ensure that the field homogeneity assumption is respected, thus being able to write this sum of voxels in integral form as:

$$\mathcal{s}_{FID_K}^{Q}(t) = \iiint_V \mathcal{s}_{FID_K}^{Q}(t, v)dv\,, \qquad \forall t \geq 0, V \subset \mathbb{R}^3 \tag{36}$$

For computational reasons, however, we must limit ourselves to a finite number of voxels J, leading to an approximation of equation (36):

$$\mathcal{s}_{FID_K}^{Q}(t) = \sum_{j=1}^{J} \mathcal{s}_{FID_K}^{Q^j}(t), \qquad \forall t \geq 0 \tag{37}$$

where $\mathcal{s}_{FID_K}^{Q^j}(t)$ is the under the field homogeneity assumption calculated FID of the voxel j.

Analogous equations can be written for a spectrum following the linearity property of the FT. Indeed, the FT of the above summation or integral over the considered 3-dimensional domain is the sum or integral of the individual FT for each voxel.

$$S_{FID_K}^{Q}(f) = \iiint_V S_{FID_K}^{Q}(f, v)dv, \qquad V \subset \mathbb{R}^3 \tag{38}$$

$$S_{FID_K}^{Q}(f) = \sum_{j=1}^{J} S_{FID_K}^{Q^j}(f) \tag{39}$$

3.1.1. Resource-efficient modelling approach

The discretization described in the previous section can be used to estimate the spectrum in a straightforward way. However, as the field inhomogeneity increases, the size of the voxels must decrease in order to respect the intra-voxel field homogeneity assumption, leading to a drastic increase in the number of voxels when the field is highly inhomogeneous. This is all the more true since generally there is no symmetry of a lesser order that can be employed to reduce the size of the discretization problem. Therefore, the discretization must take place in 3D, however often leading quickly to a quite high computation time and memory shortage issues. In the following, we propose an optimized approach that saves computational resources by using a looser mesh.

The NMR spectrum as a convolution function

For our proposed method of inhomogeneity assessment, we employ the concept of mathematical convolution:

$$(g * h)(f) = g(f) * h(f) := \int_{-\infty}^{\infty} g(v)h(f - v)dv = \int_{-\infty}^{\infty} g(f - v)h(v)dv \tag{40}$$

where g and h are two distinct mathematical functions, however both being function of the variable f.

This mathematical operation is a form of integral transform and is usually presented to engineering students when introducing the related theory concerning the study of signals and systems. In this context, f usually represents the time variable and the operation reflects the

changes that a system causes to a given signal that goes through it. Although we do not consider here f to be a time variable nor the functions g and h to be mathematical representations of a signal and a system, the analogy of an entity traversing a medium while being changed by this same medium is helpful to understand what happens physically within an NMR spectrometer.

Here these functions represent respectively a frequency spectrum and a description of the static magnetic field $\overrightarrow{B_0}$, as artistically depicted in Figure 26. What is necessary for such approach to work out is to be able to mathematically represent $\overrightarrow{B_0}$ as a function of the frequency instead of the magnetic field strength, which in NMR does not represent a big deal since the Larmor frequency and the magnitude of $\overrightarrow{B_0}$ are proportional. Hither, the considered mathematical representation fulfilling such requirement is the so-called ICF (Inhomogeneity Convolution Function).

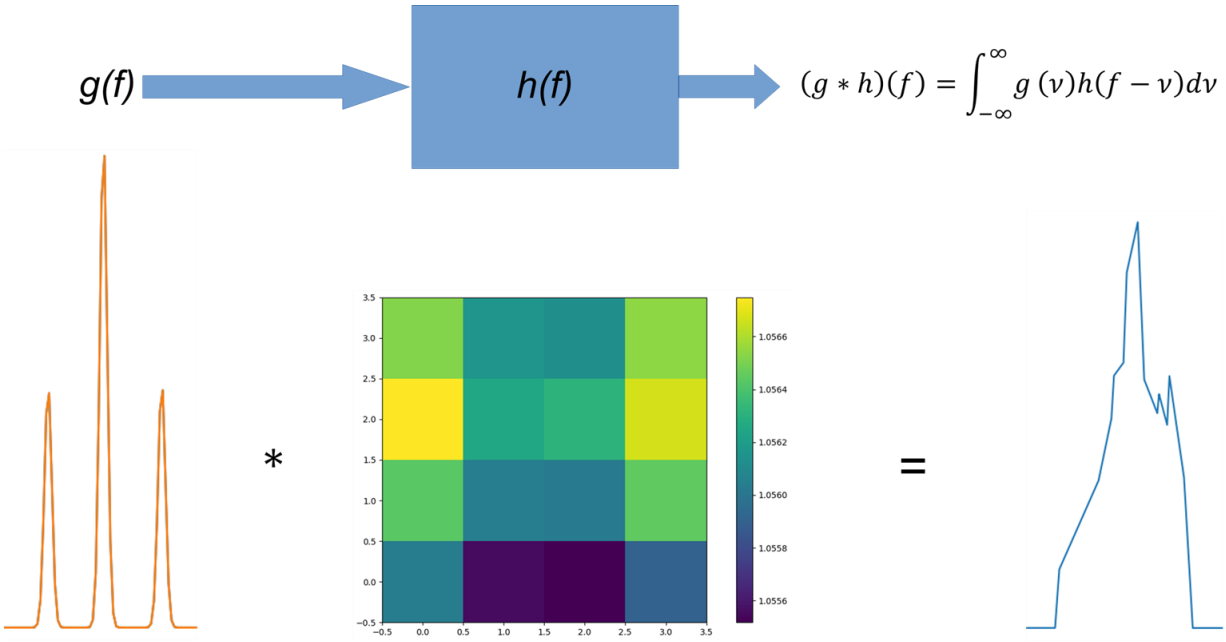

Figure 26 - By convoluting a frequency spectrum and the appropriate mathematical description of a static magnetic field $\overrightarrow{B_0}$, one is able to assess the impact of the inhomogeneity of the magnetic field on the frequency spectrum.

Indeed, the method that gives the most convenient resource-efficient assessment of the impact of the static magnetic field $\overrightarrow{B_0}$ inhomogeneity on a given ideal NMR spectrum for any kind of sample geometry is through the analytical determination of the ICF – denoted here $H(f)$ –, which mathematically describes in an analytical manner the field inhomogeneity profile within the considered volume, and the subsequently computation of a convolution of this very ICF and the considered ideal NMR spectrum.

Model assumptions

Several assumptions have to be made in order to analytically calculate the ICF. First, we have to consider that the width of the spectrum peaks in a perfectly homogeneous field is small enough compared to the width of the expected spectral deformation, so that these peaks can be described as Dirac delta functions. Another way to describe it is by considering that for every involved functional group k, the effective shorter relaxation time constant $T_{2_k}^*$, due mainly to field inhomogeneity, is much smaller than the theoretical relaxation time constant T_{2_k}, *i.e.*, $T_{2_k} \gg T_{2_k}^*$, so that T_{2_k} tends to ∞ and therefore $e^{-\frac{t}{T_{2_k}}} \sim 1$ by the end of the acquisition window. Indeed, because T_2^* typically dominates the NMR signal over T_2 in low-field NMR, a frequency spectrum on a given inhomogeneous magnetic field under these conditions is equivalent to the correlation function of the corresponding frequency spectrum within a perfectly homogeneous magnetic field and for which FID the relaxation time constant T_2 is considered to tend to infinity, and of the ICF describing this same inhomogeneous magnetic field. The resulting spectrum can then be written as:

$$S_{FID_K}^Q(f) = \sum_{k=1}^{K} S_{0_k} \mathfrak{D}(f_{FID_k} - f) \tag{41}$$

And so, the deformed spectrum $\bar{S}_{FID_K}^Q$ reads:

$$\bar{S}_{FID_K}^Q(f) = \sum_{k=1}^{K} S_{0_k} \mathfrak{D}(f_{FID_k} - f) * H(f) \tag{42}$$

where S_{0_k} is the component of the spectral complex magnitude, and $\mathfrak{D}$ is the Dirac delta function, which together provide the mathematical description of the considered ideal NMR spectrum. For convolution products and Dirac distributions, the following property stands:

$$\mathfrak{D}(f - a) * \mathfrak{H}(f) = \mathfrak{H}(f - a) \tag{43}$$

Applying this property to equation (42) leads to:

$$\bar{S}_{FID_K}^Q(f) = \sum_{k=1}^{K} S_{0_k} H(f_{FID_k} - f) \tag{44}$$

The different k peaks, each with its amplitude S_{0_k}, and each being centered at its corresponding frequency f_{FID_k} are deformed in accordance with the inhomogeneity profile of the considered static magnetic field. We present hereunder the procedure to determine the ICF, *i.e.*, $H(f)$ for a given magnetic field $\overrightarrow{B_0}$.

Another required assumption to establish our mathematical framework is to consider the solution density constant over the whole sample volume and an ideal receiving coil with a uniform spatial sensitivity over the whole sample equal to the unity.

Furthermore, we deduce the mathematics based on the assumption that the considered frequency spectrum presents only one peak corresponding to a single functional group P. As a first approach, this simplification helps to understand that the characteristic frequency shift of the single peak moves infinitesimally, since the peak is ideally represented by the unit impulse, as well as it avoids its mixing up with further peaks from other functional groups. The generalization of this case for K functional groups can be done afterwards by applying the superposition principle to the obtained results, which is already represented in equation (42).

Finally, according to equations (10) and (11), $\mathcal{s}_{0_k}$, and thus S_{0_k}, depends on $\overrightarrow{B_0}$, being therefore impacted by field inhomogeneity. As the order of magnitude of the inhomogeneity we typically work with are in the ppm range, we choose to neglect this impact in order to simplify the analytical calculations that follow.

Description of the magnetic field

Now, we consider that our non-homogeneous static magnetic field $B(x,y,z)$, with its different local field strengths being function of the considered spatial coordinates, can be normalized in regard to the perfectly homogeneous expected reference field $B_0(x,y,z) = B_0 \; \forall x,y,z \in \mathbb{R}$ within the sample volume boundaries, as follows:

$$B(x,y,z) = B_0\big(1 - h(x,y,z)\big) \tag{45}$$

where $h(x,y,z)$ is called inhomogeneity function.

The inhomogeneity function describes the local field deviations due to the inhomogeneity in regard to the reference field $\overrightarrow{B_0}$ and reads:

$$h(x,y,z) = \frac{B(x,y,z)}{B_0} + 1 \tag{46}$$

The local Larmor frequency f_l can as well be expressed as a function of h:

$$f_l(x,y,z) = \frac{\gamma B(x,y,z)}{2\pi} = \frac{\gamma B_0\big(1 - h(x,y,z)\big)}{2\pi} = f_0\big(1 - h(x,y,z)\big) \tag{47}$$

And finally, by extension, the local value of a chemical shift also become a function of h:

$$f_{FID_k}(x,y,z) = f_l(x,y,z)(1+\delta_k) = f_0\big(1 - h(x,y,z)\big)(1+\delta_k) \tag{48}$$

Both $h(x,y,z)$ and δ_k are expected to be in the ppm order of magnitude, so that the product $h(x,y,z)\delta_k$ can be neglected, leading to:

$$f_{FID_k}(x,y,z) \propto f_0(1 - h(x,y,z) + \delta_k) \tag{49}$$

And so, the local contribution to the spectrum for a given functional group k can be defined as following:

$$S^Q_{FID_k}(f,x,y,z) = S_{0_k}\mathfrak{D}(f_0(1 - h(x,y,z) + \delta_k) - f) \tag{50}$$

Computation of the Inhomogeneity Convolution Function

Combining equations (38), (42) and (50) leads to the following definition for the ICF:

$$H(f) = \iiint_{x,y,z} \mathfrak{D}(f_0(1 - h(x,y,z) + \delta_k) - f)dxdydz\,, \qquad V(x,y,z) \subset \mathbb{R}^3 \tag{51}$$

By superposition, one can then go from the specific scenario considering only one functional group k to the general scenario with K functional groups by means of equation (42).

The most intuitive computational method when working with such physical problems within a well-defined geometry is to divide the whole space in smaller space units where it is considered that the physical parameters are invariable, thus providing a local contribution to the whole. These local contributions are then put together in order to provide a global result. For the pure numerical assessment of the impact of field inhomogeneity on NMR spectra it is not different: the considered NMR experiment volume is divided into smaller units for which it is considered that the local values of the inhomogeneity function $h(x,y,z)$ are constant, *i.e.*, invariable within each small volume unit. The results of such discretization are graphs in form of a histogram, composed by contiguous vertical bars, where their width depends on the discretization resolution that was applied to the numerical model: the smaller are the discretized spatial units, the thinner are the vertical bars. With a good enough resolution, the histogram may look like a continuous curve, and therefore being more exact, to the expenses of the employed computational resources. Figure 27 exemplifies such numerical discretization phenomena for a pure illustrative Gaussian distribution.

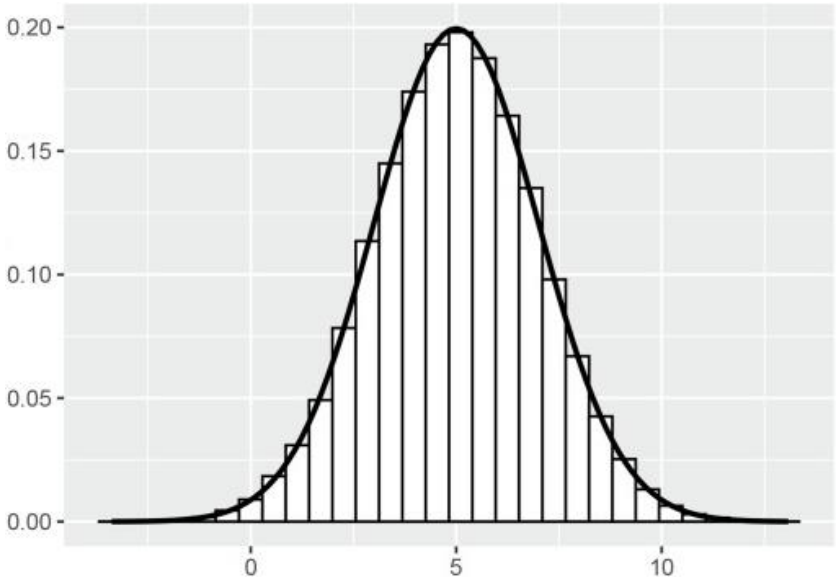

Figure 27 - Histogram resulting from a poor numerical discretization (vertical bars), and its envelope representing the exact expected values (black line). Axes and units are arbitrary. Modified. [140]

As an alternative to the histogram representation from Figure 27, one could have a point-only representation of the same graph, which does not change the nature of the

discretization, but only its visual depiction, with the final envelope due to a most intensive discretization looking the same in both cases.

As for certain kinds of realistic physical-related simulations of high-density or large-volume problems with models based on simulation architecture, gridding technique, collision model, and implementation technique, the classic computational requirements may be prohibitive [141]. In order to avoid going the way of more intensive spatial discretization on our simulations of the assessment of field inhomogeneity on NMR spectra, we propose instead to do a coarse discretization of the considered experiment space and analytically calculate the integral for a given mesh. A possible way to do this is by realizing a linear interpolation of $h(x,y,z)$ for each voxel. Since we are talking about a volume, trilinear interpolation is the appropriate declination of the employed linear interpolation method.

Again, perhaps the most intuitive way of discretizing space would be by decomposing it in small cubes. However, by doing so, we would derive an inhomogeneity function $h(x,y,z)$ that would not be analytically integrable. We could indeed proceed with a pure numerical calculation of this form, nevertheless we would not benefit from any advantages, especially in what concerns simulation time, when compared to the pure numerical method, because here as well, in order to get an outcome within the desired precision, we would be employing in last resort a further discretized spatial description of the model.

There is however another geometric discretization form that suits us because the use of the trilinear interpolation method results in an inhomogeneity function $h(x,y,z)$, which integrals are analytically solvable.

New discretization scheme

Starting, for example, from a coarse cubical decomposition of the inhomogeneous static magnetic field $\overrightarrow{B_0}$ in the form of $B(x,y,z)$, where $(x,y,z) \in [0,2]$, it is possible to decompose it further:

- initially into 24 isosceles trirectangular tetrahedra, which have 3 equal isosceles triangles as 3 of its faces, the fourth one being an equilateral triangle. Because the employment of the trilinear interpolation is not possible with this decomposition, these 24 tetrahedra must be subsequently devised into 2 each, making 48 tetrahedra in all.
- directly into 48 irregular tetrahedra, of which 2 faces are 2 identical isosceles rectangular triangles, and the other 2 faces are 2 identical scalene triangles.
- directly into 48 regular trirectangular tetrahedra, where the right angles of 3 faces share the same corner and the lengths of the edges originated in this very corner are equal to the unity.

The last alternative provides us with a fairly easy-to-understand decomposition, which can provide us as well with an analytically integrable inhomogeneity function.

Accordingly, for a given sample geometry, we discretize the sample volume in a set of N same-sized trirectangular tetrahedrons, as the one in Figure 28, so that a symmetrical trilinear interpolation of the function $h(x,y,z)$ can be performed within these trirectangular tetrahedrons. From this trirectangular tetrahedral description of the sample volume, the computation of the ICFs follows the corresponding computation for each individual trirectangular tetrahedron. Indeed, for each trirectangular tetrahedron $trt \in [1,N]$, the integrals of the local $H_{trt}(f)$ can thus be computed from analytical expressions when considering this sample geometry discretization form, allowing us to generalize this approach for any kind of sample geometry in Cartesian coordinates. Subsequently, all local trirectangular tetrahedral spectral contributions sum up to compose the resulting deformed NMR spectrum.

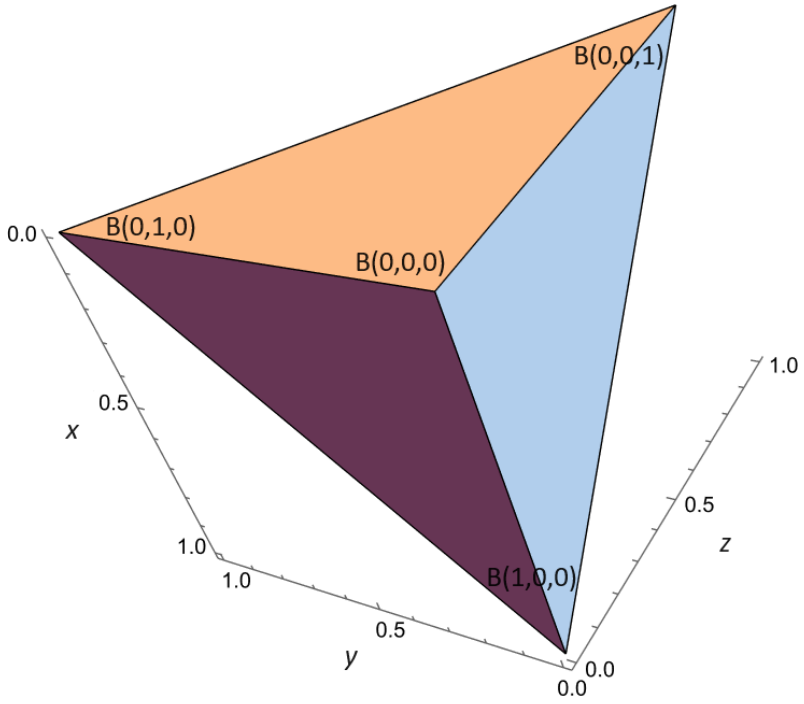

Figure 28 - A trirectangular tetrahedron with sides equal to the unity.

It is worth being noted that, for the cases in which we work with discretized values representing a giving physical quantity, for instance when considering a magnetic mapping as the description of the magnetic field and therefore of its inhomogeneity, the use of the trilinear interpolation means estimating the values between measured points, *i.e.*, a linear variation is considered between all congruent measurement coordinates.

The trilinear interpolation of $h(x,y,z)$ can be calculated as follows: let $B_{m,n,o}$ be the magnetic field at each corner $B_{0,0,0} = B(0,0,0)$, $B_{1,0,0} = B(1,0,0)$, $B_{0,1,0} = B(0,1,0)$ and $B_{0,0,1} = B(0,0,1)$ of the considered tetrahedron, as depicted in Figure 28. And let $h_{m,n,o}$ be the inhomogeneity expressed from $B_{m,n,o}$, according to equation (45). The trilinear interpolation mathematically providing $h(x,y,z)$ for the inside of the considered tetrahedron can be written in the following form:

$$h(x,y,z) = c_1 + c_2x + c_3y + c_4z \tag{52}$$

Now, by considering the value of $h(x,y,z)$ at each corner of the considered tetrahedron, we can write:

$$\begin{cases} h(0,0,0) = h_{0,0,0} = c_1 \\ h(1,0,0) = h_{1,0,0} = c_1 + c_2 \\ h(0,1,0) = h_{0,1,0} = c_1 + c_3 \\ h(0,0,1) = h_{0,0,1} = c_1 + c_4 \end{cases} \tag{53}$$

The constants c_1, c_2, c_3 and c_4 can be therefore represented by the following expressions:

$$\begin{cases} c_1 = h_{0,0,0} \\ c_2 = h_{1,0,0} - h_{0,0,0} \\ c_3 = h_{0,1,0} - h_{0,0,0} \\ c_4 = h_{0,0,1} - h_{0,0,0} \end{cases} \tag{54}$$

So finally, the following expression of the trilinear interpolation can be put forward:

$$h(x,y,z) = h_{0,0,0} + (h_{1,0,0} - h_{0,0,0})x + (h_{0,1,0} - h_{0,0,0})y + (h_{0,0,1} - h_{0,0,0})z \tag{55}$$

Results

Based on the new discretization scheme and on the definition of the ICF given by equation (51), we proceed by summing up the contributions of all J cubical voxels, each contributing with the sum of its 48 tetrahedrons, for which we define $trt \in [1,48]$, where the local contributions are calculated by a triple integral, these considering all chemical shits belonging to the K functional groups present in the sample:

$$H(f) = \sum_{j=1}^{J} \sum_{trt=1}^{48} \sum_{k=1}^{K} \int_0^1 \int_0^x \int_0^y \mathfrak{D}(f_0(1 - c_1 - c_2x - c_3y - c_4z + \delta_k) - f)dz\,dy\,dx \tag{56}$$

The analytical calculation of the triple integral is feasible under complementary assumptions. It leads however to a quite extensive function, being therefore presented in the appendix section I. Its result involves the Heaviside step function, whose mathematical definition is:

$$u(x) := \begin{cases} 1, & x \geq 0 \\ 0, & x < 0 \end{cases} \tag{57}$$

and is essentially a large sum of locally defined parabolas in the form of:

$$u(f - f')(\alpha f^2 + \beta f + \lambda) \tag{58}$$

where f', α, β and λ are functions of c_1, c_2, c_3 and c_4.

3.1.2. Validation

The simulation of the assessment of the static magnetic field $\overrightarrow{B_0}$ concerning its intrinsic inhomogeneity, which depends on the material and on the geometry and construction process of the permanent magnet or other elements generating $\overrightarrow{B_0}$, can therefore take place based on the theoretical basis presented in the previous section. On the other hand, the assessment of field drifting due to the variations of the temperature is not in the scope of this work, so that we always consider that the temperature is perfectly stable within the considered setup.

Our objective with this assessment simulation module is to evaluate the impact of field inhomogeneity of static magnetic fields on both ideal NMR spectra coming from databases, as the classic nmrdb [142] and its new version, NMRium [143], and real NMR high-quality spectra acquired with top class NMR spectrometers. Within the simulation environment, which takes place in Python, the ICF can either be derived from a mathematical function describing the static magnetic field $\overrightarrow{B_0}$ or from discretized magnetic field descriptions coming from simulations of magnetic structures or from magnetic field maps.

The validation of this part of the NMR simulator, which basically means the validation of the analytical equation used for the computation of the ICF, was performed by numeric calculation of the deformation of an ideal Dirac spectrum placed at 0 ppm for a homogeneous field with magnitude $B_0 = 1$ T, when exposing it to different inhomogeneity patterns. We compare the calculation of the ICF through our proposed method with the results employing the trivial method, which consists in discretizing the considered volume of interest $x \in [-1, 1]$ cm, $y \in [-1, 1]$ cm and $z \in [-1, 1]$ cm into as-small-as-necessary cubes so that the magnetic field within them can be considered as constant enough for the validation proof. The trivial method produces, for each cube, a value of an inhomogeneity-related chemical shift and the resulting spectrum is then calculated as a histogram of all these cubical values. And so, the ICF calculated with our approach is expected to be the envelop of this histogram produced by employing the trivial method.

The first validation scenario considered for the numeric calculation a cubic volume discretization of 301 x 301 x 301 points, while considering for both the analytical calculation using the ICF and the numeric one a $\overrightarrow{B_0}$ distribution of:

$$B_0(x, y, z) = 1 - \frac{0.5y + 0.3z + x}{10^6} \tag{59}$$

where the resulting field strength is given in Tesla and is a function of the three spatial coordinates within the considered cubic volume.

Figure 29 presents the results corresponding to this first validation scenario.

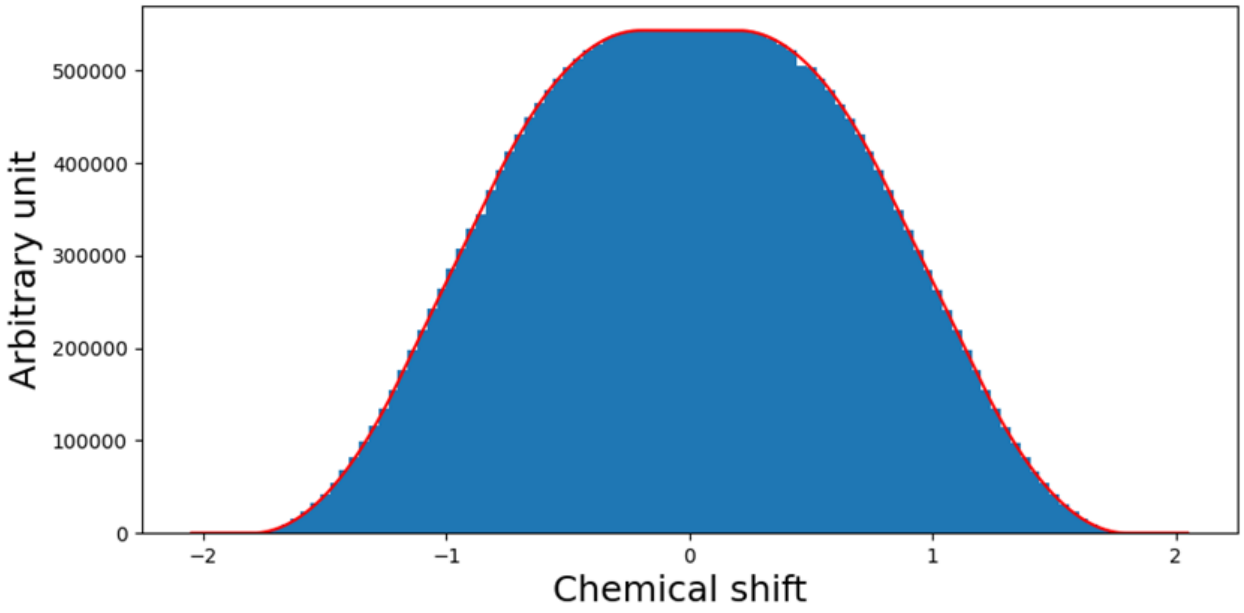

Figure 29 - First scenario successfully validates the NMR Simulator through the matching of the expected line deformation and simulated histogram. Modified. [139]

The expected chemical shift range for this spectrum was between -1.8 ppm and 1.8 ppm, which are respectively the frequency equivalent of the magnetic field strengths at (-1, -1, -1) cm and (1, 1, 1) cm. Iso-Gauss surfaces are inclined planes in the three directions and the plateau in the figure corresponds to the magnetic field range for which the iso-Gauss surfaces are completely inside the cube, which corresponds to the range between -0.2 ppm and 0.2 ppm. The same deformation curves are obtained when considering analogue magnetic fields with all possible combinations of coefficient exchange as well as with their negative forms, meaning that the simulation passes symmetry and mirror transformation tests successfully.

The second validation scenario considered for the numeric calculation a cubic volume discretization of 301 x 301 x 301 points, while considering for both the analytical calculation using the ICF and the numeric one a $\overrightarrow{B_0}$ distribution of:

$$B_0(x, y, z) = 1 - \frac{0.7y + 0.5z + x}{10^6} \tag{60}$$

where the resulting field strength is given in Tesla and is a function of the three spatial coordinates within the considered cubic volume.

Figure 30 presents the results corresponding to this second validation scenario. The expected chemical shift range for this spectrum was between -2.2 ppm and 2.2 ppm, which are respectively the frequency equivalent of the magnetic field strengths at (-1, -1, -1) cm and (1, 1, 1) cm. Iso-Gauss surfaces are inclined planes in the three directions but there is no longer a plateau because the iso-Gauss surfaces are inclined enough so that none of them is fully inside the considered cubic volume. The same deformation curves are obtained when considering analogue magnetic fields with all possible combinations of coefficient exchange as well as with

their negative forms, meaning that the simulation passes symmetry and mirror transformation tests successfully for this validation scenario as well.

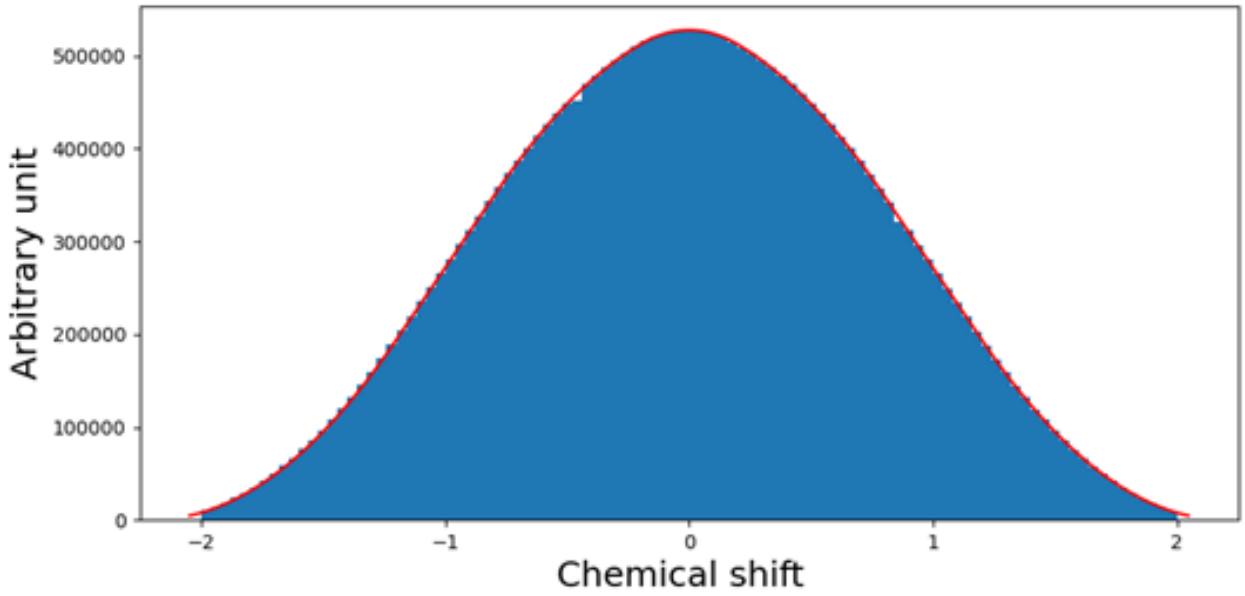

Figure 30 - Second scenario validates the NMR Simulator as well through the matching of the expected line deformation and simulated histogram.

A third validation scenario considered for the numeric calculation a cubic volume discretization of 51 x 51 x 51 points, while considering for both the analytical calculation using the ICF and the numeric one a $\overrightarrow{B_0}$ distribution of:

$$B_0(x,y,z) = 1 - \frac{\sqrt{x^2+y^2+z^2}}{10^6} \tag{61}$$

where the resulting field strength is given in Tesla and is a function of the three spatial coordinates within the considered cubic volume.

Figure 31 presents the results corresponding to this third validation scenario. The field deformation as a function of a square root term limits the resulting spectrum to one side of the cartesian plane and the analytical and numerical estimations are in accordance with each other.

It is worth noticing that the histogram calculations take about 20 seconds on a laptop with a i7-8665U CPU @ 1.90 GHz and 32 GB RAM, while our simulator takes only about 3.5 seconds to compute the equivalent on the same hardware. We could demonstrate that for the same simulation constraints in terms of precision and size of the datasets, when using finer discretized models to numerically calculate the histogram, the memory usage increases in a non-linear manner, leading to memory saturation and therefore to the practical impossibility of increasing the computation accuracy beyond certain levels, without the employment of further optimization techniques. In contrast, with our method, because we employ an analytical approach, we do not encounter any memory-related complications. This is because the computational resources usage is proportional to the simulated input models. For real sample

volumes of any spatial geometry, with regard to the employment of commercial computers for such simulations, only our approach is viable.

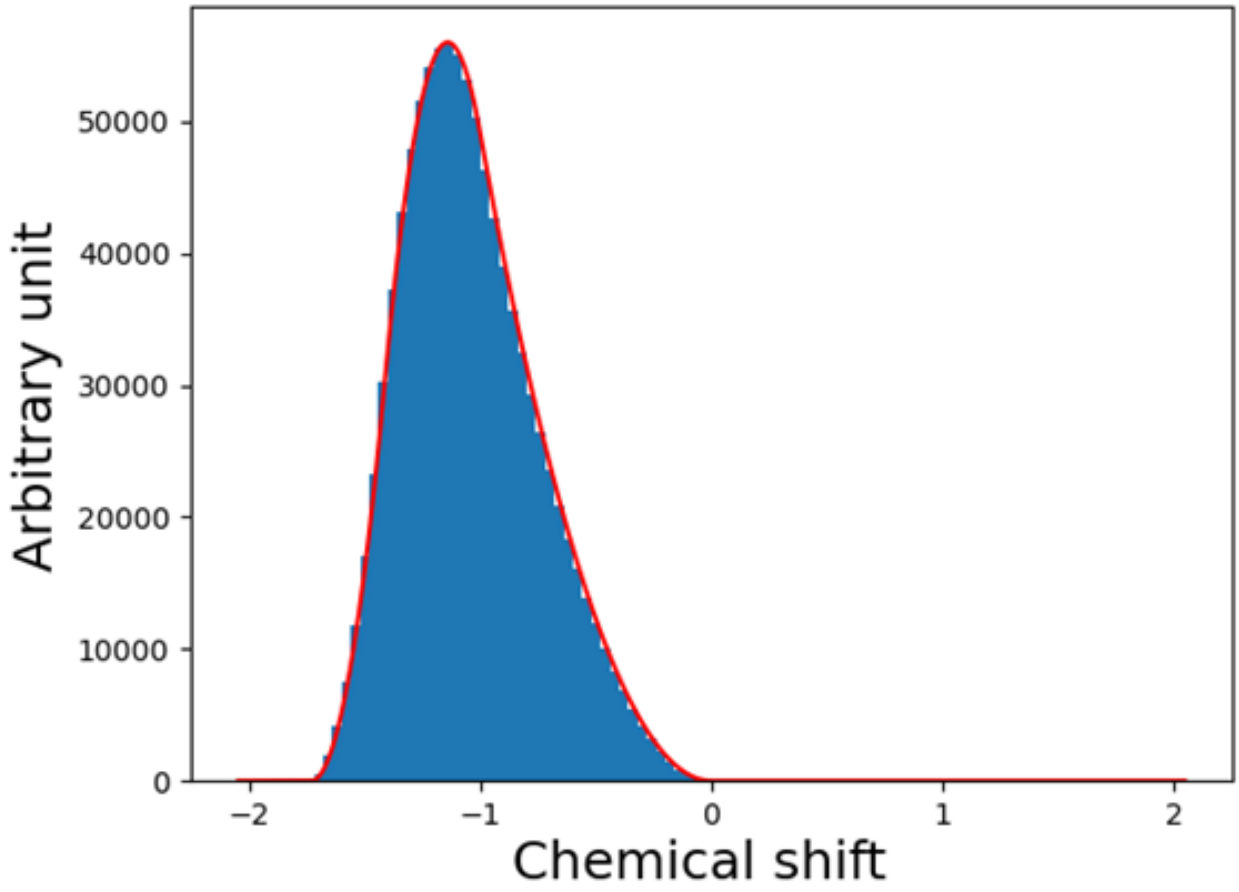

Figure 31 - Validation results for the third scenario as successful matching of line deformation and simulated histogram.

As an application use case, we consider here the scenario where a highly dense NMR spectrum of an arbitrary hydrosilylation reaction acquired with a Brucker AV-400 MHz spectrometer [144] serves as simulation input and an inhomogeneous $\overrightarrow{B_0}$ within a cube of 8 cm^3 where $x \in [-1,1]$ cm, $y \in [-1,1]$ cm and $z \in [-1,1]$ cm that can be described by the mathematical function:

$$B_0 = 1 + \frac{5}{10^6} y + \frac{5}{10^6} x \tag{62}$$

where the resulting field strength is given in Tesla and is a function of two of the three spatial coordinates within the considered cubic volume.

Figure 32 shows the original high-quality input spectrum acquired with a top-class commercial NMR spectrometer and the consequence of performing the same NMR experiment with an NMR spectrometer presenting a comparatively low-quality static magnetic field $\overrightarrow{B_0}$ instead.

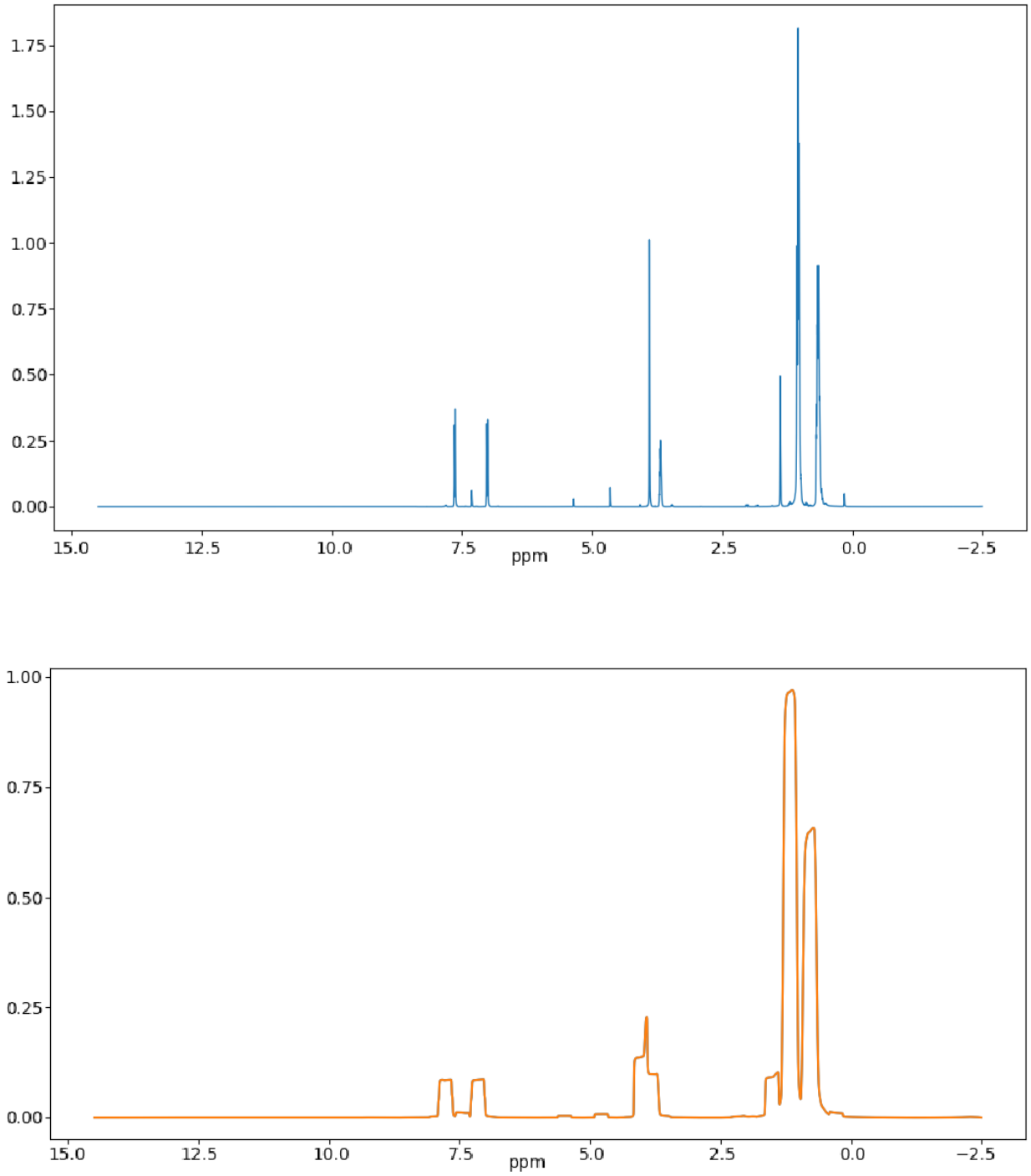

Figure 32 - Top side: acquired high-resolution NMR spectrum used as simulation input. Bottom side: the resulting simulated NMR spectrum already substantially degraded due to field inhomogeneity. Arbitrary amplitudes. Modified. [139]

This portion of the NMR Simulator was the subject of an academic publication by our research team [139], as was the corresponding code [145].

3.2. NMR spectrometer simulation

The simulation of the signal path within the considered NMR spectrometer hardware provides essential insights about its operation and the available adjustment parameters. The considered basic ideal hardware setup for the simulation can be seen in Figure 33.

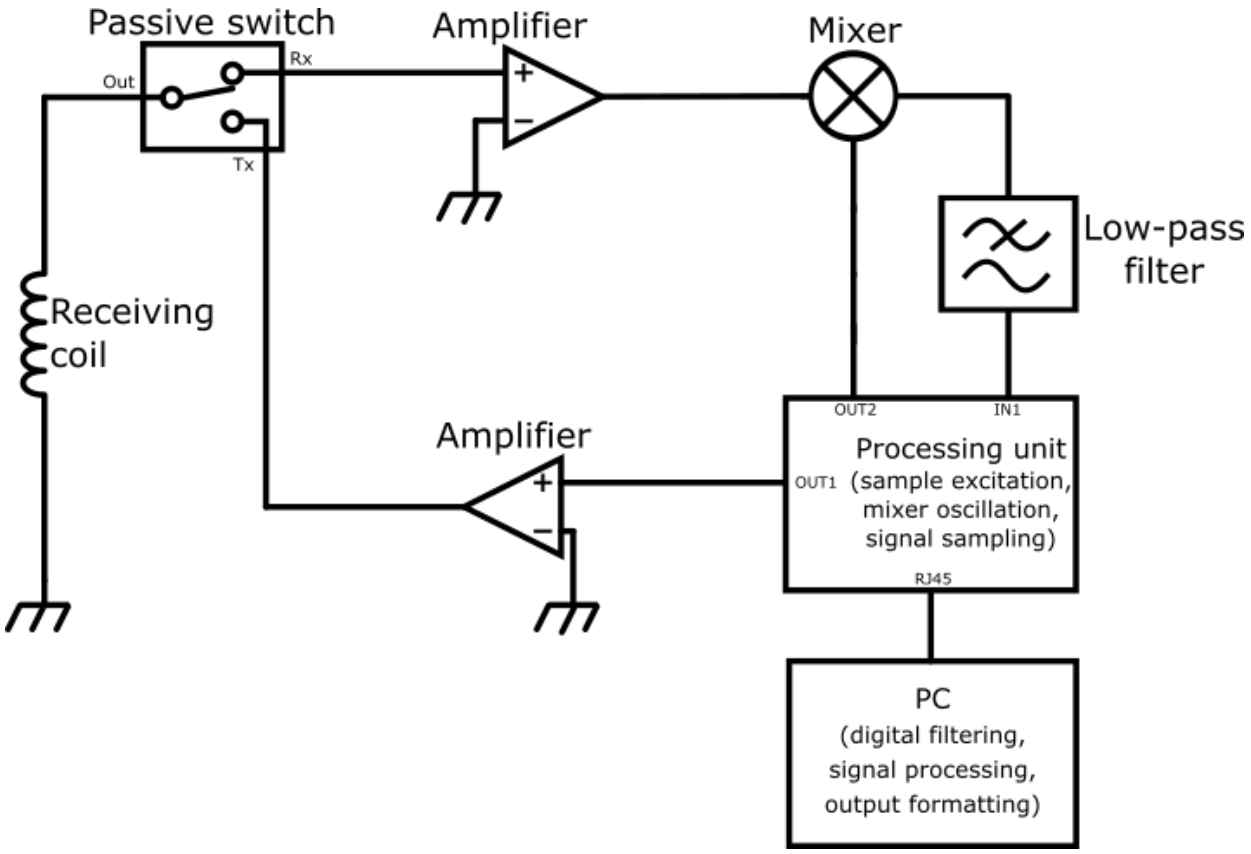

Figure 33 - Hardware setup reference for the simulation of the electronic chain.

In this simplified workflow, the processing board generates the excitation signal that is directed to the coil, resulting into the propagation of $\overrightarrow{B_1}$ through the sample. The FID is perceived by this very same coil and redirected to the mixer that will bring its frequency down so that it can be sampled by the processing unit.

3.2.1. Local oscillator and FID generation

The simulation focuses on the receiving part of the chain, which is the non-trivial signal path, starting from the moment where the FID is measured. At first, the local oscillator signal, which is basically a sinusoidal waveform at the Larmor frequency f_0 increased from the desired down-converting frequency f', and the FID signal, both being the electrical available signals within the electronic chain, are generated. On this demonstration the Larmor frequency was set

to 24 MHz and the down-converting frequency to 1 kHz, the amplitudes or initial amplitudes of the signals, as the case may be, are unitary, being the number of spectral peaks and their chemical shifts given for each scenario, when applicable and of interest for the demonstration. For simulated signals in the digital domain, the sample rate of the DAC (Digital-to-Analog Converter) is parametrizable with typical sampling rates that can be achieved by the hardware used in this study [146], *e.g.*, 125 Msps. The employed hardware is described in chapter 0. For the simulation of the analogue parts, the vectorisation of the array variables was done sufficiently dense so that the results of the simulations using discretized data reflects the analogic behaviour of the electronic chain. In this tool, the impact of $\overrightarrow{B_0}$ inhomogeneity on the relaxation time constant is parametrizable through T_2^*, for $T_2^* \in [0, T_2]$. Alternatively, the FID can be obtained from any NMR spectrum by inverse Fourier transform, and even from a degraded frequency spectrum as the ones predicted by the preceding simulation module. In this case, T_2^* has to be set to T_2 so that the static field inhomogeneity is not taken twice into account. Some simulation results for this first block are given in Figure 34 (the local oscillator waveform) and Figure 35 (simulation of an ideal FID signal).

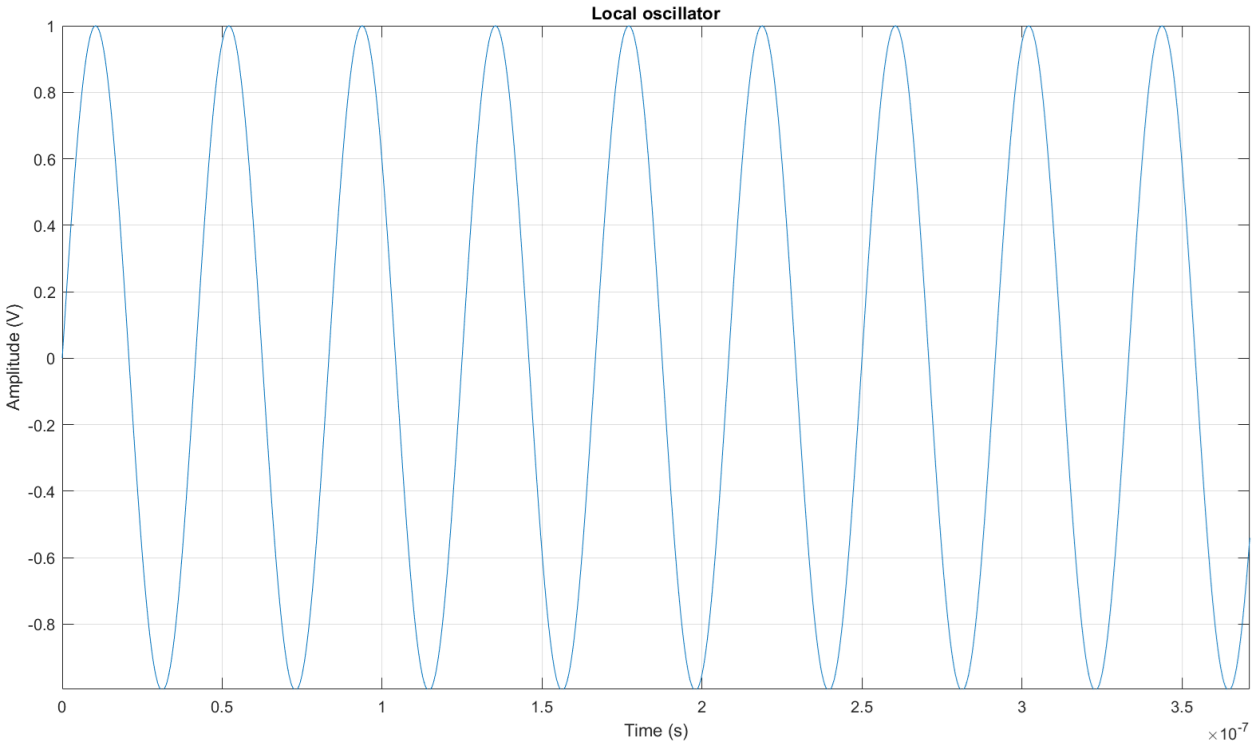

Figure 34 - Local oscillator waveform at 24 MHz + 1 kHz.

At this point, it is interesting to consider that the electronic chain is not ideal and at least white noise is forcibly introduced to the ideal measurable signal. Within the simulation, this is done by changing the SNR parametrization, what would be the equivalent of changing the intra-chain existing noise level in the practice. Figure 36 exhibits the ideal FID of Figure 35 considering a SNR of 30.

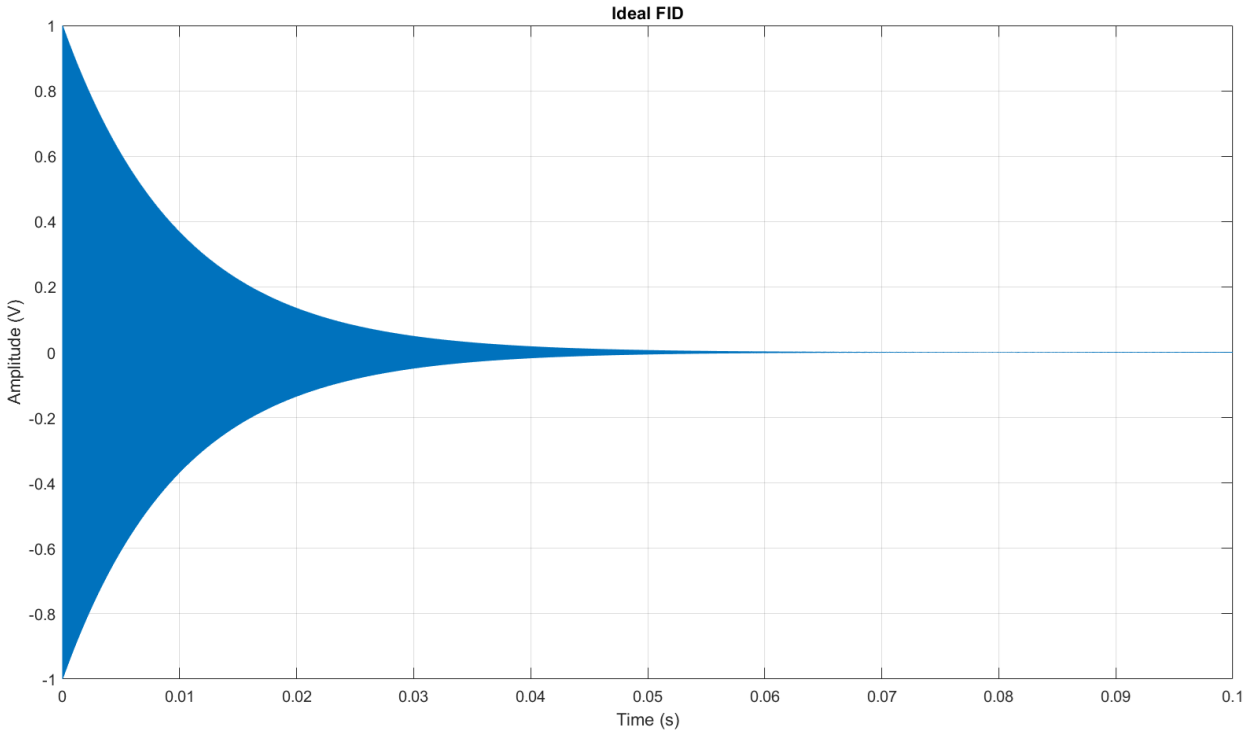

Figure 35 - FID signal at a frequency equivalent to a chemical shift of 5 ppm.

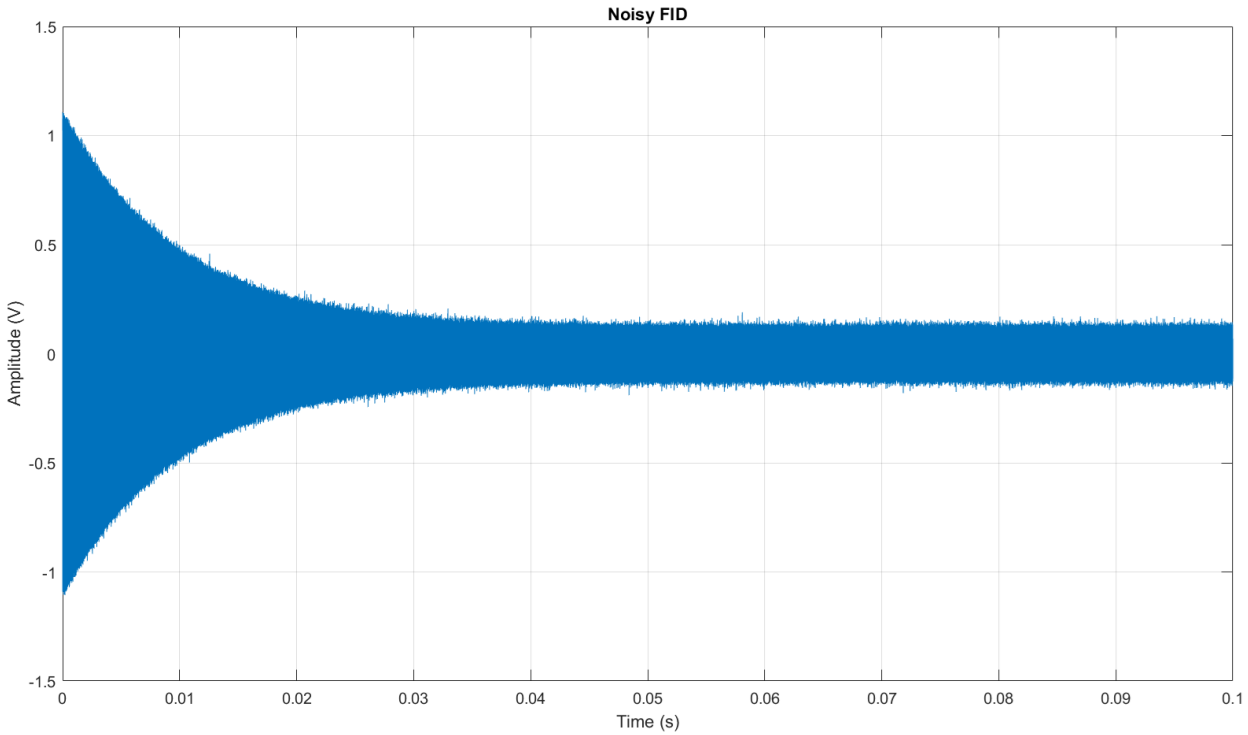

Figure 36 - FID with a noise level equivalent to a SNR of 30.

3.2.2. Analogue mixer

On the electronic level, an analogic mixer is used to implement the frequency down-conversion of the FID, typically in the presence of noise, by multiplying it with the local oscillator waveform. The local oscillator signal can be defined as a sinusoidal signal $e_s^{\varphi_1}(t)$, with arbitrary amplitude A and phase φ_1, coming to the mixer, as:

$$e_s^{\varphi_1}(t) = A\sin(2\pi(f_0 + f')t + \varphi_1), \qquad \forall t \geq 0 \tag{63}$$

And now, let us consider the alternative way of writing an FID $\mathcal{s}_{FID_P}^{\varphi_2}$ with as well arbitrary amplitude B and phase φ_2, and assuming for the sake of simplicity that there is only one functional group P responsible for the single chemical shift, as follows:

$$\mathcal{s}_{FID_P}^{\varphi_2}(t) = B\cos\left(2\pi f_{FID_P}t + \varphi_2\right)e^{-\frac{t}{T_{2P}^*}}, \qquad \forall t \geq 0 \tag{64}$$

From the trigonometric product identity:

$$\sin(\alpha)\cos(\beta) = \frac{\sin(\alpha+\beta) + \sin(\alpha-\beta)}{2} \tag{65}$$

one can then write:

$$\begin{aligned}
\mathcal{s}'_{FID_P} = e_s^{\varphi_1}(t)\mathcal{s}_{FID_P}^{\varphi_2}(t) &= A\sin(2\pi(f_0 + f')t + \varphi_1)\,B\cos\left(2\pi f_{FID_P}t + \varphi_2\right)e^{-\frac{t}{T_{2P}^*}} \\
&= \frac{AB}{2}\left(\sin\left(2\pi(f_0 + f')t + \varphi_1 + 2\pi f_{FID_P}t + \varphi_2\right)\right. \\
&\left. + \sin\left(2\pi(f_0 + f')t + \varphi_1 - 2\pi f_{FID_P}t - \varphi_2\right)\right)e^{-\frac{t}{T_{2P}^*}} \\
&= \frac{AB}{2}\sin\left(2\pi\left(f_0 + f' + f_{FID_P}\right)t + \varphi_1 + \varphi_2\right)e^{-\frac{t}{T_{2P}^*}} \\
&+ \frac{AB}{2}\sin\left(2\pi\left(f_0 + f' - f_{FID_P}\right)t + \varphi_1 - \varphi_2\right)e^{-\frac{t}{T_{2P}^*}}, \qquad \forall t \geq 0
\end{aligned} \tag{66}$$

We can observe therefore that the resulting signal is constituted by two fundamental frequency components, one high-frequency f^{HF} and the other low-frequency f^{LF}:

$$f^{HF} = f_0 + f' + f_{FID_P} = f_0 + f' + f_0\,(1 + \delta_P) = 2f_0 + f' + f_0\delta_P \cong 2f_0 + f' \approx 2f_0 \tag{67}$$

$$f^{LF} = f_0 + f' - f_{FID_P} = f_0 + f' - f_0\,(1 + \delta_P) = f' - f_0\delta_P \approx f' \tag{68}$$

The first term of $\mathcal{s}'_{FID_P}$, that is at a higher frequency ($\approx 2f_0$), can be easily removed by an electronic low-pass filter. The second term corresponds to the baseband FID, and using equation (5), one can see that under ideal conditions, the absolute value of the chemical shift δ_P corresponding to the functional group P at high and low frequencies is kept the same:

$$f_0 + f' - f_{FID_P} = f_0 + f' - f_0\,(1 + \delta_P) = f' - f_0\delta_P, \qquad \delta_P = \frac{f_{FID_P} - f_0}{f_0} \tag{69}$$

For the sake of simplicity, we consider for now that $\varphi_1 = \varphi_2$ so that $\varphi_1 - \varphi_2 = 0$. We will see, however, that this is not always the case and depends on the quality of the employed hardware, especially in what concerns the processing unit signal generation and sampling capabilities. Figure 37 and Figure 38 exemplify the analogic mixer output when having the local oscillator waveform and the noisy FID as inputs, before filtering out the high frequency component from the resulting multiplication.

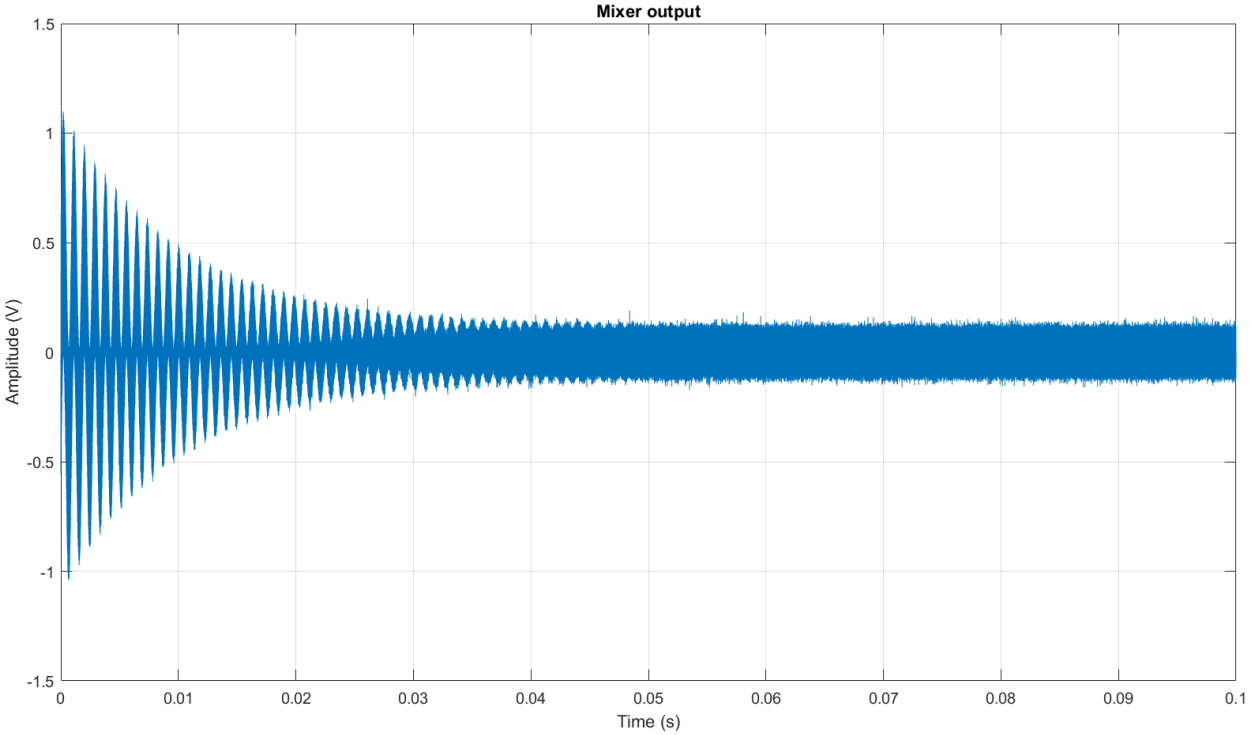

Figure 37 - Mixer output portraying the result of multiplying the local oscillator waveform and the FID signal.

After low-pass filtering the mixer output and re-sampling the resulting signal to an array of N data elements, *i.e.*, N sub-types, which corresponds to the real size of the available acquisition buffer in an NMR spectrometer, we get the resulting NMR signal presented in Figure 39 and Figure 40. Here, the sampling frequency f_s corresponds to the time value of the last time data array sub-type divided by N, since the FID starts at $t = 0$, and is given in Hz when the time is given in seconds.

3.2.3. Analog-to-digital conversion and digital signal processing

We proceed with the ADC (Analog-to-Digital Converter) quantification estimation. Each one of the N elements of the acquisition buffer is digitized within a certain number of bits M, characterizing the converter amplitude resolution. Subsequently, the N-long amplitude data array

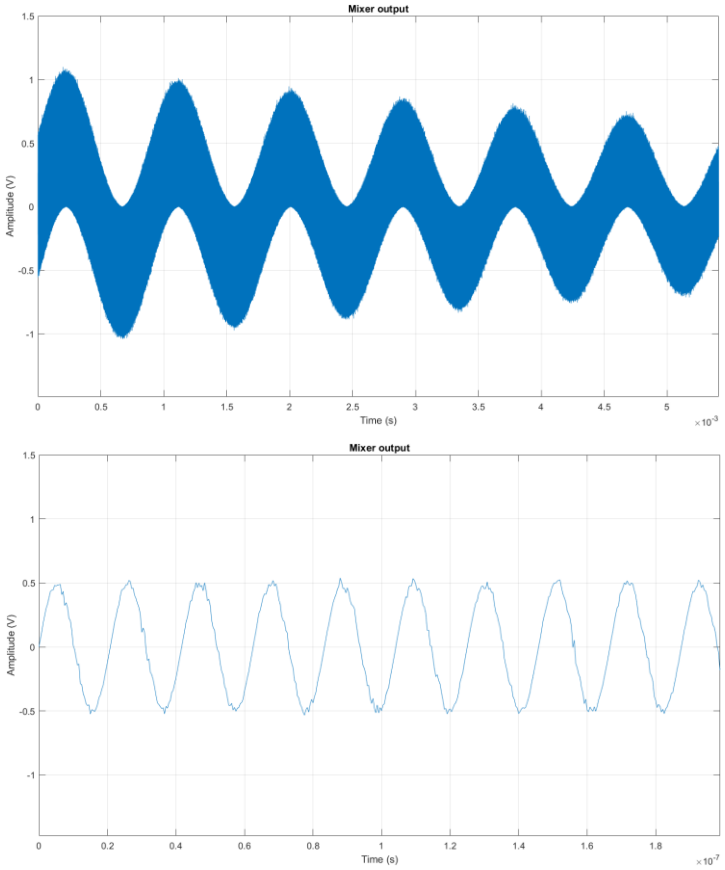

Figure 38 - Zoomed mixer output. Top side: output zoomed to a degree where the term with the lower frequency can be correctly depict and examined. Bottom side: the output was even more zoomed so that the high-frequency term is evident.

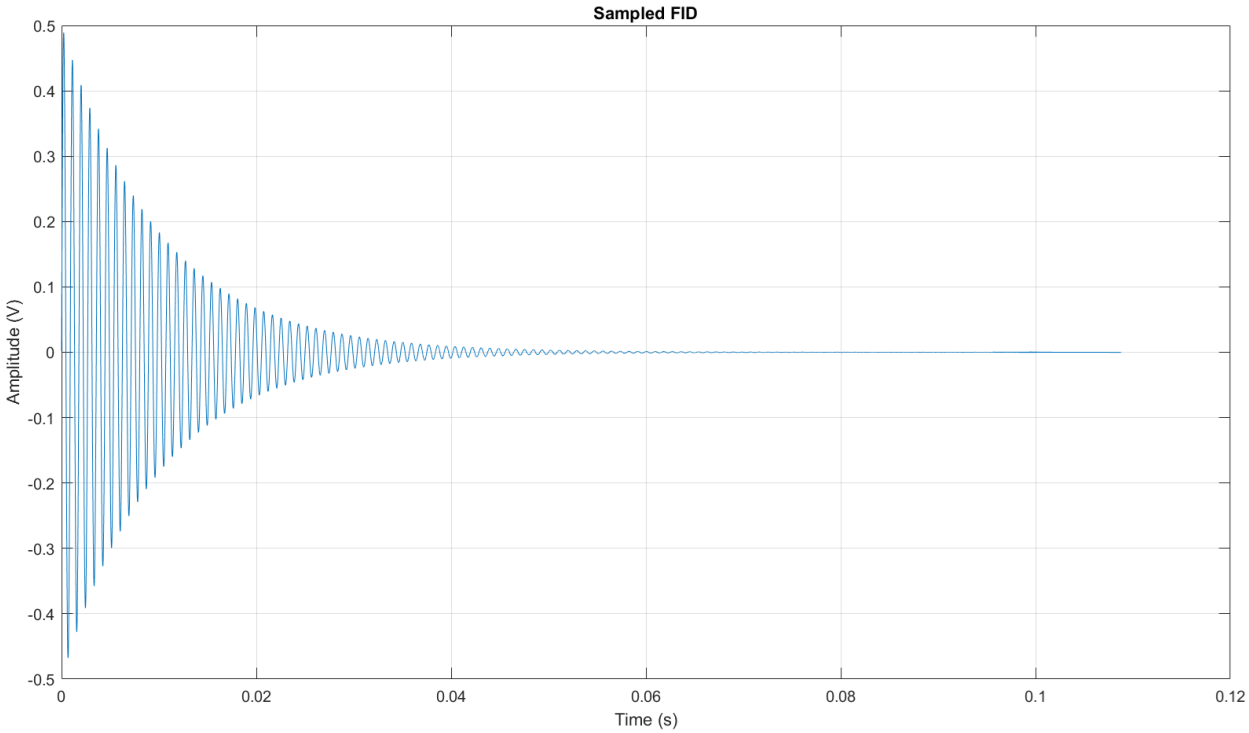

Figure 39 - Sampled FID for a $N = 2^{14} = 16384$ long array, which is the size of the available acquisition buffer in our NMR spectrometer prototype.

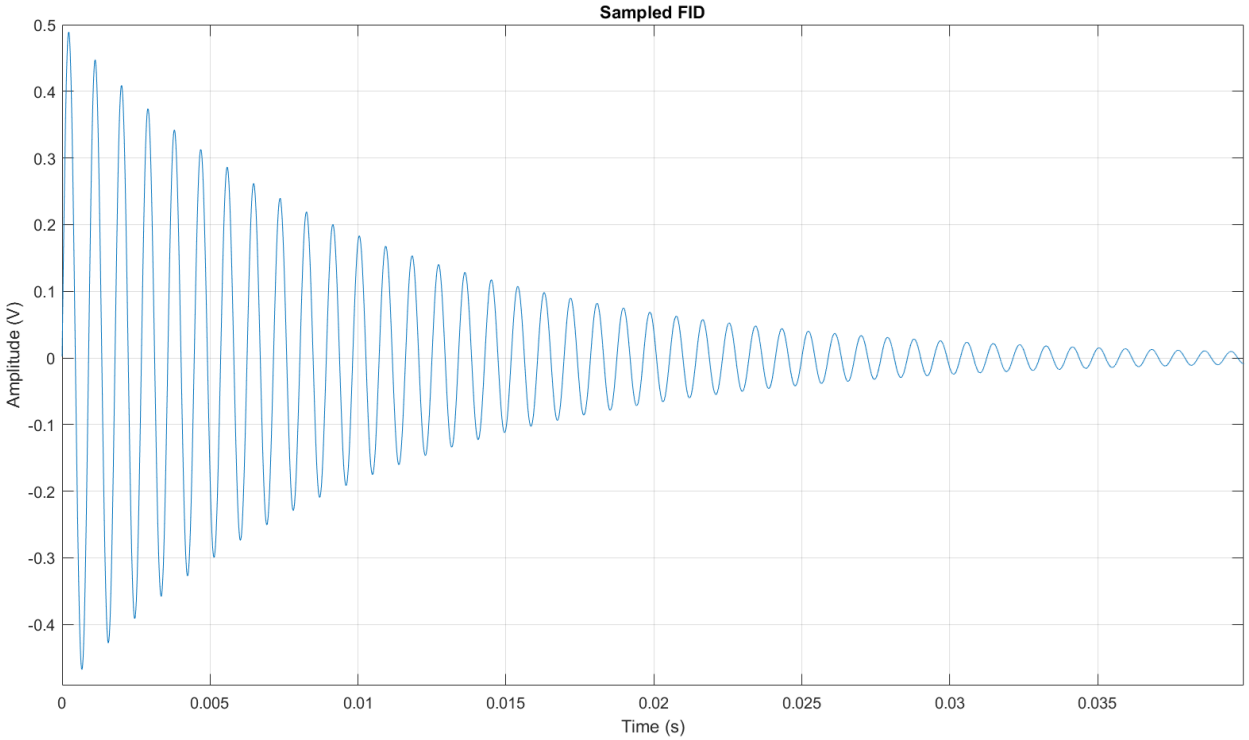

Figure 40 - The zoomed sampled FID for a better detailed view.

composed of M-bits-long sub-types is typically interpreted as a set of floating-point numbers, which scaling depends on the hardware accepted voltage input range, and on the system floating-point architecture. For instance, the processing unit currently used within our prototype presents an ADC resolution $M = 14\ bits$.

Therefore, from here is where we stop simulating the analogical part of our tool chain and proceed with the digital signal processing of the NMR signal. In our prototype, the next step actually happens on the computer on Matlab, after that the processing unit has finished transmitting the sampled FID signal. This is merely a design choice since further digital signal processing could happen as well within the signal processing unit.

Having the FID digitally available, the frequency analysis can take place. The FT of the FID provides its corresponding frequency spectrum, as presented in Figure 41.

As usual, the outcome of the FT is a symmetric set representing the positive and negative frequency components composing the temporal signal. This is already actually our NMR experiment output, however not yet in its typical form which NMR analysts are used to. In order to obtain the classic NMR outcome, half of the plot in Figure 41 is discarded since it is redundant. And following the implications of equation (69), the frequency axis is readjusted so that it can be designated in chemical shift terms. For the FID presented in the previous figures in this subsection, a chemical shift corresponding to 5 ppm deviating from the Larmor frequency was defined, and so Figure 42 shows the typical NMR analysis outcome for this considered NMR experiment.

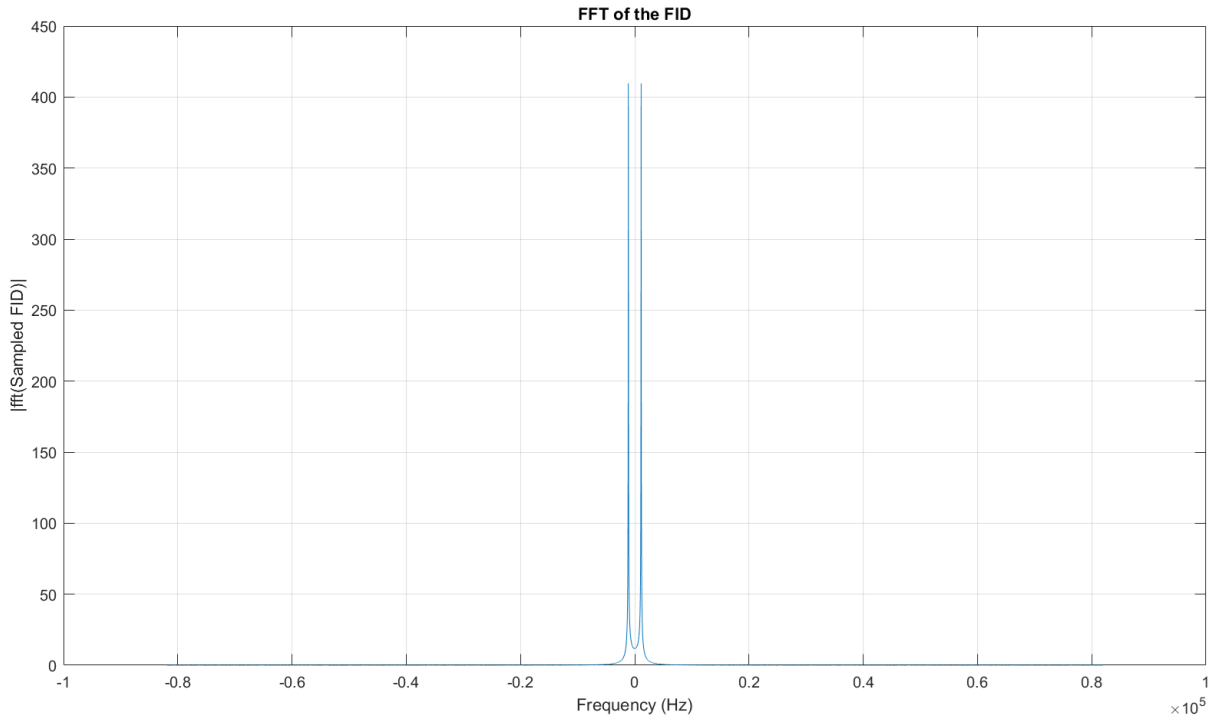

Figure 41 - Frequency spectrum corresponding to the sampled FID.

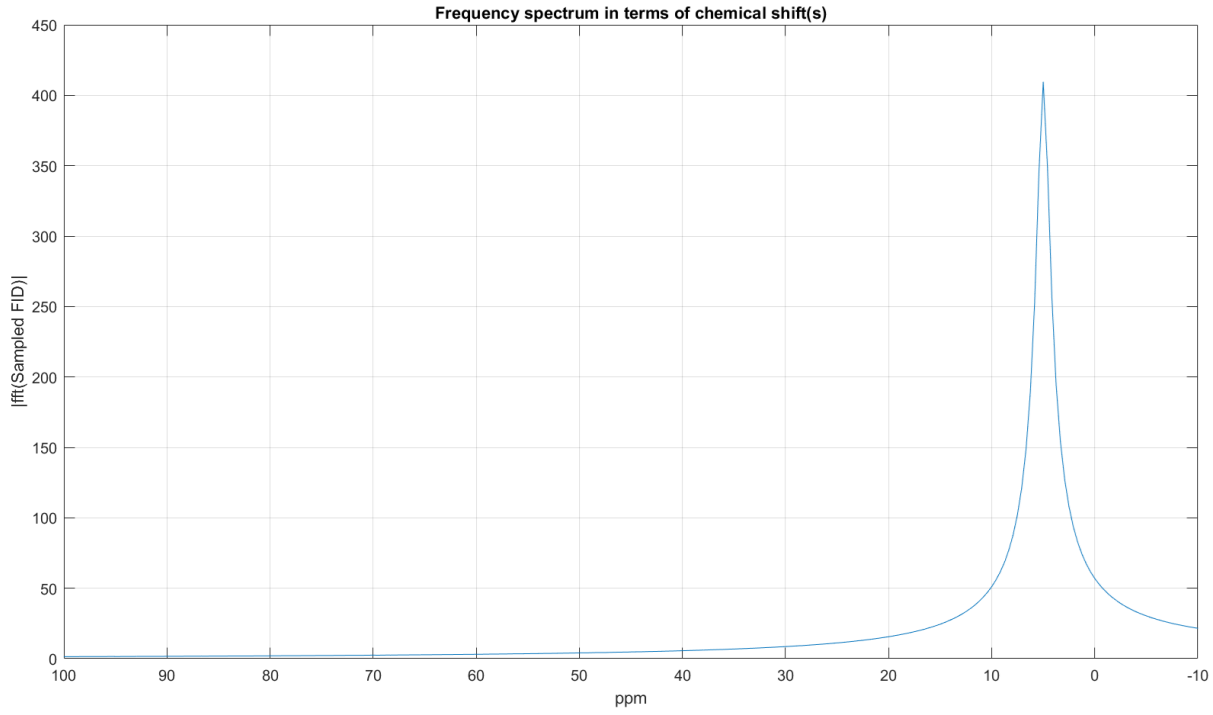

Figure 42 - Typical low-resolution NMR analysis outcome presenting a single peak centered at 5 ppm.

The size of the acquisition buffer and the employed sampling rate have a direct impact on the frequency resolution of the NMR analysis outcome. And for NMR analysts, in everyday practice, the exact amplitude of the peaks and their units are usually less important than knowing their correct chemical shifts.

As an illustration of peak-merging in low-resolution NMR, Figure 44 presents a simulated NMR spectrum for the ethanol molecule, from its corresponding simulated sampled FID presented in Figure 43.

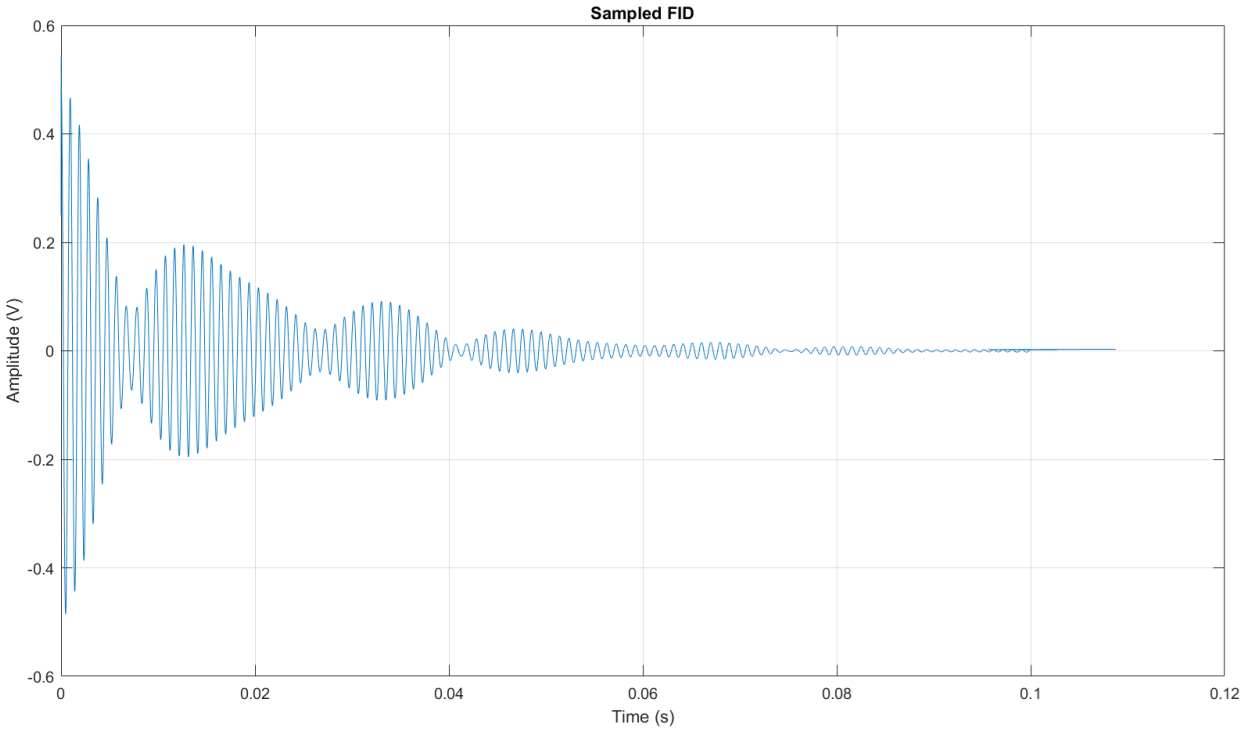

Figure 43 - Simulated sampled NMR signal for ethanol considering a perfectly homogeneous $\overrightarrow{B_0}$ and three FID components corresponding to the three existing molecular groups.

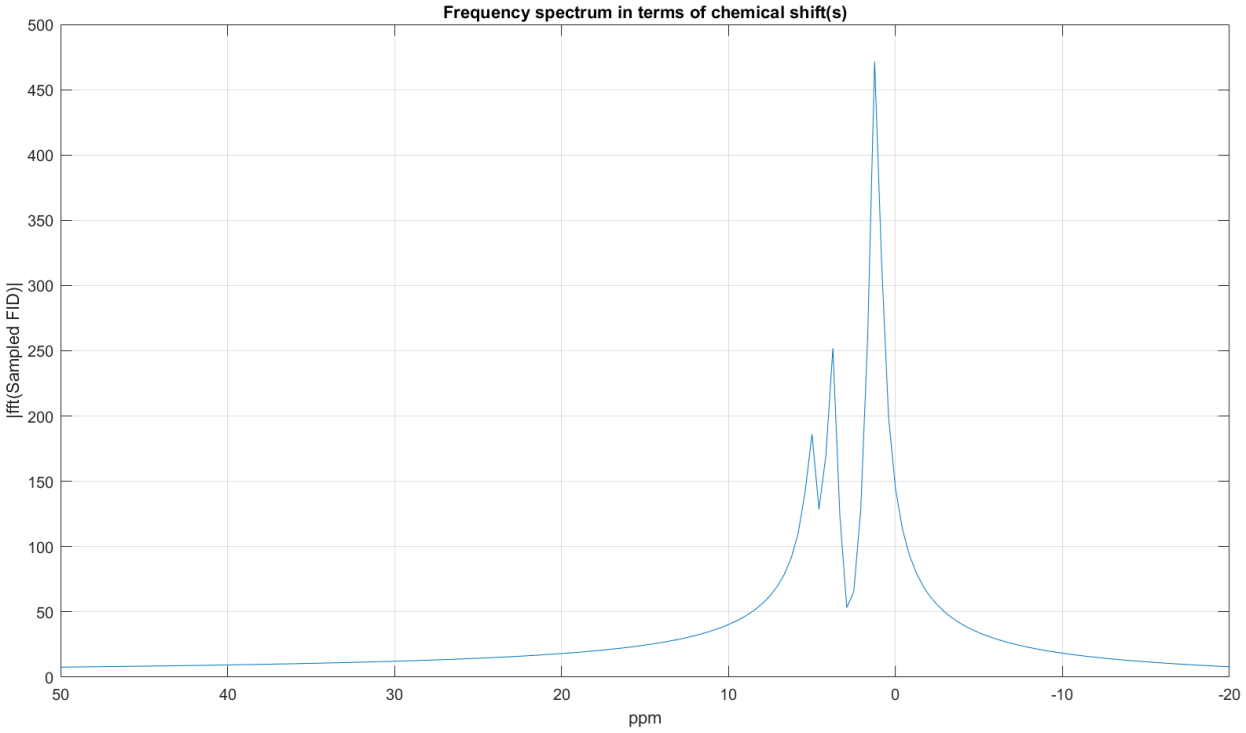

Figure 44 - Resulting simulated low-resolution NMR spectrum for the ethanol molecule.

Table 3 resumes the possible parametrization of this simulation module:

Parameter / Variable	Name / Meaning	MATLAB Argument Data Type / Unit
SNR	Signal-to-Noise Ratio.	scalar, double / dB
FID_n_max_amplitude	Maximal amplitude of the n FID.	scalar, double / V
Larmor_Frequency	f_0	scalar, double / Hz
FID_n_chemical_shift or FID_n_frequency	Chemical shift of the n FID or frequency of the n FID.	scalar, double / ppm or scalar, double / Hz
FID_n_delta_t_sampling or FID_n_phase	Time between the start of the n FID and the start of the sampling or equivalent phase shift of the n FID and the start of the sampling (considered to be 0°).	scalar, double / seconds or scalar, double / radians
Local_oscillator_max_amplitude	Maximal amplitude of the mixer reference signal.	scalar, double / V
DC_frequency or Local_oscillator_frequency	Down-conversion frequency or frequency of the mixer reference signal.	scalar, double / Hz
Local_oscillator_phase	Phase shift of the mixer reference signal and the start of the sampling (considered to be 0°).	scalar, double / radians
ppp	Points-per-Period for the dense computation (simulation of the analogical signals).	scalar, integer
T2_star	Relaxation time constant (which can be both T_2^* or T_2, if $\overrightarrow{B_0}$ is considered perfectly homogenous).	scalar, double / seconds
SDR_buffer_size	N number of sub-types composing the acquisition buffer.	scalar, integer

SDR_ADC_resolution	M number of bits defining the ADC amplitude resolution.	scalar, integer
t_init and t_end	Initial and final times of the time vector.	scalar, double / seconds
FPASS	Passband frequency of the digital low-pass filter (simulating the analogical one).	scalar, double / Hz

Table 3 - NMR Simulator parameters related to the simulation of the electronic chain, and their corresponding units.

The gains of the amplifiers are incorporated into the variables providing the maximal value for the different amplitudes. As an alternative to the parametrization of the FID following these variables, it is possible to import an FID directly into the simulation model, where their two composing axes will be vectors of doubles, one being given in terms of voltage and the other being given in terms of seconds.

The simulation code employed in this section is made available in the appendix section II.

3.3. NMR signal time domain adjustment

Once we can predict spectral degradation due to field inhomogeneity and forecast what happens within the NMR spectrometer electronic chain under ideal conditions as well as when we consider the effect of electronic noise, there is still left the estimation and correction of time inaccuracies concerning the processing unit.

Both commercial and self-made embedded system solutions, and especially the ones classified as or intended to be low-cost, can present difficulties in correctly and precisely triggering the acquisition procedure, *i.e.*, the sampling process, causing the acquired signal to start at slightly different positions of the acquisition buffer. This leads to the fact that, in the practice, when considering equation (66), the difference $\varphi_1 - \varphi_2$ can be different from zero and, even worse, it can change from one acquisition to another. Due to the modulation property of the FT, the presence of a non-null phase term is equivalent to multiplying the resulting function by a complex exponential term. As the modulus of this due-to-the-phase introduced term is 1, it bears no impact on the power spectrum, however it influences the amplitude spectrum. Therefore, this non-null phase must be taken into consideration always when considering the

amplitude spectrum, which is the case, for instance, when performing amplitude spectral accumulation.

This phase difference may be very difficult to nullify, and it should at least be kept constant by precisely controlling the time between the start of the excitation and the start of the relaxation. We must consider, however, that such time can be of the order of dozens of microseconds to hundreds of milliseconds, and additionally, the signal on which the phase is measured evolve at several tens of megahertz. For instance, at 24 MHz, a phase of 10° represents 100 ps, *i.e.*, 0.0001 ppm over one second, a precision that is virtually impossible to achieve with digital systems based on current commercial microcontrollers or FPGAs.

How best to deal with this random phase variation depends greatly on the measured FID signal. Therefore, we thought it was appropriate to add such phase effect into the NMR Simulator, and as we saw in the previous section, it has been integrated into the FID determination by means of specific parameters, which can incorporate as well random temporal offsets. In this sense, the software module described in this section is very helpful in the design and test of further digital signal processing algorithms that we may employ overall within our NMR Spectrometer as well as within the simulation chain itself.

Generally speaking, for NMR experiments where single acquisitions of strong FID signals are sufficient to generate a quality NMR spectrum, there is no big deal in having a sampled FID temporally shifting its beginning in the acquisition buffer because of two reasons. First, such a shift leads, in the Fourier domain, to the multiplication of the spectrum with a complex exponential. The power spectrum is therefore insensitive to this shift. Second, even if the amplitude spectrum is required (for accumulation purposes, for instance), rephasing can be easily achieved by standard post-processing algorithms because the noise floor does not preclude the data treatment.

However, the interest in being able to shift a temporal NMR signal in a controlled manner becomes evident when we leave behind the ideal scenario and start considering having weak FID signals with amplitudes that are barely able to emerge from the noise floor, complex NMR spectra to be analysed, temperature drifting and other forms of field inhomogeneity sources and disturbances possibly engendering significant spectral degradation and chemical shift fluctuations, and generally a poor NMR experiment environment where spectra accumulation is not feasible because simply technically not possible. In such cases, the averaging must happen on the time-domain. If the available hardware is precise enough, the signal accumulation process is greatly simplified and it suffices to add the acquisition buffers of the successive experiment scans to one another to see the FID coming out of the noise floor, as depicted in Figure 45 and Figure 46.

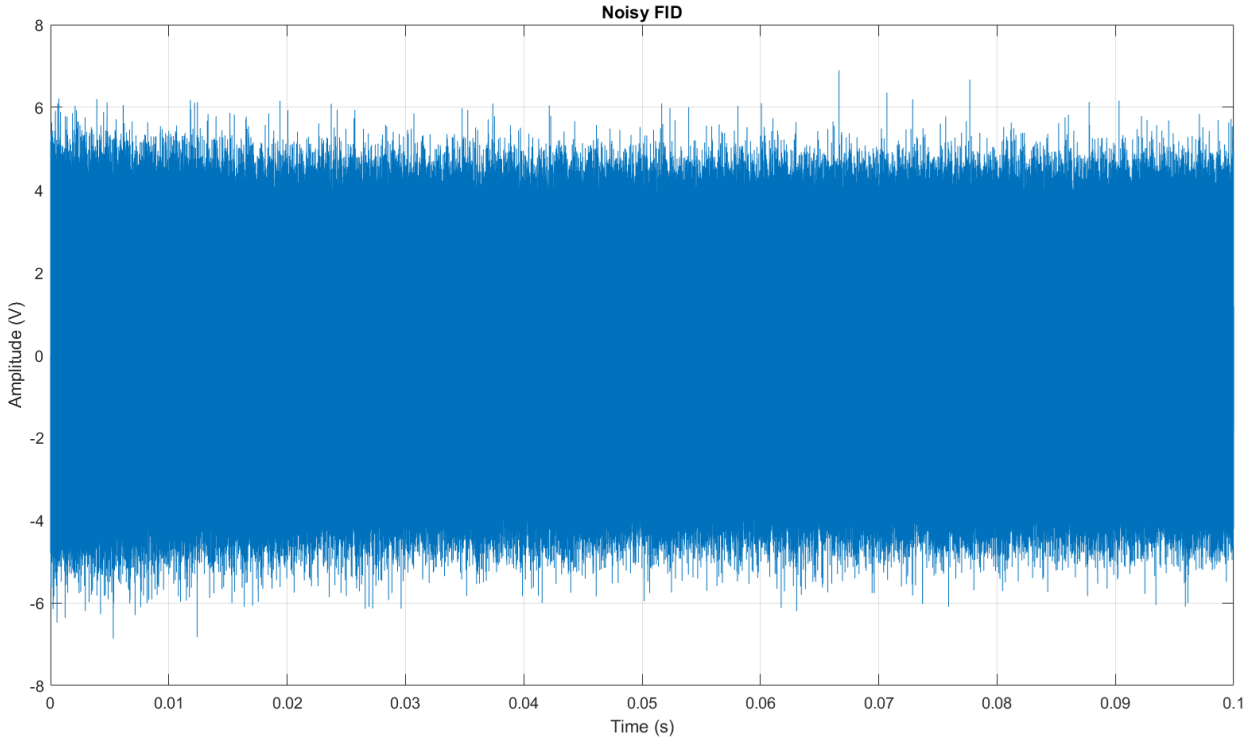

Figure 45 - A single acquisition of a weak signal. The FID is immersed in the noise floor and cannot be recognized.

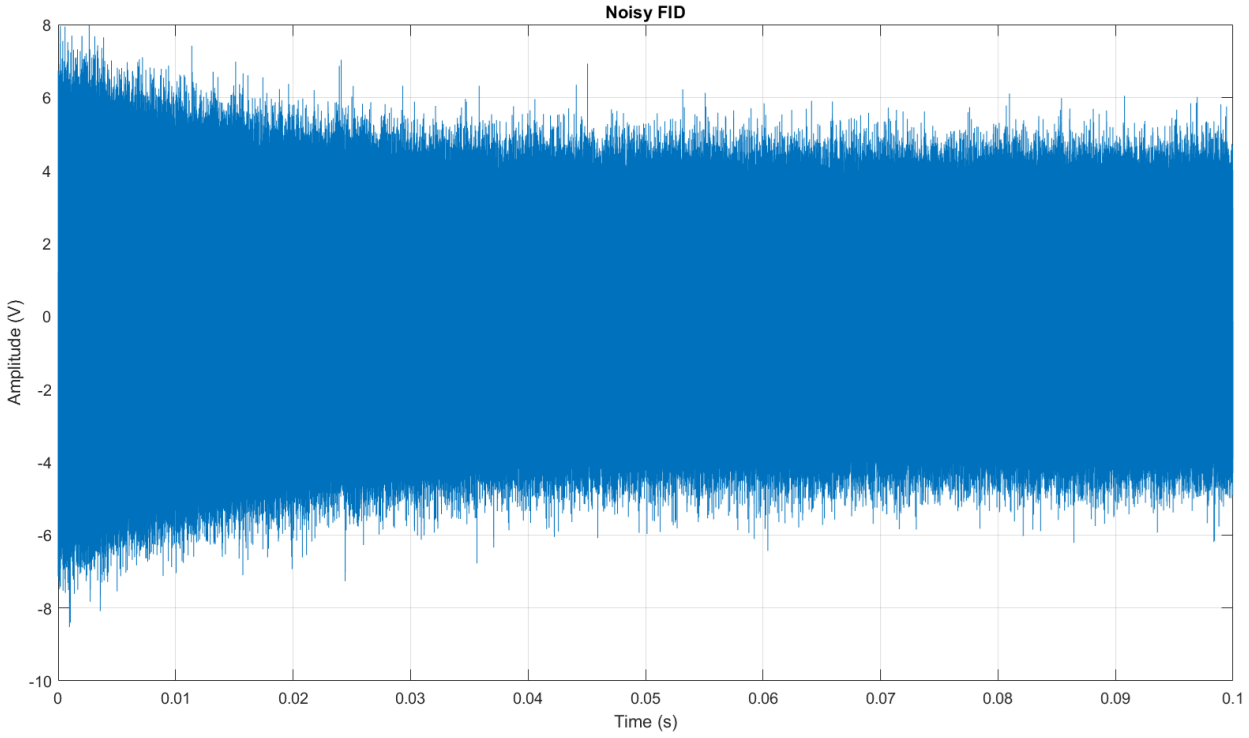

Figure 46 - The simple accumulation of three FIDs generated by three different scans already allows the resulting FID to hew out of the noise floor.

The examination of the averaging process with a somehow stronger signal, as in Figure 47 and Figure 48, allow us to concretely see the gains in terms of SNR by doing so.

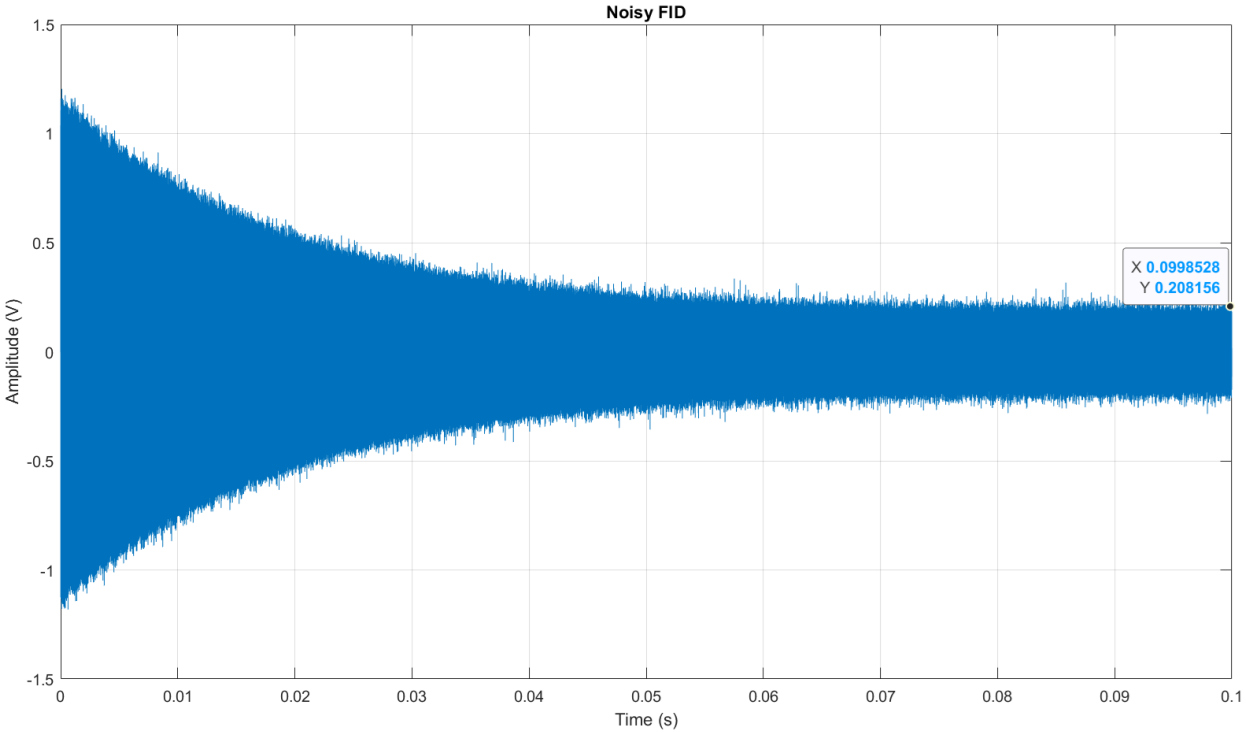

Figure 47 - A single acquisition of a reasonably strong signal. Although the FID shape is recognizable, the presence of noise is evident and quite substantial.

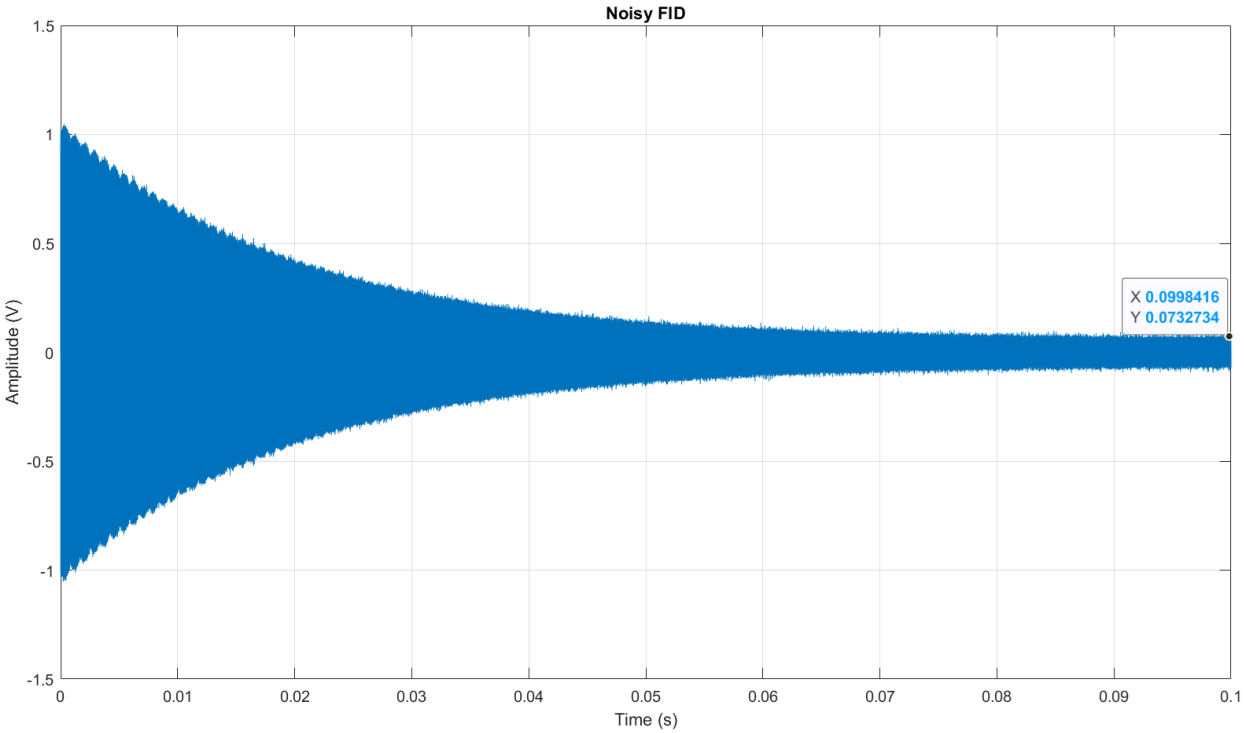

Figure 48 - After performing the averaging on three different single-acquired FIDs coming from three different scans, the SNR improved approximately threefold.

It is clear that this averaging method is the most straightforward and technically easy to implement. Nonetheless, minimal shifts in the time domain would already decrease its effectiveness because while adding the FIDs, instead of accumulating the contained wavelets,

they would start cancelling each other amplitudes, in the same way that adding two out-of-phase sinuses would not be the most optimal setting when trying to increase the overall resulting amplitude through their sum. Evidently, the worst-case scenario would be when the sum happens for a shift in time that would make positive vertices of one FID coincide with negative ones of the other. It would cause the almost complete cancelling of the FIDs and work in the opposite desired direction. Having the ability to generate FIDs with phase issues is critical in order to use our simulator for the assessment of FID accumulation methods.

At this point it is worth noticing that within our simulation chain, the parametrization of the lag time, *i.e.*, the phase between the different simulated FIDs, can be provided either in terms of a phase in radians with regard to the reference phase $\varphi = 0$, or it can be directly specified in terms of a lag time in seconds with reference to the considered starting sampling time $t = 0$. Having the possibility of defining this parameter directly as a lag time is important because it allows the simulation chain to ponder the imprecisions of the sampling unit, therefore evaluating their consequences on the NMR analysis outcome.

This software module was implemented in the Python language and integrated to our MATLAB code. Practical aspects related to this topic are further explored in the next chapter, and the simulation code employed in this section is made available in the appendix section II.

$\mathcal{NMR}$

In this chapter a complete simulation toolbox was showcased and its different outcomes including expected NMR spectra related results was demonstrated. It is composed of a first block that focuses on the inhomogeneity of the static magnetic field within the experiment volume and can predict the degradation impact on NMR spectra due to an inhomogeneous magnetic field $\vec{B}$, having as reference a perfectly homogeneous magnetic field $\overrightarrow{B_0}$. It is achieved by employing a convolution product on an ICF, which can be computed in different ways. Such framework is useful for support of magnet and shim design assessment and spectral degradation prediction. The second block corresponds to the simulation of the electronic front-end and, more specifically, of the distortions that might be introduced at each part of the electronic circuit. It takes as input a reference FID, often addressed as the ideal FID, and returns either an altered FID which quality depends on several parameters (noise of the electronic circuit, resolution of the ADC and size of the acquisition buffer, accuracy of the system sequencing, etc.), or the corresponding NMR spectrum. Finally, the last block provides the means of taking into account the impact of hardware imprecisions in terms of FID

synchronization, especially with the objective of temporal accumulation of NMR signals with a low SNR.

Concerning the simulation tool itself, with these three pieces of software, we enabled to a great extent the simulation of the complete NMR electronic chain, the temporal adjustments due to an eventually imprecise sampling process, and the estimation of spectral degradation due to the magnetic system imperfections.

Next, we present our NMR Spectrometer Prototype at its current shape and form, how it is built, what are its composing elements and their characteristics, how they work and interact with each other, their limitations and the related implications, and the results that we were able to obtain with it up to now.

Chapter 4 - NMR Spectrometer Prototype

Objectively, our research team aims at designing a functional low-field ^{1}H NMR spectrometer for in-field use. The main construction goals for such equipment are therefore its portability and miniaturization, accessorily followed by the reduction of its production overall costs, aiming to build a low-cost device. Within our research team, the efforts to accomplish such objectives started years ago with the doctoral studies of Duc-Vinh Nguyen [2] and Lucas Werling [3]. While these colleagues focused primarily on the development of the receiver and transmitter electronic modules and in the receiving coil and matching circuitry respectively, allied mainly to the employment of external commercial equipment for control and measurement, as signal generators and oscilloscopes, we were subsequently interested in introducing a processing unit respecting the requirements set forth before, therefore defining this work scope in what concerns the NMR Spectrometer Prototype in introducing the use of a commercial processing unit and general improvements of the already existing prototype electronics. A possible design choice for the processing unit was to select and employ a commercial SDR to act as interface between the operating computer and the electronic modules, being responsible for generating the necessary reference signals and sampling the measured FID. Our proposed system design architecture is presented in Figure 49. It is composed of custom circuits for the receiver and transmitter electronics, a commercial power-amplifier, a processing unit embedded in a commercial SDR, and an external processing unit module on a laptop. A commercial benchtop NMR system from the company Pure Devices [4] provides the NMR measurement chamber, *i.e.*, the permanent magnet and the shimming system for the static magnetic field $\overrightarrow{B_0}$, and the receiving coil.

The Pure Devices spectrometer, which parts are used within our prototype, can also be employed in its entirety as a stand-alone reference system, against which we compare our prototype results. The Pure Devices system is presented in this chapter first section. The second one presents the Red Pitaya module, *i.e.*, the SDR used as processing unit. The prototype custom receiver and transmitter electronics employed for the signal generation and acquisition, and a description of the setup hardware-related limitations are presented in the third section. Signal post processing and output formatting are described in the fourth section. Finally, the last section presents an overview of the prototype operation.

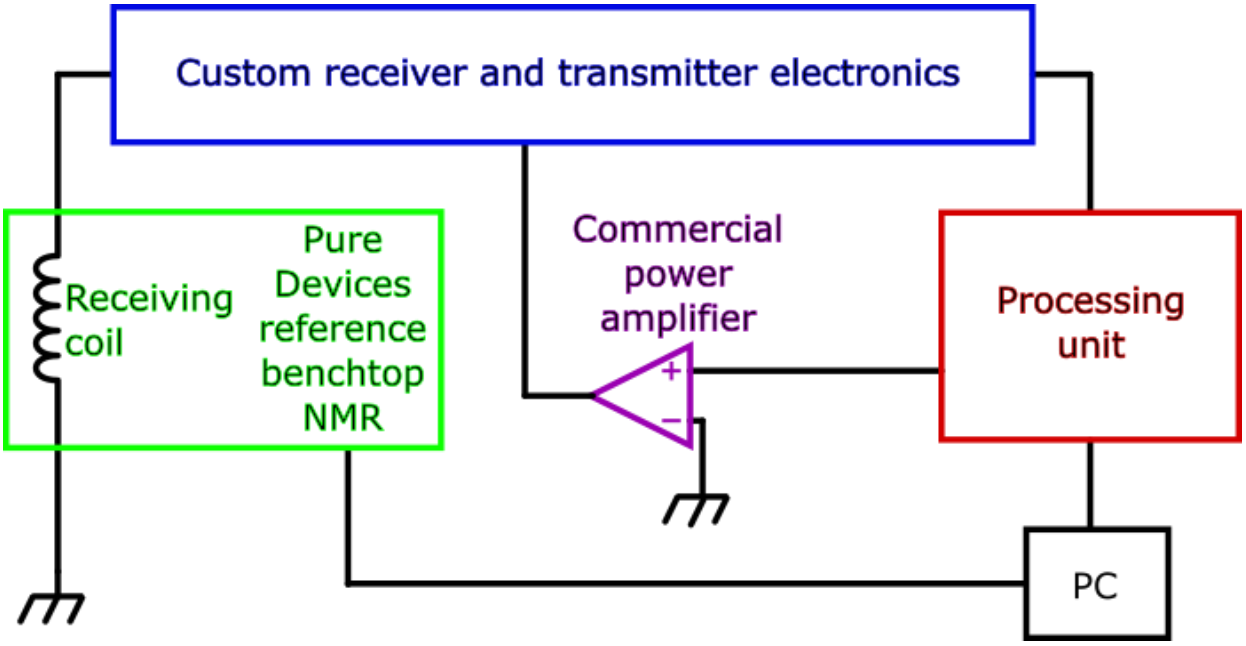

Figure 49 - NMR Spectrometer Prototype design architecture.

4.1. Reference benchtop NMR system

As explained before, for the NMR experiment to take place, at least four composing subsystems are required: a proper monodirectional static magnetic field $\overrightarrow{B_0}$ within a temperature stabilized volume, a receiving coil for the RF $\overrightarrow{B_1}$ transmission and reception, and an excitation and a reception circuit. Having a functional modular system for which each of these parts can be disconnected and replaced by an external system is a major asset, because it allows the use of reference subsystems for the individual validation of each of these developed hardware bricks. The employed reference NMR system from the company Pure Devices encompasses, among others, a measurement chamber called the *magspec* module, as presented in Figure 50. While Pure Devices system focuses on magnetic resonance imaging and therefore is not the most available optimized solution in terms of $\overrightarrow{B_0}$ homogeneity and temperature stabilization for critical NMR experiments, its apparatus provides an easy-to-use control environment by employing MATLAB programmatically as well as via specific experiment MATLAB GUIs (Graphical User Interface) intended for easy employment and teaching purposes [147], and deteriorated measurement conditions that reflects the difficulties of in-field NMR.

Figure 50 - Pure Devices magspec module consisting of a permanent magnet, a receiving coil, and shimming coils. Modified. [4]

This module provides a $\overrightarrow{B_0}$ field strength of approximately 550 mT, with gradient strengths for the shimming coils that vary between 250 mT/m in the x and y directions and 350 mT/m in the z direction, and 1200 mT/m in the x and y directions and 1500 mT/m in the z direction, depending on the related employed external module. We tested our prototype with the two configurations, and both were sufficient for preliminary testing measurements. The gradient efficiency is of 250 mT/m/A in the x and y directions and 330 mT/m/A in the z direction. Nominal field homogeneities are < 10 ppm for imaging experiments employing 10 mm diameter sample tubes and < 3 ppm for spectroscopy experiments using 5 mm diameter sample tubes, with a spectral resolution of < 1 ppm. Pure Devices applies diverse signal processing techniques within their equipment to allow for an improved analysis outcome, also in order to overcome field inhomogeneity and spectral resolution related limitations. The container depicted in Figure 50 alone already weights 20.5 kg, which hardly makes such a system a portable enough solution for in-field NMR and further miniaturization is clearly necessary. However, it allows us to easily perform a variety of NMR experiments in the lab with different-sized sample tubes and an inside targeted stabilization temperature of 30 °C, while providing direct access to the receiving and shimming coils from the connectors in its front part. Figure 51 illustrates the geometric conformation of $\overrightarrow{B_0}$ within the Pure Devices apparatus.

The receiving and shimming coils surround the volume in which the sample tube is to be inserted, as shown in Figure 52. The shimming coils provide the possibility of first order shimming correction through the injection of DC (Direct Current).

Finally, the receiving coil is in the form of a LGR (Loop-Gap Resonator) RF-coil, as shown in Figure 53.

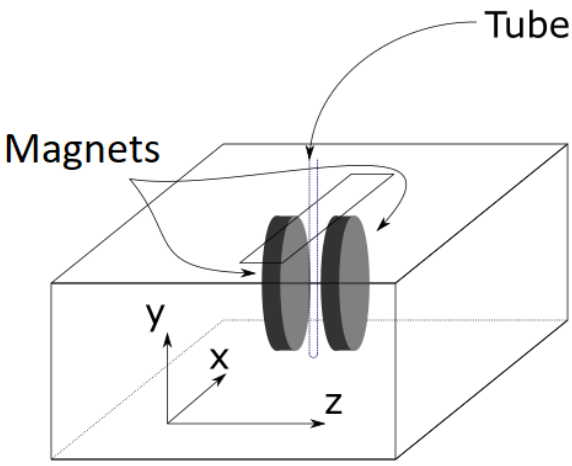

Figure 51 - Permanent magnet arrangement producing $\overrightarrow{B_0}$ within the Pure Devices unit.

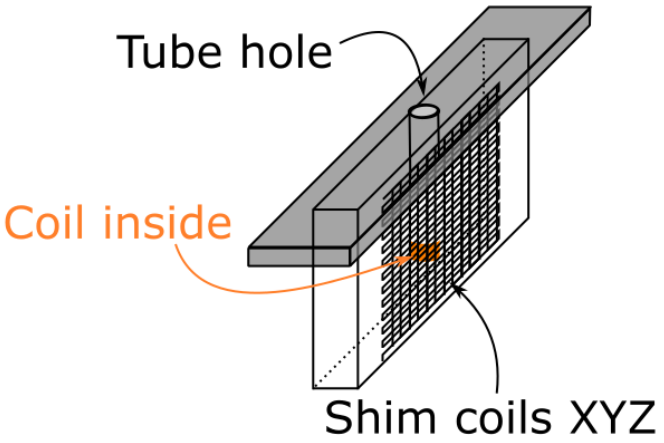

Figure 52 - Pure Devices coils unit, that can be fixed or removable, and can be tuned for different nuclei spectroscopy experiments. In orange the receiving coil, and in black the shimming ones.

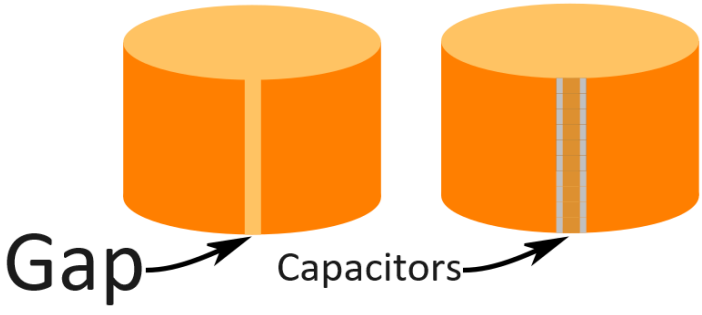

Figure 53 - Pure Devices LGR RF-coil employed as receiving coil. The gap is fulfilled with chosen capacitances in order to regulate its intended resonant frequency.

The receiving coil line impedance is 50 Ω and its resonant frequency is regulated to be equal to the Larmor frequency of the desired nuclei considering the available $\overrightarrow{B_0}$ by adjusting the gap capacitance C for:

$$f_0 \approx \frac{1}{2\pi\sqrt{LC}} \tag{70}$$

where:

$$L = \mu \frac{\pi {r_0}^2}{\ell} \tag{71}$$

with μ being the permeability within the coil, r_0 the inner radius of the coil and ℓ its length, following the representations in Figure 54.

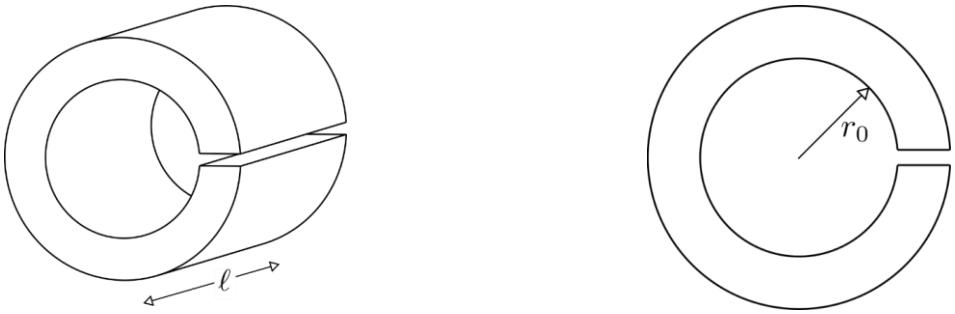

Figure 54 - Left side: a cylindrical loop-gap resonator of length ℓ. Right side: cross-sectional view of the cylindrical loop-gap resonator depicting its inner radius r_0. Modified. [148]

4.2. Employed commercial off-the-shelf Software Defined Radio

An SDR is an embedded system providing the means of employing the classic analogical functionalities and components of a RF system as a software implementation instead. These software defined RF embedded systems analogue functionalities can comprise components such as modulators and demodulators, filters, amplifiers, mixers, and other elements of radio communication. Therefore, such SDR boards are clearly flexible pieces of hardware to be employed within systems that work with RF signals in given basebands and that require often reparameterization and further adjustments of the involved application parameters. In order to automatize NMR experiments and make their parametrization highly customizable, while trying to keep the total design cost as low as possible as well as keeping design complexity from exploding, a SDR as processing unit was therefore preferred as the most suitable alternative overall. Hence, the selected SDR must be able to generate the necessary RF signal to excite the sample and, subsequently, digitize the resulting NMR signal.

Some examples of low-cost commercially available SDRs that work within our desired baseband, *i.e.*, around 24 MHz, are the LimeSDR and declinations [149], HackRF One [150], and the boards from the company Red Pitaya [151]. After a market analysis comparing the different commercially available boards, taking into consideration as well customer feedback, Red Pitaya with its low-cost SDR solutions aligning flexibility and robustness was selected as

our preferred SDR supplier. Indeed, within the available commercial off-the-shelf low-cost SDRs, the Red Pitaya company offers great demanded options, which are used in many different research branches [152] as open-source software boards with proprietary hardware design that provide flexibility to run custom code, performance, and reliability, while having a small form factor and a very attractive price. Among the applications in which these boards are used, we can cite slow and fast signal acquisition, signal generation, and real-time FPGA and / or CPU signal processing. The fact that the Red Pitaya boards present ethernet connectivity as well as many software APIs (Application Programming Interface), including a MATLAB one, make them the natural choice for fast prototyping applications in industry and academia.

From Red Pitaya's assortment, the STEMlab 125-14 board [153] was selected to be used within our prototype due to its versatility while being the most economic overall. An example of this board can be seen in Figure 55.

Figure 55 - The Red Pitaya STEMlab 125-14 SDR board.

This SDR has two RF inputs which are able to sample simultaneously with a resolution of 14 bits at a maximal rate of 125 Msps (MegaSamples Per Second) with an input impedance of 1 MΩ, and two RF outputs with the same resolution for their DAC, however with an output impedance of 50 Ω. Its acquisition buffer size equals to $2^{14} = 16384$ samples. Furthermore, it features CPU and FPGA integration for the two main electronic components of the board within a single chip: a Dual-Core ARM Cortex-A9 MPCore with CoreSight PS (Processing System) together with a 28 nm Xilinx PL (Programmable Logic), unified called as ZYNQ-7010 SoC (System-on-a-Chip) [154]. The supported communication interfaces are I2C, SPI, and UART, and it weights approximately 0.4 kg for a volume of 22 x 12 x 7 cm^3. The general block diagram of the STEMlab 125-14 SDR board is shown in Figure 56.

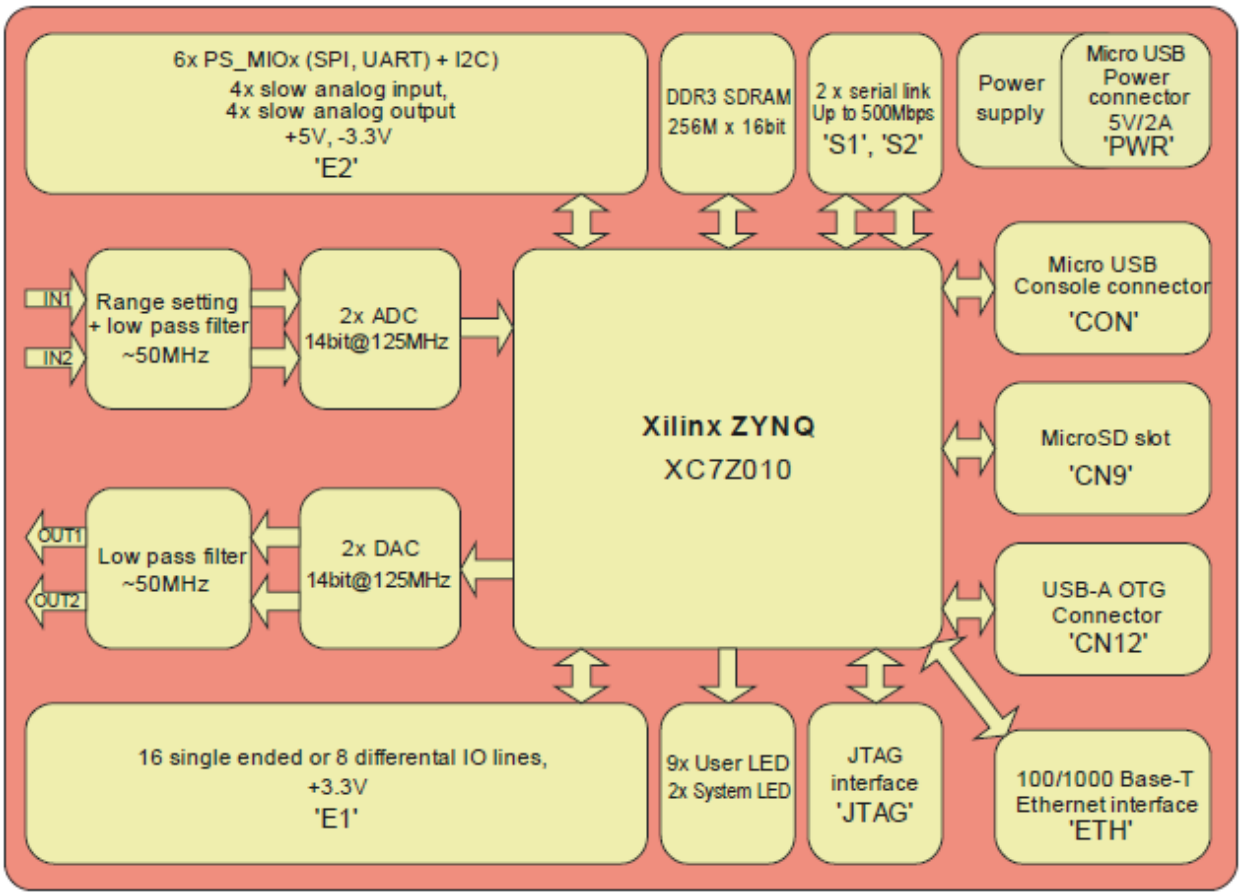

Figure 56 - Block diagram of the STEMlab 125-14 SDR board hardware. Modified. [155]

So that the SDR board could be integrated into our prototype hardware architecture with maximal practical convenience, we programmed a remote-controlled application using MATLAB and communicated with the board by means of the MATLAB API and the SCPI communication protocol over the available ethernet connection. In this way, all the SDR board and the experiment parametrization was set in the MATLAB script, and in this way, it would automatically send the desired excitation signal to the transmitter, receive the measured and adjusted NMR signal from the receiver for sampling, and complementarily generate the necessary oscillation signal for the frequency down-conversion of the FID, while forwarding to the computer the sampled data.

The SDR board code employed in the configuration and automatization of the NMR experiments within our NMR spectrometer prototype is made available in the appendix section III.

4.3. Prototype electronics and underlying setup limitations

Following the already existing work [2] on this topic, that was previously realized within our research team, we proceeded with the integration and overall improvement and adjustment

of the custom electronics related to the receiver and transmitter modules. This section depicts how our prototype electronics works, focusing on the explanation of the receiver and transmitter elements in Figure 49, which are shown in greater detail in Figure 57.

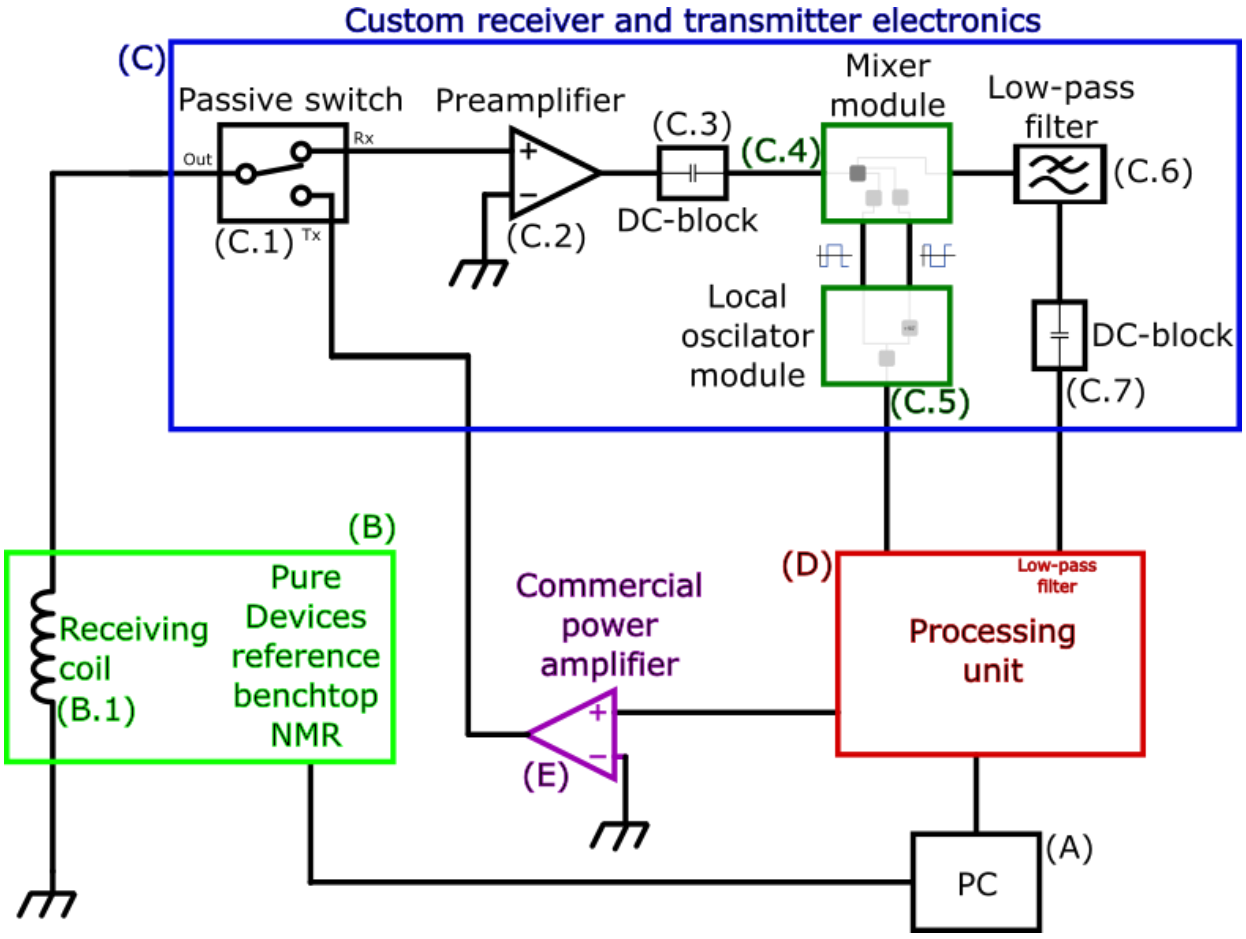

Figure 57 - NMR Spectrometer Prototype custom receiver and transmitter electronics in detail.

The high-level parametrization of this electronic setup is done at the PC (Personal Computer, *i.e.*, to be understood as the computer being employed) (A), which handles the co-work between the Pure Devices reference benchtop NMR (B) and the rest of the NMR Spectrometer Prototype, in particular with our developed custom electronics (C). The computer (A) will set, activate, and deactivate the best possible shim of $\overrightarrow{B_0}$, while parametrizing and triggering the NMR experiments. Prior to running a given NMR experiment, an automatized shim tuning procedure has to be executed by the reference benchtop NMR (B) in order to find the most suitable shim electric current values for the considered targeted sample. The shim optimization procedure can be done directly on the sample to be measured, the algorithm trying to adjust the shim currents to minimize the FWHM of the spectral peaks. Assuming that the reference benchtop NMR (B) is able to correctly shim $\overrightarrow{B_0}$ for the targeted sample, the shim currents are kept within our programming environment at the computer (A) in order to be used when running the NMR experiment. In case the shim procedure is not finished successfully, it is advised to rerun the shim procedure of $\overrightarrow{B_0}$ employing another sample, as for instance pure

water, for which it is guaranteed that the reference benchtop NMR (B) can resolve his optimization shim algorithm. As outcome of the shim process, the reference benchtop NMR (B) returns the fine-tuned value of the Larmor frequency f_0 corresponding to the shimmed $\overrightarrow{B_0}$ field. This frequency value will be then used in the transmitting and down-conversion steps of our prototype.

Following the sequential steps of an NMR experiment, we then parametrize the processing unit (D) for the number of times that we want to measure an NMR signal, taking as well into account the time between succeeding measurements. The processing unit (D) generates the sinusoidal excitation signal at the Larmor frequency f_0 after shim accordingly and will send it to the employed commercial RF power amplifier (E) of the kind ZHL-32A+ / ZHL-32A-S+ [156] from the company Mini-Circuits for a fixed strong low noise amplitude and current amplification of around 27 dB before sending it to the receiving coil (B.1) through the passive switch (C.1).

The passive switch (C.1) is a redirection mechanism and guarantees that the excitation and measured signals go through the designed paths. Figure 58 illustrates how it is built within our prototype.

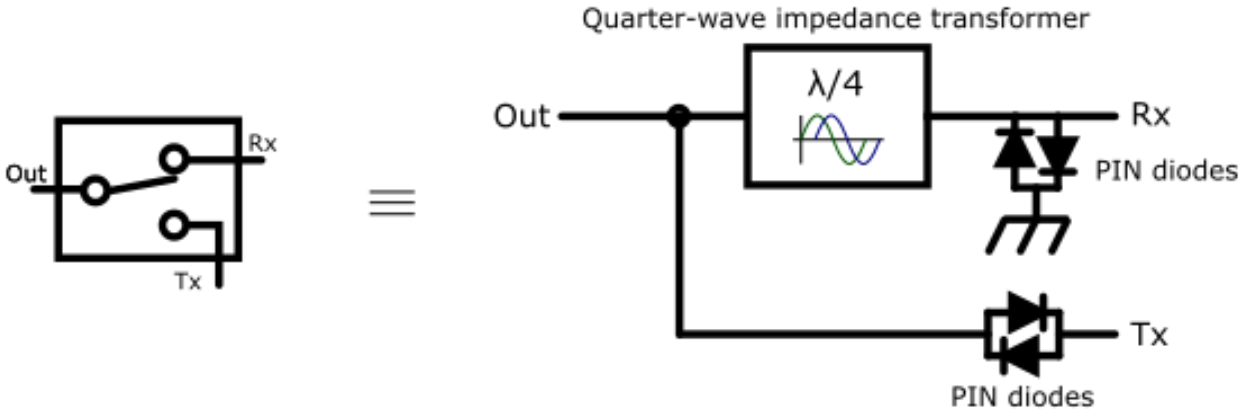

Figure 58 - A passive switch built with an integrated quarter-wave impedance transformer and PIN diodes.

PIN diodes are a particular kind of diode that operates under high-level injection and are particularly suitable for being used in fast switches, photodetectors, attenuators, and high-voltage power electronics applications. Through the convenient choice of these diodes positioning within the electronic circuit, one is able to filter out a signal by means of attenuation, while letting another one pass through the circuitry. Since the whole electronics line and components are adjusted to an impedance of 50 Ω, the quarter-wave impedance transformer at the receiving path guarantees the impedance adjustment also for this specific RF signal path. For the quarter-wave impedance transformer we employed the circuit presented in Figure 59.

With this circuit is possible to adjust the impedance of the receiver electronics to be equal to 50 Ω, which is the line impedance overall in the electronic chain. By therefore choosing

$\mathcal{Z} = 50\ \Omega$ and f to be equal to the Larmor frequency f_0, and by employing the resulting L and C, one places the effective complex impedance from the outside perspective at $(50 + 0i)\ \Omega$ by cancelling the existing complex term. This is best observed with the help of a Smith chart, as presented in Figure 60. The Smith chart is a nomogram commonly employed in RF to visually assist in solving problems with transmission lines and matching circuits. It is a mathematical transformation of the 2D Cartesian complex plane and therefore impedance / admittance values can be indicated on the chart as complex numbers, for which the real part corresponds to the resistance, while the imaginary one to the capacitance / inductance components. By adding appropriate electronic components to a circuit, like capacitors and inductors, one can adjust the complex part of the impedance to a given desired value.

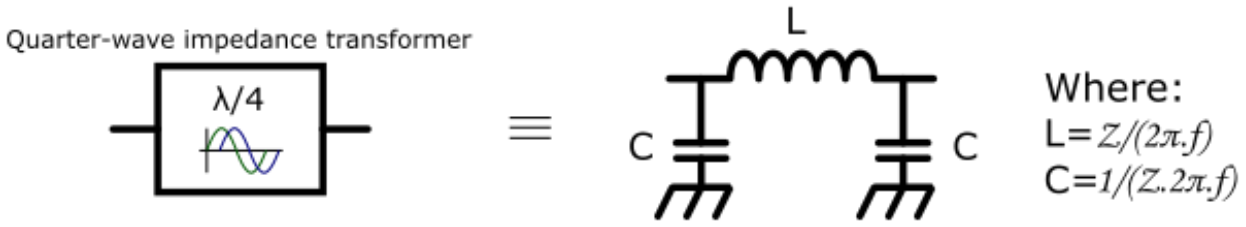

Figure 59 - Employed quarter-wave impedance transformer: to the left there is the receiving coil and to the right the receiving signal path.

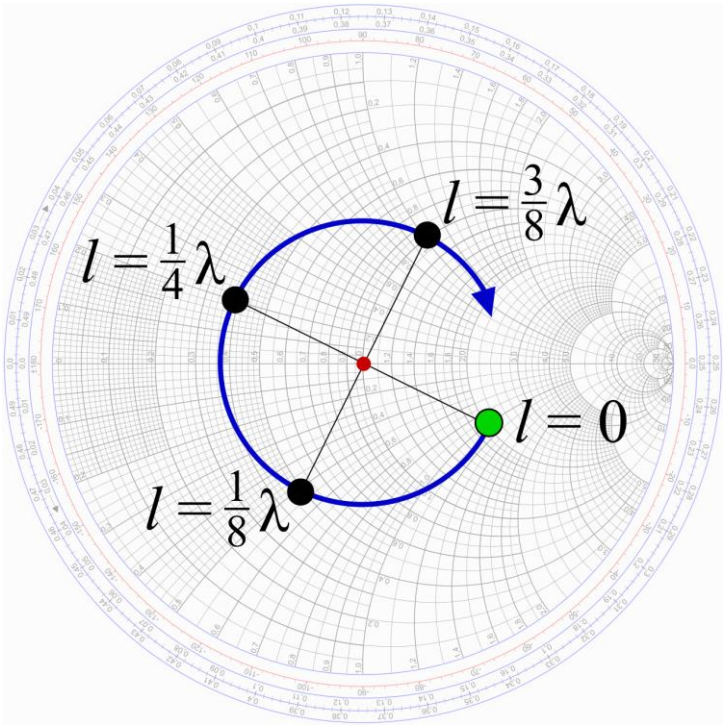

Figure 60 - Smith chart depicting how a quarter-wave impedance transformer brings the line impedance to the desired 50 Ω by reflecting the normalized impedance to the center of the chart. Modified. [157]

In such resonance circuits it is relatively complicated to match the Smith chart centre by directly employing capacitive and inductive components with nominal values corresponding to

the calculated ones, so that it is advised that a VNA (Vector Network Analyzer) be used allied to variable capacitors and inductors for the fine-tuning process.

Once the excitation signal reached the receiving coil (B.1) through the passive switch (C.1), it will be propagated to the sample. This RF magnetic field at the Larmor frequency f_0 is the so-called $\overrightarrow{B_1}$ field by NMR professionals. In the moment that $\overrightarrow{B_1}$ ceases to exist, the magnetic NMR signal will start propagating from the sample and will be sensed by the same receiving coil (B.1). This measured signal in the form of an FID will be electrically conducted through the passive switch (C.1) into the receiver electronics.

The first step within the receiver path is to pre-amplify the measured signal through the preamplifier (C.2), since it is usually many orders of magnitude smaller than the excitation signal, perhaps only a few μV or even less. It is important to notice that, at this point, all the already existing combined noise is amplified together with the useful NMR signal. The preamplification objective through the preamplifier (C.2) is to bring the overall signal level to at least some hundreds of μV or a couple of mV to be able to process it, doing so without introducing an elevated level of noise. For that purpose, it is important for the preamplification to be done as close as possible to the receiving coil. As preamplifier (C.2), we employed the PGA-103+ from Mini-Circuits [158]. It is a commercially available LNA (Low-Noise Amplifier) designed to work at high frequency [159], eventually allied to dedicated stabilization circuits [160]. After the preamplification, AC-coupling is achieved by employing the DC-block (C.3), which basically removes the DC level of the incoming signal.

At this point, the measured high-frequency FID arrives at the mixer module (C.4) and is ready to be down-converted in frequency terms. However, for the mixer element to successfully execute the down-conversion, an oscillator at the Larmor frequency f_0 increased by the targeted down-conversion frequency f' must be available to it. This local oscillator signal is provided by the Red Pitaya board (D) as well, following the previous high-level parametrization done in MATLAB. In the Figure 57, this is illustrated by the connection between the processing unit (D) and the local oscillator module (C.5), the latter being shown in Figure 61.

The sinusoidal oscillation provided by the processing unit (D) arrives to the local oscillator module (C.5) at the SMA (SubMiniature version A) connector to the left and is split into two phase complementary square wave signals, both of which are required by the electronic mixer component [2] at the mixer module (C.4). These are made available at the other two SMA connectors. At the electronic level, there is, for the input and the outputs, a 50 Ω resistance for the line impedance adjustment, always followed or preceded by an AC-coupling mechanism in form of a 10 nF capacitance. To transform the sinusoidal wave into the two complementary square waves, NAND (NOT-AND, *i.e.*, $\overline{IN_1 \wedge IN_2}$) gates are used: one compares the incoming sinusoidal signal to an arbitrary constant tension level provided by a resistive voltage divider so that its output becomes a square wave at the same fundamental frequency of the very incoming

signal, and the other inverts this resulting square wave lows and highs. The practice showed us that a voltage divider with two close but somewhat different values for its resistances produces the best results in terms of generated outcoming signal shape and it became therefore our *rule of thumb* for this circuit, although it may not be a universal applicable rule for all similar oscillating circuits.

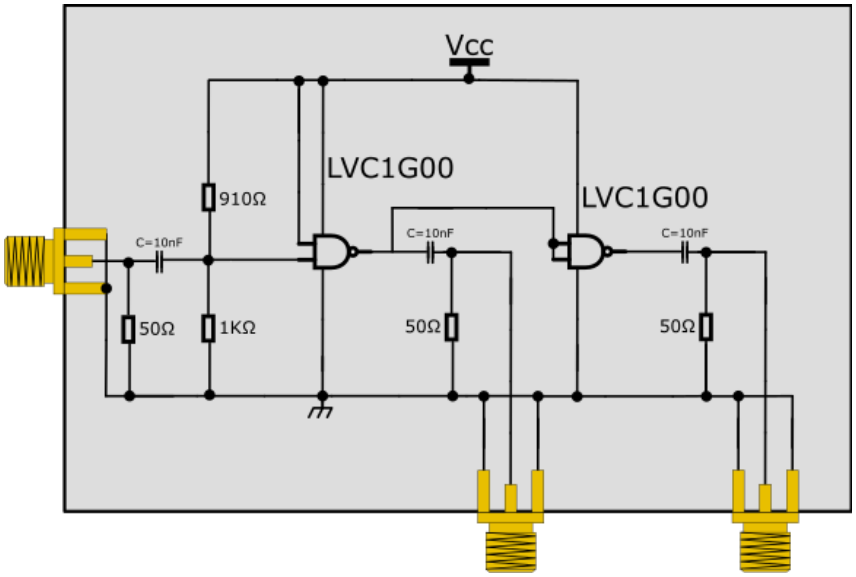

Figure 61 - Local oscillator module as a mixed representation of the physical PCB and connectors, and its discrete electronic components symbols.

Once the mixer module (C.4) has available all the necessary inputs, the mixing, *i.e.*, the frequency down-conversion of the NMR signal can take place. Figure 62 shows the mixer module (C.4) in detail.

Figure 62 is a mixed representation of discrete electronic components directly soldered onto the mixer module (C.4) and the equivalent representation of the functional blocks belonging to an ASIC (Application-Specific Integrated Circuit) specially developed by our research team for NMR related applications [2]. Figure 63 exemplifies the internal functioning of this customized chip.

The incoming FID is added to a DC level of 1.65 V so that it is exactly at the centre of the available voltage range of 3.3 V, which is the voltage source of our ASIC. In this way, the FID has room to oscillate from 0 V to 3.3 V around the stationary value of 1.65 V. The LNA is responsible for amplifying the still very low-power high-frequency incoming signal with a design gain of 26 dB [2] without degrading its SNR, *e.g.*, by avoiding adding additional noise to it during the amplification. After amplified, the FID enters the mixer block itself. And so do the local oscillator signals coming from the local oscillator module (C.5), after passing through the dedicated buffers that provide the necessary electrical current without attenuating the oscillation waves. The mixer works following the principle mathematically described by equation (66), and

at its output we can observe therefore the resulting signal constituted by two fundamental frequency components, one high-frequency f^{HF} and the other low-frequency f^{LF}, as in equations (67) and (68). The mixer block alone presents a gain, when loaded, of about 0 dB, while it amounts to around 20 dB when unloaded [2]. After leaving the mixer block, the signal passes through a further amplification block. This output amplifier adjusts the outcoming signal by converting it from differential mode to single-ended mode with the help of the potentiometer in Figure 62. It aims at an output voltage level adjustment targeting 1.65 V as well, while realizing the last amplification of the FID before sampling it, with a design gain of about 37 dB [2]. The design bandwidth of the output amplifier is limited to 200 kHz [2], what ensures that the high-frequency component f^{HF} is filtered out at this point, therefore only keeping the low frequency component f^{LF}, which is the one we are interested in.

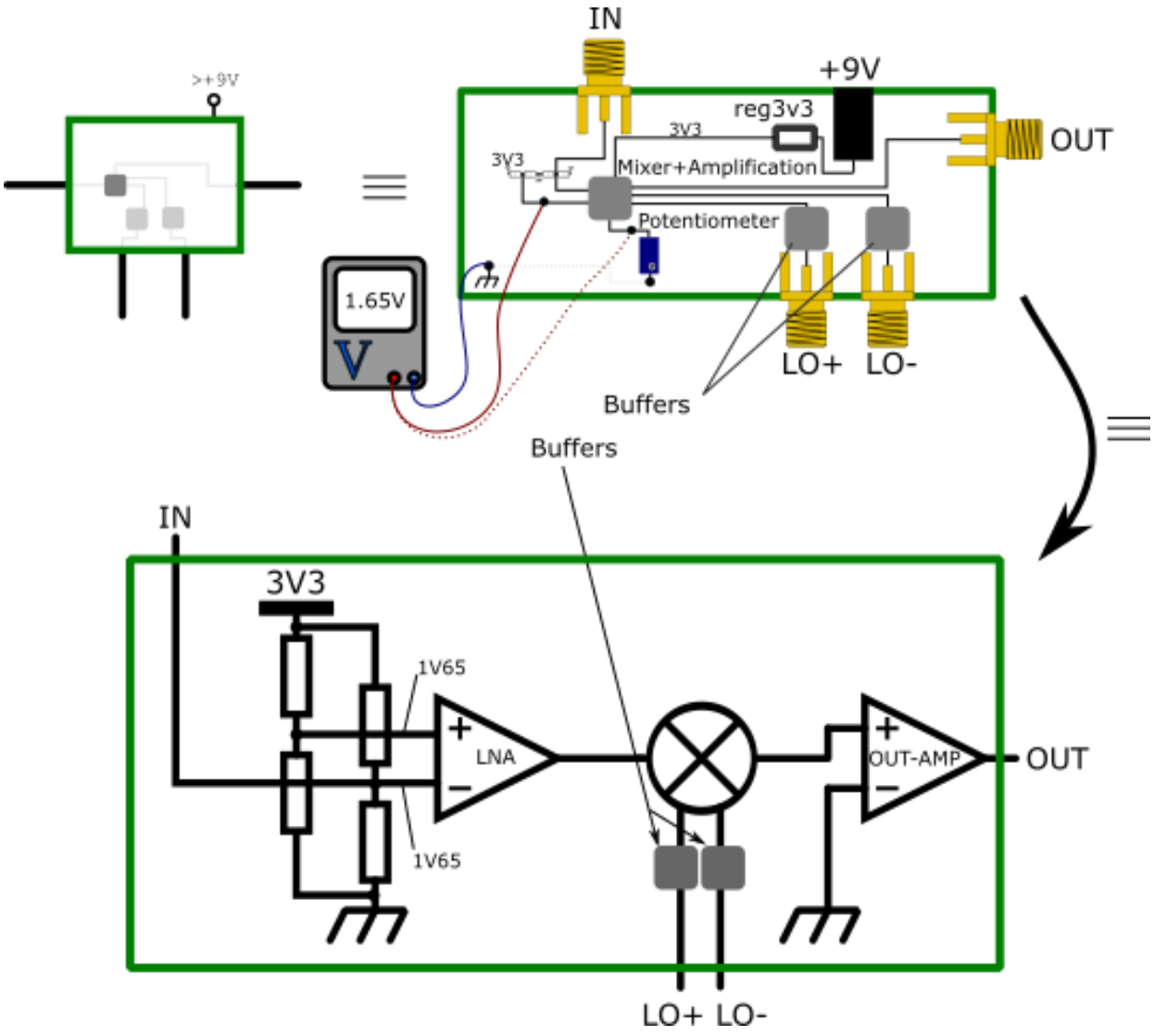

Figure 62 - Mixer module where the frequency down-conversion of the FID happens. There is further signal amplification and voltage level adjustment.

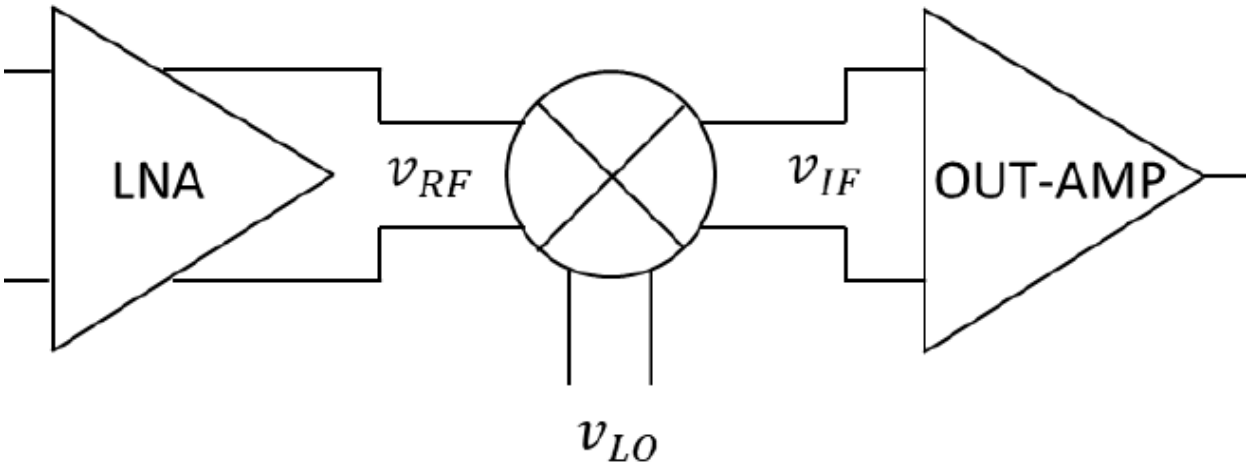

Figure 63 - Previously developed integrated receiver prototype as an ASIC. Modified. [2]

After leaving the mixer module (C.4), the outcoming signal is analogically filtered in accordance with the down-conversion frequency f' by means of the low-pass filter (C.6). Finally, the down-converted and filtered NMR signal passes through a DC-block (C.7) to eliminate any existing DC level, before reaching the processing unit (D). The analogue RF input of the SDR has as well a built-in low-pass filter including range setting to guarantee the removal of high-frequency components of incoming signals, so to respect the Nyquist–Shannon sampling theorem.

The FID is finally digitized by the processing unit (D) and samples are made available for further digital signal processing steps and the Fourier analysis. These steps were chosen to be implemented in MATLAB, with the processing unit sending the discretized down-converted FID immediately back to the host computer (A) after the sampling process has completed.

The employed electronic setup, which functioning was described above, presents some hardware-related limitations that are critical for NMR spectrometer systems. The intrinsic gain of our home-build receiver ASIC is limited when considering a typically severely reduced incoming NMR signal, which leads to a corresponding limitation in what concerns the LoD of the system. In addition, the chosen processing unit (D) was shown to present critical limitations in what concerns the generation of RF signals at our setup targeted Larmor frequency f_0, *i.e.*, around 24 MHz. Indeed, the chosen SDR could satisfactorily generate excitation pulses at low frequency, but close to the necessary 24 MHz, the beginnings and ends of the $\overrightarrow{B_1}$ excitation bursts would degenerate. More deranging was the fact that these deformations would take an aleatory form. Figure 64 shows the generated pulse at low frequency, while Figure 65 und Figure 66 illustrate respectively what happens with the beginnings and the ends of the pulses when the frequency of the generated signals increase.

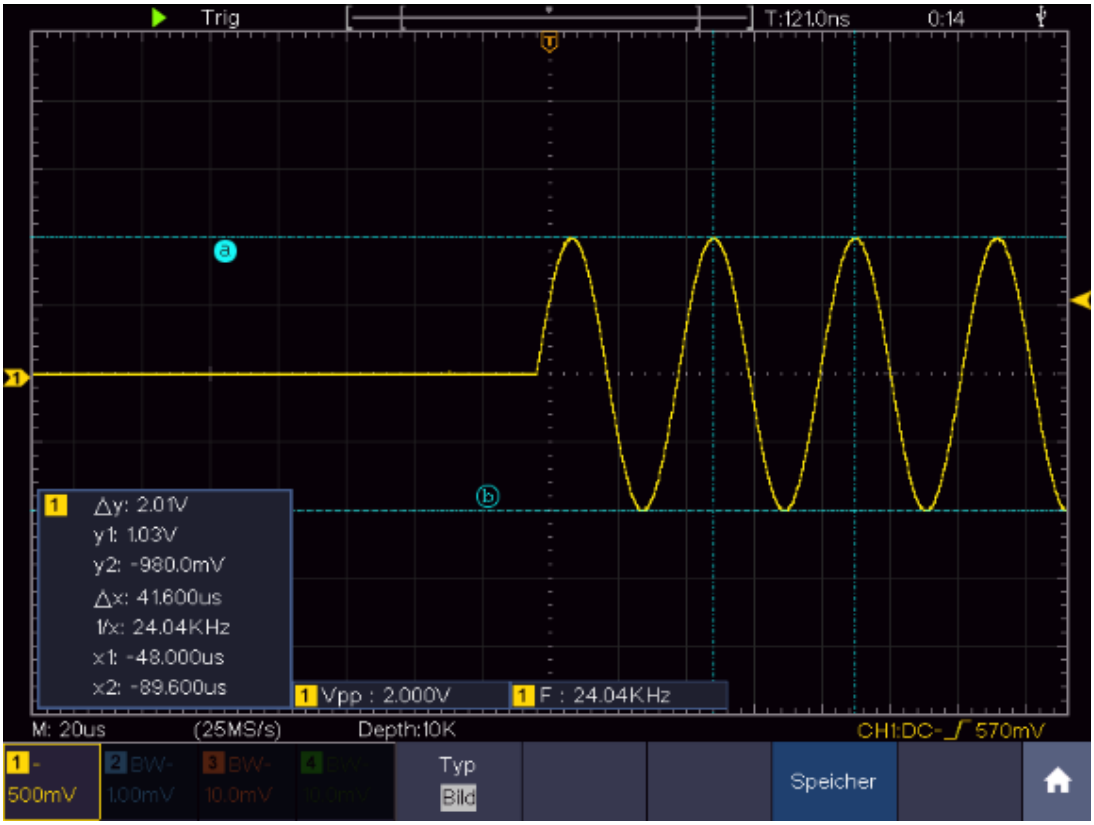

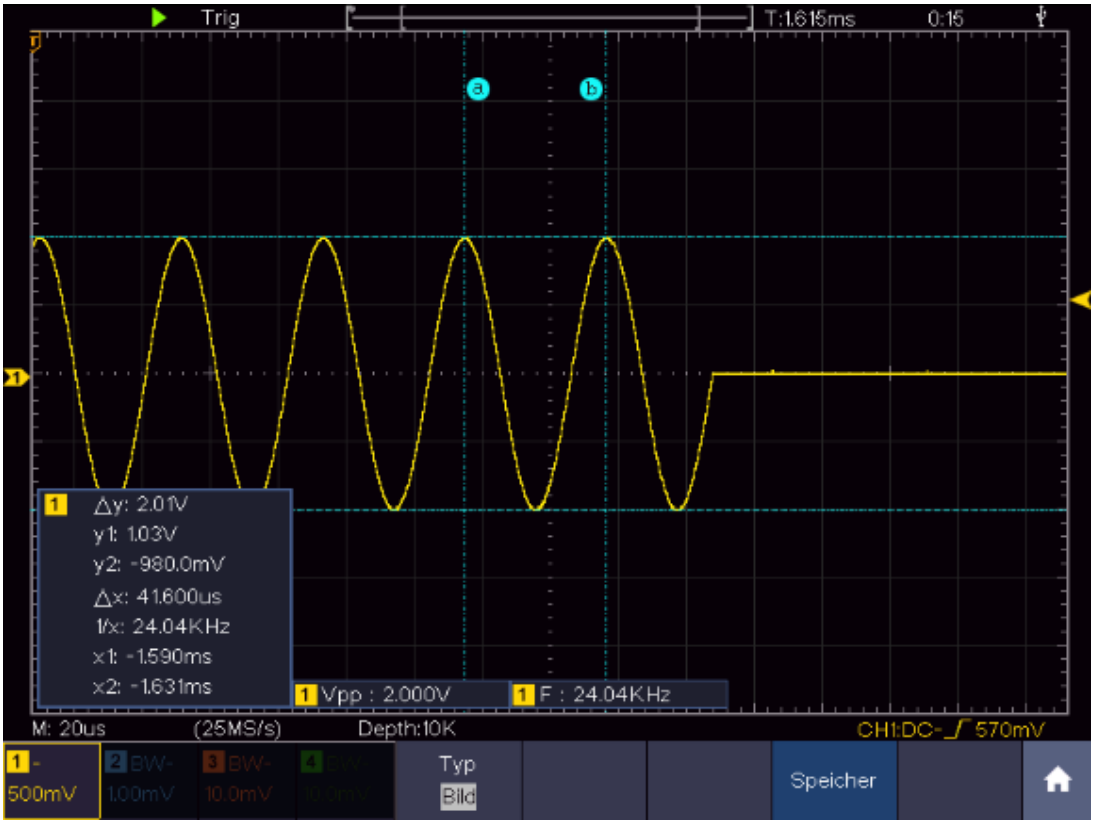

Figure 64 - Top side: beginning of the generated sinusoidal pulse at about 24 MHz: its overall shape looks quite good. Bottom side: the end of the same pulse: it is proper as well.

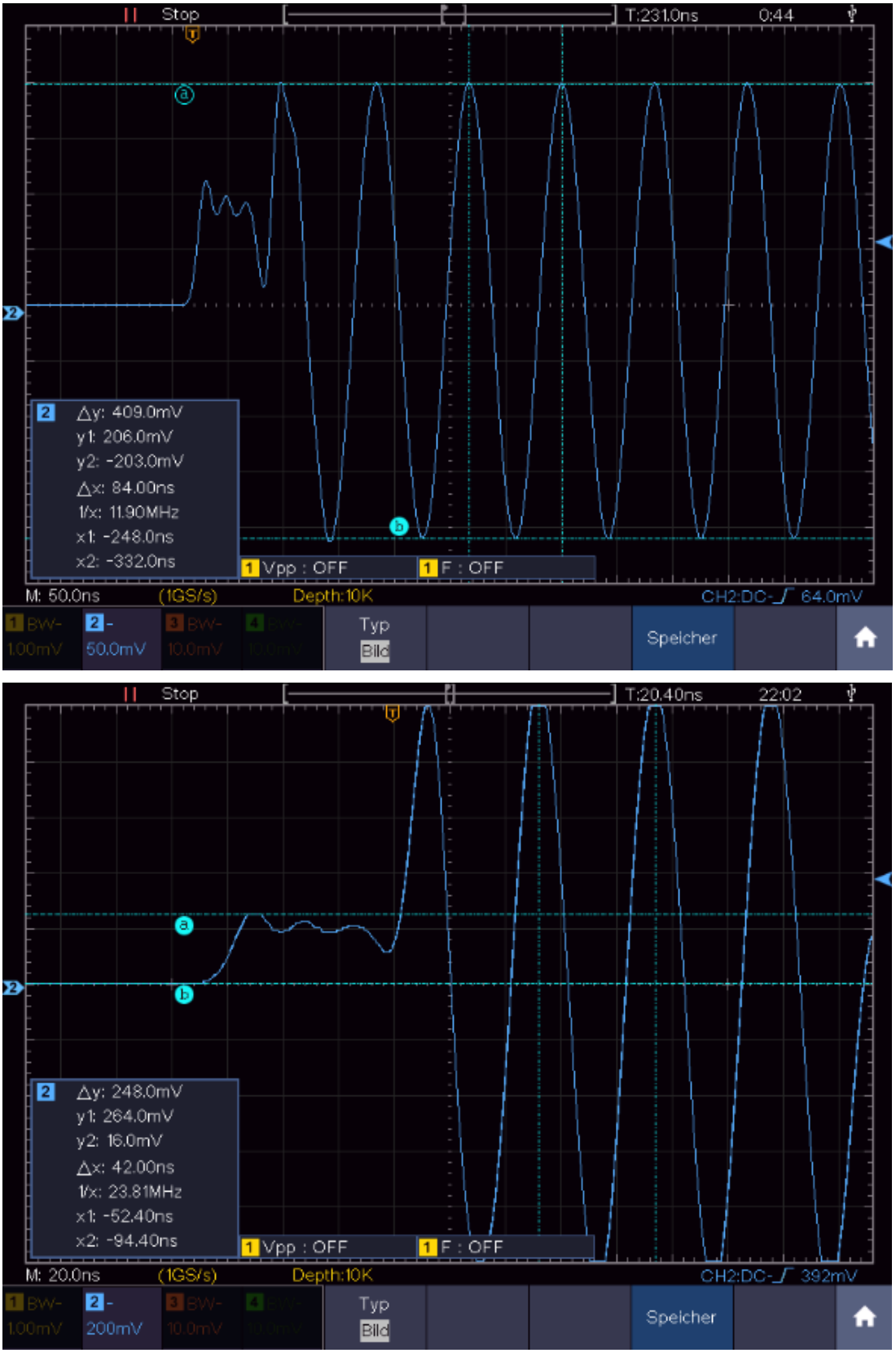

Figure 65 - Top side: typical waveform deformation presented at the beginning of the generated sinusoidal pulse: it mainly changes according to the pulse amplitude. Bottom side: the same for a different pulse amplitude and frequency: for comparison purposes.

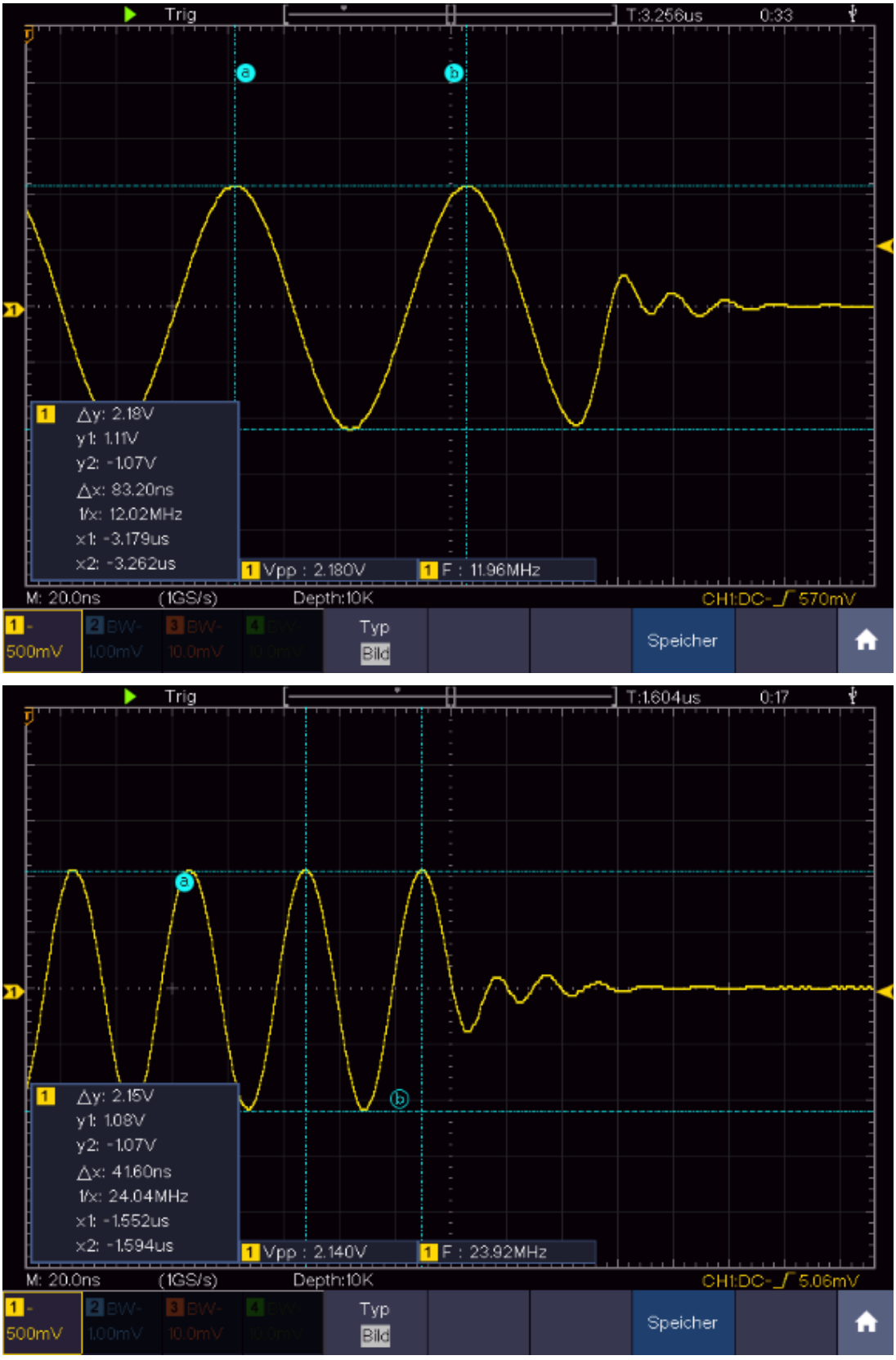

Figure 66 - Top side: typical waveform deformation presented at the end of the generated sinusoidal pulse: it mainly changes according to the pulse frequency. Bottom side: the same for a different pulse frequency: for comparison purposes.

From Figure 65 and Figure 66, one directly understands that the generation of the beginning and of the end of $\overrightarrow{B_1}$ happens in a somewhat aleatory way, and therefore the succeeding FID starts each time under different aleatory conditions. Although it is not a critical problem when talking about single acquisitions, it turns out to be one when we talk about temporal signal averaging, because the successful accumulation of FIDs happens only for same-phased consecutively signals. It is worth noting that, during the time of these doctoral studies, the company Red Pitaya released multiple firmware updates following our feedback on the matter. Although the quality of the beginning of the sinusoidal bursts improved considerably, as the undesired initial odd form was suppressed from the sinuses, the generated signal kept being relatively instable, presenting visible changes from bust to burst. Furthermore, the problems concerning the end of the sinusoidal bursts still prevail to this day.

On top of that, one has to consider the aleatory impact of the existing temperature drifting within the system, which can produce FID frequency shifts even during a still occurring measurement. This, allied to the inherent imprecisions in the triggering of the sampling process, which is mainly due to the remote communication setup architecture and the intrinsic imprecisions of the involved electronic components, and to the low-quality RF signals provided by the processing unit (D), make the straightforward temporal averaging process of weak signals virtually unfeasible with our current prototype setup. Indeed, under such hardware conditions, the implementation of temporal averaging methods for weak NMR signals is severely compromised. This happens because of the time-related imprecisions in the triggering of the sampling process as well as because of the observed low-quality signals coming from the employed SDR, which are responsible for introducing random values of φ_1 and φ_2 to equation (66).

There are as well some further SDR-limitations concerning the acquisition process. The employed SDR provides us with a 16384, *i.e.*, 2^{14} samples-long acquisition buffer, where the ADC resolution amounts to 14 bits, with the possibility of floating-point representation. Therefore, a whole FID data collection accounts for $16384\,x\,14 = 229{,}376$ bits. The communication between the processing unit (D) and the host computer (A) is done via LAN (Local Area Network) employing the SCPI protocol over a RJ45 connection. The use of multiple acquisitions within one single measurement, *i.e.*, the use of multiple acquisition buffers for sampling one single NMR signal, is not suitable due to important dead times between successive sampling triggering [161]. Also not suitable is the parallel use of two acquisition channels for the quadrature measurement of weak signals, because of the impossibility of precise enough triggering of the acquisition procedure for each of these two acquisition channels. Indeed, since the high-level communication interface does not allow for simultaneous triggering of the sampling process for both acquisition channels, these must be therefore

triggered independently and subsequently, and so introducing further time-related imprecisions to the NMR signal acquisition process.

Taking these setup limitations and surrounding physical aspects into account, the best possible strategy within such hardware-related constrained environment is to parametrize the sampling process so that a whole acquisition buffer covers the visible part of the FID, *i.e.*, as many FID periods out of the noise floor as possible. Therefore, the sampling rate is best adjusted when fulfilling such empirical requirement, although the underlying downside is logically that the final NMR plot resolution is eventually more degraded than it could be, which can lead to an even lower-resolution NMR spectrum.

4.4. Digital signal processing and output formatting

At the processing unit, the incoming signal was digitized with a sampling frequency f_s corresponding to a sampling rate that can reach up to 125 Msps, varying from NMR experiment to NMR experiment, being optimized to match the size of the acquisition buffer by taking into account the effective relaxation time constant T_2^*. In what concerns data handling at the processing unit level, it happens only one *per* acquired NMR signal: since the acquisition buffer of the SDR is circular, with first sampling position at its centre, we shift the whole data array of $16384/2 = 8192$ positions to the left, so that the beginning of the acquisition coincides with the beginning of the buffer and therefore of the data array. This procedure is not important for the upcoming frequency analysis through the employed discrete version of the Fourier Transform, since its algorithm considers the signal within the temporal data array as being an elementary part of a forever repeating infinite signal. However, this initial temporal shift makes the FID look nicer to the NMR analyst, since it is the natural physical form that the real measured FID possesses. Thereafter, the digitized NMR signal is sent to the computer.

Once the data array is available on the computer, the digital signal processing can take place. The standard signal processing path, which can be seen in Figure 67 for what concerns the amplitude- and magnitude-related data arrays of the involved signals, starts by employing a digital pass-band filter. It is used at first to guarantee that only the frequency components around the considered down-conversion frequency of a couple of kilohertz, usually somewhere between 1 and 2 kHz depending on the current experiment adjustment, are kept for the upcoming Fourier analysis. This is easily done by means of the MATLAB *bandpass* function $y = bandpass(x, f_{pass}, f_s)$, with x being the input data array, f_s the sampling frequency, f_{pass} the passband frequency range to be applied, and y the output data array. Afterwards, the MATLAB functions *fft* and *fftshift* are used in order to generate the correspondent representation of the frequency equivalent of the measured FID [162]. By employing the MATLAB function *fft* (with

the syntax $Y = fft(X)$, where X is a time series and Y its FT), we compute the DFT by employing a standard FFT (Fast Fourier Transform) algorithm. Y is of the same size as the temporal data array X, *i.e.*, 16384 values in our case. One sees that the size of the acquisition buffer allied to the sampling rate will directly impact the resolution of the generated NMR spectra. The MATLAB *fft* function provides nonetheless only an array corresponding to spectral magnitudes. We must therefore adjust it to the corresponding frequency axis of the FT, where the frequency of 0 Hz is placed at the centre of the data array. By doing so, we are able to visualize the spectrum in the classic way where it is composed by two mirrored halves, one positive and one negative. This data array adjustment is done by employing the MATLAB *fftshift* function, with the syntax $Y = fftshift(X)$, where Y is the adjusted spectral magnitude data array corresponding to the original one, X. Concretely, because our data array storing the frequency magnitudes is a 1D (1 Dimension, *i.e.*, unidimensional) data array, *i.e.*, a MATLAB vector, this function swaps the left and right halves of X, placing the result in Y. Finally, by employing the MATLAB function *abs*, we consider only the absolute values of the spectral magnitudes within our data array, correcting thus eventual phase-related distortions that we may have in our measured spectra. Its syntax is $Y = abs(X)$ where, for non-complex numbers, Y is the absolute value of X. Analogously to Figure 67, the resulting spectral magnitude data array represented with MATLAB programming-like syntax is therefore:

$$FT_s = abs\left(fftshift\left(fft\left(bandpass\left(FID_s, f_{pass}, f_s\right)\right)\right)\right) \tag{72}$$

where FT_s is the formatted data array containing the spectral magnitudes and FID_s is the sampled amplitudes of the FID in the time domain.

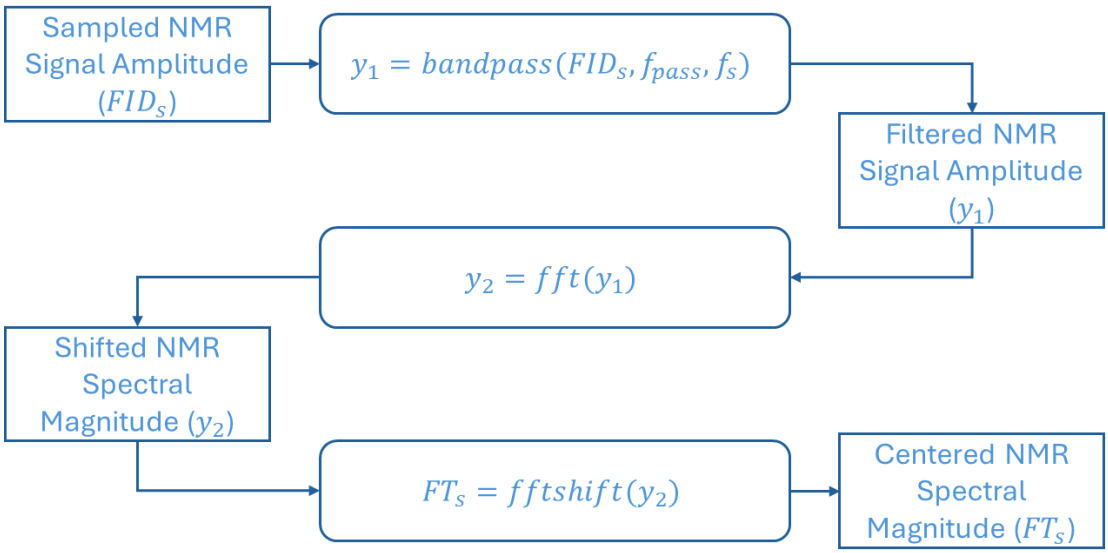

Figure 67 - Signal processing steps to generate spectral magnitude from the amplitude of a time-domain signal.

Once the data array corresponding to the spectral magnitudes is prepared, the data array corresponding to the frequencies composing the spectrum must be built. The number of

discrete frequencies of this data array is the same as the number of discrete times of the sampled FID, in our case 16384. The first thing to do is to operate a coarse adjustment of the frequency axis, where equation (73) is not mathematically rigorous but a mathematical representation of vector manipulation employing MATLAB programming syntax:

$$f_{axis}^{coarse} = \left(\left(-\frac{SampleAmount}{2}\right):\left(\frac{SampleAmount}{2}-1\right)\right) * \left(\frac{SamplingRate}{SampleAmount}\right) \tag{73}$$

where f_{axis}^{coarse} is the resulting coarse-adjusted frequency axis in Hz for, in our case, $SampleAmount = 16384$ and a given $SamplingRate$ specified in samples per seconds, or sps [163]. By defining the minimal value of the frequency axis as being $f_{min} = -\frac{SamplingRate}{2}$, the maximal value as being $f_{max} = SamplingRate(\frac{SampleAmount-2}{2SampleAmount})$, and the frequency amount among two subsequent axis values as $f_{step} = \frac{f_{max}-f_{min}}{SampleAmount}$, equation (73) becomes the equivalent to the MATLAB vector:

$$f_{axis}^{coarse} = \left(f_{min}{:}\, f_{step}{:}\, f_{max}\right) \tag{74}$$

Because the exact central position of the data array in the frequency domain is supposed to be equal to 0 Hz and our acquisition data array has however an even number of elements, and as a mean of generalization for each possible acquisition scenario, a fine adjustment of the frequency axis of a one final tiny compensation might be necessary. If not required, the following data array manipulation leaves the frequency axis exactly as in (73):

$$f_{axis}^{fine} = f_{axis}^{coarse} + abs\left(\frac{f_{min}+f_{max}}{2}\right) = f_{axis} \tag{75}$$

where f_{axis}^{coarse} is the data array originating from (73), *abs* is the previous mentioned MATLAB function for the extraction of the absolute value from its argument, f_{min} is the first, most negative frequency value of f_{axis}^{coarse}, f_{max} is the last, most positive frequency value of f_{axis}^{coarse} for, in our case, $SampleAmount = 16384$, and f_{axis}^{fine} is the fine-adjusted frequency axis in Hz, which can therefore be considered our resulting frequency axis f_{axis}.

Taking the previously formatted spectral magnitude data array given by equation (72) and plotting it versus the adjusted frequency axis data array from equation (75), one has the resulting Fourier Transform as a graphical representation.

From it, it is possible to generate the prototype output in the classic NMR way of representing frequency spectra, *i.e.*, in terms of chemical shift instead of frequency *per se*. Indeed, the classic NMR representation in terms of chemical shift is nothing more than the left half of the above-mentioned plot with a new adjustment of the frequency axis. The restructuring of the frequency axis in terms of chemical shifts, which programmatically implementation can take a variety of forms, takes into consideration the defined down-conversion frequency f' used by the electronic mixer as the low-frequency equivalent reference of the employed Larmor

frequency f_0 used to excite the sample. Because we are working with the negative frequencies of the frequency axis of our Fourier Transform outcome when we select the first half of the data array of f_{axis}, we must convert the negative frequencies to positive chemical shifts by considering their absolute values, so that the NMR analysis outcome is presented in its classic format. Indeed, the differences $|f_{FID} - f_0|$ corresponding to the high frequencies and $|f_{axis} - f'|$ corresponding to the low frequencies of the NMR signal are the same in terms of Hz. These both differences reflect the NMR signal before the mixer and after passing through it. Therefore, by adjusting equation (5) and considering these assertions, one has:

$$f_{axis}^{ppm} = \frac{|f_{axis}| - f'}{f_0} 10^6 \tag{76}$$

where the factor 10^6 adjusts the relation to the ppm unit.

Therefore, by plotting the first half of FT_s from equation (72) versus f_{axis}^{ppm} from equation (76), one gets the classic NMR spectral representation in terms of chemical shift, which happens to be the final produced outcome of our NMR spectrometer prototype. FT_s is a data array which elements unit are a measure of spectral magnitude. The consideration of this unit as a measure of spectral power is possible by squaring each of its elements and realizing a normalization by dividing them by the number of frequency samples N. This is however highly optional within the NMR field since NMR analysts consider magnitudes mostly as arbitrary amplitudes, being much more interested in the outcoming chemical shifts of the spectral peaks.

Artifacts, which are local spikes with high amplitudes at specific frequency values, can also be easily dealt with by employing different filtering techniques, as for instance, a median filter (MATLAB function *medfilt1* with syntax $y = medfilt1(x, n)$ for an nth-order one-dimensional median filter applied to x). Such signal processing techniques can greatly increase the visual quality of the fashioned NMR spectra by avoiding polluting the plot with artifacts due to external magnetic field interferences and other sources of electric noise at specific frequencies. However, median filters deform the frequency peaks coming from the NMR signal measurements as well, and therefore must be used with caution and much parsimony.

The classic signal processing procedure presented in this section works fine for single-acquisition NMR experiments of strong NMR signals, which present elevated levels of SNR. However, when dealing with low-SNR NMR signals, we may be interested in improving the SNR level by averaging multiple acquisitions. One can actually do it by either accumulating the FIDs or the resulting NMR spectra, as the involved hardware capabilities may allow to happen. Hybrid methods are also possible to be implemented, however they are less employed in the practice because they increase the complexity of the signal processing software module without bringing a clear advantage to the final NMR analysis outcome.

Spectral accumulation is pretty much straightforward and resumes itself by adding up the data arrays corresponding to the single spectra, eventually shifting their frequencies prior to

the sum so to correct field drifting-related influences into the calculations of the chemical shifts. This may be a good averaging method for high-resolution NMR spectroscopy, where the NMR experiment environment is better controlled, and noise levels may be low when compared to the acquired NMR signals. Indeed, in such conditions, one might be directly able to identify the spectral peaks present in a single spectrum and use them as reference for the eventual correction and accumulation algorithm.

In low-resolution NMR, especially when considering portable miniaturized equipment subject to a hostile external environment and where SNR levels are typically low, spectral averaging might not be an option. In such scenario, spectral peaks from single acquisitions might not be distinguishable from the noise floor. And even when they barely are, when one takes into consideration all existing time-related imprecisions previously described, the temperature drifting and the spectral degradations due to field inhomogeneity, there is no deterministic way of defining a correct reference chemical shift to be used in the correction algorithm. This makes a simple accumulation procedure based on frequency shift and posterior addition of the resulting data arrays impossible. Indeed, this would only generate NMR spectra with undistinguishable merged spectral peaks, which do not provide useful information about the sample.

4.5. Time-shifting for signal averaging

Therefore, the averaging of temporal NMR signals seems more appropriate to portable miniaturized low-resolution NMR spectrometers. If we take into account the hardware time-related imprecisions that were exposed before, we must temporally shift the FIDs before accumulating them, since their optimized superposition offers the best results in what concerns accumulation efficiency. For NMR signals with a somewhat high SNR level, *i.e.*, $SNR > 1$, a trivial peak detection algorithm can be used for the temporal shifting, before the signal accumulation. As the SNR decreases, especially when it heads towards $SNR = 1$ and less, classic peak detection algorithms do not work anymore, and the method employed in our NMR simulator, which was presented in section 3.3, becomes the only viable alternative. Such method implements what we call the FID temporal shifting algorithm.

Our FID temporal shifting algorithm relies on the assumption that the energy of a signal composed of the sum of two non-periodic signals, one being shifted compared to the other, is at the maximum when the shift between both signals is equal to zero.

For this demonstration, we consider $s(t)$ as an FID signal and $s'(t)$ the same FID but shifted by Δt: $s'(t) = s(t + \Delta t)$. According to Fourier analysis, $S'(f)$ and $S(f)$, respectively the FT of $s'(t)$ and $s(t)$, are associated by the following property:

$$S'(f) = S(f)e^{-2i\pi f\Delta t} \tag{77}$$

The energy of the signal $s(t) + s'(t)$, called cumulated energy, or simply E, in the following, can be either calculated in the time or in the frequency domain. In frequency domain, this energy $E(\Delta t)$ is given by:

$$\begin{aligned} E(\Delta t) &= \int_{-\infty}^{+\infty} \left(S(f) + S'(f)\right)^2 df \\ &= \int_{-\infty}^{+\infty} S^2(f)\left(1+e^{-2i\pi f\Delta t}\right)^2 df = \int_{-\infty}^{+\infty} S^2(f)(2\cos(2\pi f\Delta t))df \end{aligned} \tag{78}$$

It is easy to see that the value of Δt that maximize $E(\Delta t)$ is when $\cos(2\pi f\Delta t) = 1$, *i.e.,* when $\Delta t = 0$.

In practice, $s(t)$ and $s'(t)$ are two discrete signals. The calculation of $E(\Delta t)$ can be directly performed by realizing a squared sum of the samples of the time series over a window that encompasses these both FIDs.

We exploited exactly this property in order to resynchronize shifted FIDs. The first FID is established as reference. For the next FID, we first compute $E(kT_s)$ with T_s being the sampling period while k is an integer varying within the by us defined sweep range -500 to 500. We then look for the value k_{max} that maximizes the function $E(kT_s)$. This value represents the number of samples that the second FID has to be shifted so that it be resynchronized with the first one. This process can be repeated for any number of new FIDs that are to be accumulated.

The FID simulator depicted in the section 3.3 was used to assess this method. First, we looked at the evolution of E as a function of k. To do this, we generated two FIDs shifted between themselves by a phase equal to π/10. E as a function of k for k ranging from -320 to -120 samples is shown in Figure 68.

We can see that the evolution of E can be quite well modeled by a second-order polynomial. This fact is exploited in the following to obtain a better estimate of k_{max}: first, the curve $E = f(k)$ is fitted by a parabola $P = ak^2 + bk + c$, and then the value of k_{max} is calculated as:

$$k_{max} = -\frac{b}{2a} \tag{79}$$

Concerning this specific algorithm, given the shape of the curve, optimization methods such as gradient descent could have been implemented instead, in order to obtain the same results with less computation effort if compared with this exhaustive method which consists in testing all shifts. However, considering that significant noise may be present in the considered NMR signals and that there was no computation time constraint for the resolving of the fitting, we decided to only implement the exhaustive method, which fully attended our demands.

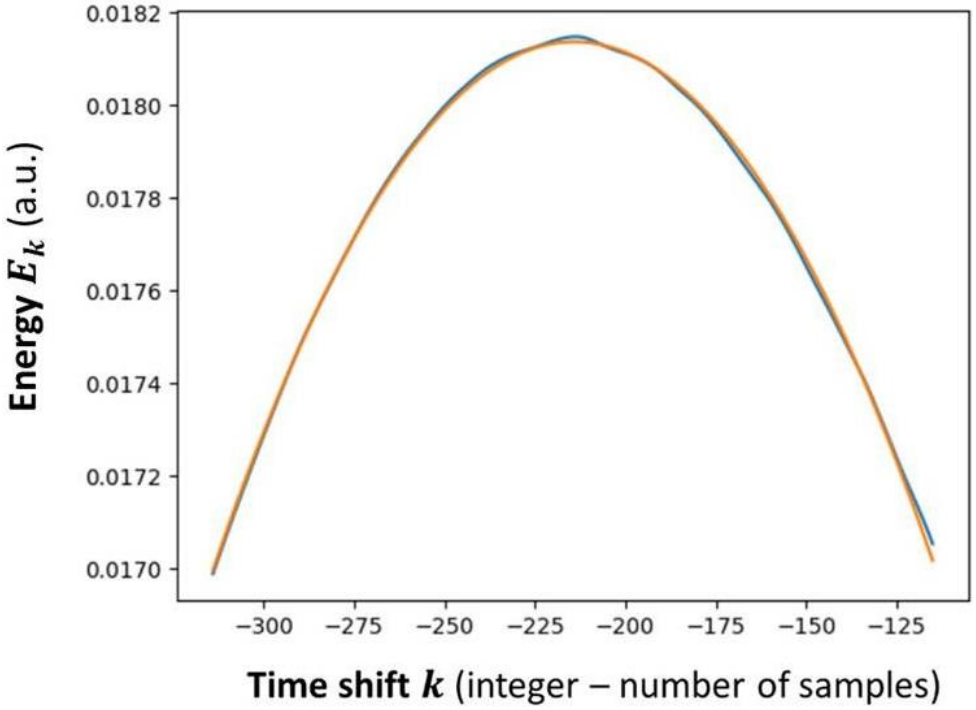

Figure 68 - Cumulated energy E as a function of the time shift k, therefore $\mathrm{E_k}$. Simulation results in blue, second order fit in orange. The polynomial used for the fit is $\mathrm{E(k)} = -1.142 * 10^{-7}\mathrm{k}^2 - 4.888 * 10^{-5}\mathrm{k} + 0.01291$ and the calculated value of $\mathrm{k_{max}} = -214$. Amplitude units are arbitrary.

Results for our time-shifting algorithm on a simulated FID

Figure 69 shows two simulated FIDs for which their highest vertices are initially 90° apart from each other, and the result of applying our resynchronization algorithm.

Figure 70 showcases the effectiveness of this resynchronization algorithm for multiple FIDs. Here, 3 out-of-phase among themselves simulated FIDs and with two of them having a lag equivalent to a 180° phase difference are correctly prepared for the averaging process.

Results for our time-shifting algorithm on a measured FID

Subsequently, from a measured reference FID, we generated a set of 10 FIDs, each of them being shifted from the previous one by a phase equivalent to a lag of 5 ms, as shown in Figure 71.

Figure 72 shows the result of the resynchronization algorithm on this FID set. The results are qualitatively conclusive.

Figure 73 shows the linearity that exists between the initial delay amongst FIDs and the estimated value of k_{max} calculated employing our algorithm.

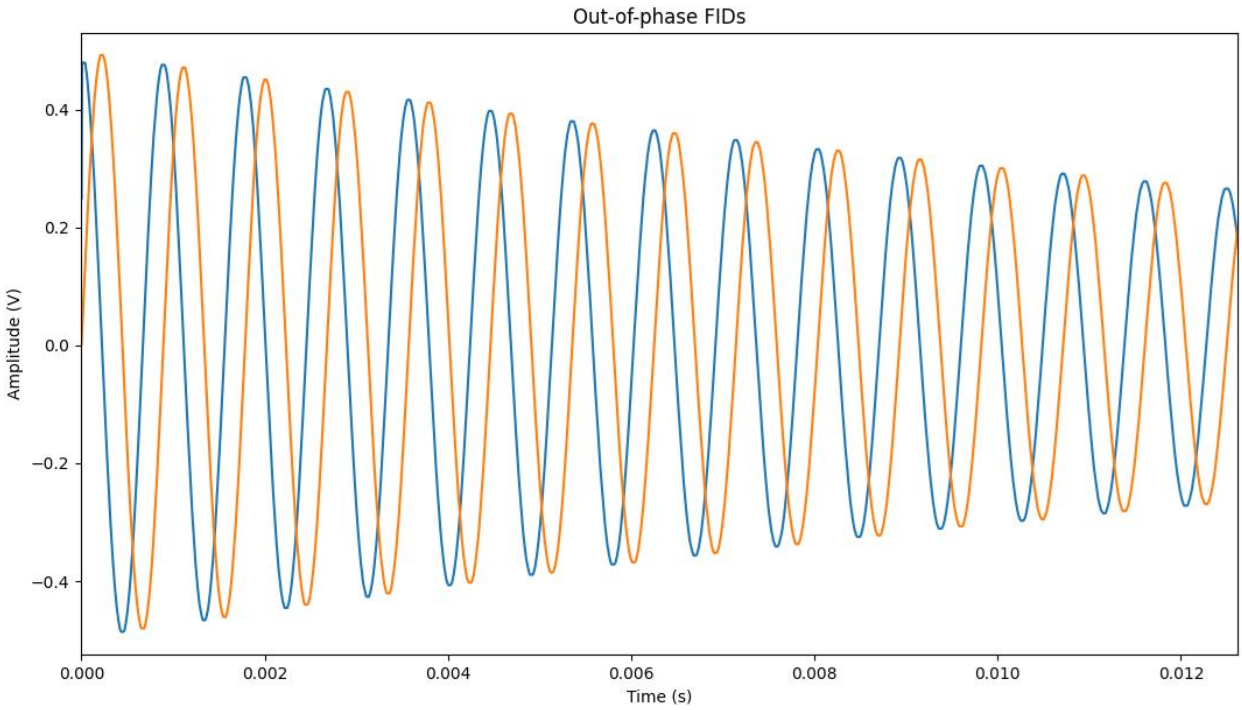

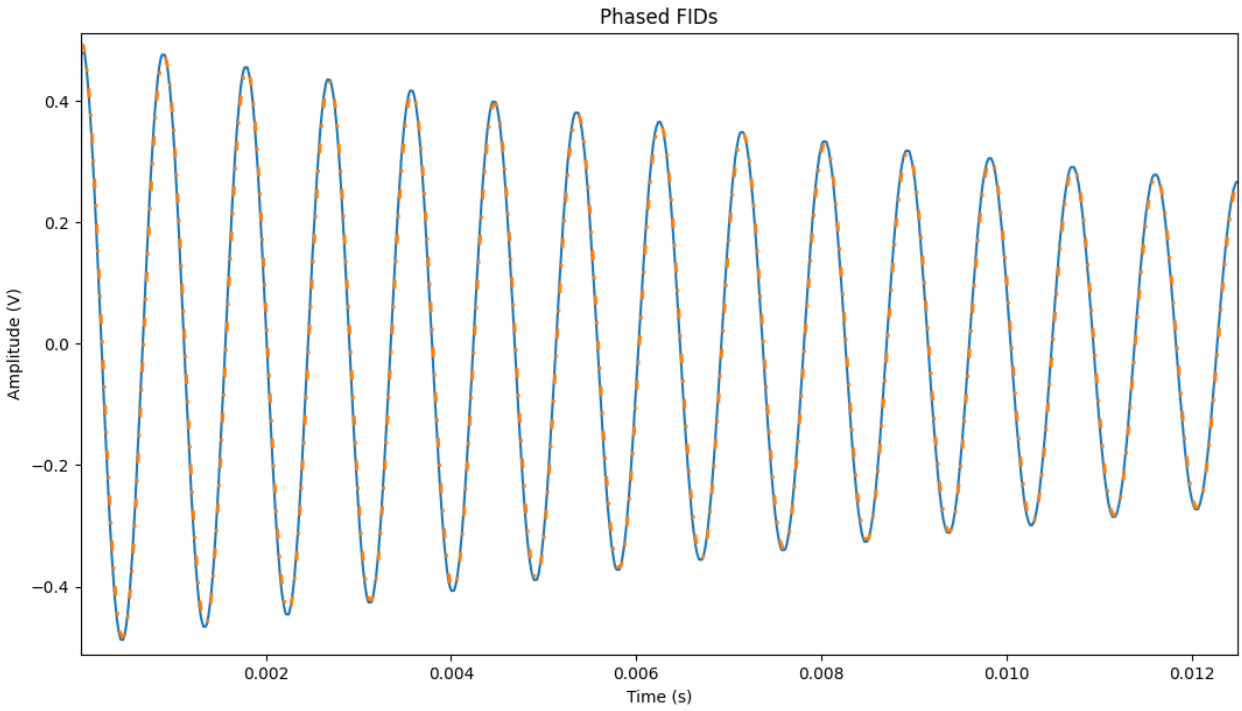

Figure 69 - Top side: two different simulated FIDs with a phase difference of π/2. Accumulating them in the current form is not the best approach. Bottom side: the same two FIDs after applying the time-shifting algorithm. Now they can be added up optimally.

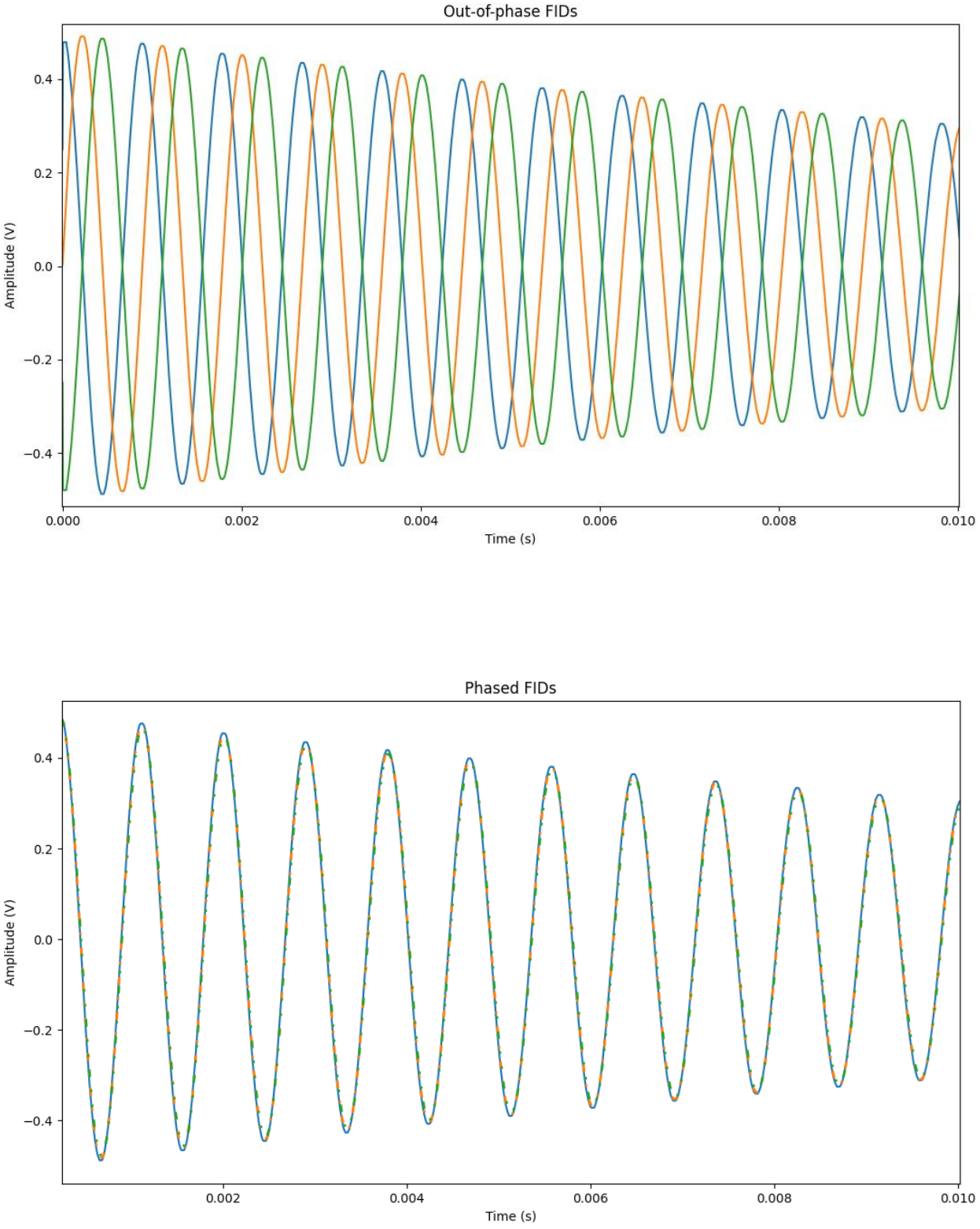

Figure 70 - Top side: three different simulated FIDs with a phase difference of π/2 each. Accumulating them in the current form is not the best approach, because two of them would almost completely cancel each other. Bottom side: the same three FIDs after the time-shifting intended to adjust their phases. Now they can be added up optimally.

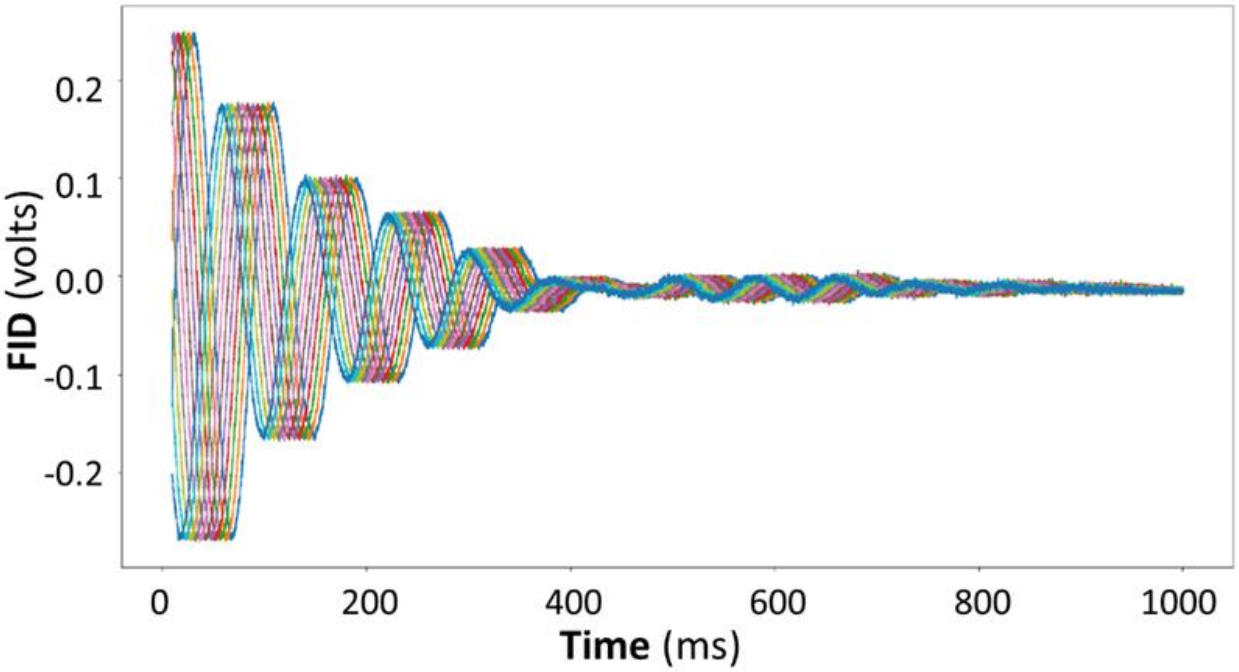

Figure 71 - 10 FIDs generated by the NMR Simulator with succeeding phase shifting equivalent to a lag of 5 ms between each other, starting from a measured reference FID.

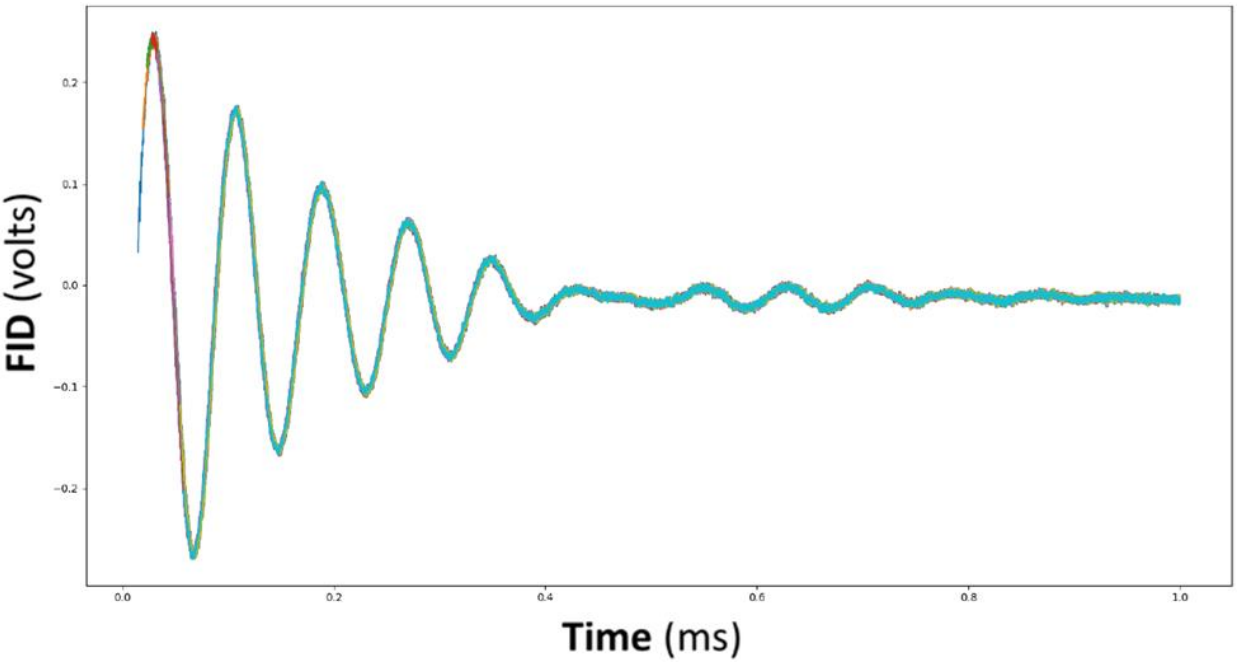

Figure 72 - 10 FIDs generated by the FID simulator with succeeding phase shifting equivalent to a lag of 5 ms between each other and resynchronized employing our method.

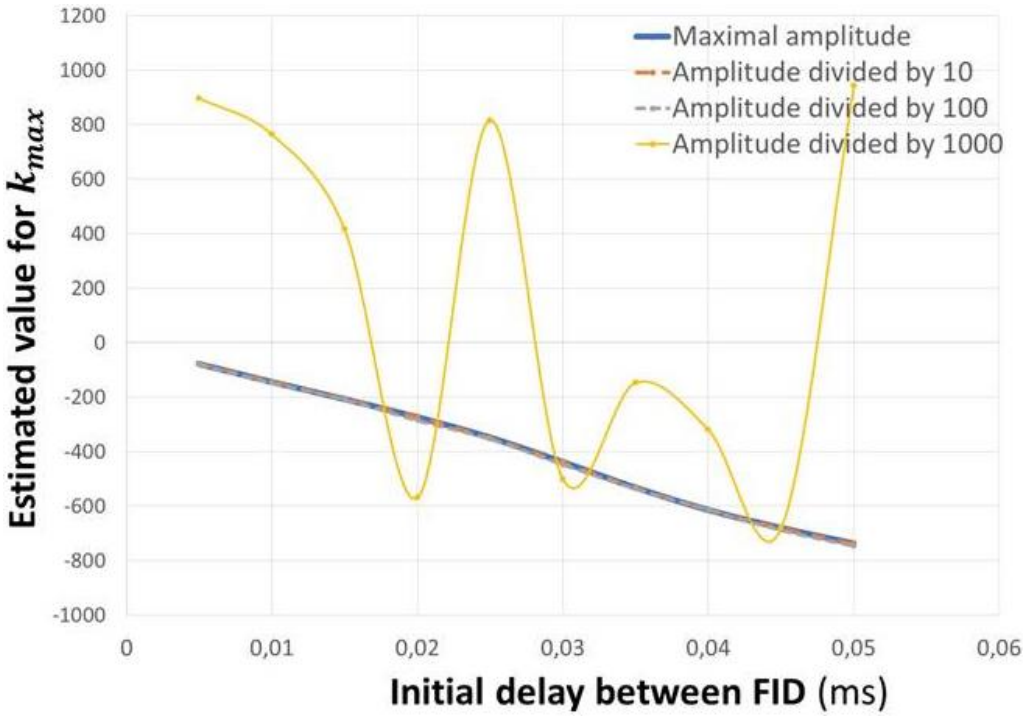

Figure 73 - k_{max} calculated by our algorithm as a function of the initial delay between FIDs given in milliseconds for 4 different signal amplitudes.

Up to now, the calculations were not challenging because the signals were strong enough when compared to the existing noise. Thus, a manually operated recalibration or an automated procedure based on the vertex of the FID would have been sufficient.

Still using the NMR Simulator, we proceeded assessing the robustness of our resynchronization algorithm by successively reducing the amplitude of the reference FID, which presented a SNR of about 33 dB, by a factor of 10, until it drowns completely into the noise. Figure 74 depicts the calculation results for a set of FIDs generated in the same condition (10 FIDs shifted from each other by a phase equivalent to a lag of 5 ms). It becomes evident that the resynchronization algorithm is perfectly effective, even for low-amplitude signals (10% and 1% of the original amplitude, which correspond respectively to a SNR of 13 dB and of -7 dB). A conclusive statement concerning the scenario with an attenuation factor of 0.1% (-27 dB) cannot be proffered.

In order to quantitatively evaluate the performance of our algorithm, we compared the k_{max} values obtained for each phase shift from the set composed of FIDs with reduced amplitudes to the values of k_{max} for the same phase shift, however from the set with the FIDs with the largest amplitudes. A way of demonstrating this quantitative evaluation is by means of the plot in Figure 73. The results are conclusive down to the factor of 1% of the reference amplitude, *i.e.*, for a SNR of -7 dB, but not for one order of magnitude below in what concerns the attenuation factor of the original FID amplitudes, confirming the visual impression that one can get from Figure 74. Furthermore, we could estimate that the limit of validity of our method is around a SNR of -13 dB.

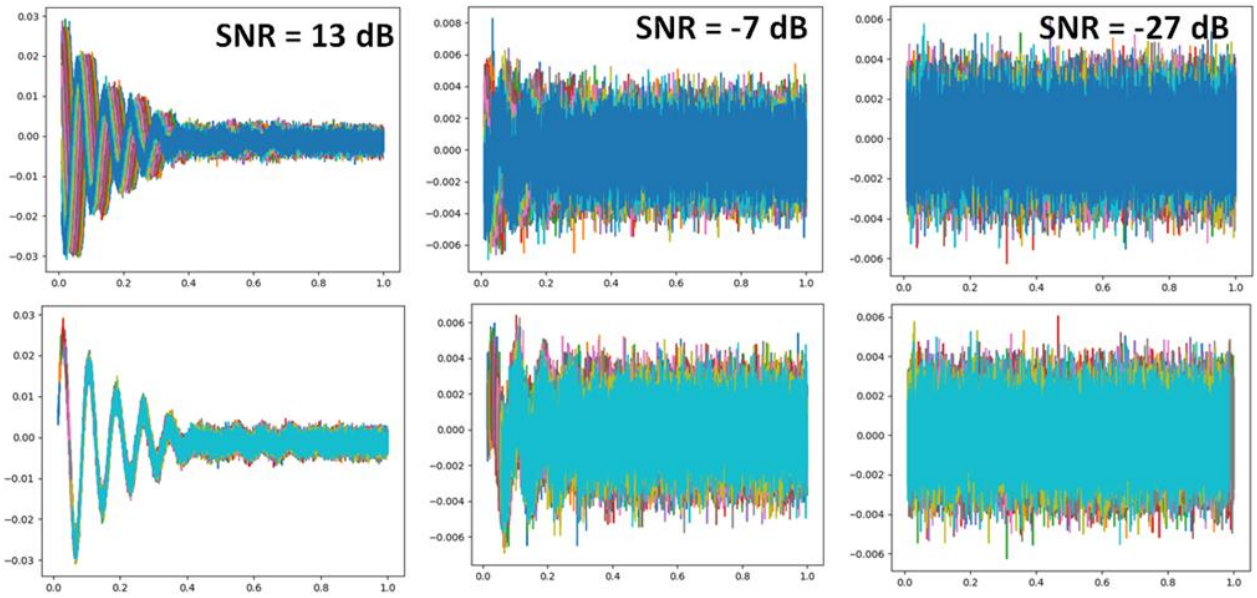

Figure 74 - On the top: set of FIDs generated by the NMR Simulator with a phase shifting equivalent to a lag of 5 ms between each other, and amplitudes multiplied by an attenuation factor of 10, 100 and 1000, which corresponds to SNR of 13 dB, -7 dB and -27 dB respectively. On the bottom: the result of the resynchronization algorithm for each column. The unit of the vertical axes is volts, and of the horizontal ones is milliseconds.

Finally, Figure 75 presents the outcome obtained by resynchronizing with our method and subsequently accumulating a set of 100 generated FIDs, each with a random phase shift. We could clearly see the resulting FID coming out from the noise on each succeeding accumulation, whereas individually they are hardly distinguishable from the noise floor.

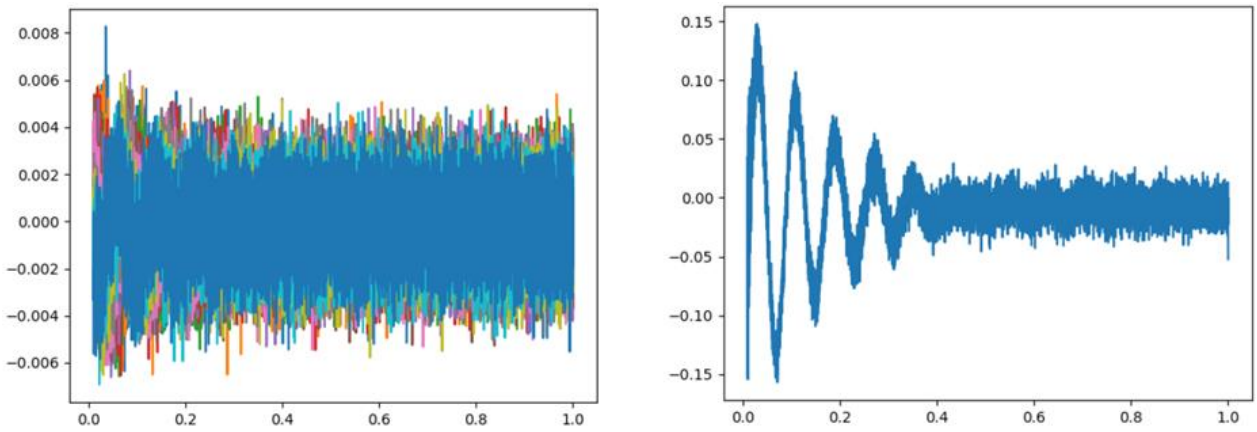

Figure 75 - On the left: the 100 FIDs generated with an amplitude attenuation factor of 1%, *i.e.*, corresponding to a SNR of -7 dB, and a random phase shift each. On the right: the result of the accumulation of these 100 FIDs, after resynchronization by our method. The unit of the vertical axes is volts and of the horizontal ones is milliseconds.

From this demonstration, it can be pointed out that the resynchronization method we propose here gives accurate results, even for signals where $SNR < 1$. A similar approach was also tested in order to compensate for frequency shifts (assuming the signals were initially in phase). These frequency shifts could be due, for instance, to temperature changes between two

measurements. Such algorithm proved however to be less robust than the one presented here for the FID resynchronization. Indeed, the spectral resynchronization would fail with errors start occurring as soon as the SNR decreases down to 1.

The MATLAB code implementing the acquisition and signal processing parts of our NMR Spectrometer Prototype, including processing unit configuration and parametrization, is made available in the appendix section III.

4.6. Operation overview

Our NMR Spectrometer Prototype currently works on the design basis presented in the previous sections. From the perspective of the end user, *e.g.*, an NMR analyst or a chemistry teacher, the employment workflow has not necessarily to require a knowledge that deep into design matters. We therefore show under this section an overview of the use of the prototype at the user level, including intermediary outcomes and explanations. Figure 76 shows the physical prototype with its different parts interconnected, however without power supply for a cleaner view.

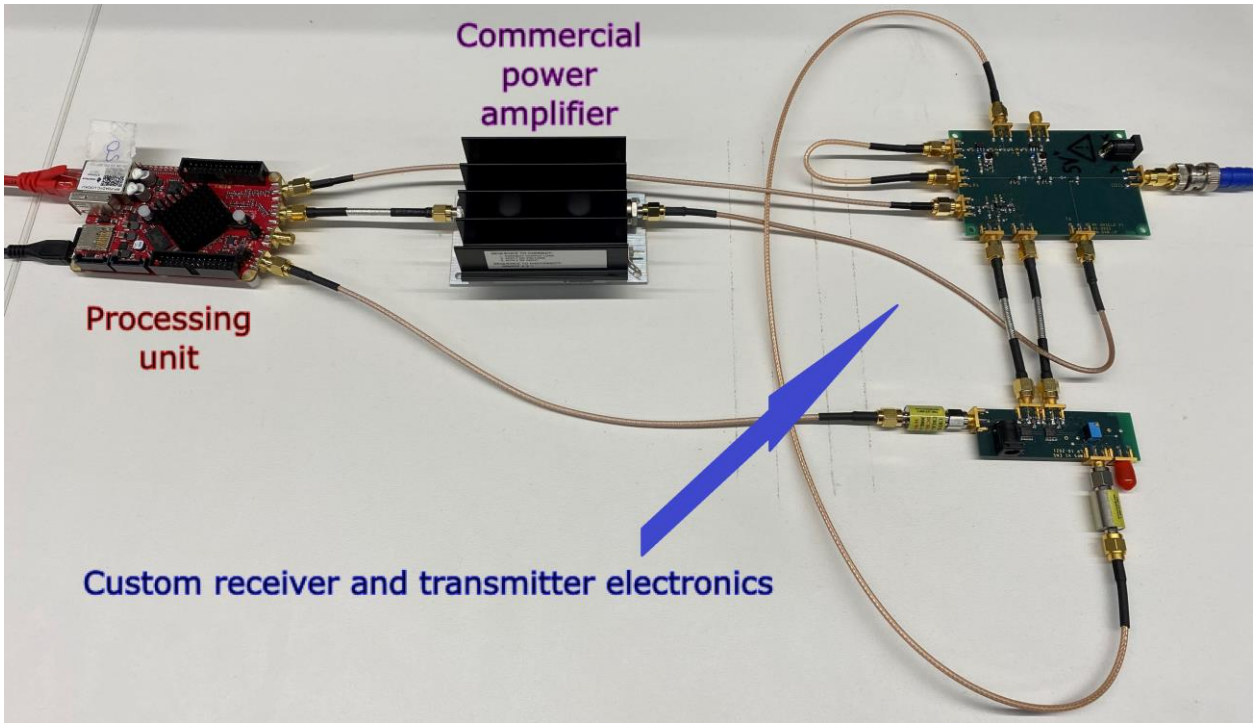

Figure 76 - The current NMR Spectrometer Prototype: processing unit, power amplifier and custom receiver and transmitter electronic boards. Only for illustration purposes.

A less clean view of the prototype, however illustrating how it can be interconnected to the reference benchtop NMR spectrometer from the company Pure Devices, can be seen in Figure 77.

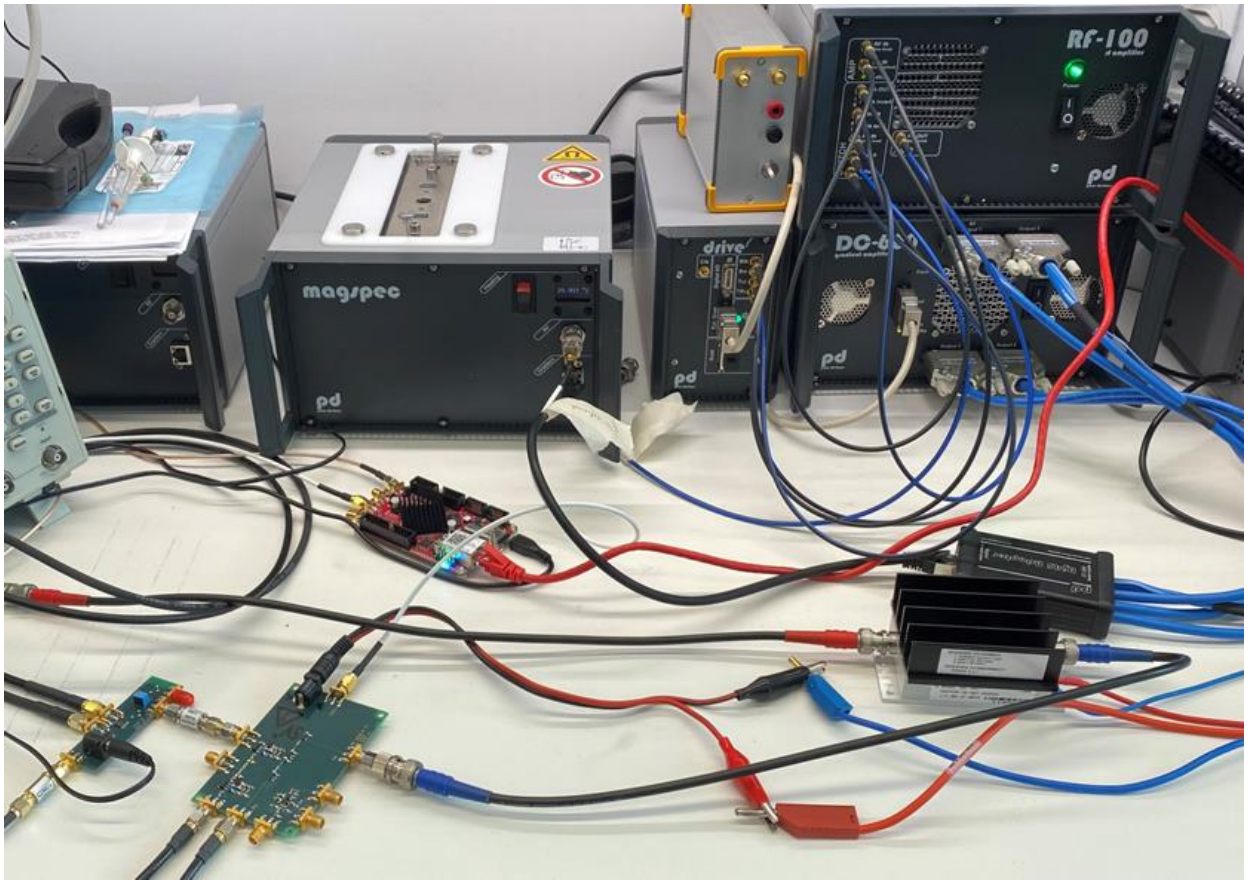

Figure 77 - The current NMR Spectrometer Prototype being used together with the reference benchtop NMR spectrometer from the company Pure Devices. Only for illustration purposes.

The first step when employing the prototype is providing all the different elements with the necessary power supply and turning them on. The reference benchtop NMR has however to be turned on in advance in order for it to stabilize the temperature within the measurement gap: this process takes usually from 5 to 15 minutes, though it can vary depending on external conditions and the moment of its previous use. With the temperature stabilized at 30 °C, the shim procedure has to take place, ideally with the sample to be later analysed, otherwise with a substance providing a one peak strong NMR signal. The shim process is done either by running the automatic search parameter algorithm from Pure Devices available within *openMATLAB* [147] using the MATLAB script *Demo_Auto_ParameterSearch.m*, or by manually setting the shim currents. From the automatic script, one receives the new derived Larmor frequency considering the adjusted shimming, while by the manual method the determination of the new Larmor frequency is not straightforward. Anyways, the new Larmor frequency is going to be posteriorly employed within the prototype processing unit for the excitation and local oscillator signal generation.

Once everything is up and running and the shim was successfully performed, the host computer has to initialize a SCPI server on the SDR. This can be easily done via a browser, as

seen in Figure 78. With the given IP address and port, one is then able to communicate with the processing unit using the ethernet port.

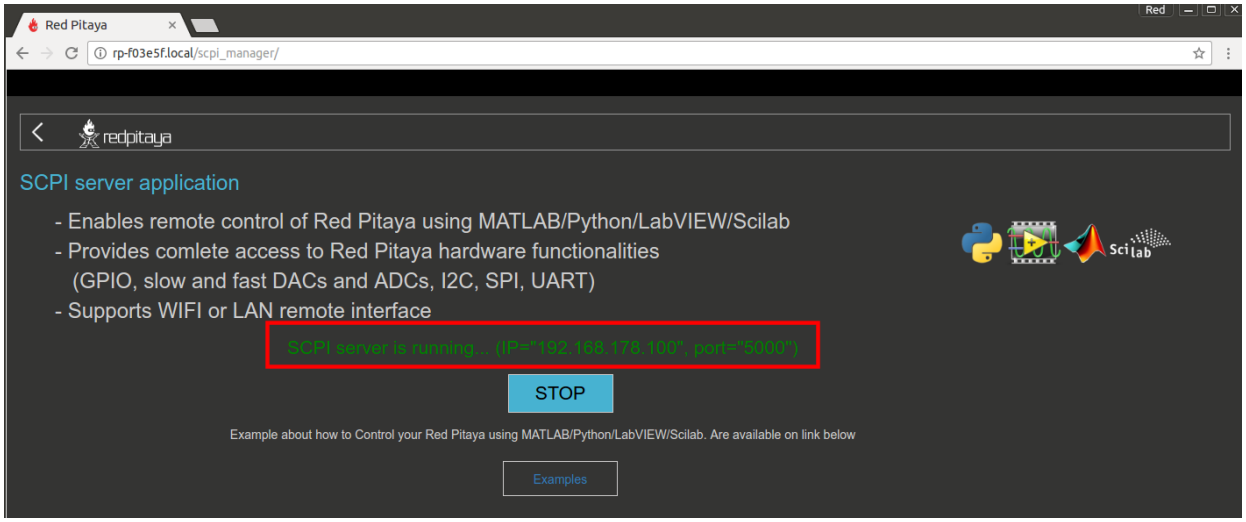

Figure 78 - SCPI server initialization on the host computer. Modified. [164]

Employing our developed MATLAB script to be used within the openMATLAB package from Pure Devices, it is possible to start an NMR experiment. However, one should at first define the parametrization of the experiment by setting the variables shown in Table 4, which names are mostly self-explanatory.

After the correct parametrization, by running the prototype MATLAB script, the NMR experiment happens. The application provides intermediary outputs before providing the user with the obtained NMR spectrum for each scan. Illustratively, we present hereunder a real acquisition process with our prototype having as sample pure water (H_2O). The NMR experiment with pure water is relatively easy and straightforward to be performed because it is a safe substance for humans to handle in any work environment and it possesses a relative strong NMR signal corresponding to a single characteristic NMR spectral peak. The first intermediary outcome is the sampled raw FID, *i.e.*, the sampled FID after the mixer without any digital signal processing. Figure 79 shows a raw FID for the water molecule. It is to be noticed that the analogical amplification gain is adjustable and depends on the current experiment, and therefore the amplitudes of the different samples FIDs correspond to the voltage level at the entry point of the processing unit, after that a manual gain optimization process was successfully performed. The absolute values of the amplitudes are a sign of its strongness or weakness. These cannot however be formally used to compare different experiments after the gain correction. SNR should be used for that matter instead.

Parameter / Variable	Name / Meaning	MATLAB Argument Data Type / Unit
acquisitions_amount	Number of acquisitions to be performed.	scalar, integer
pause_between_acquisitions_seconds	Waiting time between two subsequent acquisitions, if applicable.	scalar, double / seconds
scans_amount	Number of scans to be performed within each acquisition. If scans_amount is different from 1, all the scans are averaged.	scalar, integer
pause_between_scans_seconds	Waiting time between two subsequent scans, if applicable.	scalar, double / seconds
minimal_displayed_ppm_value	Right side boundary of the chemical shift axis.	scalar, double / ppm, usually: a negative integer
maximal_displayed_ppm_value	Left side boundary of the chemical shift axis.	scalar, double / ppm, usually: a positive integer
experiment_name	Name of the experiment for setting up the output folder.	string
experiment_directory	Relative directory to the openMATLAB folder where analysis outcomes are saved.	string
sample_amount	Size of the acquisition buffer.	scalar, integer
Larmor_frequency_Hertz	f_0	scalar, double / Hz
down_conversion_frequency_Hertz	f'	scalar, double / Hz
excitation_duration_seconds	$\overrightarrow{B_1}$ duration.	scalar, double / seconds
excitation_amplitude_volts	$\overrightarrow{B_1}$ amplitude before amplification.	scalar, double / volts

oscillator_amplitude_volts	Amplitude of the mixer reference oscillator for $f_0 + f'$.	scalar, double / volts
sampling_decimation	Decimation factor as in [165].	scalar, integer: powers of 2 up to 16 and then any whole number up to 65536
IP	IP address of the SCPI server, as in Figure 78.	string
port	Port of the SCPI server, as in Figure 78.	scalar, integer

Table 4 - NMR experiment and setup parametrization within the prototype, and their corresponding units.

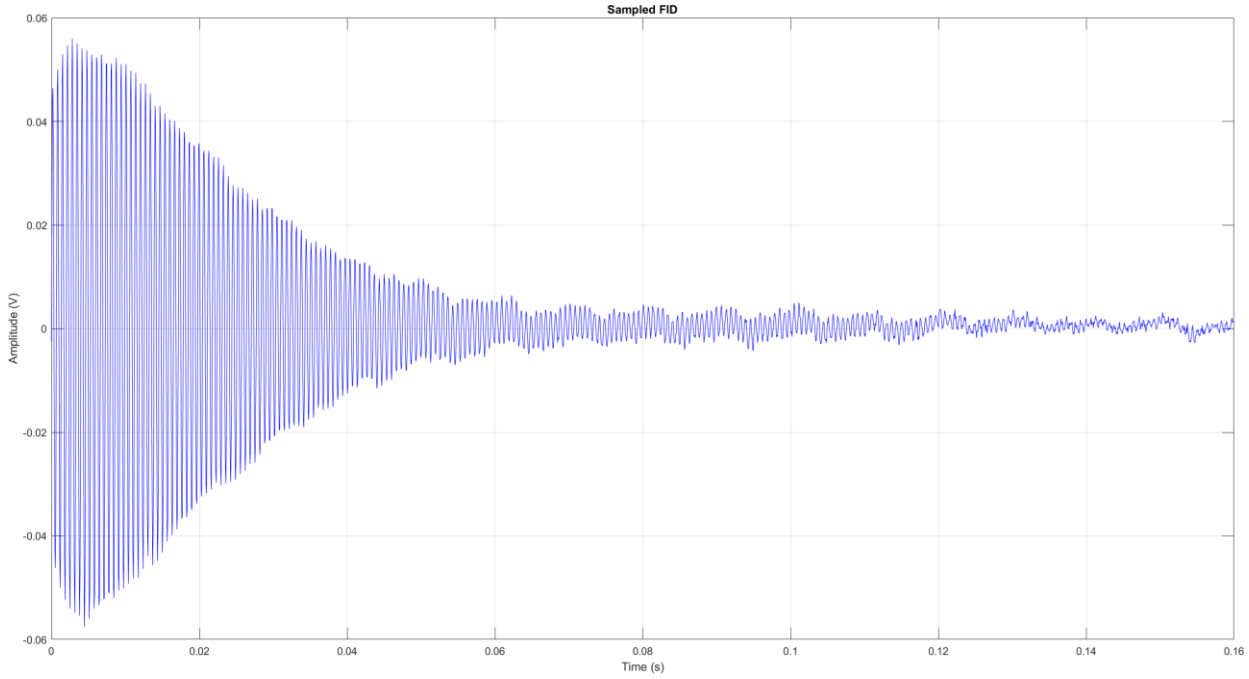

Figure 79 - Sampled NMR signal for pure water. (303.15 K, around 24.35 MHz, developed NMR Spectrometer Prototype)

Although this FID presents a quite correct shape, the presence of noise is perceivable. This noise accounts for different kinds of thermal and electronic noise and other magnetic interferences that may be present in the measurement environment. Indeed, a non-white noise pattern is as well visible on the raw FID, what happened as well for certain measurements with the reference benchtop NMR from Pure Devices alone. This indicates that at least one external-to-our-prototype source of parasitic frequencies was present within the experiment environment. At different moments, we would detect different patterns of non-white noise on our acquired

FIDs. This noise level is much more deleterious for weak signals. Therefore, the way forward is to filter out the undesired frequency components from it. By doing so, an NMR signal in the form of the filtered FID in Figure 80 results.

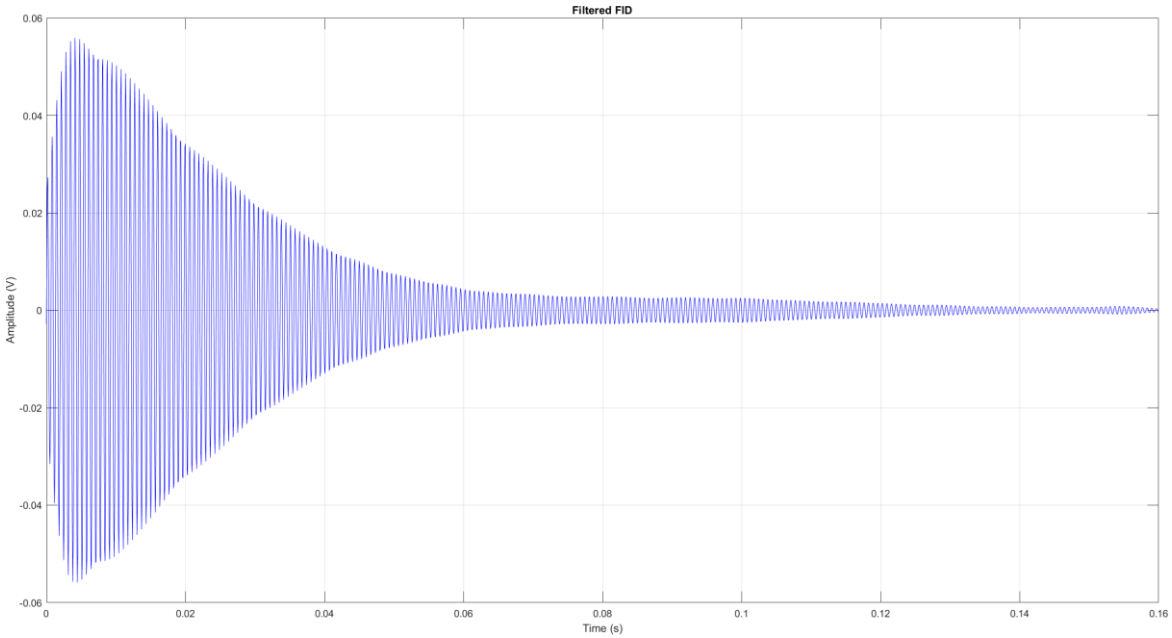

Figure 80 - Sampled FID after proper filtering. (303.15 K, around 24.35 MHz, developed NMR Spectrometer Prototype)

From the digitally filtered NMR signal, the Fourier analysis takes place as explained before. The outcome of it for the considered pure water experiment can be seen in Figure 81.

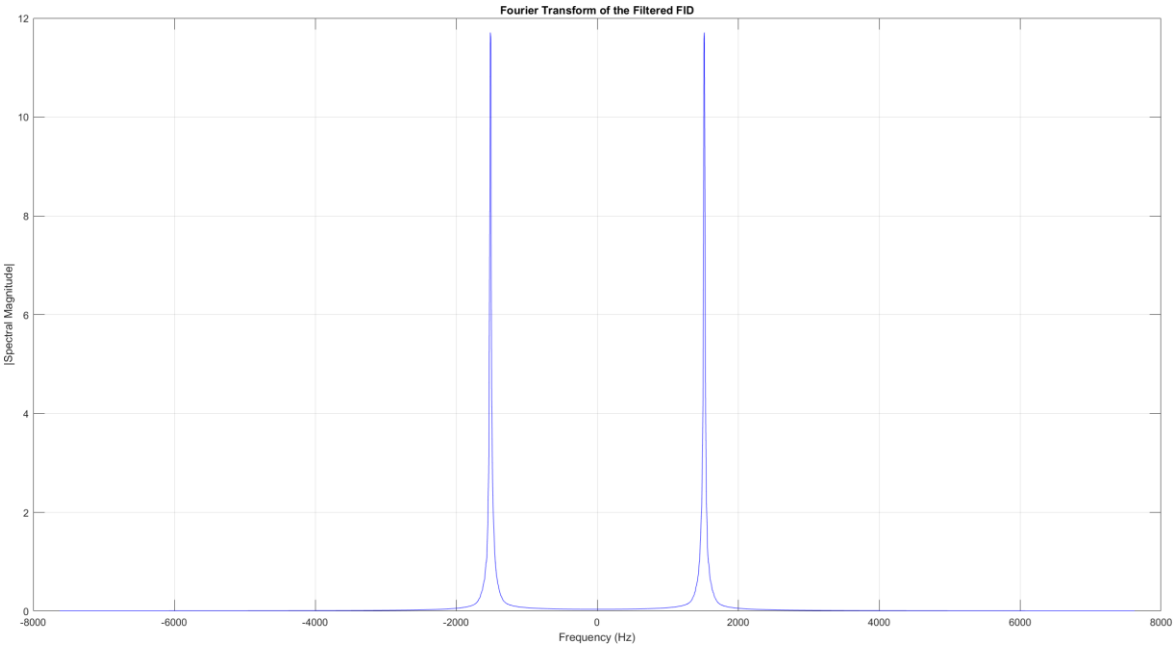

Figure 81 - Graphical spectral representation of the results of the Fourier analysis. (303.15 K, around 24.35 MHz, developed NMR Spectrometer Prototype)

The resulting Fourier analysis is successively used for the generation of the classic NMR output. Figure 82 depicts it for the case of the considered pure water experiment.

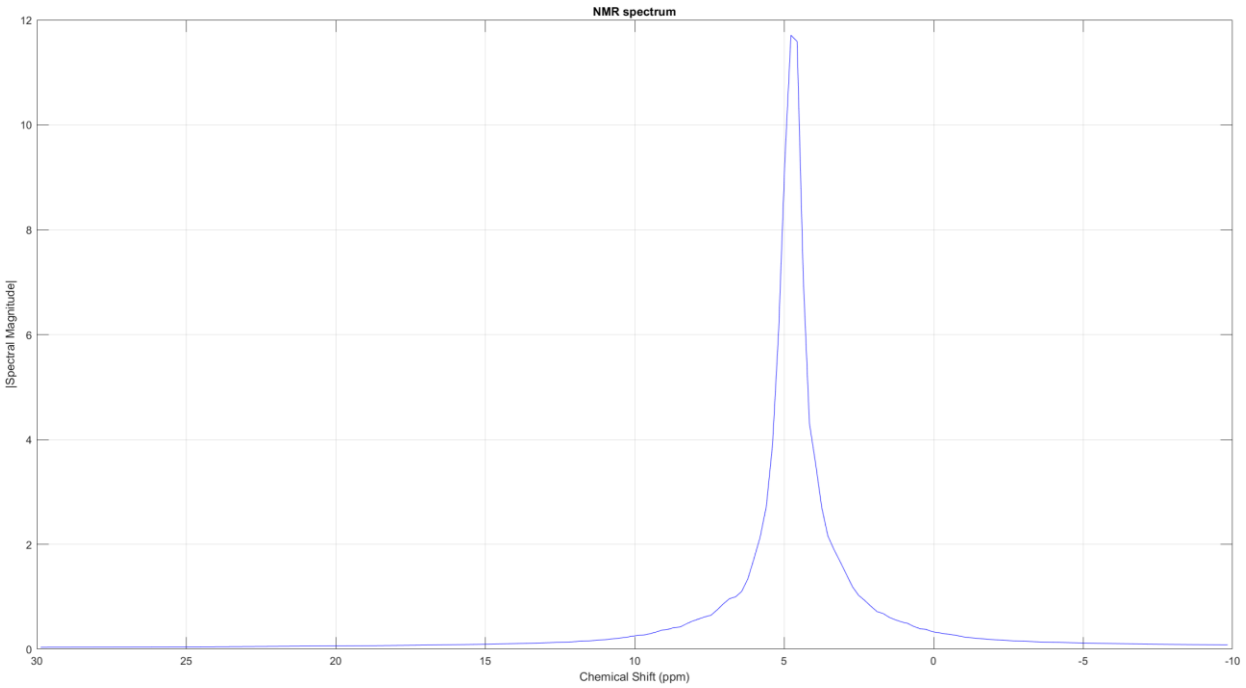

Figure 82 - Low-resolution NMR spectrum for pure water as the outcome of our NMR Spectrometer Prototype. (303.15 K, around 24.35 MHz, developed NMR Spectrometer Prototype)

The final and the intermediary results provided by the prototype can be easily saved as figures or text files and be used as inputs within other software applications and simulation tools.

NMR

In this chapter, we presented our NMR Spectrometer Prototype and its composing elements. We demonstrated how we employ some parts of the benchtop NMR reference system from Pure Devices within our prototype and what are its technical characteristics. We proceeded by introducing the Red Pitaya SDR board to the reader and how it is employed as the prototype processing unit. Then, the prototype custom receiver and transmitter electronics was put forward, and hardware-related limitations of the resulting setup were illustrated. Currently, these limitations prevent the implementation of averaging techniques for very weak signals, which are important for improving the LoD of our NMR Spectrometer Prototype for the targeted applications. As a mean of enabling signal accumulation in cases where the FID is barely distinguishable from the noise floor, an FID shifting algorithm was proposed, being as well implemented within the NMR Simulator, as seen in section 3.3. To conclude this chapter, an overview of the prototype operation and the outcomes for ^{1}H NMR measurements of pure water using the prototype were presented.

The next chapter illustrates the different experimental results, including for the targeted applications, that were obtained with our prototype, as well as outcomes and setup-related assessments, especially in what concerns spectral quality and field deterioration conditions.

Chapter 5 - Experimental results

From the theoretical and practical basis exposed up to this point, a set of NMR experiments were designed and performed in order to present the usability and applicability of our NMR Spectrometer Prototype within its current limitations. Each following section introduces a given experiment, presents and evaluates its outcome, and makes an aimed concluding assessment of it. This chapter is therefore organized in five different sections. First, ethanol solutions are used in order to assess the performances and characterize the electronics of our prototype. Secondly, the same solutions are used in order to assess the performances of our home-designed coils. The following sections are related to our targeted applications. The third one concerns the analysis of highly concentrated glyphosate solutions in order to estimate the LoD for this pollutant with our prototype. In the fourth section, high- and low-field NMR measurements performed during an esterification reaction are compared in order to assess the performance or our current setup in the context of chemical reaction monitoring. Finally, a magnetic field drifting assessment concerning our current benchtop NMR reference system is put forward.

5.1. Ethanol molecule

The ethanol molecule (C_2H_6O) presents a characteristic 3-peak frequency spectrum in low-resolution NMR. It is as well a pretty much safe chemical compound to work with and an interesting validation use-case because we can assess the overall applicability of the prototype in what concerns spectral resolution and general spectral degradation. Figure 83 presents a measured FID for ethanol employing our prototype.

One can compare its similarity to the simulated version of Figure 43. The presence of electrical noise is evident, although at acceptable levels for a single-acquisition experiment. After employing an adapted bandpass filter, the resulting FID looks like the one given in Figure 84.

The resulting NMR signal has a much more harmonious shape and in accordance with what is expected from an NMR measurement of a pure ethanol sample. The results of the Fourier analysis already present the overall shape of the comprising frequency elements of its NMR spectrum, as it can be seen in Figure 85.

It is a promising sign that three peaks are visible because it means that the spectral resolution is at least enough to depict distinct peaks separated by chemical shifts of the order of 1 ppm, as long as their relative individual spectral magnitudes, *i.e.*, the energy contained in each spectral peak are important enough and not many orders of magnitude away from each

other. This is the exact case of the ethanol molecule, for which the outcoming NMR spectrum is presented in Figure 86. As a mean of comparison, the reader is invited to consult Figure 20 again.

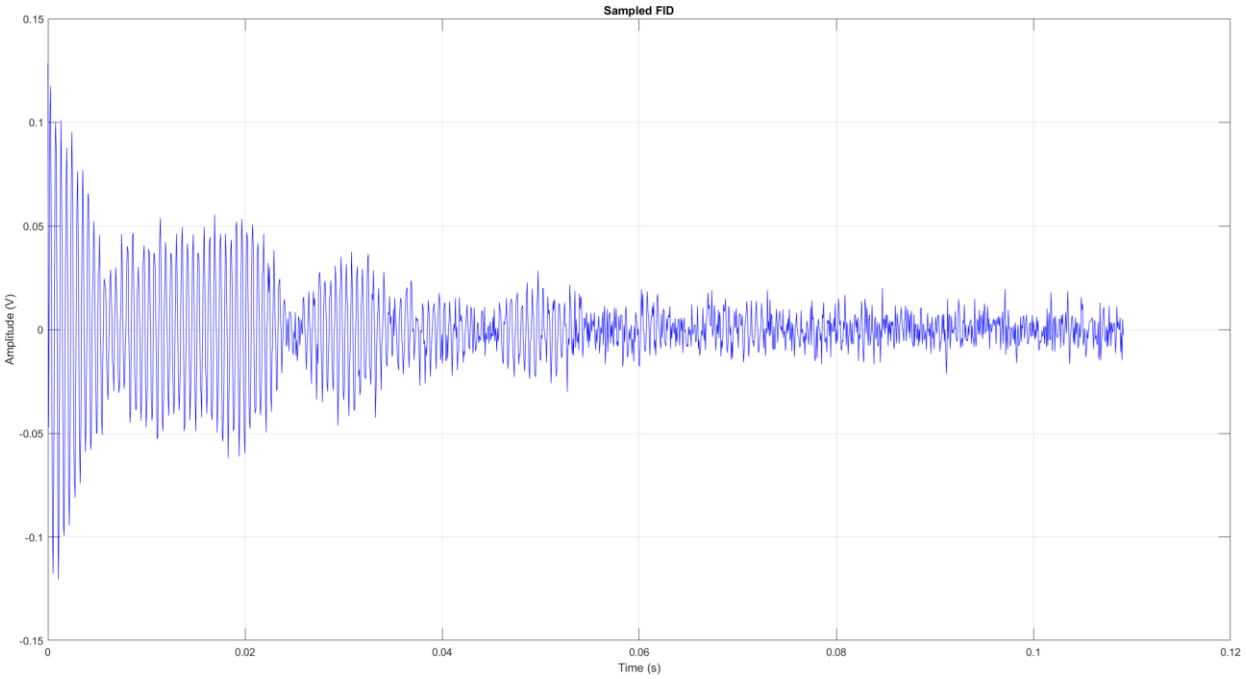

Figure 83 - Acquired NMR signal for the ethanol molecule using our prototype. (303.15 K, around 24.35 MHz, developed NMR Spectrometer Prototype)

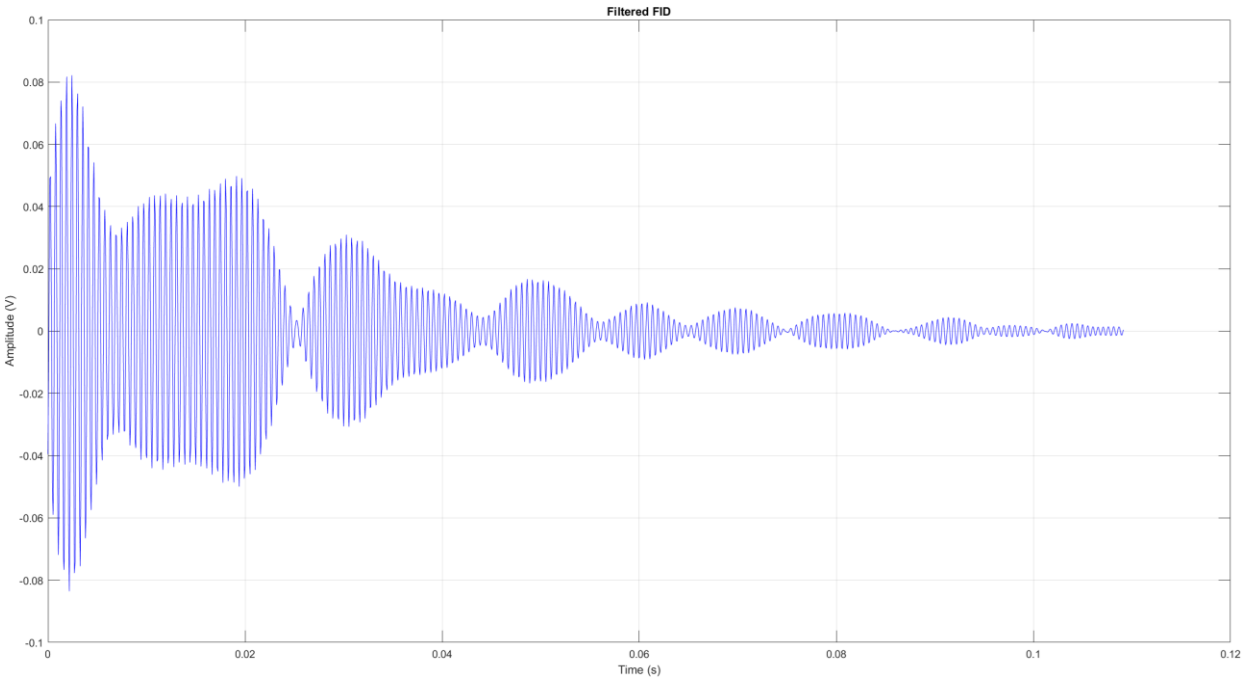

Figure 84 - Filtered FID resulting from a single-acquisition on an ethanol sample. (303.15 K, around 24.35 MHz, developed NMR Spectrometer Prototype)

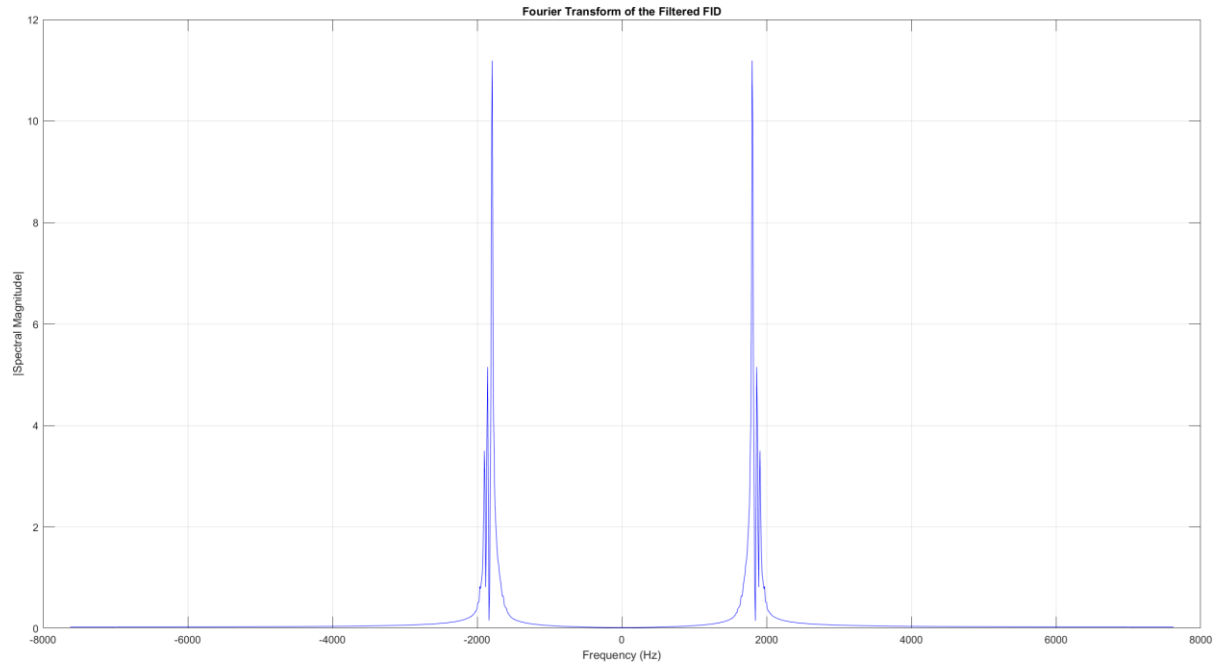

Figure 85 - Fourier transform of the filtered FID measured for the ethanol molecule. (303.15 K, around 24.35 MHz, developed NMR Spectrometer Prototype)

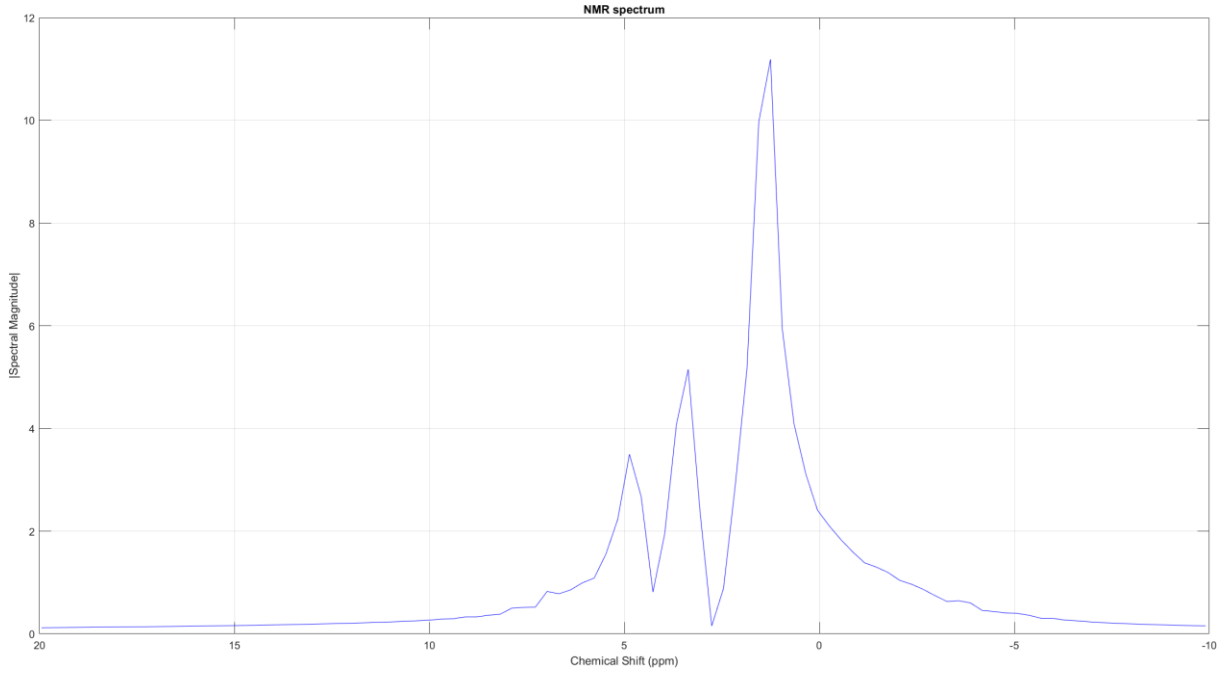

Figure 86 - Low-resolution NMR spectrum acquired from an ethanol sample. (303.15 K, around 24.35 MHz, developed NMR Spectrometer Prototype)

For a stationary enough temperature stabilization during the measurement of the FID, *i.e.*, within the acquisition process, the spectral resolution of the prototype is therefore of the order of 1 ppm for suitable chemical compounds considering the current setup of our prototype, *i.e.*, $B_0 \approx 550$ mT including shim adjustments within the measurement volume. Local temperature variation within the measurement gap, also known as temperature drifting, entails

local magnetic field drifting, in our case the local magnetic field drifting of $\overrightarrow{B_0}$ following the equation (11). Temperature drifting has therefore a direct impact on the applied excitation at the Larmor frequency f_0, but also at the different frequency components of the measured NMR signal, following equation (1). It clearly worsens the already diminished T_2^*-relaxation time when compared with its theoretical value T_2 – which is setup- as well as experiment-related and for the ethanol molecule is typically in the order of some hundreds of milliseconds –, by means of the equation (4). And finally, because temperature drifting engenders magnetic field drifting, it brings spectral degradation and therefore loss of the overall spectral magnitude to the outcoming spectra, as the mathematical framework from equation (26) to equation (42) demonstrates. For important variations of the temperature during a measurement, the resulting ethanol NMR spectrum would present a single deformed, wider peak with a smaller spectral magnitude when compared to the would-be spectral magnitude of the highest of its non-deformed peak. In practice, the three low-resolution peaks would have merger. In extreme cases, its overall spectral magnitude could decrease so much that the peak would not be distinguishable from the spectral noise floor. For not so drastic scenarios of temperature drifting, as often experienced by us during laboratory measurements with the current prototype setup, the merging of only two of the spectral peaks, *i.e.*, the ones with the smaller chemical shift difference between themselves, would happen, making the characteristic three-peak low-resolution NMR spectrum from ethanol depicted in Figure 86 become a two-peak NMR spectrum, as shown in Figure 87.

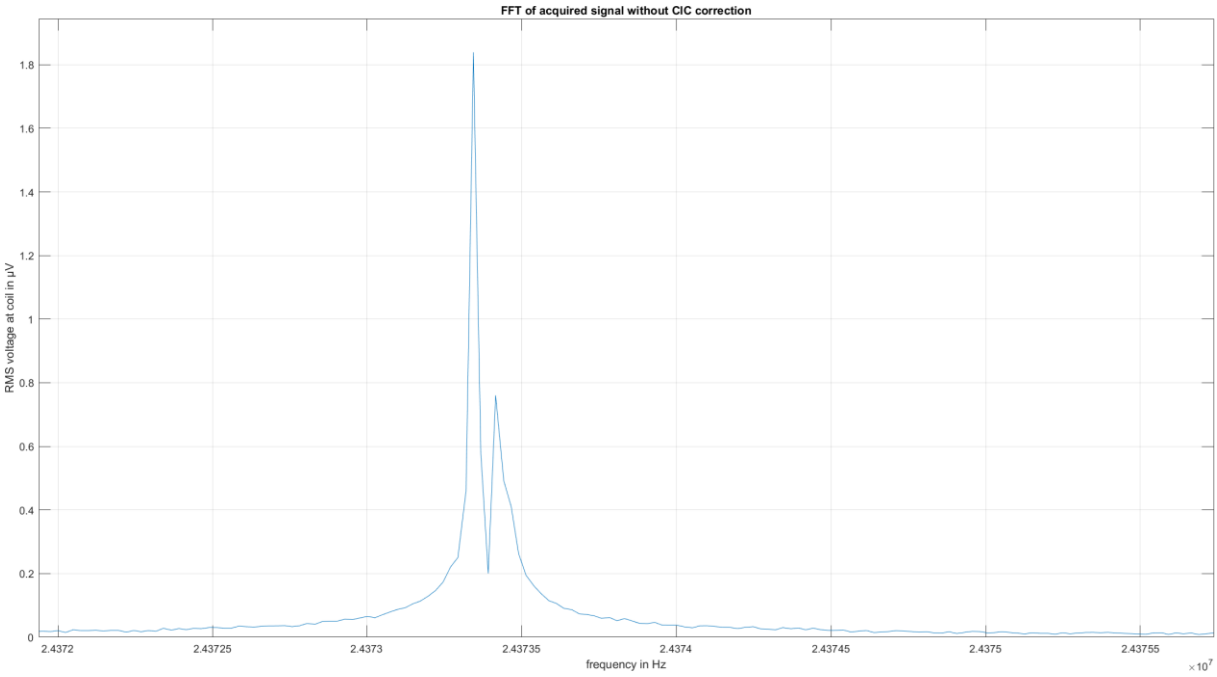

Figure 87 - Low-resolution frequency spectrum for Ethanol acquired with the benchtop NMR spectrometer from Pure Devices [4] only: the expected three spectral peaks are not there. Instead, we have a two-peak configuration. It is due to the merging of the two smaller peaks due to temperature drifting during the acquisition of the FID. This is only the positive half of the resulting Fourier analysis data array and not the classic NMR spectrum representation and

therefore the frequencies increase to the right. (303.15 K, around 24.35 MHz, benchtop NMR from Pure Devices)

The correct temperature stabilization of the system to an acceptable application-related level is, with the existing homogeneity correction of $\overrightarrow{B_0}$, a major design aspect to be taken into account during the system specification phase. The equipment systems engineering requirements must reflect the handling of such technical and physical specificities.

5.2. Ethanol molecule using a self-made miniaturized receiving coil

The NMR experiment for the ethanol molecule was as well performed using one of our self-made miniaturized NMR receiving coils instead of using the one from the reference benchtop NMR spectrometer from Pure Devices. Although the obtained results are promising, the current prototype setup including the reference benchtop NMR spectrometer from Pure Devices is not genuinely suitable for such replacement or aggregation of receiving coils. The shim system of the reference benchtop NMR spectrometer from Pure Devices was designed for its own specific spatial conformation and material elements composition. By inserting an extrinsic receiving coil, the automatized shim procedure does not work anymore, and an optimized field correction is not possible for the new physical measurement structure. At present, it means that, at the best, we can use the previous successful shim correction – without having inserted our self-made receiving coil into the measurement gap – and try to see if it is still good enough to measure an NMR signal with our receiving coil being inserted posteriorly. Figure 88 presents the outcoming low-resolution NMR spectrum of the ethanol molecule acquired under these conditions with one of our self-made receiving coils.

Comparing Figure 88 to Figure 86, both acquired with our prototype, we directly perceive that the use of our own receiving coil within the current prototype setup and under the shim conditions exposed above degraded the quality of the acquired NMR spectrum. A spectral shape degradation due to at least the non-optimal shim, *i.e.*, to $\overrightarrow{B_0}$ becoming locally less homogeneous can be clearly identified. But most noticeable is the loss in the spectral amplitude when comparing both results: for the highest spectral peak, we have an attenuation factor of about 3 orders of magnitude between our self-made receiving coil and the original one from Pure Devices. Such evaluation cannot be seen as formal since we just compared the magnitude of one peak and have not considered the spectral deformation, *i.e.*, the broadness of the compared peaks. However, it is enough to qualitatively illustrate that the current setup cannot be used optimally with our self-made miniaturized receiving coils. A more robust quantitative evaluation of the signal loss between both scenarios is provided by calculating the area under

both NMR spectra and comparing the outcomes. This can be done by means of numerical integration with MATLAB. Considering the same chemical shift range for both NMR outcomes, *i.e.*, from -10 to 20 ppm, the attenuation factor between the two coils when comparing the area under the spectral peaks within the defined range is of about 400.

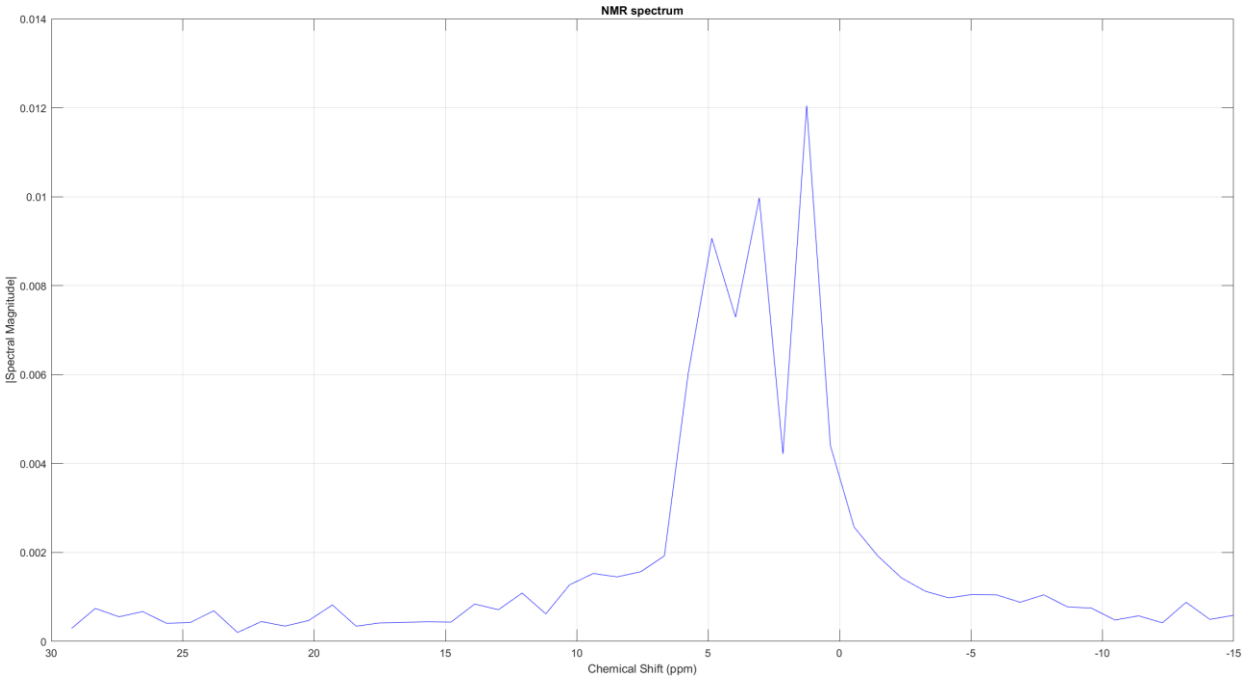

Figure 88 - Low-resolution NMR spectrum of ethanol acquired with our prototype and one of our self-made miniaturized receiving coils. It is both qualitatively and quantitatively inferior to the same spectrum acquired with the original Pure Devices receiving coil because the shim is not optimal anymore. (303.15 K, around 24.35 MHz, developed NMR Spectrometer Prototype)

Among the reasons of why the signal is so much weaker when measuring with our customized receiving coils, additionally to (1) the non-optimal shim and (2) the impossibility to improve it to the necessary quality standard, we can cite (3) the non-optimal geometry of the pair customized receiving coil and measurement gap, (4) the coexistence of two receiving coils at the same setup without the possibility of correctly suppressing the original one while not damaging its structure, (5) and generally other receiving coil construction parameters that cannot be correctly evaluated without a specific dedicated testing setup. To the last point belong design requirements concerning the receiving coil (6) geometry, *e.g.*, form and diameter of the coil, number of turns and wire diameter if solenoidal, spatial disposition, etc., (7) material, (8) impedance matching, *e.g.*, 50 Ω or high impedance, (9) further aspects related to the receiving coil sensitivity, and so on. For the present experiment, a miniaturized receiving coil with a 50 Ω impedance matching was employed. Its use within the reference benchtop NMR spectrometer and its impedance matching board can be seen in Figure 89.

Figure 89 - Self-made miniaturized NMR receiving coil and its impedance matching board.

The difficulties concerning the design of customized receiving coils and their use together with another possibly incompatible NMR systems highlight the necessity of an early definition of the system requirements already anticipating the successive distinct development steps, including possibilities of partial validation and integration with other elementary parts. Indeed, the NMR effect agglomerates within a NMR spectrometer so many physical variables and technology related aspects, that a false system requirement decision can greatly impact or even invalidate a part of the design process. For the specific case of the duo receiving coil and shim system, from the very beginning they should be designed taking into consideration the targeted application, the mutual impact on each other, and geometry aspects of the equipment-to-be, as for instance the available measurement volume.

5.3. Saturated solution of glyphosate in heavy water

One of the targeted applications of our NMR spectrometer is the detection of pollutants in drinking water. Pure water, which presents the chemical formula H_2O, is known as the universal solvent or the solvent of life, presenting at room temperature tasteless and odourless characteristics apart a hint of blue, and being a polar inorganic solvent – the most studied chemical compound in history [166]. Furthermore, water molecules form hydrogen bonds with each other, and because they are strongly polar, it allows the dissociation of ions in salts and further bonding to other polar substances such as alcohols and acids, therefore dissolving these

substances. Water alone presents an ^{1}H NMR chemical shift around 4.79 ppm, however in solutions it depends as well on the coexisting chemical compounds [167].

Among the possible pollutants to be detected, the glyphosate molecule is of particular concern because of its confirmed and implied impact on human health, as seen in the chapter 0. Glyphosate presents the chemical formula $C_3H_8NO_5P$ and exhibits therefore ^{1}H NMR spectral peaks whose chemical shifts can vary according to the solvent in which it is inserted, usually ranging from 3 to 4 ppm. Indeed, the chemical shift is sensible to the nucleus environment, *i.e.*, to the temperature, the pH concentration of the solution, to further nearby nuclei, etc., therefore modifying it, sometimes only slightly. In what concerns the interactions solute-solvent, considering as reference a given duo solute-solvent, these interactions are not kept the same when either the solute or the solvent of the reference solution is replaced. For instance, when we look at the example of water as solvent, its hydrogen bonds have an impact on the electronic cloud surrounding the nucleus, which can affect this nucleus chemical shift. Indeed, the density and magnetic response of the electron cloud varies with the chemical environment, which in turn modifies the magnetic field at nearby nuclear sites, resulting in magnetic field values at a given nucleus that are different from the externally applied magnetic field $\overrightarrow{B_0}$, impacting this nucleus magnetic shielding, and therefore its chemical shift [168].

Glyphosate in water presents an extremely weak NMR signal within realistic scenarios, *i.e.*, small concentrations found routinely in polluted waters. The only way of detecting it with a single acquisition NMR experiment would be by increasing its concentration. In the framework of the Interreg Offensive Science Water Pollution Sensor project, the use of molecularly imprinted polymer dedicated to the extraction of glyphosate in natural waters has been explored [169]. Such method is expected to remove the pollutant from water at the concentration at which it is present and incorporates it into a polymer matrix. After successful extraction, enrichment and subsequent desorption of the pollutant happens in order to achieve the minimal required concentration factors for NMR detection. However, even employing pollutant concentration techniques, the use of averaging techniques, *i.e.*, accumulation of NMR temporal signals or spectra may be mandatory.

For the validation of our current prototype, we put forward a high-concentration scenario with glyphosate added to a pure solvent to the point where the solution gets saturated. The term saturated means that the further addition of glyphosate does not increase its concentration within the solvent but rather will start making it precipitate, therefore getting accumulated at the bottom of the tube. Although this is not a realistic scenario *per se*, because we do not expect to typically find waters so polluted that these would be saturated with glyphosate, such unrealistic scenario would however show that low-resolution NMR combined with a beforehand concentration process could be *a priori* used to detect glyphosate in drinking water, provided that the acquisition hardware be able to correctly implement averaging techniques.

However, as solvent, we employed heavy water, *i.e.*, D_2O or ^2H_2O, instead of regular water (H_2O). This would give us the benefit of supressing the proton spectral peak of the solvent (for regular water expected to be around the range 4.5 to 4.8 ppm) from close to the spectral peaks of the glyphosate molecule for a better appreciation. Nonetheless, as it is the case when working with heavy water, there might be a residual amount of semi-heavy water (HDO or H^2HO) within it, what would prevent the complete suppression of the spectral peak around the range 4.5 to 4.8 ppm.

The choice of saturated glyphosate in heavy water, knowing their typical chemical shifts for ^1H NMR, presents therefore an interesting validation scenario for our prototype, especially if we take into consideration its current limitations in terms of spectral resolution and boundaries of the acquisition procedure. For reference and as a mean of validation, Figure 90 presents the ^1H NMR high-field spectrum for the saturated solution of glyphosate in heavy water.

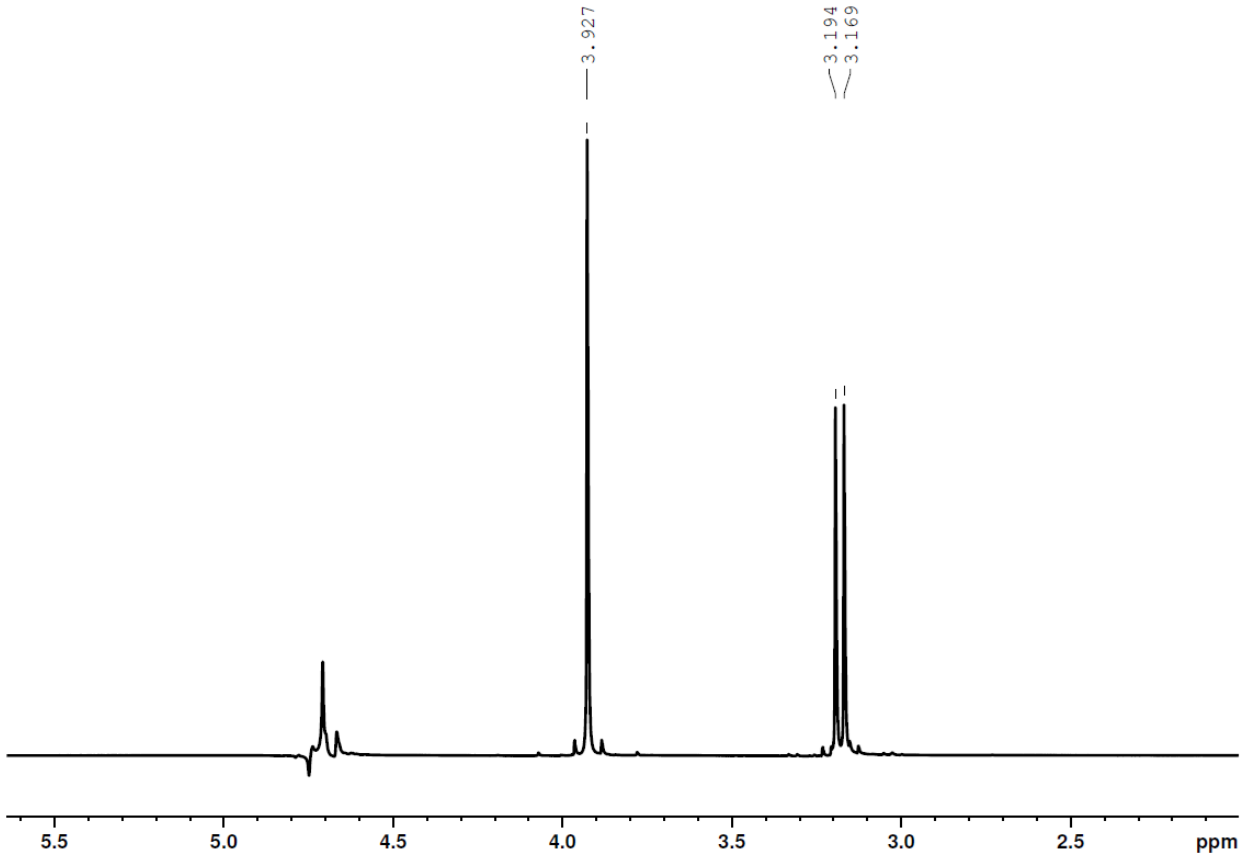

Figure 90 - High-resolution ^1H NMR spectrum of a saturated solution of glyphosate in heavy water: residual semi-heavy water proton peak at around 4.7 ppm and the further peaks correspond to the glyphosate molecule. (Saturated $C_3H_8NO_5P$ in D_2O, 298.15 K, 500 MHz).

Figure 91 depicts the different discernible chemical shifts of the glyphosate molecule when considering ^1H NMR spectroscopy. While the interactions of the hydrogen atom depicted in red within the structure of the glyphosate in Figure 91 are responsible in Figure 90 for the peak at around 3.9 ppm and for the doublet at around 3.19 ppm and 3.16 ppm, the solvent, *i.e.*, heavy water produces no peak within the visible chemical shift range. The residual semi-heavy

water within the solution causes the peak at around 4.7 ppm to emerge. The would-be proton peaks corresponding to the interactions of the hydrogen atoms depicted in blue are not detectable by ^{1}H NMR spectroscopy due to hydrogen-deuterium exchange, which is a natural reaction replacing covalently bonded hydrogen atoms by deuterium atoms and conversely. As a side note, from the structure of the glyphosate, one can see that its detection through phosphorus-31 NMR, *i.e.*, ^{31}P NMR spectroscopy is possible [48]. ^{31}P NMR signals present a gyromagnetic ratio γ^P of about $40.5\ \%$ of the gyromagnetic ratio γ^H of the ^{1}H NMR, what places the Larmor frequency f_0^P of the ^{31}P NMR experiment relatively to the Larmor frequency f_0^H of the ^{1}H NMR experiment at about $0.405 f_0^H$. In our prototype, it would bring the Larmor frequency f_0^P to about 9.87 MHz.

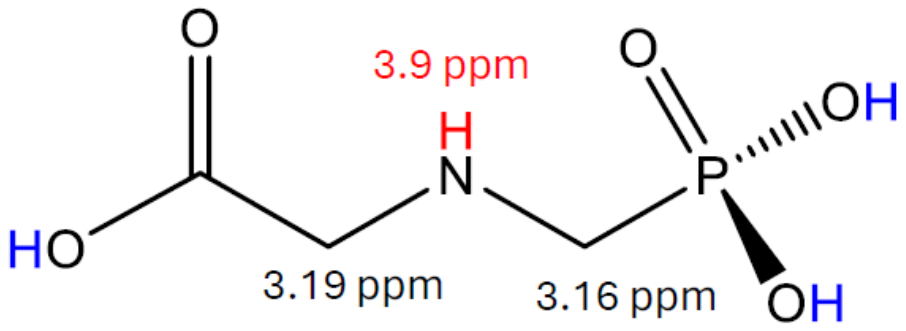

Figure 91 - Glyphosate detectable ^{1}H NMR chemical shifts per hydrogen biding.

In low-resolution ^{1}H NMR, glyphosate can present two spectral peaks that are around 0.73 ppm apart from each, and the question of if we are able to see them as two separated peaks or if it will come out as a single peak depends on the spectral resolution of the NMR spectrometer, *i.e.*, its $\overrightarrow{B_0}$ inhomogeneity after shim, and at a lesser extent on the temperature stabilization during the measurement.

The NMR experiment described above was performed as well with our prototype as a single-acquisition scan procedure at a temperature of around 30 °C. The measured FID is presented in Figure 92.

Purely as an illustration of what happens at low-resolution NMR, Figure 93 presents the FT of the above NMR signal without any filtering. There, we can see a single deformed peak, while the expected was at least 3 peaks, maybe 4, as one could infer from Figure 90. However, looking attentively to the spectral shape of this single peak in Figure 93, it is possible to see that the side peaks (orange and green) merged with the central one (red).

Because we already know which are the outcomes of this NMR experiment in terms of number of peaks and chemical shifts, a targeted filtering could be employed as means of improving the analysis outcome. Such targeted filtering consists of parametrizing the filter function with the exact frequency range of the spectral peak, therefore cutting every other

existing frequency component out of the spectrum. After filtering, the NMR signal looks like the one in Figure 94.

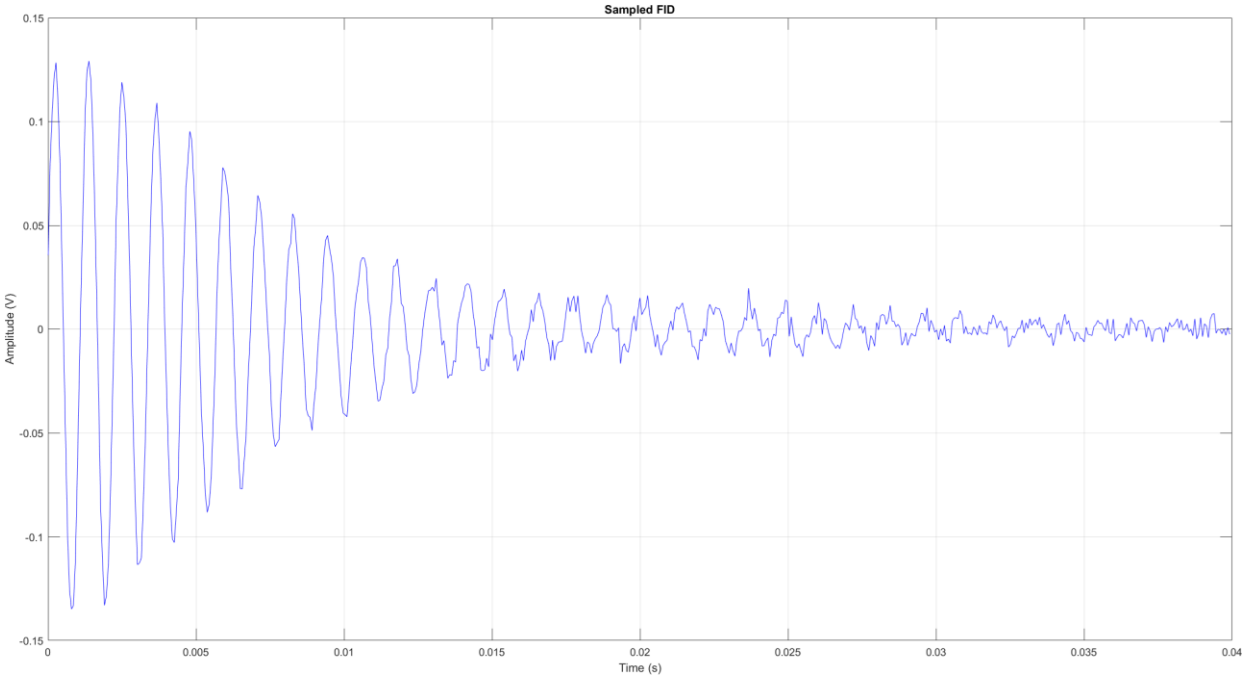

Figure 92 - NMR signal corresponding to a single acquisition for the saturated solution glyphosate in heavy water measured with the NMR Spectrometer Prototype. (303.15 K, around 24.35 MHz, developed NMR Spectrometer Prototype)

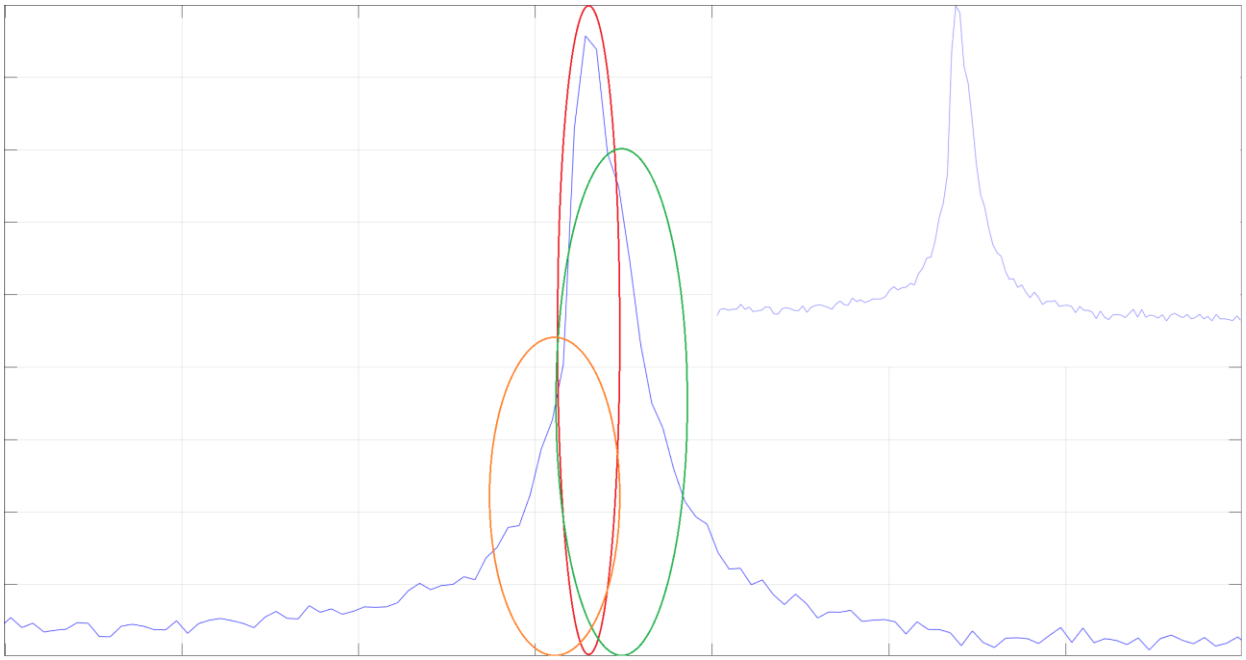

Figure 93 - Artistical depiction of the merging of the spectral peaks of the saturated solution of glyphosate in heavy water for low-resolution proton NMR. (303.15 K, around 24.35 MHz, developed NMR Spectrometer Prototype)

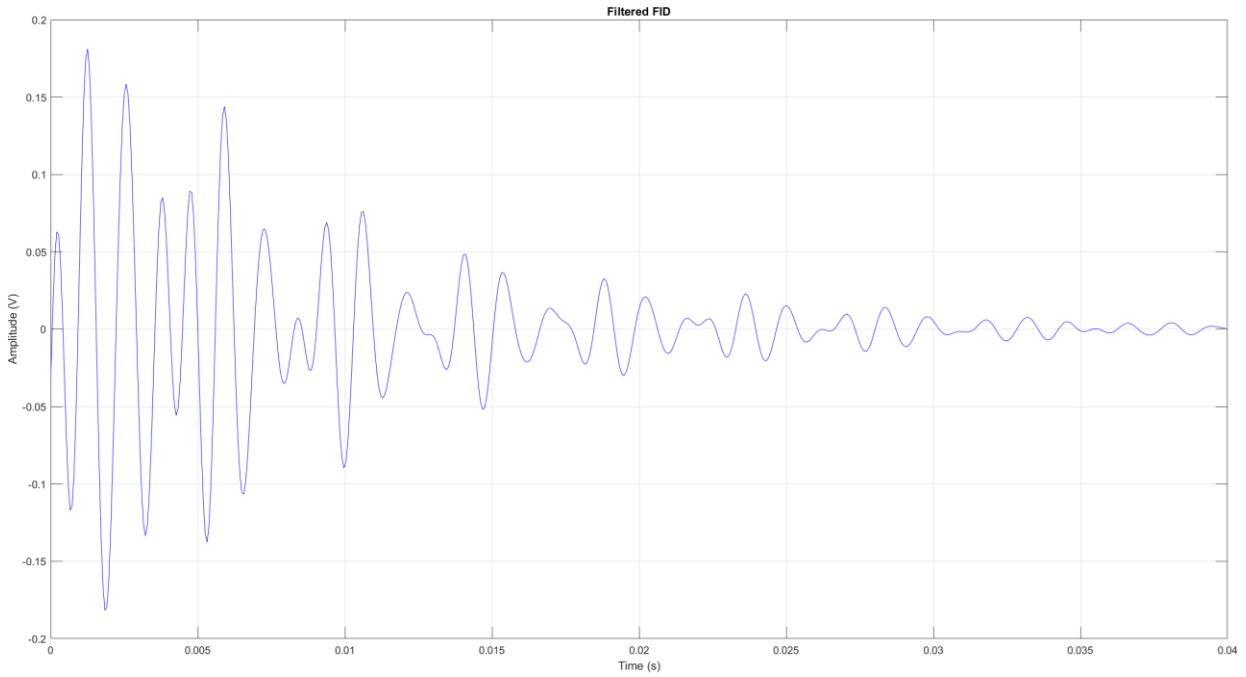

Figure 94 - Digitally filtered NMR signal of glyphosate in heavy water. (303.15 K, around 24.35 MHz, developed NMR Spectrometer Prototype)

The result of employing this targeted filtering approach is that we remain with only the 3 fundamental frequency components corresponding to the expected 3 spectral peaks. We also have a pretty much limited number of samples composing our spectral magnitude data array. These both facts clarify the unexpected shape of the resulting FID after filtering, as presented in Figure 94. The Fourier analysis of the filtered FID produces a low-resolution 3-peak frequency spectrum, which can be seen in Figure 95.

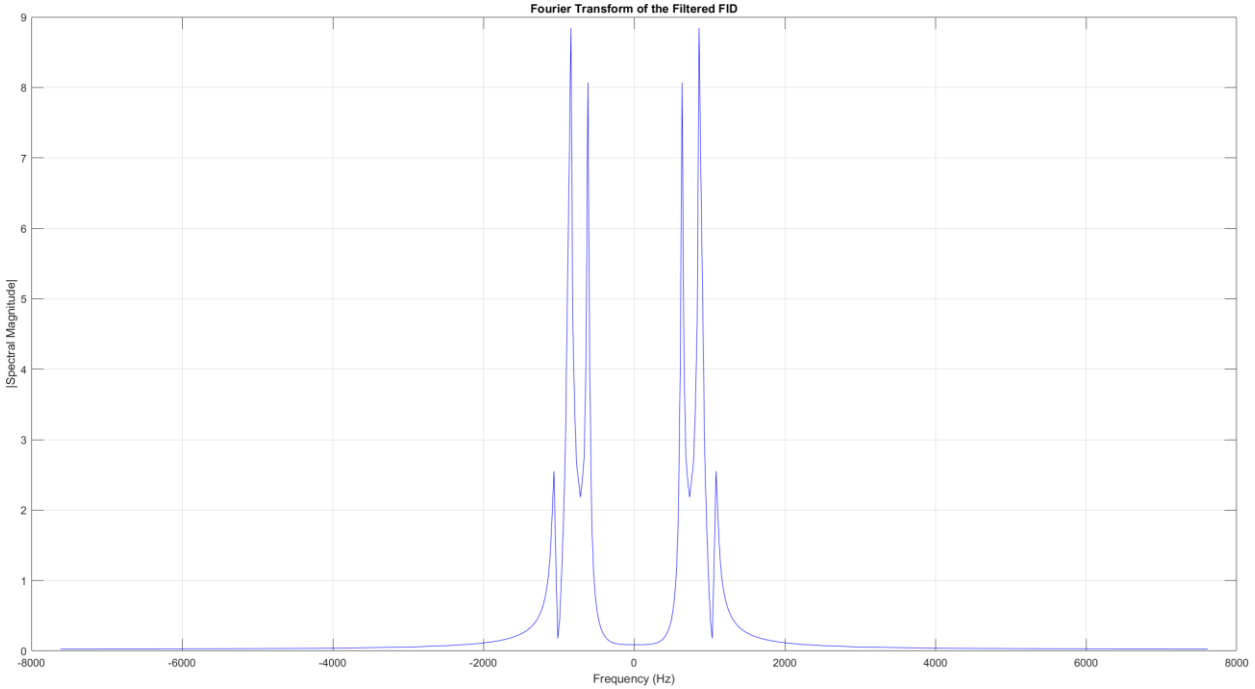

Figure 95 - Frequency spectrum for the sample glyphosate in heavy water. (303.15 K, around 24.35 MHz, developed NMR Spectrometer Prototype)

Finally, Figure 96 depicts the resulting NMR spectrum in terms of chemical shift for the considered NMR experiment.

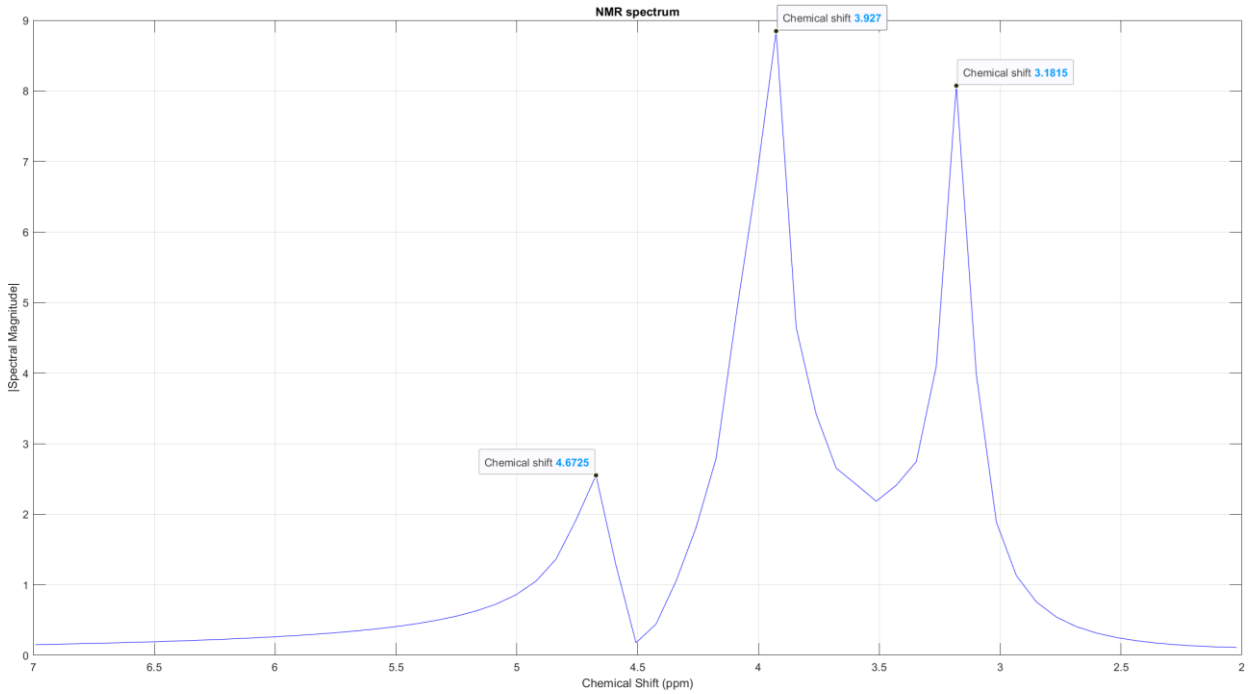

Figure 96 - Low-resolution NMR spectrum of glyphosate in heavy water acquired with the NMR Spectrometer Prototype. (303.15 K, around 24.35 MHz, developed NMR Spectrometer Prototype)

We clearly see 3 peaks instead of 4. The chemical shift of the semi-heavy water being the one to the left, the remaining two are from the glyphosate. The peak most to the right is the result of the merging of the doublet in Figure 90. Indeed, temperature fluctuation and other field drifting effects as the minimal change in the shim currents and the moving of the sample tube within the measurement gap can lead to even worse spectral degradation. The results presented here were a combination of optimized shim and no strong temperature variation during the measurement, allied to the use of targeted filtering that could only be employed because we knew what we were expecting to find as an analysis outcome. Nonetheless, considering both the peaks spectral magnitudes and the noise floor obtained from this experiment with saturated glyphosate solution, we can estimate that the resulting LoD for single acquisition glyphosate-related experiments might be around one order of magnitude below the saturation concentration. The maximum concentration of glyphosate in water, and therefore in heavy water, is of around 12 g/L, noting that solubility can however vary with the sample temperature. This means that our prototype LoD for glyphosate in water might be of the order of 1 g/L.

Should the field inhomogeneity worsen, or the temperature vary importantly, and should we contemplate an NMR experiment in which low concentrations of glyphosate are considered, *i.e.*, making mandatory the use of temporal averaging techniques, for instance FID

accumulation, would we observe the appearing of none or one peak spectra, instead of three peak ones, even employing targeted filtering. Indeed, for averaging with a not optimized setup, the resulting spectrum would become at the best a one peak spectrum where the external peaks would merge with the central one due to field drifting between scans and further shim-related changes. In worst case, there will be no peak left if the field drifting and the local changes in the field inhomogeneity between scans are more important. In such scenarios, the detection of the glyphosate molecule may be compromised.

Averaging in the frequency domain is with our current NMR Spectrometer Prototype setup also not effectively feasible because of the important field drifting between succeeding scans that shifts the peaks while eventually widening them as well. However, with a more stable setup concerning temperature drift, the heavy water peak may work well as a lock in mechanism, considering however that the intrinsic spectral resolution from the employed magnet and shim system must allow for peak distinction within the considered range, *i.e.*, approximately < 0.7 ppm, ideally even less. Finally, in what concerns peak spectral magnitudes from spectra acquired with our current prototypical setup, although they tend to grossly respect the same theoretical ratios - also found in the high-field measured spectra - in what concerns the spectral energy apportion among measured peaks, due to the steady temperature fluctuation and further spectral degradation caused by the inhomogeneity of $\overrightarrow{B_0}$, such comparison metrics is currently not reliable and should be merely considered as a matter of not-biding correctness indication instead of quantification estimation.

5.4. Esterification reaction monitoring

The second main application of concern for our prototype is the monitoring of chemical reactions. Monitoring chemical reactions via NMR spectroscopy means monitoring the change over time in the amplitudes of the spectral peaks, and occasionally also in the position of the chemical shifts. For the monitoring of a chemical reaction to be possible by employing NMR spectroscopy, there must be a sample containing a solution where there is a happening chemical reaction for which the changing in the different chemical shifts belonging to the chemical reaction related compounds are quantifiable over time. Important reaction factors to be considered when selecting the right experiment were the reaction time, the substrates solubility, an internal standard reference, as well as well-resolved reactants proton peaks [170]. For the assessment of our prototype on the monitoring of chemical reactions, an esterification reaction was chosen to be monitored because this kind of reaction was already proven to be successfully followed by a low-field 45 MHz benchtop NMR, although under specific circumstances and with limited results [99]. The chosen esterification reaction of carboxylic acid

($C_2H_4O_2$) and alcohol (C_2H_6O) catalysed by sulfuric acid (H_2SO_4) is usually followed by observing changes in the peak intensity of the respective proton peaks of ethanol and the ester and a moving chemical shift corresponding to the hydroxy group [170]. Figure 97 depicts the chemical description of the considered esterification reaction and its temporal monitoring with a high-field NMR spectrometer, with a time step of around 5 minutes between succeeding measurements.

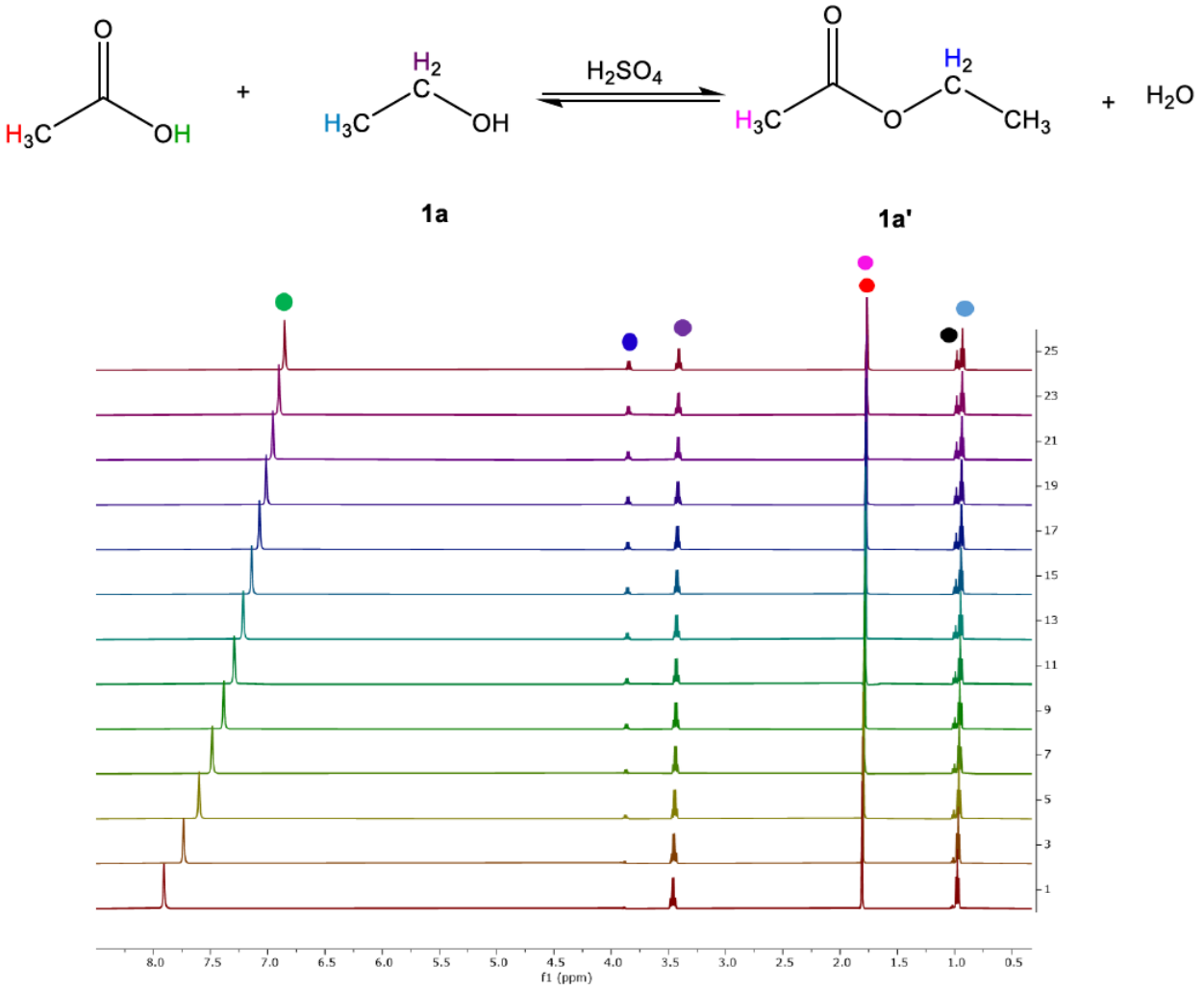

Figure 97 - Top side: starting material (left side) and product (right side), with highlighted reactants: ethanol (1a) and ester (1a'). Bottom side: superimposed set of ^{1}H NMR spectra from the esterification reaction, where the reaction progress from the bottom to the top with a measurement cadence of 5 minutes. ($CDCl_3$, 298.15 K, 500 MHz). Modified. [170]

This esterification reaction can be quantified by the temporal magnitude changes of the $–CH_2$ (purple dot at around 3.5 ppm) and $–CH_3$ (opaque blue dot at around 1 ppm) peaks of the ethanol and of the $–CH_2$ (intense blue dot at 3.9 ppm) and $–CH_3$ (pink dot at around 1.8 ppm) peaks of the ester. A chemical shift change of around 1 ppm is noticeable for the hydroxy group (moving green dot). Beginning with the starting material, this esterification reaction reaches an equilibrium at room temperature, although we limited the monitoring time to a total of around 2

hours. Within this monitoring time, the spectral magnitudes of the groups composing the ethanol and the ester presented the evolution depicted in Figure 98.

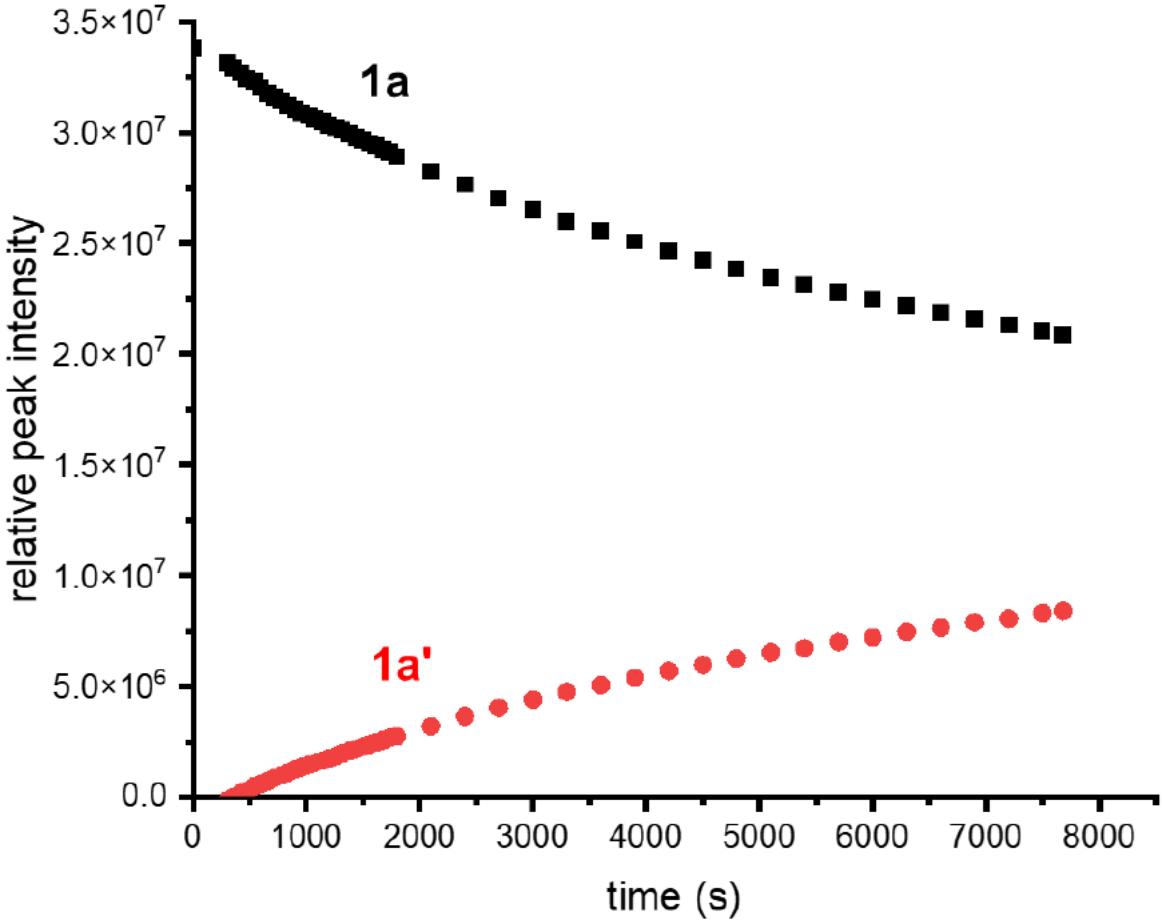

Figure 98 - Plot of relative peak intensity of reactants over the time as inferred from ^{1}H NMR monitoring for the considered esterification reaction at 25 °C. ($CDCl_3$, 298.15 K, 500 MHz). Modified. [170]

This same experiment, for the same duration, was performed as well using our NMR Spectrometer Prototype for acquiring the FIDs, with the only difference that the sample compartment had its temperature stabilized at 30 °C. Figure 99 illustrates the outcome for arbitrary chemical shift values.

From this preliminary drawing of the reaction monitoring, one can already see that there is an important drift of chemical shifts during the experiment time. This is due to the fact that temperature fluctuations from one scan to another, and also intra-scan depending on the behaviour of the temperature fluctuation, are in turn responsible for inducing $\overrightarrow{B_0}$ fluctuations, consequently engendering a shift of the chemical shift axis. This happens as well when employing the reference benchtop NMR from Pure Devices by itself and it is linked to its design, especially from the magnet compartment. Furthermore, a blatant overlapping of multiple contiguous peaks and spectral lines happen. Instead of being able to see at least 6 different spectral peaks as in Figure 97, we are left with only 3 peaks. Indeed, the magnet available at the reference benchtop NMR from Pure Devices, which has a $\overrightarrow{B_0}$ strength of around 550 mT, is

not suitable for peak resolving of less than 0.5 ppm. When considering the recurrent intra-scan temperature drifting, this limitation increases easily to 1 ppm or more due to the resulting widening of the spectral peaks, which often leads to peak merging. The overlapping of the spectral peaks complicates the reaction monitoring, as the peaks of reactants and of products mix with each other, leading to an approximately constant area under the observed peak. This happens because the increase of the product peak compensates the decrease of the reactant peak. Under these conditions, only the change in the shape of the resulting merged spectral peak could give a clue about the relative variation of the involved product and reactant individual peaks.

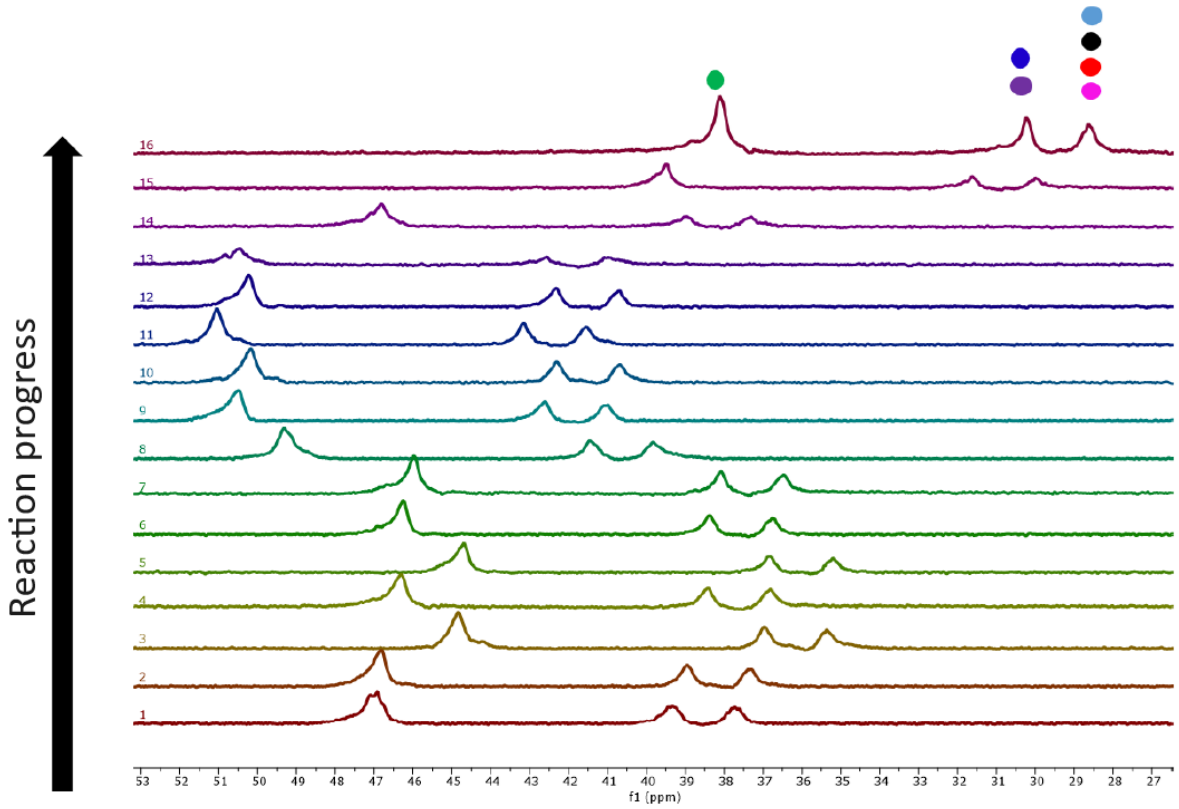

Figure 99 - Superimposed set of ^{1}H NMR spectra from the esterification reaction. (303.15 K, around 24.35 MHz, developed NMR Spectrometer Prototype). Arbitrary units. Modified. [170]

As concluded by the fellow project partner Chunchesh Malangi Gajendramurthy in his doctoral work [170], there should be a minimum of a 2 ppm chemical shift difference between the peaks of the starting material and the product, without any intervening peaks, in order for us to be able to visualize changes in the progress of the reaction using this Pure Devices magnet without requiring further dedicated signal post-processing, which could indeed enhance this peak resolving limitation. Anyways, this is important because it illustrate why the change in the chemical shift of the hydroxy group is not a reliable monitoring metric within the current setup.

To further exhaust the analysis possibilities of this outcome, we adjusted selected measurement plots corresponding to single acquisitions during this reaction monitoring experiment so that the proton peak with the smallest chemical shift of each plot would

superpose. And so, we tried to see if we could detect even a small deterministic change in the positioning of the superposed proton peaks with the greatest chemical shift, identified by the green dot in Figure 99. The selected 8 scans correspond to the following times relatively to the beginning of the esterification reaction and encompasses all the vital reaction moments, including late measures for comparison:

- $t_1 = 0$, the very beginning of the NMR experiment.
- $t_2 = 30\ min$, half an hour after t_1.
- $t_3 = 60\ min$, one hour after t_1.
- $t_4 = 90\ min$ after t_1.
- $t_5 = 120\ min$ after t_1.
- $t_6 = 210\ min$ after t_1.
- $t_7 \approx 2\ days$ after t_1.
- $t_8 \approx 6\ days$ after t_1.

As from Figure 98, we consider that at t_1, the sample solution is predominantly composed by the reaction reactants, while from t_7 it has already reached equilibrium. The acquired FID at the very beginning of the esterification reaction and the corresponding spectra are shown in Figure 100 as an illustration of the pursued analysis path.

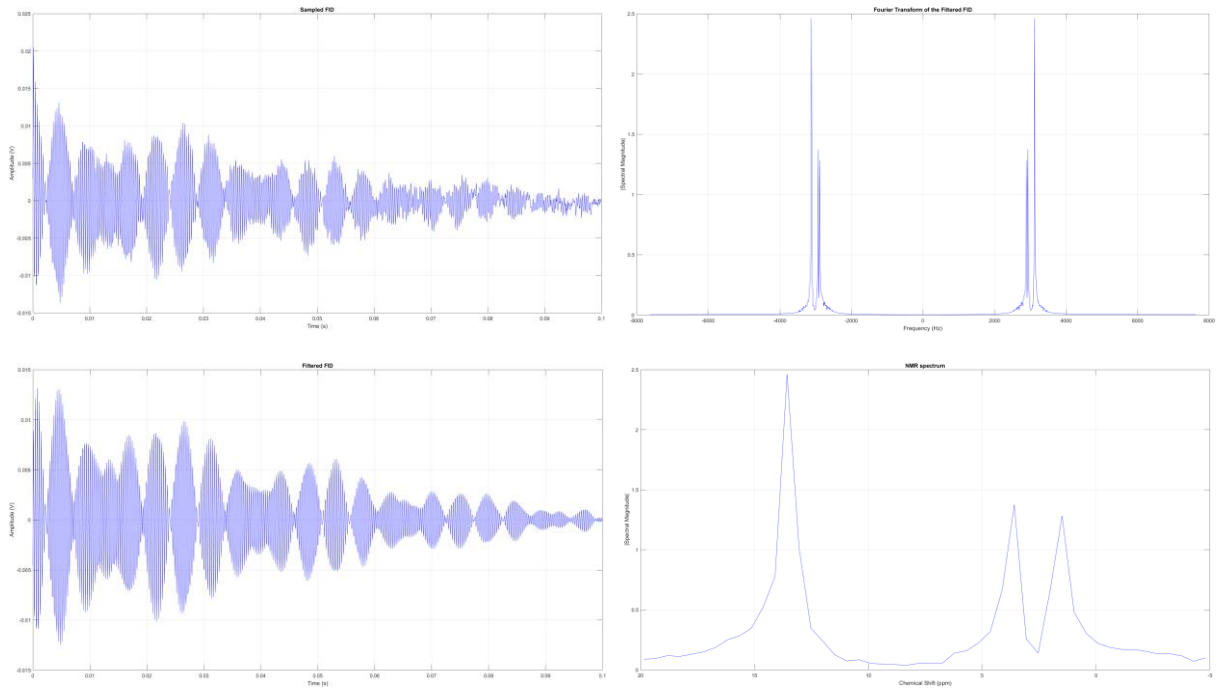

Figure 100 - Top side left: FID acquired with our NMR Spectrometer Prototype at the very beginning of the considered esterification reaction. Bottom side left: the FID after proper filtering. Top side right: the Fourier transform of the filtered FID. Bottom side right: the acquired NMR spectrum. (303.15 K, around 24.35 MHz, developed NMR Spectrometer Prototype)

Once all NMR spectra was available, a superposing 2D plot was performed for first visual evaluation, which can be seen in Figure 101.

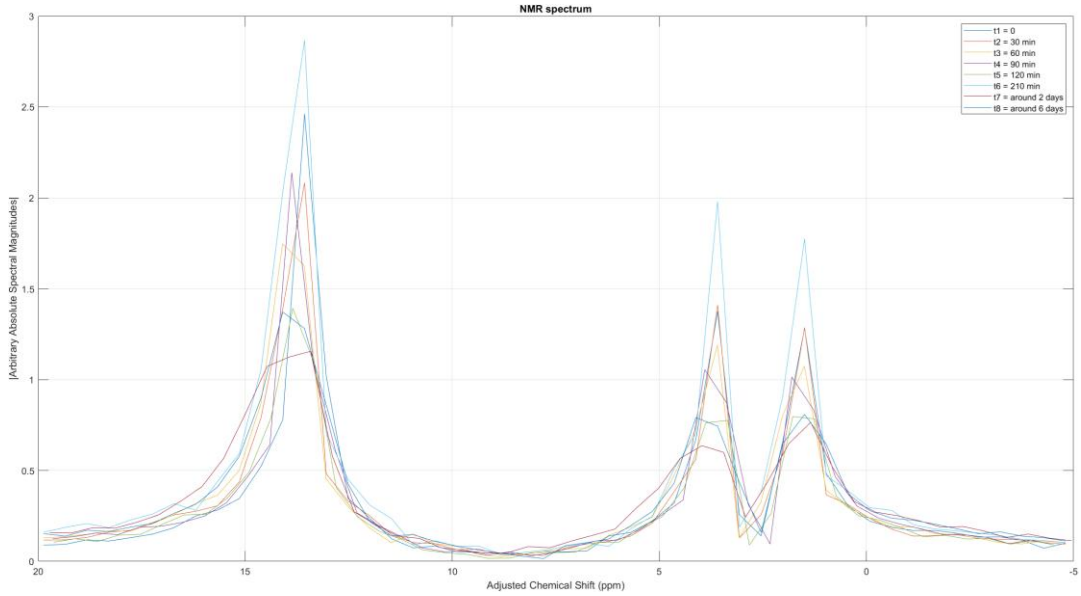

Figure 101 - 2D plot of the 8 considered scans, after peak alignment. (303.15 K, around 24.35 MHz, developed NMR Spectrometer Prototype)

The same plot was drawn in classic reaction monitoring format, which is presented in Figure 102.

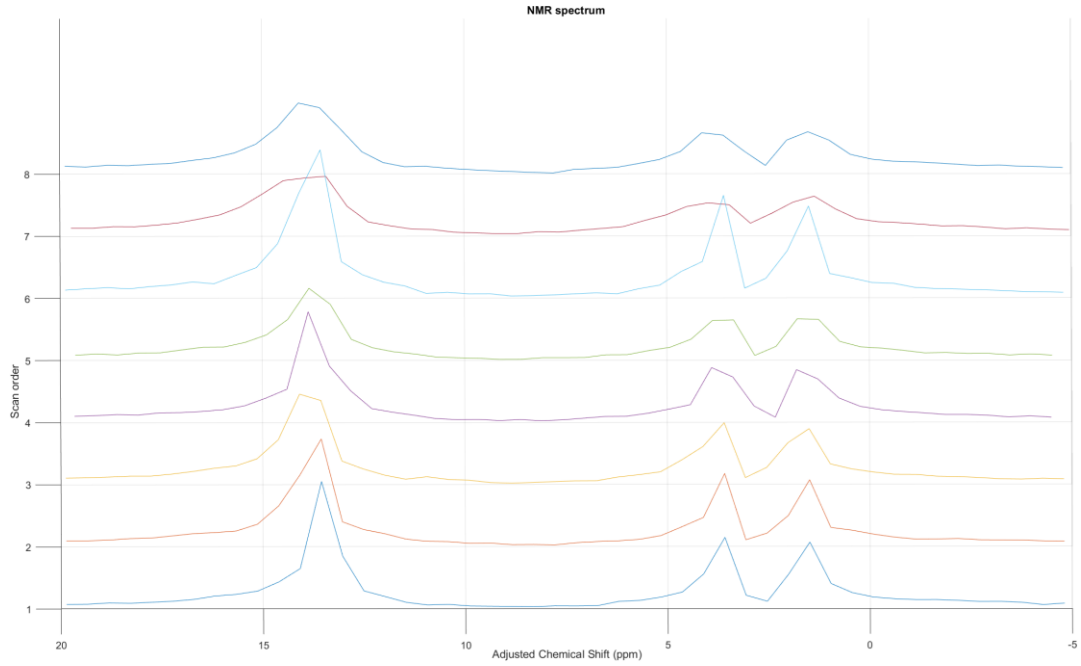

Figure 102 - 3D plot of the 8 considered scans, after peak alignment. (303.15 K, around 24.35 MHz, developed NMR Spectrometer Prototype)

It is confirmed that the poor spectral resolution and the field drifting do not allow for a successful esterification reaction monitoring: we cannot indisputably use the spectral magnitude to detect the reaction progress, nor can we observe the expected change in the chemical shift, even if looking at it in relative terms to the other spectral peaks. Because spectral magnitudes vary substantially among succeeding scans, we tried a final spectral analysis by standardizing

the spectral magnitudes, arbitrarily choosing to normalize the peak corresponding to the hydroxy group to the unity, and trying to detect if somehow the other peaks magnitudes would vary in the foreseen way. Figure 103 illustrates the 2D plot for the superposing magnitude-normalized NMR spectra.

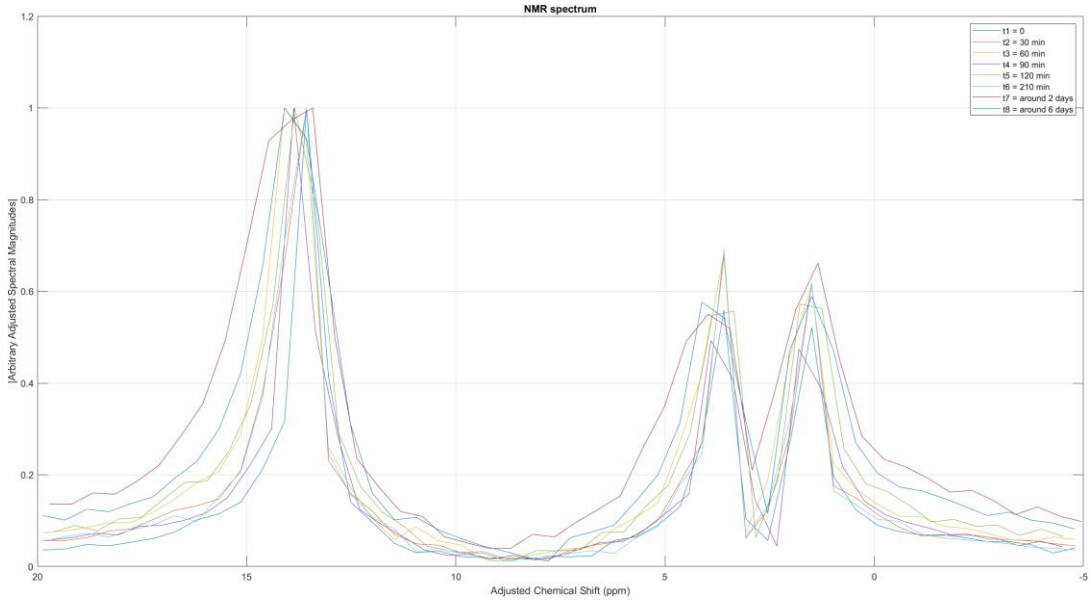

Figure 103 - 2D plot of the 8 considered scans, after magnitude normalization. (303.15 K, around 24.35 MHz, developed NMR Spectrometer Prototype)

Figure 104 depicts its 3D view in classic reaction monitoring format.

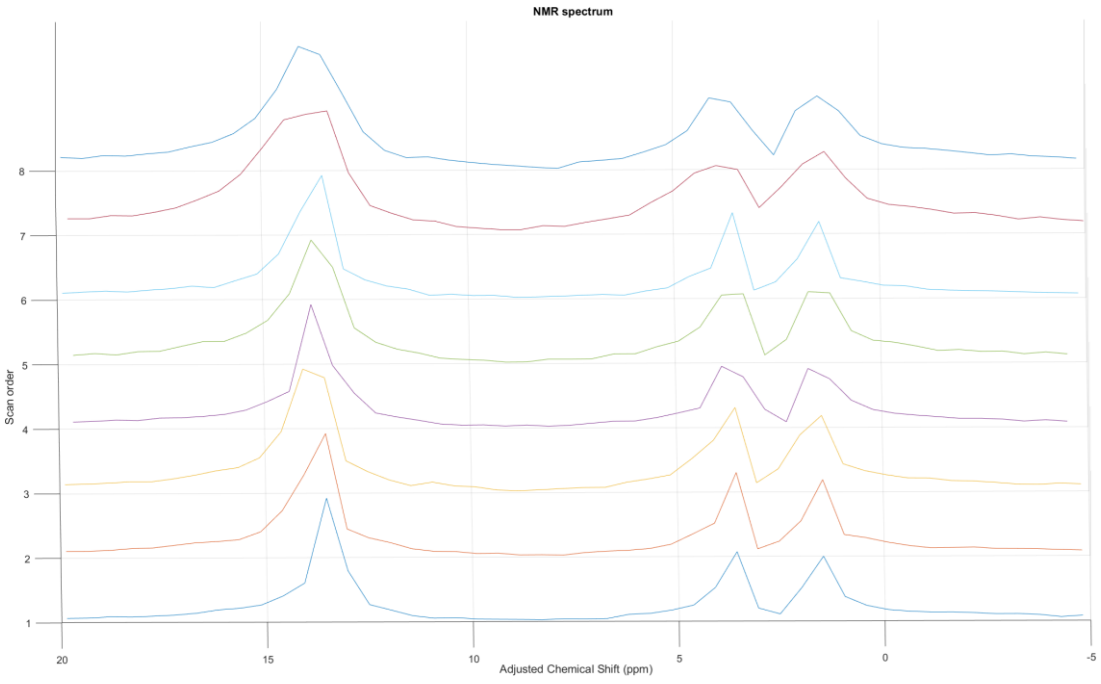

Figure 104 - 3D plot of the 8 considered scans, after magnitude normalization. (303.15 K, around 24.35 MHz, developed NMR Spectrometer Prototype)

Also here, no chemical shift change can be correctly detected. Furthermore, the field drifting seems to be so important during some acquisitions, as for instance the scans number 4,

5, 7 and 8, that the respective peaks become to start folding flat and a spectral magnitude comparison cannot be trustfully performed. Even the normalization of the peaks in such a degraded state does not seem to be a good way forward in what concerns a formal analysis step.

Although the changing spectral magnitude of the existing frequency peaks can be used as a reference of reaction progress, this metric is for the current development stage of our NMR Spectrometer Prototype much less reliable that the one using chemical shifts because, due to a few system-intrinsic characteristics, *e.g.*, field inhomogeneity, field drifting, and other experiment- and user-related possible reasons, *e.g.*, physical move of the sample tube between scans, re-shim, etc., the width of the frequency peaks can change. Since the spectral energy provided by an FID for the whole composing frequency elements cannot change, the alteration of the peaks widths engenders a related change in the spectral magnitude of the peaks. These changes are hardly quantifiable and such analysis approach is discouraged in the practice. Hence, the analysis of the temporal changes of the chemical shifts is preferred because it is more robust, specially within low-resolution NMR in a highly instable measurement environment. For that, however, the chemical shift change must be important enough so that it can be observed within the above-mentioned system design limitations.

5.5. Magnetic field drifting assessment

In partnership with the NMR analyst project fellow Chunchesh Malangi Gajendramurthy, a study of the recurrent fluctuation of the shimmed static magnetic field $\overrightarrow{B_0}$ was performed [170]. These results apply for both the reference benchtop NMR from Pure Devices working alone as well as for the combo NMR Spectrometer Prototype using the magnet and shim elements belonging to the reference benchtop NMR. For this study, the reference benchtop NMR from Pure Devices was considered alone and worked within its nominal characteristics: $B_0 \approx 550\,mT$ shimmed for the best homogeneity outcome, $T \approx 30$ °C constantly readjusted, and periodic acquisitions of an stable chemical compound in order to observe the changing in the measured chemical shift, which without field fluctuations, should be always the same. It is without saying that our low-field setup does not endue a lock unit for field fluctuation correction, as often is the case for high-field NMR equipment, which usually lock in on the deuterated solvent, in practice working as a reference for chemical shift corrections. For this experiment, our chosen chemical compound was water because it presents a single peak when analysed on ^{1}H NMR spectrometers, no matter the equipment resolution, and its NMR signal is relatively strong, being easy to acquire with single acquisitions. A total of 25 single acquisitions over two and a half hours were performed. Figure 105 illustrates the outcome of these measurements.

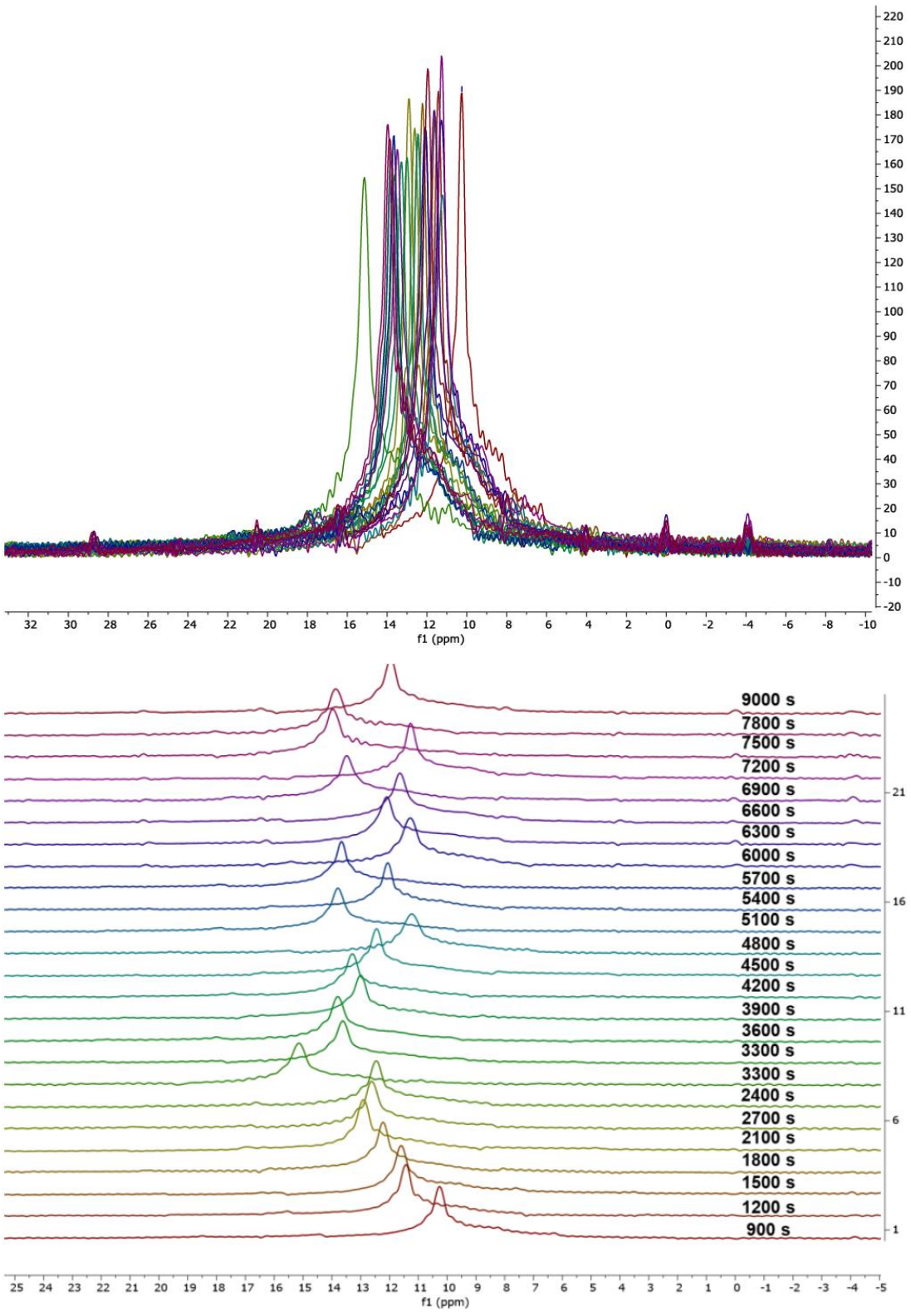

Figure 105 - Top side: the superposed 25 single acquisitions for water. Bottom side: the same 25 single acquisitions over time. (303.15 K, around 24.35 MHz, benchtop NMR from Pure Devices). Modified. [170]

The observed change in the chemical shift of the single peak is blatant. For this particular experiment, a change of the order of 5 ppm on a lab setting was already observed, and depending on the environment where the magnet module is placed, especially in the

outside, it can easily get worse. It is possible to see that the field drifting happens in a random manner around a central value and that its exact behaviour is not predictable. For well-resolved peaks, a software post-correction is feasible, however the spectral averaging of weak signals in this context cannot be effective.

NMR

As showed above, we currently employ a reference benchtop NMR system from the company Pure Devices, which provides our prototype with the static magnetic field $\overrightarrow{B_0}$, the shim system, the temperature control system, and typically the receiving coil. The main goal of this chapter was to explore the possibility of employing a low-field NMR system to address our both targeted applications (water quality measurement and chemical reaction monitoring) while as well validating our alternative low-cost electronic system. For that, acquisitions were made by employing the reference benchtop NMR from Pure Devices as a standalone system, as well as by replacing the control and processing related electronics of this reference benchtop NMR by our own prototype, therefore keeping only the static magnetic field $\overrightarrow{B_0}$ and the receiving coil of the Pure Devices system.

The reference system presents limitations that are in some cases decisive for the failure of some of our proposed validation NMR experiments. Such reference system is however a necessity until we are able to produce our own magnetic system composed by the prior quoted elements and is, in fact, a good emulation of the challenges that we will have emerge when trying outdoor measurements. The chosen processing unit from Red Pitaya, in the same way, is a nice and versatile piece of hardware, yet currently presenting some relatively minor limitations that are however crucial for the implementation of some of our acquisition methods. Nonetheless, our custom electronics works fine and is able to deliver what it was intended for. We demonstrated that the prototype in its current state can provide single-acquisition low-resolution NMR spectra for some raw materials, including when using a custom NMR receiving coil, it can detect glyphosate in a saturated solution of heavy water if experiment conditions are particularly favourable, and it might be able to monitor selected chemical reactions, although not the esterification reaction. Hardware improvements are clearly required in order to get better results out of it.

Despite such limitations, great preliminary results were already obtained with a pretty much low-cost NMR spectrometry system solution. We intend to develop it further so to enable low-field NMR spectrometry to be used in pollutants detection at typical concentrations in drinking water and chemical reaction monitoring of more relevant ones. In this perspective, the

next and final chapter highlights some of our future perspectives concerning our research efforts and intends to provide a non-exhaustive set of engineering requirements for the further development of our NMR Spectrometer Prototype, especially regarding the design experience gained during this doctoral work.

Chapter 6 - Discussions and conclusion

Great accomplishments were possible within the project engineering requirements boundaries. We were able to establish an entire support simulation chain encompassing many of the critical aspects of the NMR experiment from the perspective of the NMR spectrometer process design, starting with the simulation of the spectrometer electronics, through the evaluation and correction of imprecisions in the sampling process, up to the visualization of the impact of $\overrightarrow{B_0}$ inhomogeneities in the resulting NMR spectra. Furthermore, we advanced the state of our low-resolution, low-cost portable miniaturized NMR Spectrometer Prototype by incorporating into it a processing unit, making hardware improvements and circuit integration into its boards, and going further into coil design and production process, including impedance tuning. Among the NMR experiments that we were able to successfully perform with the current setup of our low-field NMR Spectrometer Prototype, we can cite the acquisition of ^{1}H NMR low-resolution spectra of: (1) strong signal raw materials, (2) including employing one of our self-made micro-coils, (3) a saturated solution of glyphosate in heavy water, and (4) the compounds of an esterification reaction, however without being able to monitor the progress of this specific reaction due to the setup intrinsic poor spectral resolution.

Nevertheless, the conception of such a portable miniaturized NMR spectrometer device, that additionally aims at being as low-cost as possible, is currently no trivial mission. As we could see in the previous chapters, many are the challenges that make its design and implementation an arduous task:

1. The duo homogeneity / inhomogeneity of $\overrightarrow{B_0}$ is probably the most critical aspect to be considered for the successful conception of an NMR spectrometer. Local field changes within the measurement gap, *i.e.*, within the receiving coil volume, can deform a spectrum in a variety of ways, producing general loss of spectral magnitude, peak merging, chemical shift shifting, etc. A good *per se* magnet makes the resulting use of a shim system all the more effective concerning the resulting homogeneity of $\overrightarrow{B_0}$.
2. Temperature-drifting is an important element to be taken into account, especially when measuring weak signals, which, in addition, eventually present frequency peaks with close central chemical shift values. The temperature, and therefore $\overrightarrow{B_0}$, *i.e.*, f_0, vary in accordance and can produce in-measurement FID frequency oscillations, producing peak merging and other forms of spectral degradation that will make the post-measurement analysis of the NMR spectra unfeasible. Temperature fluctuations among succeeding scans are commonplace within our current setup and make frequency-domain averaging unfeasible.

3. Receiving coil conception, although not the most critical part of the conception process, can usually be great optimized and improve the level of signal acquisition, by correctly optimizing its sensibility within a given measurement volume [3]. Here, two approaches are possible: use a tuned and matched resonator, as Pure Devices does and as we ourselves did for our self-made micro-coils, or employ untuned receiving coils [171].
4. The shim system must be constructed in accordance with the overall spectrometer setup and geometry, otherwise surprises are guaranteed to arise. From experience, inserting a different kind of receiving coil into the measurement gap can already make the automatic shimming process of the reference benchtop NMR from Pure Devices fail by not being able to find correct and acceptable shim current values within the possible designed equipment range. Without the best possible shim, the results obtained with the spectrometer device are usually deceptive, or even invalidating.
5. Low-cost electronic hardware limits our measurement resolution and precision, and thus the possibilities of satisfactorily implementing more sophisticated acquisition methods, *e.g.*, measurement averaging and in quadrature. As a rule of thumb, more precise electronic sampling architectures with bigger acquisition buffers being able to sample faster are always better technical options, impacting however the overall costs of the final designed equipment. Excitation and reference oscillation signal generation enjoys as well from employing better hardware by allowing the implementation of specific however flexible excitation techniques, especially for weak NMR signals. The use of low-cost electronics means as well that the minimal required quality of the generated excitation and reference oscillation signals at higher frequencies than that of our current Larmor frequency f_0 of around 24 MHz is hardly attained, which in turn limits the static magnetic field $\overrightarrow{B_0}$ to an intensity of about 550 mT. A possible better approach concerning the processing unit would be to conceive a dedicated embedded system able to run multiple channels in real time and with the required precision and clock, or to find an equivalent ready to use COTS alternative.

For the future improvement of our device, it is advised that specific measures be taken into consideration when designing or redesigning each of the listed topics above. While other engineering systems might be composed of functional elements that are somehow less dependent on each other and therefore present less mutual influence, providing therefore the possibility of classic conception based on V-shaped designing methodology as common industrial systems engineering practice, with less collateral effect introduced by eventually necessary redesign steps, an NMR spectrometer is more prone to the total invalidation of the developed work concerning its many system modules if only one of the critical functional blocks cannot perform correctly its intended role within a given set of system specifications.

Therefore, the following aspects concerning the minimal set of specification requirements for the given functional modules of interest is put forward to serve as the basis for the next improvement effort. It should be noticed the order in which, in our view, the development of the system should take place:

1. The magnetic system providing $\overrightarrow{B_0}$ may be the most complex element to be developed, considering that a high homogeneity is usually necessary for every useful use case application. In our considered NMR experiments, we saw that a spectral resolution allowing peak differentiation with less than 1 ppm was necessary for being able to distinguish between (1) a solution with pure water and water impregnated with glyphosate, and (2) an already finished esterification reaction and one happening. With the current setup, the first one was successfully accomplished due to favourable conditions allied to the fact that a single scan was necessary. When averaging or monitoring reactions, this spectral resolution requirement must be always respected in a stable manner, otherwise the resulting NMR analysis may be inconclusive. The final local inhomogeneity within the measurement volume does not depend only on the magnet, however the better the intrinsic homogeneity of this element, the more homogeneous it stays even after considering other influencing factors. Basically, even if some postprocessing could be applied to improve the spectral resolution, a 1 ppm requirement on the spectral resolution means a requirement of about 1 ppm concerning the maximal allowed static magnetic field inhomogeneity.
2. Temperature isolation of the measurement volume is as well highly important depending on the meant application of the developed spectrometer. We saw that in a relatively controlled indoor environment, *i.e.*, our labs, the temperature drift has an important impact on the resulting spectra and on the possibility of employing measurement accumulation techniques. Related field drifting for succeeding scans would make peaks shift of up to 5 ppm and even within an occurring acquisition, the peak shifting could attain 1 ppm or more. It is not without saying that on a hypothetical field employment of the NMR Spectrometer Prototype, *i.e.*, outdoors, under the sun or rain, in a windy environment, etc., these conditions would worsen, possibly by a lot. While high-field NMR spectrometers tend to cool down the magnet temperature, the reference benchtop NMR from Pure Devices elevates its magnet temperature to 30 °C and tries to keep it stabilized at this same temperature. Additionally, Pure Devices benchtop NMR presents no dedicated comprehensive thermal isolation of the measurement volume. For many applications it may be a valid setup, especially when always considering an indoor employment environment, however we must ensure that temperature drifting be much less impactful. One can look at equation (11) from another perspective and see that isolating B_0, it becomes a function of the measurement volume temperature. The Larmor

and the resulting NMR signal frequency being related to $\overrightarrow{B_0}$ as in equation (1), one can directly understand what happens with the excitation and measured signals by varying the temperature. Although it is conceptually easy to understand the impact of this varying temperature on the frequency components of the involved signals, monitor the effective temperature change within the measurement volume and correct the acquired spectra accordingly is practically inviable: the temperature might change from one position to the other and thus it has to be measured very accurately and at different positions. Moreover, the very fact of inserting a temperature measuring device within the measurement volume automatically affects the local homogeneity of $\overrightarrow{B_0}$ and impacts the effectiveness of the current shim and the setting up of a new one, potentially bringing more harm than good overall. The design of an appropriate temperature isolated setup to keep field drifting less than at least 1 ppm seems to be the most convenient to be pursued. Depending on future applications, this value must be reviewed to an even smaller one.

3. The design of self-made miniaturized receiving coils must take into account the setup measurement gap geometry and be sensibility-optimized to the considered sample volume. As basically anything that is inserted within the measurement gap, the receiving coil impacts the already existing inhomogeneity of $\overrightarrow{B_0}$, even if only in a limited fashion. The minimization of this impact by selecting the most suitable design geometry and material may be of interest for future work. As may be the possibility of choosing to tune it to a specific impedance value, *e.g.*, 50 Ω, or employ an untuned approach, for instance a high-impedance one.
4. The shim system perceives the existing magnetic field within the measurement gap as the raw magnetic field produced by the magnetic system, however locally deteriorated by the many elements that somehow influence it: (1) the sample itself, (2) the receiving coil, (3) the varying temperature within the measurement volume, and (4) other external sources of magnetic disturbance. Shim systems can be implemented in a variety of manners and can be of multiple orders, which will engender more complex design choices and processing power. Once the previous design points were addressed in the best way possible, the design of the shim system comes into play and is adjusted for the necessary field correction it must effectuate considering the targeted application. In other words, with the correct design of the shim system, we correct the resulting magnetic field (raw field from the magnet, degraded by disturbing sources) by bringing the existing local field inhomogeneity down to a certain level. This level is experiment related and must be made beforehand a clear system requirement in order to guide the whole design process. For some of our current considered NMR experiments, a spectral resolution of less than 1 ppm was mandatory and limited somehow the results we were

able to produce, especially taking into consideration limitations of other system parts, *i.e.*, temperature drifting, sampling and excitation imprecisions, etc.

5. The processing unit must be chosen by taking into account which tasks are required from it and how good it must perform them. The foreseeable tasks to be undertaken are: (1) the communication with the host computer and the associated transfer from experiment data, (2) the generation of the local oscillator signal for the electronic mixer, (3) the flexible generation of the excitation signal at Larmor's frequency, (4) the sampling of the measured and down-converted NMR signal, (5) the implementation of averaging techniques, (6) the parallel acquisition in quadrature, and (7) the setting up and control of the shim system. The sampling resolution and the sampling rate are key factors when talking about the acquisition procedure, as it is the size of the acquisition buffer and the capability of parallel-sampling two input channels in real time without any kind of dead times. Because of the known limitations of our current employed processing unit in terms of the size of its sampling buffer, we had to work with down-conversion frequencies of the order of the unit of kHz, usually within the range 1 to 2 kHz, even meaning that we consequently decreased the resulting SNR, because close to 0 Hz noise dominates the game. For a given limited-in-time NMR signal, there is a coupled choice between selecting a not so low down-conversion frequency and the related increase in the necessary sampling rate and buffer size of the processing unit in order to properly sample this incoming signal. Also to be noticed is that the resulting spectral resolution due to the sampling resolution of the processing unit should preferably be as good as the effective spectral resolution due to the resulting magnetic field $\overrightarrow{B_0}$, but not necessarily better than it, because it would not be useful and would only engender higher costs related to the selection of a more expensive than necessary processing unit. The ideal characteristics of the processing unit are highly dependent on the characteristics of the NMR signal to be acquired, and these are in turn a direct consequence of the quality of $\overrightarrow{B_0}$, since the increase in the field inhomogeneity can greatly reduce the FID duration through T_2^*, as from equation (4), as well as worsen spectral resolution overall. Considering the generation of the mixer reference down-conversion signal and of the excitation one, these must be provided with minimal quality requirements at the considered Larmor frequency so that the implementation of averaging techniques can be viable. A given NMR experiment, when executed repeatedly in the exact same manner under the exact same surrounding physical conditions, will produce the exact same outcome, and this is the basis for the implementation of temporal signal averaging. It means that the local oscillator signal for the mixer must be provided in a well-defined synchronized timely manner respectively to the excitation signal, and that this excitation signal must respect minimal shape-related

characteristics considering the produced waveform, including enough precise and well-defined beginning and end of the excitation bursts. Once this whole set of excitation-related requirements can be fulfilled, the sampling must as well start each time in a precise enough and stable manner. These precision boundaries depend on the NMR signal characteristics, as previously described. Finally, the picked processing unit must be able to perform shim related tasks, including retrieving the optimal shim currents by means of, for example, recurring FID estimation or another optimization method of adjustment of shim field correction, and posteriorly operate the shim system during the execution of the NMR experiments. Therefore, it is said that, if the final cost of the system is a major design factor from the very beginning of the design phase, the processing unit must be the last element to be pitched, because it can be adjusted to the effective performance quality of the other composing elements. If, however, the system costs are secondary, especially during the prototyping phase, a high-performance processing unit may be first used during development and then later one it might be downgraded following the equipment effective final characteristics, so to optimize the final system overall cost.

As a general design-related remark, possibly the best development approach of such NMR spectrometers is to first design the measurement chamber with the magnet and the temperature control system, and the receiving and the shim coils, based on solid engineering requirements which are derived from the concrete intended applications. The further design of the electronics and the processing unit may be more easily adaptable to these physical system elements. It allows one to choose then its minimal requirements and economize in regard to the overall equipment cost. To speed up the development phase, the ideal is to choose better-than-necessary electronic hardware elements and adjust them for product release after successful prototype validation.

Regarding our considered applications, we could demonstrate that low-resolution ^{1}H NMR spectroscopy is capable of detecting glyphosate in water under specific circumstances as well as monitoring selected chemical reactions. Although the use cases put forward are not quite the most realistic ones, they are proof that our developed low-resolution NMR Spectrometer Prototype can be successfully employed in such NMR analysis scenarios. And with further targeted improvements it may be possible to employ it fully in everyday field NMR analysis assignments of actual real daily situations.

Bibliography

[1] S. S. Zalesskiy, E. Danieli, B. Blümich and V. P. Ananikov, “Miniaturization of NMR Systems: Desktop Spectrometers, Microcoil Spectroscopy, and “NMR on a Chip” for Chemistry, Biochemistry, and Industry,” *Chemical Reviews,* vol. 114, no. 11, pp. 5641-5694, 2014.

[2] D.-V. Nguyen, *Portable nuclear magnetic resonance spectroscopy probe,* Strasbourg: École doctorale des mathématiques, sciences de l'information et de l'ingénieur (MSII), 2020.

[3] L. Werling, *Contribution to the integration of a high resolution needle probe for localized nuclear magnetic resonance spectroscopy,* Strasbourg: École doctorale des mathématiques, sciences de l'information et de l'ingénieur (MSII), 2022.

[4] Pure Devices GmbH, “Benchtop MRI Systems,” [Online]. Available: https://www.pure-devices.com/.

[5] P. K. Tyagi, A. Arya, S. Ramniwas and S. Tyagi, “Editorial: Recent trends in nanotechnology in precision and sustainable agriculture,” *Frontiers in Plant Science,* vol. 14, no. 1256319, 2023.

[6] A. du Plessis, "Persistent degradation: Global water quality challenges and required actions," *One Earth,* vol. 5, no. 2, pp. 129-131, 2022.

[7] European Commission and European Environment Agency (EEA), “Water bodies failing to achieve Good Surface water status, by RBD,” Water Information System for Europe (WISE), [Online]. Available: https://water.europa.eu/freshwater/resources/metadata/dashboards/ecological-status/water-bodies-failing-to-achieve-good-surface-water-status-by-rbd.

[8] J. von Gönner, D. E. Bowler, J. Gröning, A.-K. Klauer, M. Liess, L. Neuer and A. Bonn, “Citizen science for assessing pesticide impacts in agricultural streams,” *Science of The Total Environment,* vol. 857, no. 159607, 2023.

[9] O. Weisner, J. Arle, L. Liebmann, M. Link, R. B. Schäfer, A. Schneeweiss, V. C. Schreiner, P. Vormeier and M. Liess, “Three reasons why the Water Framework Directive (WFD) fails to identify pesticide risks,” *Water Research,* vol. 208, no. 117848, 2022.

[10] E. W. A. Visser, J. Yan, L. J. van IJzendoorn and M. W. J. Prins, “Continuous biomarker monitoring by particle mobility sensing with single molecule resolution,” *Nature Communications,* vol. 9, no. 2541, 2018.

[11] A. D. Buskermolen, Y.-T. Lin, L. van Smeden, R. B. van Haaften, J. Yan, K. Sergelen, A. M. de Jong and M. W. J. Prins, “Continuous biomarker monitoring with single molecule resolution by measuring free particle motion,” *Nature Communications,* vol. 13, no. 6052, 2022.

[12] L. Carvalho, E. B. Mackay, A. C. Cardoso, A. Baattrup-Pedersen, S. Birk, K. L. Blackstockf, G. Borics, A. Borja, C. K. Feld, M. T. Ferreira, L. Globevnik, B. Grizzetti, S. Hendry, D. Heringe, M. Kelly, S. Langaas, K. Meissner, Y. Panagopoulos, E. Penning, J. Rouillard, S. Sabater, U. Schmedtje, B. M. Spears, M. Venohr, W. van de Bund and A. L. Solheim, “Protecting and restoring Europe's waters: An analysis of the future development needs of the Water Framework Directive,” *Science of The Total Environment,* vol. 658, pp. 1228-1238, 2019.

[13] S. Wuijts, P. P. J. Driessen and H. F. M. W. Van Rijswick, “Governance Conditions for Improving Quality Drinking Water Resources: the Need for Enhancing Connectivity,” *Water Resources Management,* vol. 32, p. 1245–1260, 2018.

[14] M. Z. Bieroza, R. Bol and M. Glendell, “What is the deal with the Green Deal: Will the new strategy help to improve European freshwater quality beyond the Water Framework Directive?,” *Science of The Total Environment,* vol. 791, no. 148080, 2021.

[15] J. Ruiz-Toledo, R. Castro, N. Rivero-Pérez, R. Bello-Mendoza and D. Sánchez, "Occurrence of Glyphosate in Water Bodies Derived from Intensive Agriculture in a Tropical Region of Southern Mexico," *Bulletin of Environmental Contamination and Toxicology,* vol. 93, pp. 289-293, 2014.

[16] S. Kanwal, M. A. Khan, S. Saleem, M. N. Tahir, S. T. Muntaha, T. Samreen, S. Javed, M. Z. Nazir and B. Shahzad, "Integration of Precision Agriculture Techniques for Pest Management," *Environmental Sciences Proceedings,* vol. 23, no. 1, p. 19, 2022.

[17] US EPA, "U.S. Environmental Protection Agency," [Online]. Available: https://www.epa.gov/.

[18] European Commission, "Food Safety," [Online]. Available: https://food.ec.europa.eu/.

[19] BAFU, "Bundesamt für Umwelt," [Online]. Available: https://www.bafu.admin.ch/.

[20] ©2024 Valent U.S.A. LLC, "Asana® XL Insecticide | Valent," [Online]. Available: https://www.valent.com/products/asana-xl.

[21] © 2002-2023 Bayer Group., "Weed Control | Roundup," [Online]. Available: https://roundup.com/en-us/home.

[22] ©2022 Environmental Science U.S. Inc., "Harmonix Rodent Paste," [Online]. Available: https://www.uk.envu.com/pest-management/harmonix-rodent-paste.

[23] © 2024 BioSafe Systems, LLC., "SaniDate® 16.0 WWT - BioSafe Systems," [Online]. Available: https://biosafesystems.com/product/sanidate-16-wwt/.

[24] © Bayer AG, "Aliette® WG Systemic Fungicide | Bayer Crop Science," [Online]. Available: https://www.crop.bayer.com.au/products/fungicides/aliette-wg-systemic-fungicide.

[25] © BASF SE 2024, "Abate® Larvicides," [Online]. Available: https://agriculture.basf.com/global/en/business-areas/public-health/products/abate.html.

[26] V. M. Pathak, V. K. Verma, B. S. Rawat, B. Kaur, N. Babu, A. Sharma, S. Dewali, M. Yadav, R. Kumari, S. Singh, A. Mohapatra, V. Pandey, N. Rana and J. M. Cunill, "Current status of pesticide effects on environment, human health and it's eco-friendly management as bioremediation: A comprehensive review," *Frontiers in microbiology,* vol. 13, no. 962619, 2022.

[27] R. L. Kellogg, R. F. Nehring, A. Grube, D. W. Goss and S. Plotkin, Agricultural Productivity - Chapter: Environmental Indicators of Pesticide Leaching and Runoff from Farm Fields, Boston, MA: Springer, 2002.

[28] IARC Monographs on the Evaluation of Carcinogenic Risks to Humans, Some Organophosphate Insecticides and Herbicides, IARC Monographs Working Group, 2017.

[29] Minnesota Department of Health - Health Risk Assessment Unit, "Glyphosate and Drinking Water," October 2017. [Online]. Available: https://www.health.state.mn.us/communities/environment/risk/docs/guidance/gw/glyphosateinfo.pdf.

[30] C. Panis, L. Z. P. Candiotto, S. C. Gaboardi, S. Gurzenda, J. Cruz, M. Castro and B. Lemos, "Widespread pesticide contamination of drinking water and impact on cancer risk in Brazil," *Environment International,* vol. 165, no. 107321, 2022.

[31] Z. Wang, G. W. Walker, D. C. G. Muir and K. Nagatani-Yoshida, "Toward a Global Understanding of Chemical Pollution: A First Comprehensive Analysis of National and Regional Chemical Inventories," *Environmental Science and Technology,* vol. 54, no. 5, pp. 2575-2584, 2020.

[32] European Commission, "Water - European Commission," [Online]. Available: https://environment.ec.europa.eu/topics/water_en.

[33] European Commission, *Directive 2000/60/EC of the European Parliament and of the Council of 23 October 2000 establishing a framework for Community action in the field of water policy,* Official Journal, 2000.

[34] European Commission, *Directive 2006/118/EC of the European Parliament and of the Council of 12 December 2006 on the protection of groundwater against pollution and deterioration,* Official Journal of the European Union, 2006.

[35] European Commission, *Directive 2008/105/EC of the European Parliament and of the Council of 16 December 2008 on environmental quality standards in the field of water policy,* Official Journal of the European Union, 2008.

[36] European Commission, “Proposal for a Directive amending the Water Framework Directive, the Groundwater Directive and the Environmental Quality Standards Directive,” [Online]. Available: https://environment.ec.europa.eu/publications/proposal-amending-water-directives_en.

[37] S. N. Zulkifli, H. A. Rahim and W.-J. Lau, “Detection of contaminants in water supply: A review on state-of-the-art monitoring technologies and their applications,” *Sensors and Actuators B: Chemical,* vol. 255, no. 3, pp. 2657-2689, 2018.

[38] J. Berberich, T. Li and E. Sahle-Demessie, “Chapter 11 - Biosensors for Monitoring Water Pollutants: A Case Study With Arsenic in Groundwater,” *Separation Science and Technology,* vol. 11, pp. 285-328, 2019.

[39] G. Russo, S. Laneri, R. Di Lorenzo, I. Neri, I. Dini, R. Ciampaglia and L. Grumetto, “Monitoring of Pollutants Content in Bottled and Tap Drinking Water in Italy,” *Molecules,* vol. 27, no. 13, p. 3990, 2022.

[40] S. O. Duke and S. B. Powles, “Glyphosate: a once-in-a-century herbicide,” *Pest Management Science,* vol. 64, no. 4, pp. 319-325, 2008.

[41] European Commission, *Commission IR (EU) 2023/2660 of 28 November 2023 renewing the approval of the active substance glyphosate in accordance with Regulation (EC) No 1107/2009 of the European Parliament and of the Council and amending Commission IR (EU) No 540/2011,* Official Journal of the European Union, 2023.

[42] J. Raich, “Review of sensors to monitor water quality. ERNCIP thematic area Chemical & Biological Risks in the Water Sector. Deliverable 1 - Task 1,” Publications Office of the European Union, Luxembourg (Luxembourg), 2013.

[43] C. Vélot, F. Poitou and J. S. de Vendômois, "Comparative analysis of detection techniques for glyphosate in urine and in water," *Environmental Sciences Europe,* vol. 34, no. 59, 2022.

[44] H. Moldovan, S. Imre, R. C. Duca and L. Farczádi, "Methods and Strategies for Biomonitoring in Occupational Exposure to Plant Protection Products Containing Glyphosate," *International Journal of Environmental Research and Public Health,* vol. 20, no. 4, p. 3314, 2023.

[45] H. Zhang, X. Liu, Z. Huo, H. Sun, F. Zhang and B. Zhu, "An ion chromatography tandem mass spectrometry (IC-MS/MS) method for glyphosate and amino methyl phosphoric acid in serum of occupational workers," *Microchemical Journal,* vol. 170, no. 106614, 2021.

[46] A. L. Valle, F. C. C. Mello, R. P. Alves-Balvedi, L. P. Rodrigues and L. R. Goulart, "Glyphosate detection: methods, needs and challenges," *Environmental Chemistry Letters,* vol. 17, p. 291–317, 2019.

[47] S. J. Dickson, R. H. Meinhold, I. D. Beer and T. D. Koelmeyer, “Rapid Determination of Glyphosate in Postmortem Specimens Using 31P NMR,” *Journal of Analytical Toxicology,* vol. 12, no. 5, pp. 284-286, 1988.

[48] B. Cartigny, N. Azaroual, M. Imbenotte, D. Mathieu, G. Vermeersch, J. P. Goullé and M. Lhermitte, “Determination of glyphosate in biological fluids by 1H and 31P NMR spectroscopy,” *Forensic Science International,* vol. 143, no. 2-3, pp. 141-145, 2004.

[49] K. D. Thelen, E. P. Jackson and D. Penner, “2,4-D Interactions with Glyphosate and Sodium Bicarbonate,” *Weed Technology,* vol. 9, no. 2, pp. 301-305, 1995.

[50] X. Ge, D. A. d'Avignon, J. J. H. Ackerman and R. D. Sammons, “In Vivo 31P-Nuclear

Magnetic Resonance Studies of Glyphosate Uptake, Vacuolar Sequestration, and Tonoplast Pump Activity in Glyphosate-Resistant Horseweed," *Plant Physiology,* vol. 166, no. 3, pp. 1255-1268, 2014.

[51] D. A. d'Avignon and X. Ge, "In vivo NMR investigations of glyphosate influences on plant metabolism," *Journal of Magnetic Resonance,* vol. 292, pp. 59-72, 2018.

[52] E. Shumilina, C. Andreasen, Z. Bitarafan and A. Dikiy, "Determination of Glyphosate in Dried Wheat by 1H-NMR Spectroscopy," *Molecules,* vol. 25, no. 7, p. 1546, 2020.

[53] G. S. Jacob, J. Schaefer, E. O. Stejskal and R. A. McKay, "Solid-state NMR Determination of Glyphosate Metabolism in a Pseudomonas sp.," *Journal of Biological Chemistry,* vol. 260, no. 10, pp. 5899-5905, 1985.

[54] European Commission, "Horizon 2020," [Online]. Available: https://research-and-innovation.ec.europa.eu/funding/funding-opportunities/funding-programmes-and-open-calls/horizon-2020_en.

[55] European Commission, "Horizon 2020," [Online]. Available: https://wayback.archive-it.org/12090/20220216161414/https://ec.europa.eu/programmes/horizon2020/.

[56] European Commission, "Horizon Europe," [Online]. Available: https://research-and-innovation.ec.europa.eu/funding/funding-opportunities/funding-programmes-and-open-calls/horizon-europe_en.

[57] Ministère de l'Enseignement supérieur et de la Recherche, "Stratégie nationale de recherche," [Online]. Available: https://www.enseignementsup-recherche.gouv.fr/fr/strategie-nationale-de-recherche.

[58] NIOK, "NIOK Website," [Online]. Available: https://niok.nl/.

[59] VIRAN, "Viran Website | The Associaton of the Industrial Advisory Board of NIOK," [Online]. Available: https://viran.nl/.

[60] M. H. Keller, R. Moreira and B. S. Souza, "Automated monitoring the kinetics of homogeneous and heterogeneous chemical processes using a smartphone," *Scientific Reports,* vol. 12, no. 15774, 2022.

[61] Y. Zhang, J. Wang, Y. Wang and K. Zhao, "In-situ real-time monitoring of chemical kinetics by an automated micro-reaction device," *Sensors and Actuators: B. Chemical,* vol. 392, no. 134069, 2023.

[62] K. J. Buschow, M. C. Flemings, E. J. Kramer, P. Veyssière, R. W. Cahn, B. Ilschner and S. Mahajan, Encyclopedia of Materials: Science and Technology, Pergamon: Elsevier Ltd., 2001.

[63] G. M. Fernandes, W. R. Silva, D. N. Barreto, R. S. Lamarca, P. C. F. L. Gomes, J. F. d. S. Petruci and A. D. Batista, "Novel approaches for colorimetric measurements in analytical chemistry – A review," *Analytica Chimica Acta,* vol. 1135, pp. 187-203, 2020.

[64] R. Wang, A. Prabhakar, R. A. Iglesias, X. Xian, X. Shan, F. Tsow, E. S. Forzani and N. Tao, "A Microfluidic-Colorimetric Sensor for Continuous Monitoring of Reactive Environmental Chemicals," *IEEE Sensors Journal,* vol. 12, no. 5, pp. 1529-1535, 2012.

[65] T. L. Doane, K. J. Cruz, T.-H. Chiang and M. M. Maye, "Using the Photoluminescence Color Change in Cesium Lead Iodide Nanoparticles to Monitor the Kinetics of an External Organohalide Chemical Reaction by Halide Exchange," *ACS Nanoscience Au,* vol. 3, no. 5, pp. 418-423, 2023.

[66] C. Lin, Y. Zhu, J. Yu, X. Qin, X. Xian, F. Tsow, E. S. Forzani, D. Wang and N. Tao, "Gradient-Based Colorimetric Sensors for Continuous Gas Monitoring," *Analytical Chemistry,* vol. 90, no. 8, pp. 5375-5380, 2018.

[67] A. Ray, T. Bristow, C. Whitmore and J. Mosely, "On-line reaction monitoring by mass spectrometry, modern approaches for the analysis of chemical reactions," *Mass Spectrometry Reviews,* vol. 37, no. 4, p. 565–579, 2018.

[68] J. Sun, Y. Yin, W. Li, O. Jin and N. Na, "Chemical reaction monitoring by ambient mass spectrometry," *Mass Spectrometry Reviews,* vol. 41, no. 1, pp. 70-99, 2022.

[69] P. Bergveld, "Development of an Ion-Sensitive Solid-State Device for Neurophysiological Measurements," *IEEE Transactions on Biomedical Engineering,* Vols. BME-17, no. 1, pp. 70-71, 1970.

[70] P. Bergveld, "Thirty years of ISFETOLOGY: What happened in the past 30 years and what may happen in the next 30 years," *Sensors and Actuators B: Chemical,* vol. 88, no. 1, pp. 1-20, 2003.

[71] Y. Hu and P. Georgiou, "A Robust ISFET pH-Measuring Front-End for Chemical Reaction Monitoring," *IEEE Transactions on Biomedical Circuits and Systems,* vol. 8, no. 2, pp. 177-185, 2014.

[72] L. Van der Schueren and K. De Clerck, "Coloration and application of pH-sensitive dyes on textile materials," *Coloration Technology,* vol. 128, no. 2, pp. 82-90, 2012.

[73] © 2023 by the U.S. Secretary of Commerce on behalf of the United States of America., "Toluene," [Online]. Available: https://webbook.nist.gov/cgi/cbook.cgi?Name=Toluene&Units=SI&cMS=on.

[74] S. Pandey, G. K. Goswami and K. K. Nanda, "Nanocomposite based flexible ultrasensitive resistive gas sensor for chemical reactions studies," *Scientific Reports,* vol. 3, no. 2082, 2013.

[75] M. Khajeh, M. A. Bernstein and G. A. Morris, "A simple flowcell for reaction monitoring by NMR," *Magnetic resonance in chemistry,* vol. 48, no. 7, pp. 516-522, 2010.

[76] K. H. Ebrahimi, P.-L. Hagedoorn, D. Jacobs and W. R. Hagen, "Accurate label-free reaction kinetics determination using initial rate heat measurements," *Scientific Reports,* vol. 5, no. 16380, 2015.

[77] M. J. Jaroszewicz, M. Liu, J. Kim, G. Zhang, Y. Kim, C. Hilty and L. Frydman, "Time- and site-resolved kinetic NMR for real-time monitoring of off-equilibrium reactions by 2D spectrotemporal correlations," *Nature Communications,* vol. 13, no. 833, 2022.

[78] A. Brächer, R. Behrens, E. von Harbou and H. Hasse, "Application of a new micro-reactor 1H NMR probe head for quantitative analysis of fast esterification reactions," *Chemical Engineering Journal,* vol. 306, pp. 413-421, 2016.

[79] F. Dalitz, M. Cudaj, M. Maiwald and G. Guthausen, "Process and reaction monitoring by low-field NMR spectroscopy," *Progress in Nuclear Magnetic Resonance Spectroscopy,* vol. 60, pp. 52-70, 2012.

[80] S. Kern, K. Meyer, S. Guhl, P. Gräßer, A. Paul, R. King and M. Maiwald, "Online low-field NMR spectroscopy for process control of an industrial lithiation reaction—automated data analysis," *Analytical and Bioanalytical Chemistry,* vol. 410, p. 3349–3360, 2018.

[81] D. Bouillaud, D. Drouin, B. Charrier, C. Jacquemmoz, J. Farjon, P. Giraudeau and O. Gonçalves, "Using benchtop NMR spectroscopy as an online non-invasive in vivo lipid sensor for microalgae cultivated in photobioreactors," *Process Biochemistry,* vol. 93, pp. 63-68, 2020.

[82] A. Friebel, E. von Harbou, K. Münnemann and H. Hasse, "Online process monitoring of a batch distillation by medium field NMR spectroscopy," *Chemical Engineering Science,* vol. 219, no. 115561, 2020.

[83] C. Claaßen, K. Mack and D. Rother, "Benchtop NMR for Online Reaction Monitoring of the Biocatalytic Synthesis of Aromatic Amino Alcohols," *ChemCatChem,* vol. 12, no. 4, p. 1190–1199, 2020.

[84] S. T. Knox, S. Parkinson, R. Stone and N. J. Warren, "Benchtop flow-NMR for rapid online monitoring of RAFT and free radical polymerisation in batch and continuous reactors," *Polymer Chemistry,* vol. 10, pp. 4774-4778, 2019.

[85] M. A. Bernstein, M. Štefinović and C. J. Sleigh, "Optimising reaction performance in the pharmaceutical industry by monitoring with NMR," *Magnetic Resonance in Chemistry,* vol. 45, no. 7, pp. 564-571, 2007.

[86] Magritek, "Benchtop NMR Reaction Monitoring for Kinetic Profiling," [Online]. Available:

https://magritek.com/wp-content/uploads/2020/08/App-Note-Kinetics-1.pdf.

[87] Magritek, “Online monitoring of the formation of a diimine,” [Online]. Available: https://magritek.com/wp-content/uploads/2020/06/App-Note-14-RM-Diimine10.2019-web-2.pdf.

[88] Magritek, “Online Monitoring of the N-Acetylation Reaction of L-Phenylalanine,” [Online]. Available: https://magritek.com/wp-content/uploads/2020/06/App-Note-13-Monitoring-of-an-N-Acetylation-reaction.pdf.

[89] Magritek, “On-line reaction monitoring of an SNAr reaction by 1H and 19F NMR,” [Online]. Available: https://magritek.com/wp-content/uploads/2020/09/App-Note-RM-1H-19F.pdf.

[90] Magritek, “Quantifying the formation of stereoisomers by benchtop NMR spectroscopy,” [Online]. Available: https://magritek.com/wp-content/uploads/2020/10/Quantifying-the-formation-of-stereoisomers.pdf.

[91] Magritek, “Monitoring a Claisen-Schmidt Condensation Reaction by NMR in the teaching Class,” [Online]. Available: https://magritek.com/wp-content/uploads/2020/12/Claisen-Schmidt.pdf.

[92] Magritek, “Magritek,” [Online]. Available: https://magritek.com/applications/reaction-monitoring/.

[93] Bruker, “Reaction Monitoring,” [Online]. Available: https://www.bruker.com/en/applications/pharma/drug-development/reaction-monitoring.html.

[94] R. G. Brinson, “Practical Applications of NMR to Solve Real-World Problems,” *Molecules,* vol. 26, no. 23, p. 7091, 2021.

[95] A. Krunić and J. Orjala, “Application of high-field NMR spectroscopy for characterization and quantitation of submilligram quantities of isolated natural products,” *Magnetic Resonance in Chemistry,* vol. 53, no. 12, p. 1043–1050, 2015.

[96] M. Schiavina, L. Bracaglia, M. A. Rodella, R. Kümmerle, R. Konrat, I. C. Felli and R. Pierattelli, “Optimal 13C NMR investigation of intrinsically disordered proteins at 1.2 GHz,” *Nature Protocols,* vol. 19, p. 406–440, 2024.

[97] H.-Y. Yu, S. Myoung and S. Ahn, “Recent Applications of Benchtop Nuclear Magnetic Resonance Spectroscopy,” *Magnetochemistry,* vol. 7, no. 9, p. 121, 2021.

[98] T. Castaing-Cordier, D. Bouillaud, J. Farjon and P. Giraudeau, “Chapter Four - Recent advances in benchtop NMR spectroscopy and its applications,” Academic Press, 2021.

[99] M. V. Silva Elipe and R. R. Milburn, “Monitoring chemical reactions by low-field benchtop NMR at 45 MHz: pros and cons,” *Magnetic Resonance in Chemistry,* vol. 54, no. 6, pp. 437-443, 2016.

[100] K. Buckenmaier, M. Rudolph, C. Back, T. Misztal, U. Bommerich, P. Fehling, D. Koelle, R. Kleiner, H. A. Mayer, K. Scheffler, J. Bernarding and M. Plaumann, “SQUID-based detection of ultra-low-field multinuclear NMR of substances hyperpolarized using signal amplification by reversible exchange,” *Scientific Reports,* vol. 7, no. 13431, 2017.

[101] I. V. Zhukov, A. S. Kiryutin, A. V. Yurkovskaya, J. W. Blanchard, D. Budker and K. L. Ivanov, “Correlation of high-field and zero- to ultralow-field NMR properties using 2D spectroscopy,” *The Journal of Chemical Physics,* vol. 154, no. 14, p. 144201, 2021.

[102] E. Moser, E. Laistler, F. Schmitt and G. Kontaxis, “Ultra-High Field NMR and MRI—The Role of Magnet Technology to Increase Sensitivity and Specificity,” *Frontiers in Physics,* vol. 5, no. 33, 2017.

[103] Y. Yanagisawa, M. Hamada, K. Hashi and H. Maeda, “Review of recent developments in ultra-high field (UHF) NMR magnets in the Asia region,” *Superconductor Science and Technology,* vol. 35, no. 4, p. 044006, 2022.

[104] K. Halbach, “Design of permanent multipole magnets with oriented rare earth cobalt material,” *Nuclear Instruments and Methods,* vol. 169, no. 1, pp. 1-10, 1980.

[105] E. Danieli, J. Perlo, B. Blümich and F. Casanova, “Small Magnets for Portable NMR Spectrometers,” *Angewandte Chemie,* vol. 49, no. 24, pp. 4133-4135, 2010.

[106] T. L. Peck, R. L. Magin, J. Kruse and M. Feng, “NMR microspectroscopy using 100 um planar RF coils fabricated on gallium arsenide substrates,” *IEEE Transactions on Biomedical Engineering,* vol. 41, no. 7, pp. 706-709, 1994.

[107] H. Wensink, F. Benito-Lopez, D. C. Hermes, W. Verboom, H. J. G. E. Gardeniers, D. N. Reinhoudt and A. van den Berg, “Measuring reaction kinetics in a lab-on-a-chip by microcoil NMR,” *Lab on a Chip,* vol. 5, no. 3, pp. 280-284, 2005.

[108] N. Sun, Y. Liu, H. Lee, R. Weissleder and D. Ham, “CMOS RF Biosensor Utilizing Nuclear Magnetic Resonance,” *IEEE Journal of Solid-State Circuits,* vol. 44, no. 5, pp. 1629-1643, 2009.

[109] H. Lee, E. Sun, D. Ham and R. Weissleder, “Chip–NMR biosensor for detection and molecular analysis of cells,” *Nature Medicine,* vol. 14, p. 869–874, 2008.

[110] Y. Liu, N. Sun, H. Lee, R. Weissleder and D. Ham, “CMOS Mini Nuclear Magnetic Resonance System and its Application for Biomolecular Sensing,” *2008 IEEE International Solid-State Circuits Conference - Digest of Technical Papers,* 2008.

[111] A. McDowell and E. Fukushima, “Ultracompact NMR: 1H Spectroscopy in a Subkilogram Magnet,” *Applied Magnetic Resonance,* vol. 35, p. 185–195, 2008.

[112] J. D. Trumbull, I. K. Glasgow, D. J. Beebe and R. L. Magin, “Integrating Microfabricated Fluidic Systems and NMR Spectroscopy,” *IEEE Transactions on Biomedical Engineering,* vol. 47, no. 1, pp. 3-7, 2000.

[113] J. A. Norcross, C. T. Milling, D. L. Olson, D. Xu, A. Audrieth, R. Albrecht, K. Ruan, J. Likos, C. Jones and T. L. Peck, “Multiplexed NMR: An Automated CapNMR Dual-Sample Probe,” *Analytical Chemistry,* vol. 82, no. 17, p. 7227–7236, 2010.

[114] B. Keil and L. L. Wald, “Massively parallel MRI detector arrays,” *Journal of Magnetic Resonance,* vol. 229, pp. 75-89, 2013.

[115] K. Takeda, “A highly integrated FPGA-based nuclear magnetic resonance spectrometer,” *Review of Scientific Instruments,* vol. 78, no. 3, p. 033103, 2007.

[116] K. Takeda, “OPENCORE NMR: Open-source core modules for implementing an integrated FPGA-based NMR spectrometer,” *Journal of Magnetic Resonance,* vol. 192, no. 2, pp. 218-229, 2008.

[117] K. Takeda, Annual Reports on NMR Spectroscopy, Academic Press, 2011.

[118] Y. Tominaga and K. Takeda, “An electro-mechano-optical NMR probe for 1H–13C double resonance in a superconducting magnet,” *Analyst,* vol. 147, no. 9, pp. 1847-1852, 2022.

[119] N. Kachkachi, A. Gansmuller and H. Rabah, “Design and Experimental Validation of a SoC-FPGA-Based Compact NQR Spectrometer,” *IEEE Transactions on Instrumentation and Measurement,* vol. 73, no. 2003012, pp. 1-12, 2024.

[120] J. B. W. Webber and P. Demin, “Digitally Based Precision Time-Domain Spectrometer for NMR Relaxation and NMR Cryoporometry,” *Micro,* vol. 3, no. 2, pp. 404-433, 2023.

[121] J. B. W. Webber, “A review of the use of simple time-domain NMR/MRI for material-science,” *SN Applied Sciences,* vol. 3, no. 809, 2021.

[122] J. B. W. Webber and H. Liu, “The implementation of an easy-to-apply NMR cryoporometric instrument for porous materials,” *Magnetic Resonance Imaging,* vol. 100, pp. 36-42, 2023.

[123] J. B. W. Webber and P. Demin, “Credit-card sized field and benchtop NMR relaxometers using field programmable gate arrays,” *Magnetic Resonance Imaging,* vol. 56, pp. 45-51, 2019.

[124] J. B. W. Webber, “Some Applications of a Field Programmable Gate Array Based Time-Domain Spectrometer for NMR Relaxation and NMR Cryoporometry,” *Applied Sciences,* vol. 10, no. 8, p. 2714, 2020.

[125] Lab-Tools Ltd., “Advanced Time-Domain NMR Spectrometer for Materials Science and Process Control,” [Online]. Available: https://nmrspectrometer.lab-tools.com/.

[126] I. I. Rabi, J. R. Zacharias, S. Millman and P. Kusch, "A New Method of Measuring Nuclear Magnetic Moment," *Physical Review,* vol. 53, no. 4, p. 318, 1938.

[127] W. Gerlach and O. Stern, "Der experimentelle Nachweis der Richtungsquantelung im Magnetfeld," *Zeitschrift für Physik,* vol. 9, pp. 349-352, 1922.

[128] D. I. Hoult and B. Bhakar, "NMR Signal Reception: Virtual Photons and Coherent Spontaneous Emission," *Concepts in Magnetic Resonance,* vol. 9, no. 5, pp. 277-297, 1998.

[129] A. D. Elster, “Questions and Answers in MRI - MRI Questions & Answers; MR imaging physics & technology,” © 2024 AD Elster, ELSTER LLC, Courtesy of Allen D. Elster, MRIquestions.com, [Online]. Available: https://mriquestions.com/index.html.

[130] R. K. Harris, E. D. Becker, S. M. C. de Menezes, R. Goodfellow and P. Granger, “NMR nomenclature. Nuclear spin properties and conventions for chemical shifts. (IUPAC Recommendations 2001),” *Pure and Applied Chemistry,* vol. 73, no. 11, pp. 1795-1818, 2001.

[131] S. M. Blinder - Wolfram Demonstrations Project, “Nuclear Magnetic Resonance Spectrum of Ethanol,” © 2024 Wolfram Demonstrations Project & Contributors, 7 March 2011. [Online]. Available: https://demonstrations.wolfram.com/NuclearMagneticResonanceSpectrumOfEthanol/.

[132] D. F. Koster and W. Jones, “Pascal Type Triangles For Nuclei With I > 1/2,” *Journal of Chemical Education,* vol. 59, no. 4, p. 289, 1982.

[133] C. L. Perrin, “Polynomial coefficients. Application to spin–spin splitting by N equivalent nuclei of spin I > 1/2,” *Magnetic Resonance in Chemistry,* vol. 56, no. 9, p. 799–802, 2018.

[134] ChemistHans at the English Wikipedia, “Proton nuclear magnetic resonance,” Wikimedia Foundation, Inc., 2007/2009. [Online]. Available: https://en.wikipedia.org/wiki/Proton_nuclear_magnetic_resonance.

[135] National Institute of Standards and Technology (NIST), “Meet the Constants,” [Online]. Available: https://www.nist.gov/si-redefinition/meet-constants.

[136] A. Yadav, "Effect of Temperature on Electric Current, Magnets and Electromagnet," *International Journal of Advancements in Technology,* vol. 7, no. 4, 2016.

[137] K. Trainor, J. A. Palumbo, D. W. S. MacKenzie and E. M. Meiering, "Temperature dependence of NMR chemical shifts: Tracking and statistical analysis," *Protein Science,* vol. 29, no. 1, pp. 306-314, 2020.

[138] A. K. Mall and A. K. Pramanik, "Temperature dependent 89Y NMR study on multiferroic YCrO3," *Journal of Physics: Condensed Matter,* vol. 33, no. 12, 2021.

[139] G. Baumgarten, M. Madec, D.-V. Nguyen, L. Werling, J. Pascal, C. M. Gajendramurthy, P. Bertani, J.-P. Djukic and L. Hébrard, “Assessment of the Impact of Static Field Inhomogeneity on the Performance of Miniaturized NMR Devices,” *IEEE Transactions on Magnetics,* vol. 59, no. 2, pp. 1-6, 2023.

[140] E. Nikita, Encyclopedia of Archaeology (Second Edition) - Statistics: Part II - Confirmatory Data Analysis, Academic Press, 2024.

[141] M. A. Rieffel, "A Method for Estimating the Computational Requirements of DSMC Simulations," *Journal of Computational Physics,* vol. 149, no. 1, pp. 95-113, 1999.

[142] J. Wist, "Simulate and predict NMR spectra," Copyright: Luc Patiny, [Online]. Available: https://www.nmrdb.org/.

[143] L. Patiny, M. Zasso, D. Kostro, A. Bolaños, N. E. Schlörer, J. C. Liermann, J. Wist, H. Musallam, M. Wenk and D. Jeannerat, "NMRium - Visualize and process NMR spectra online," © Zakodium Sàrl, [Online]. Available: https://www.nmrium.org/.

[144] Bruker, “NMR Instruments - AvanceCore,” © Copyright Bruker 2024, [Online]. Available:

https://www.bruker.com/en/products-and-solutions/mr/nmr/avancecore.html.

[145] G. Baumgarten and M. Madec, “OSF | NMR simulator - Assessment of the impact of static field inhomogeneity on the performance of miniaturized NMR devices,” Copyright © 2011-2024 Center for Open Science, 13 09 2022. [Online]. Available: https://doi.org/10.17605/OSF.IO/MR2FU.

[146] Red Pitaya, "STEMlab 125-14 - Red Pitaya," Red Pitaya © 2024, [Online]. Available: https://redpitaya.com/stemlab-125-14/.

[147] Pure Devices GmbH, “openMATLAB® interface - Research Lab,” [Online]. Available: https://www.pure-devices.com/index.php/products/products-research/products-research-matlab.html.

[148] BlizzPhyz at the English Wikipedia, “Loop-gap resonator,” Wikimedia Foundation, Inc., 2019. [Online]. Available: https://en.wikipedia.org/wiki/Loop-gap_resonator.

[149] Lime Microsystems, "Software defined radio technology for wireless networks. - Lime Microsystems," © 2020 Lime Microsystems Ltd, [Online]. Available: https://limemicro.com/products/boards/.

[150] Great Scott Gadgets, "HackRF One - Great Scott Gadgets," © 2009 - 2023 greatscottgadgets.com, [Online]. Available: https://greatscottgadgets.com/hackrf/one/.

[151] Red Pitaya, "Red Pitaya - Swiss Army Knife For Engineers," Red Pitaya © 2024, [Online]. Available: https://redpitaya.com/.

[152] Red Pitaya, “Red Pitaya in Research,” [Online]. Available: https://redpitaya.com/red-pitaya-in-research/.

[153] Red Pitaya, “STEMlab 125-14,” [Online]. Available: https://redpitaya.com/product-category/stemlab-125-14/.

[154] AMD, “Zynq-7000 SoC Data Sheet: Overview (DS190) - Viewer - AMD Technical Information Portal,” © 2024 Advanced Micro Devices, Inc., [Online]. Available: https://docs.amd.com/v/u/en-US/ds190-Zynq-7000-Overview.

[155] Red Pitaya, “RTD Documentation,” 6 March 2014. [Online]. Available: https://downloads.redpitaya.com/doc//Red_Pitaya_Schematics_v1.0.1.pdf.

[156] Mini-Circuits, “RF Gain Block Amplifier, 0.05 - 130 MHz, 50Ω | ZHL-32A-S+,” [Online]. Available: https://www.minicircuits.com/WebStore/dashboard.html?model=ZHL-32A-S%2B.

[157] Sbyrnes321 at the English Wikipedia, “Quarter-wave impedance transformer,” Wikimedia Foundation, Inc., 2012. [Online]. Available: https://en.wikipedia.org/wiki/Quarter-wave_impedance_transformer.

[158] Mini-Circuits, "SMT Low Noise Amplifier, 50 - 4000 MHz, 50Ω | PGA-103+ | Mini-Circuits," © 2017 Mini-Circuits, [Online]. Available: https://www.minicircuits.com/WebStore/dashboard.html?model=PGA-103%2B.

[159] Mini-Circuits, "Ultra Linear Low Noise Monolithic Amplifier 50Ω / 0.05 to 4 GHz - PGA-103+," [Online]. Available: https://www.minicircuits.com/pdfs/PGA-103+.pdf.

[160] Mini-Circuits, "PGA-103+ Stablilizing Network - Mini-Circuits Blog," © Mini-Circuits 2020, 27 April 2015. [Online]. Available: https://blog.minicircuits.com/pga-103-stablilizing-network/.

[161] Red Pitaya, “1.6. FAQ - Red Pitaya 2.00-30 documentation,” 2024. [Online]. Available: https://redpitaya.readthedocs.io/en/latest/quickStart/troubleshooting/troubleshooting.html.

[162] The MathWorks, Inc., “Fourier Transforms - MATLAB & Simulink - MathWorks Deutschland,” 1994-2024. [Online]. Available: https://de.mathworks.com/help/matlab/math/fourier-transforms.html.

[163] Analog Devices, Inc., “Samples per Second,” [Online]. Available: https://www.analog.com/en/resources/glossary/samples-per-second.html.

[164] Red Pitaya, “2.3.1. SCPI server (MATLAB, LabVIEW, Scilab or Python) - Red Pitaya

2.00-30 documentation," 2024. [Online]. Available: https://redpitaya.readthedocs.io/en/latest/appsFeatures/remoteControl/scpi.html.

[165] Red Pitaya, "2.3.6.4.4. Sampling rate and decimations - Red Pitaya 2.00-30 documentation," © Copyright 2024 Red Pitaya, [Online]. Available: https://redpitaya.readthedocs.io/en/latest/appsFeatures/examples/acquisition/acqRF-samp-and-dec.html.

[166] N. N. Greenwood and A. Earnshaw, Chemistry of the Elements - 2nd Edition, Butterworth-Heinemann, 1997.

[167] H. E. Gottlieb, V. Kotlyar and A. Nudelman, "NMR Chemical Shifts of Common Laboratory Solvents as Trace Impurities," *The Journal of Organic Chemistry,* vol. 62, no. 21, pp. 7512-7515, 1997.

[168] P. Zarzycki and J. R. Rustad, "Theoretical Determination of the NMR Spectrum of Liquid Ethanol," *The Journal of Physical Chemistry A,* vol. 113, no. 1, pp. 291-297, 2009.

[169] K. Puzio, B. Claude, L. Amalric, C. Berho, E. Grellet, S. Bayoudh, R. Nehmé and P. Morin, "Molecularly imprinted polymer dedicated to the extraction of glyphosate in natural waters," *Journal of Chromatography A,* vol. 1361, pp. 1-8, 2014.

[170] C. M. Gajendramurthy, *Towards the Design of an Immersible NMR Probe for Solution Reaction Monitoring,* Strasbourg: École doctorale des sciences chimiques (EDSC), 2024.

[171] H. Davoodi, N. Nordin, H. Munakata, J. G. Korvink, N. MacKinnon and V. Badilita, "Untuned broadband spiral micro-coils achieve sensitive multi-nuclear NMR TX/RX from microfluidic samples," *Scientific Reports,* vol. 11, no. 7798, 2021.

[172] D. I. Hoult and R. E. Richards, "The signal-to-noise ratio of the nuclear magnetic resonance experiment," *Journal of Magnetic Resonance,* vol. 24, no. 1, pp. 71-85, 1976.

[173] J. J. van der Klink, "The NMR Reciprocity Theorem for Arbitrary Probe Geometry," *Journal of Magnetic Resonance,* vol. 148, no. 1, pp. 147-154, 2001.

Publications and communications

Abstract and oral presentation: Simulator dedicated to the assessment of the effect of static field inhomogeneity on NMR spectrum of portable miniaturized NMR devices. Authors: Guilherme Baumgarten, Duc-Vinh Nguyen, Lucas Werling, Philippe Bertani, Igor Perreta, Joris Pascal, Morgan Madec and Luc Hébrard. Compact NMR Conference II 2021.

Poster and oral presentation: Simulator dedicated to the assessment of the effect of static field inhomogeneity on NMR spectrum of portable miniaturized NMR devices. Authors: Guilherme Baumgarten, Duc-Vinh Nguyen, Lucas Werling, Philippe Bertani, Igor Perreta, Joris Pascal, Morgan Madec and Luc Hébrard. Compact NMR Conference II 2021.

Abstract and oral presentation: Assessment of the impact of static field inhomogeneity on the performance of miniaturized NMR devices. Authors: Guilherme Baumgarten, Morgan Madec, Duc-Vinh Nguyen, Lucas Werling, Joris Pascal, Chunchesh Malangi Gajendramurthy, Philippe Bertani, Jean-Pierre Djukic and Luc Hébrard. EMSA 2022.

Abstract and oral presentation: Inhomogeneity assessment of a commercial Benchtop NMR permanent magnet and corresponding simulated NMR spectrum degradation. Authors: Guilherme Baumgarten, Duc-Vinh Nguyen, Lucas Werling, Luc Hébrard, Joris Pascal and Morgan Madec. EMSA 2022.

Journal paper [139]: Assessment of the Impact of Static Field Inhomogeneity on the Performance of Miniaturized NMR Devices. Authors: Guilherme Baumgarten, Morgan Madec, Duc-Vinh Nguyen, Lucas Werling, Joris Pascal, Chunchesh Malangi Gajendramurthy, Philippe Bertani, Jean-Pierre Djukic, and Luc Hébrard. IEEE Transactions on Magnetics.

Poster and oral presentation: Assessment of the impact of static field inhomogeneity on the performance of miniaturized NMR devices. Authors: Guilherme Baumgarten, Morgan Madec, Duc-Vinh Nguyen, Lucas Werling, Chunchesh Malangi Gajendramurthy, Philippe Bertani, Jean-Pierre Djukic, Joris Pascal and Luc Hébrard. GDR SoC2 2022.

Poster: Chaîne d’acquisition intégrée pour spectroscope de RMN portable. Authors: Duc-Vinh Nguyen, Guilherme Baumgarten, Lucas Werling, Norbert Dumas, Morgan Madec, Latifa Fakri-Bouchet, José Bernardo, Wilfried Uhring, Luc Hébrard and Joris Pascal. GDR SoC2 2022.

Poster: Adaptation 50-ohms versus haute impédance d’une antenne RMN avec son préamplificateur. Authors: Duc-Vinh Nguyen, Lucas Werling, Guilherme Baumgarten, Norbert Dumas, Morgan Madec, Latifa Fakri-Bouchet, José Bernardo, Wilfried Uhring, Luc Hébrard and Joris Pascal. GDR SoC2 2022.

Abstract and oral presentation: Low-cost electronics for miniaturized NMR spectrometers. Authors: Guilherme Baumgarten, Duc-Vinh Nguyen, Lucas Werling, Joris Pascal, Morgan Madec and Luc Hébrard. AIM 2023.

Appendixes

This complementary segment puts forward a series of subsections with further information on the developed work, including (1) the calculation of the analytical equations composing the ICF, (2) simulations of magnetic structures in order to obtain magnetic maps, (3) the NMR Simulator code, (4) the NMR Prototype code, (5) schematics and board designs of our NMR Prototype electronics, (6) an illustration of our developed receiving coil manufacturing and tuning process, and (7) a signal processing analysis concerning the implementation of zero padding for weak NMR signals.

I. Analytical calculation of the Inhomogeneity Convolution Function

The local ICF can be determined by resolving an analytical integral on three distinct spatial variables, as presented in equation (51). Since we are working with continuous functions and the single integrals are Lebesgue ones, Fubini's theorem applies and the multiple integral problem becomes an iterated integral problem, *i.e.*, a series of integrals of one variable.

Therefore, the resolution of the triple integral of equation (51) results to be three independent integrations. In the following, $\mathfrak{D}$ denotes the Dirac delta function defined as in equation (6), while u is the Heaviside step function as given in equation (57). For the sake of simplicity, we also consider in this section that the constant c_1 incorporates the chemical shift δ_k, which is assumed to be constant as well.

The first integral reads:

$$\int_0^y \mathfrak{D}(f - c_1 - c_2x - c_3y - c_4z)dz = \frac{u(c_1 + c_2x + c_3y + c_4y - f) - u(c_1 + c_2x + c_3y - f)}{c_4} = \frac{u(c_1 + c_2x + (c_3 + c_4)y - f) - u(c_1 + c_2x + c_3y - f)}{c_4} \tag{80}$$

Then, the second integral results to be:

$$
\begin{aligned}
&\int_0^x \frac{u(c_1 + c_2x + (c_3 + c_4)y - f) - u(c_1 + c_2x + c_3y - f)}{c_4}\,dy \\
&= \frac{1}{c_4}\left(\frac{u\big((c_1 + c_2x + c_3x + c_4x - f)(c_1 + c_2x + c_3x + c_4x - f)\big)}{c_3 + c_4} - \frac{u\big((c_1 + c_2x - f)(c_1 + c_2x - f)\big)}{c_3 + c_4}\right. \\
&\left. - \frac{u\big((c_1 + c_2x + c_3x - f)(c_1 + c_2x + c_3x - f)\big)}{c_3} + \frac{u\big((c_1 + c_2x - f)(c_1 + c_2x - f)\big)}{c_3}\right) \\
&= \frac{1}{c_4}\left(\frac{u\big((c_1 + c_2x + c_3x + c_4x - f)(c_1 + c_2x + c_3x + c_4x - f)\big) - u\big((c_1 + c_2x - f)(c_1 + c_2x - f)\big)}{c_3 + c_4}\right. \\
&\left. + \frac{u\big((c_1 + c_2x - f)(c_1 + c_2x - f)\big) - u\big((c_1 + c_2x + c_3x - f)(c_1 + c_2x + c_3x - f)\big)}{c_3}\right) \\
&= \frac{\dfrac{u((c_1 + c_2x + c_3x + c_4x - f)^2) - u((c_1 + c_2x - f)^2)}{c_3 + c_4} + \dfrac{u((c_1 + c_2x - f)^2) - u((c_1 + c_2x + c_3x - f)^2)}{c_3}}{c_4} \\
&= \frac{\dfrac{u((c_1 + (c_2 + c_3 + c_4)x - f)^2) - u((c_1 + c_2x - f)^2)}{c_3 + c_4} + \dfrac{u((c_1 + c_2x - f)^2) - u((c_1 + (c_2 + c_3)x - f)^2)}{c_3}}{c_4} \\
&= \frac{u((c_1 + (c_2 + c_3 + c_4)x - f)^2) - u((c_1 + c_2x - f)^2)}{c_3c_4 + {c_4}^2} + \frac{u((c_1 + c_2x - f)^2) - u((c_1 + (c_2 + c_3)x - f)^2)}{c_3c_4}
\end{aligned}
\tag{81}
$$

Since a direct analytical calculation of the third integral is as well not feasible, given that it encompasses nondeterministic mathematical functions, a polynomial approximation fits it at its best. This way, by rewriting the previous outcome as polynomials of second degree of the difference $(f - c_1)$, which work very well for fitting into peak distribution-like shapes, a handleable expression with very limited worst-case error can be attained. Therefore, the third integral results to be:

$$
\begin{aligned}
&\int_0^1 \left(\frac{u((c_1+(c_2+c_3+c_4)x-f)^2)-u((c_1+c_2x-f)^2)}{c_3c_4+{c_4}^2} + \frac{u((c_1+c_2x-f)^2)-u((c_1+(c_2+c_3)x-f)^2)}{c_3c_4} \right) dx \\
&\approx \frac{1}{c_4}\left(u(c_1+c_2+c_3+c_4-f)\left(\frac{1}{2}\frac{(f-c_1)^2}{(c_3+c_4)(c_2+c_3+c_4)}-\frac{f-c_1}{c_3+c_4}+\frac{1}{2}\frac{c_2+c_3+c_4}{c_3+c_4}\right)\right. \\
&-\frac{1}{2}\frac{u(c_1-f)(f-c_1)^2}{(c_3+c_4)(c_2+c_3+c_4)}-u(c_1+c_2-f)\left(\frac{1}{2}\frac{(f-c_1)^2}{c_2(c_3+c_4)}-\frac{f-c_1}{c_3+c_4}+\frac{1}{2}\frac{c_2}{c_3+c_4}\right) \\
&+\frac{1}{2}\frac{u(c_1-f)(f-c_1)^2}{c_2(c_3+c_4)}-u(c_1+c_2+c_3-f)\left(\frac{1}{2}\frac{(f-c_1)^2}{c_3(c_2+c_3)}-\frac{f-c_1}{c_3}+\frac{1}{2}\frac{c_2+c_3}{c_3}\right) \\
&\left.+\frac{1}{2}\frac{u(c_1-f)(f-c_1)^2}{c_3(c_2+c_3)}+u(c_1+c_2-f)\left(\frac{1}{2}\frac{(f-c_1)^2}{c_2c_3}-\frac{f-c_1}{c_3}+\frac{1}{2}\frac{c_2}{c_3}\right)-\frac{1}{2}\frac{u(c_1-f)(f-c_1)^2}{c_2c_3}\right) \\
&=\left(\frac{(f-c_1)^2}{2c_4(c_3+c_4)(c_2+c_3+c_4)}-\frac{f-c_1}{c_4(c_3+c_4)}+\frac{c_2+c_3+c_4}{2c_4(c_3+c_4)}\right)u(c_1+c_2+c_3+c_4-f) \\
&-\left(\frac{(f-c_1)^2}{2c_3c_4(c_2+c_3)}-\frac{f-c_1}{c_3c_4}+\frac{c_2+c_3}{2c_3c_4}\right)u(c_1+c_2+c_3-f) \\
&+\left(\frac{(f-c_1)^2}{2c_2c_3c_4}-\frac{f-c_1}{c_3c_4}+\frac{c_2}{2c_3c_4}\right)u(c_1+c_2-f) \\
&-\left(\frac{(f-c_1)^2}{2c_2c_4(c_3+c_4)}-\frac{f-c_1}{c_4(c_3+c_4)}+\frac{c_2}{2c_4(c_3+c_4)}\right)u(c_1+c_2-f) \\
&-\frac{(f-c_1)^2}{2c_4(c_3+c_4)(c_2+c_3+c_4)}u(c_1-f)+\frac{(f-c_1)^2}{2c_2c_4(c_3+c_4)}u(c_1-f)+\frac{(f-c_1)^2}{2c_3c_4(c_2+c_3)}u(c_1-f) \\
&-\frac{(f-c_1)^2}{2c_2c_3c_4}u(c_1-f) \qquad (82) \\
&=\frac{1}{c_4(c_3+c_4)}\left(\frac{(f-c_1)^2}{2(c_2+c_3+c_4)}-(f-c_1)+\frac{c_2+c_3+c_4}{2}\right)u(c_1+c_2+c_3+c_4-f) \\
&-\frac{1}{c_3c_4}\left(\frac{(f-c_1)^2}{2(c_2+c_3)}-(f-c_1)+\frac{c_2+c_3}{2}\right)u(c_1+c_2+c_3-f) \\
&+\frac{1}{c_3c_4}\left(\frac{(f-c_1)^2}{2c_2}-(f-c_1)+\frac{c_2}{2}\right)u(c_1+c_2-f) \\
&-\frac{1}{c_4(c_3+c_4)}\left(\frac{(f-c_1)^2}{2c_2}-(f-c_1)+\frac{c_2}{2}\right)u(c_1+c_2-f)+\frac{1}{c_2(c_3+c_4)}\frac{(f-c_1)^2}{2c_4}u(c_1-f) \\
&+\frac{1}{c_3(c_2+c_3)}\frac{(f-c_1)^2}{2c_4}u(c_1-f)-\frac{1}{(c_3+c_4)(c_2+c_3+c_4)}\frac{(f-c_1)^2}{2c_4}u(c_1-f) \\
&-\frac{1}{c_2c_3}\frac{(f-c_1)^2}{2c_4}u(c_1-f) \\
&=\frac{1}{c_4(c_3+c_4)}\left(\frac{(f-c_1)^2}{2(c_2+c_3+c_4)}-(f-c_1)+\frac{c_2+c_3+c_4}{2}\right)u(c_1+c_2+c_3+c_4-f) \\
&-\frac{1}{c_3c_4}\left(\frac{(f-c_1)^2}{2(c_2+c_3)}-(f-c_1)+\frac{c_2+c_3}{2}\right)u(c_1+c_2+c_3-f) \\
&+\frac{1}{c_4}\left(\frac{1}{c_3}-\frac{1}{c_3+c_4}\right)\left(\frac{(f-c_1)^2}{2c_2}-(f-c_1)+\frac{c_2}{2}\right)u(c_1+c_2-f) \\
&+\frac{1}{2c_4}\left(\frac{1}{c_2(c_3+c_4)}+\frac{1}{c_3(c_2+c_3)}-\frac{1}{(c_3+c_4)(c_2+c_3+c_4)}-\frac{1}{c_2c_3}\right)(f-c_1)^2u(c_1-f)
\end{aligned}
$$

Equation (82) being a very good approximative deterministic solution for the triple integral within equation (56), we employ it as the mathematical description of the ICF within a tetrahedron.

II. NMR Simulator Toolchain code

i. NMR spectrometer simulation code

```
clear all; close all; clc;

%% Parameterization:
SNR = 30;
FID_1_max_amplitude = 1;
FID_2_max_amplitude = 1;
FID_3_max_amplitude = 1;
Larmor_Frequency = 24e6;
FID_1_chemical_shift = 5;
FID_2_chemical_shift = 5;
FID_3_chemical_shift = 5;
FID_1_frequency = Larmor_Frequency-((Larmor_Frequency/1e6)*FID_1_chemical_shift);
FID_2_frequency = Larmor_Frequency-((Larmor_Frequency/1e6)*FID_2_chemical_shift);
FID_3_frequency = Larmor_Frequency-((Larmor_Frequency/1e6)*FID_3_chemical_shift);
FID_1_delta_t_sampling = 0;
FID_2_delta_t_sampling = 1/(4*FID_2_frequency);
FID_3_delta_t_sampling = 1/(2*FID_2_frequency);
FID_1_phase = 2*pi*FID_1_delta_t_sampling*FID_1_frequency;
FID_2_phase = 2*pi*FID_2_delta_t_sampling*FID_2_frequency;
FID_3_phase = 2*pi*FID_3_delta_t_sampling*FID_3_frequency;
%FID_1_phase = 0;
%FID_2_phase = pi;
%FID_3_phase = pi/2;
Local_oscillator_max_amplitude = 1;
DC_frequency = 1e3;
Local_oscillator_frequency = Larmor_Frequency+DC_frequency;
Local_oscillator_phase = 0;
ppp = 10;
T2_star = 0.02;
FPASS = 10e3;
SDR_buffer_size = 16384;
SDR_ADC_resolution = 14;
t_init = 0;
t_end = 0.1;
t = linspace(t_init,t_end,ppp*(Larmor_Frequency*(t_end-t_init)));
f = ((1/((t_end-t_init)/SDR_buffer_size))/SDR_buffer_size)*(-
SDR_buffer_size/2:SDR_buffer_size/2-1);
ppm = f(SDR_buffer_size/2+1:SDR_buffer_size);
ppm = ppm-(f(SDR_buffer_size/2+1));
ppm = (ppm-DC_frequency)*(1e6/Larmor_Frequency);

%% The local oscillator:
Local_oscillator =
Local_oscillator_max_amplitude*sin(2*pi*Local_oscillator_frequency*t+Local_oscillator
_phase);
Fig1 = figure;
plot(t,Local_oscillator);
grid on;
ylabel('Amplitude (V)');
```

```
xlabel('Time (s)');
title('Local oscillator');

%% The ideal FID:
Ideal_FID_1 = FID_1_max_amplitude*sin(2*pi*FID_1_frequency*t+FID_1_phase).*exp(-
t/T2_star);
Ideal_FID_2 = FID_2_max_amplitude*sin(2*pi*FID_2_frequency*t+FID_2_phase).*exp(-
t/T2_star);
Ideal_FID_3 = FID_3_max_amplitude*sin(2*pi*FID_3_frequency*t+FID_3_phase).*exp(-
t/T2_star);
Ideal_FID = (Ideal_FID_1 + Ideal_FID_2 + Ideal_FID_3) / (FID_1_max_amplitude +
FID_2_max_amplitude + FID_3_max_amplitude);
Fig2 = figure;
plot(t,Ideal_FID);
grid on;
ylabel('Amplitude (V)');
xlabel('Time (s)');
title('Ideal FID');

%% The noisy FID (measured signal):
Noisy_FID_1 = awgn(Ideal_FID_1,SNR);
Noisy_FID_2 = awgn(Ideal_FID_2,SNR);
Noisy_FID_3 = awgn(Ideal_FID_3,SNR);
Noisy_FID = awgn(Ideal_FID,SNR);
Fig3 = figure;
plot(t,Noisy_FID);
grid on;
ylabel('Amplitude (V)');
xlabel('Time (s)');
title('Noisy FID');

%% The mixer output:
Mixer_output_FID_1 = Noisy_FID_1.*Local_oscillator;
Mixer_output_FID_2 = Noisy_FID_2.*Local_oscillator;
Mixer_output_FID_3 = Noisy_FID_3.*Local_oscillator;
Mixer_output = Noisy_FID.*Local_oscillator;
Fig4 = figure;
plot(t,Mixer_output);
grid on;
ylabel('Amplitude (V)');
xlabel('Time (s)');
title('Mixer output');

%% Lowpass filtering:
Filtered_FID_1 = lowpass(Mixer_output_FID_1,FPASS,numel(Mixer_output_FID_1)/(t_end-
t_init));
Filtered_FID_2 = lowpass(Mixer_output_FID_2,FPASS,numel(Mixer_output_FID_2)/(t_end-
t_init));
Filtered_FID_3 = lowpass(Mixer_output_FID_3,FPASS,numel(Mixer_output_FID_3)/(t_end-
t_init));
Filtered_FID = lowpass(Mixer_output,FPASS,numel(Mixer_output)/(t_end-t_init));
Fig5 = figure;
plot(t,Filtered_FID);
grid on;
ylabel('Amplitude (V)');
xlabel('Time (s)');
title('Filtered FID');

%% Sampled by the SDR
Sampled_FID_1 =
```

```
cast(fi(resample(Filtered_FID_1,SDR_buffer_size,numel(Filtered_FID_1)),1,SDR_ADC_reso
lution),"double");
Sampled_FID_2 =
cast(fi(resample(Filtered_FID_2,SDR_buffer_size,numel(Filtered_FID_2)),1,SDR_ADC_reso
lution),"double");
Sampled_FID_3 =
cast(fi(resample(Filtered_FID_3,SDR_buffer_size,numel(Filtered_FID_3)),1,SDR_ADC_reso
lution),"double");
Sampled_FID =
cast(fi(resample(Filtered_FID,SDR_buffer_size,numel(Filtered_FID)),1,SDR_ADC_resoluti
on),"double");
t = resample(t,SDR_buffer_size,numel(t));
Fig6 = figure;
plot(t,Sampled_FID);
grid on;
ylabel('Amplitude (V)');
xlabel('Time (s)');
title('Sampled FID');

%% FIDs saved to a txt file (for Python integration)
% 1st FID
for aux = 1:size(Sampled_FID_1,2)
    index_for_TXT(aux) = aux;
end
A=[];
A(:,1) = index_for_TXT;
A(:,2) = Sampled_FID_1;
A(:,3) = t;
filename_txt = sprintf('FID_1.txt');
dlmwrite(fullfile(filename_txt),A,',');
% 2nd FID
for aux = 1:size(Sampled_FID_2,2)
    index_for_TXT(aux) = aux;
end
A=[];
A(:,1) = index_for_TXT;
A(:,2) = Sampled_FID_2;
A(:,3) = t;
filename_txt = sprintf('FID_2.txt');
dlmwrite(fullfile(filename_txt),A,',');
% 3rd FID
for aux = 1:size(Sampled_FID_3,2)
    index_for_TXT(aux) = aux;
end
A=[];
A(:,1) = index_for_TXT;
A(:,2) = Sampled_FID_3;
A(:,3) = t;
filename_txt = sprintf('FID_3.txt');
dlmwrite(fullfile(filename_txt),A,',');
% FID_1 + FID_2 + FID_3
for aux = 1:size(Sampled_FID,2)
    index_for_TXT(aux) = aux;
end
A=[];
A(:,1) = index_for_TXT;
A(:,2) = Sampled_FID;
A(:,3) = t;
filename_txt = sprintf('FID.txt');
dlmwrite(fullfile(filename_txt),A,',');
```

```
%% Runs Python programm
pyrunfile("ReadFID.py");

%% Fourier transform
FFT = abs(fftshift(fft(Sampled_FID)));
Fig7 = figure;
plot(f,FFT);
grid on;
ylabel('|fft(Sampled FID)|');
xlabel('Frequency (Hz)');
title('FFT of the FID');

%% NMR format
NMR = FFT(SDR_buffer_size/2+1:SDR_buffer_size);
Fig8 = figure;
plot(ppm,NMR);
grid on;
ylabel('|fft(Sampled FID)|');
xlabel('ppm');
xlim([-10 100]);
set(gca,'xdir','reverse');
title('Frequency spectrum in terms of chemical shift(s)');
```

ii. NMR signal time domain adjustment code

```
import numpy as np
import matplotlib.pyplot as plt
from scipy.ndimage import median_filter
from scipy.optimize import curve_fit
from scipy.interpolate import CubicSpline

#files = ['./Block1/Raw/FID_Acquisition_1_of_3.fig.txt',
'./Block1/Raw/FID_Acquisition_2_of_3.fig.txt',
'./Block1/Raw/FID_Acquisition_3_of_3.fig.txt']
files = ['FID_1.txt', 'FID_2.txt', 'FID_3.txt']

def dilate(t, x, k):
    newt = t * k
    newt = [z for z in newt if z < t[-1]]
    csModel = CubicSpline(newt, x[0:len(newt)])
    newx = csModel(newt)
    return newt, newx

def interpolCubic(t, x, t2):
    csModel = CubicSpline(t, x)
    return csModel(t2)

class FID:

    def __init__(self):
        self.t = np.array([])
        self.x = np.array([])
        self.phase = 0
        self.shift = 0
```

```
    def loaddata(self, fileName):
        data = np.loadtxt(fileName, delimiter=',')
        self.t = np.array([])
        self.x = np.array([])
        for k in data:
            if k[2] <= 1:
                self.t = np.append(self.t, k[2])
                self.x = np.append(self.x, k[1])

    def plot(self, linestyle=None, linewidth=None):
        plt.plot(self.t, self.x, linestyle=linestyle, linewidth=linewidth)

    def medianFiltering(self, size):
        self.x = median_filter(self.x, size=size, cval=0, mode='nearest')

    def phaseShiftCalculation(self, FIDref, phaseRange, overwrite=False):

        def target_func(k):
            if k > 0:
                vect1 = FIDref.x[0:-(int(k) + 1)]
                vect2 = self.x[int(k):-1]
            else:
                vect1 = FIDref.x[int(abs(k)):-1]
                vect2 = self.x[0:-(int(abs(k)) + 1)]
            return np.mean((vect1 + vect2) ** 2)

        score = np.array([])
        phase = np.array([])
        for k in phaseRange:
            score = np.append(score, target_func(k))
            phase = np.append(phase, k)

        def poly2_func(x, a, b, c):
            return a * x * x + b * x + c

        idx_max = np.argmax(score)
        val_max = np.max(score)
        popt = np.polyfit(phase[idx_max - 100:idx_max + 100], score[idx_max
- 100:idx_max + 100], 2)
        a, b, c = popt
        plt.plot(phase[idx_max - 100:idx_max + 100], score[idx_max -
100:idx_max + 100])
        plt.plot(phase[idx_max - 100:idx_max + 100], poly2_func(phase, a, b,
c)[idx_max - 100:idx_max + 100])
        plt.show()
        print(a, b, c)
        self.phase = -b / (2 * a)
        if overwrite:
            self.applyPhaseShift()

    def frequencyShiftCalculation(self, FIDref, ditaleFactorRange,
overwrite=False):

        def target_func(k):
            newt, newFID = dilate(self.t, self.x, k)
            newRef = interpolCubic(FIDref.t, FIDref.x, newt)
            return np.mean((newFID + newRef) ** 2)
        score = np.array([])
        factor = np.array([])
        for k in ditaleFactorRange:
            score = np.append(score, target_func(k))
```

```
            factor = np.append(factor, k)

        def quad_func(x, a, b, c, d):
            return a*np.exp(-(x-b)**2/c)+d
        popt, pcov = curve_fit(quad_func, factor, score)
        a, b, c, d = popt
        self.factor = b
        print(b)
        if overwrite:
            self.t, self.x = dilate(self.t, self.x, b)

FID1 = FID()
FID1.loaddata(files[0])
FID1.medianFiltering(9)
FID1.plot()

FID2 = FID()
FID2.loaddata(files[1])
FID2.medianFiltering(9)
FID2.plot()

FID3 = FID()
FID3.loaddata(files[2])
FID3.medianFiltering(9)
FID3.plot()
plt.title("Out-of-phase FIDs")
plt.xlabel("Time (s)")
plt.ylabel("Amplitude (V)")
plt.show()

FID1.phaseShiftCalculation(FID2, np.arange(-500,500,1), overwrite=True)
FID3.phaseShiftCalculation(FID2, np.arange(-500,500,1), overwrite=True)
FID1.plot(linestyle="solid")
FID2.plot(linestyle=(0, (3, 5, 1, 5)), linewidth=2)
FID3.plot(linestyle=(0, (3, 5, 1, 5, 1, 5)), linewidth=2)
plt.title("Phased FIDs")
plt.xlabel("Time (s)")
plt.ylabel("Amplitude (V)")
plt.show()
```

III. NMR Spectrometer Prototype code

```
clear all; close all; clc;

%% parameters
acquisitions_amount = 1;
pause_between_acquisitions_seconds = 60*0;
scans_amount = 1;
pause_between_scans_seconds = 60*0;
minimal_displayed_ppm_value = -10;
maximal_displayed_ppm_value = 100;
experiment_name = 'Accumulation_test_2023-11-02';
experiment_directory = sprintf('_Outputs/%s/%s', experiment_name, datestr(now,'yyyy-
mm-dd_HH-MM-SS'));
```

```
mkdir(experiment_directory);
sample_amount = 16384;
Larmor_frequency_Hertz = 24379288.130;
down_conversion_frequency_Hertz = 1000;
local_oscillator_shifted_frequency_Hertz = Larmor_frequency_Hertz +
down_conversion_frequency_Hertz;
excitation_duration_seconds = 41.027e-06;
excitation_burst_cycles = uint32(Larmor_frequency_Hertz *
excitation_duration_seconds);
excitation_amplitude_volts = 0.19;
oscillator_amplitude_volts = 0.8;
oscillator_offset_volts = 0.0;
sampling_decimation = 512*2;
sampling_rate_samples_per_second = 125000000 / sampling_decimation;
sampling_duration_seconds = sample_amount / sampling_rate_samples_per_second;
trigger_delay_samples = uint32((sample_amount/2) + ((sample_amount *
excitation_duration_seconds) / sampling_duration_seconds) + 1);
x_axis_seconds = (0:(sample_amount - 1)) * (sampling_duration_seconds /
(sample_amount - 1));
x_axis_Hertz_shifted = ((-sample_amount/2):((sample_amount/2)-1)) *
(sampling_rate_samples_per_second / sample_amount);
x_axis_Hertz_shifted = x_axis_Hertz_shifted + abs((x_axis_Hertz_shifted(1) +
x_axis_Hertz_shifted(sample_amount))/2);
x_axis_ppm_shifted = x_axis_Hertz_shifted(((sample_amount/2) + 1):sample_amount);
x_axis_ppm_shifted = x_axis_ppm_shifted - (x_axis_Hertz_shifted((sample_amount/2) +
1));
x_axis_ppm_shifted = (x_axis_ppm_shifted - down_conversion_frequency_Hertz) *
(1000000 / Larmor_frequency_Hertz);
if (maximal_displayed_ppm_value < x_axis_ppm_shifted(sample_amount/2)) &&
(minimal_displayed_ppm_value > x_axis_ppm_shifted(1)) && (maximal_displayed_ppm_value
> minimal_displayed_ppm_value)
    minimal_displayed_ppm_value_adjuster_x_axis = round((abs(x_axis_ppm_shifted(1) -
minimal_displayed_ppm_value)) / (abs(x_axis_ppm_shifted(1) -
x_axis_ppm_shifted(2))));
    maximal_displayed_ppm_value_adjuster_x_axis = round(((1 +
maximal_displayed_ppm_value + abs(x_axis_ppm_shifted(1))) /
(abs(x_axis_ppm_shifted(1) - x_axis_ppm_shifted(2)))));
    minimal_displayed_ppm_value_adjuster_y_axis = round(abs(sample_amount/2 +
round((abs(x_axis_ppm_shifted(1) - minimal_displayed_ppm_value)) /
(abs(x_axis_ppm_shifted(1) - x_axis_ppm_shifted(2))))));
    maximal_displayed_ppm_value_adjuster_y_axis = round(abs(sample_amount/2 +
round(((1 + maximal_displayed_ppm_value + abs(x_axis_ppm_shifted(1))) /
(abs(x_axis_ppm_shifted(1) - x_axis_ppm_shifted(2)))))));
else
    minimal_displayed_ppm_value_adjuster_x_axis = 1;
    maximal_displayed_ppm_value_adjuster_x_axis = sample_amount/2;
    minimal_displayed_ppm_value_adjuster_y_axis = 1;
    maximal_displayed_ppm_value_adjuster_y_axis = sample_amount/2;
end
x_axis_ppm_shifted = x_axis_ppm_shifted
(minimal_displayed_ppm_value_adjuster_x_axis:maximal_displayed_ppm_value_adjuster_x_a
xis);
IP = '169.254.115.97';
port = 5000;
SDR_Red_Pitaya = tcpclient(IP, port);
SDR_Red_Pitaya.ByteOrder = "big-endian";
configureTerminator(SDR_Red_Pitaya, "CR/LF");
flush(SDR_Red_Pitaya);
writeline(SDR_Red_Pitaya, 'SOUR1:FUNC SINE');
excitation_frequency_OCH1 = sprintf('SOUR1:FREQ:FIX %f', Larmor_frequency_Hertz);
```

```
writeline(SDR_Red_Pitaya, excitation_frequency_OCH1);
excitation_amplitude_OCH1 = sprintf('SOUR1:VOLT %f', excitation_amplitude_volts);
writeline(SDR_Red_Pitaya, excitation_amplitude_OCH1);
writeline(SDR_Red_Pitaya, 'SOUR1:BURS:STAT BURST');
excitation_pulses_OCH1 = sprintf('SOUR1:BURS:NCYC %f', excitation_burst_cycles);
writeline(SDR_Red_Pitaya, excitation_pulses_OCH1);
writeline(SDR_Red_Pitaya, 'SOUR2:FUNC SINE');
oscillation_frequency_OCH2 = sprintf('SOUR2:FREQ:FIX %f',
local_oscillator_shifted_frequency_Hertz);
writeline(SDR_Red_Pitaya, oscillation_frequency_OCH2);
oscillation_amplitude_OCH2 = sprintf('SOUR2:VOLT %f', oscillator_amplitude_volts);
writeline(SDR_Red_Pitaya, oscillation_amplitude_OCH2);
oscillation_offset_OCH2 = sprintf('SOUR2:VOLT:OFFS %f', oscillator_offset_volts);
writeline(SDR_Red_Pitaya, oscillation_offset_OCH2);
writeline(SDR_Red_Pitaya, 'ACQ:RST');
sampling_decimation_ICH1 = sprintf('ACQ:DEC %d', sampling_decimation);
writeline(SDR_Red_Pitaya, sampling_decimation_ICH1);
sampling_delay_ICH1 = sprintf('ACQ:TRIG:DLY %d', trigger_delay_samples);
writeline(SDR_Red_Pitaya, sampling_delay_ICH1);
writeline(SDR_Red_Pitaya, 'ACQ:SOUR1:GAIN LV');
writeline(SDR_Red_Pitaya, 'ACQ:SOUR2:GAIN HV');

%% acquisition and signal processing
for r = 1:scans_amount
    if r ~= 1
        pause(pause_between_scans_seconds);
    end
    for k = 1:acquisitions_amount
        if k ~= 1
            pause(pause_between_acquisitions_seconds);
        end
        LoadSystem;
        [Raw, SeqOut, data, data_1D] = set_sequence(HW, Seq, AQ, TX, Grad);
        writeline(SDR_Red_Pitaya, 'OUTPUT2:STATE ON');
        writeline(SDR_Red_Pitaya, 'ACQ:START;:ACQ:TRIG NOW;:OUTPUT1:STATE
ON;:OUTPUT1:STATE OFF');
        while 1
            trig_rsp = writeread(SDR_Red_Pitaya, 'ACQ:TRIG:STAT?');
            if strcmp('TD', trig_rsp(1:2))
                break
            end
        end
        writeline(SDR_Red_Pitaya, 'ACQ:STOP');
        writeline(SDR_Red_Pitaya, 'OUTPUT2:STATE OFF');
        signal_str = writeread(SDR_Red_Pitaya, 'ACQ:SOUR1:DATA?');
        y_axis_volts = str2num(signal_str(1, 2:length(signal_str) - 3));
        h1 = figure;
        plot(x_axis_seconds, y_axis_volts);
        grid on;
        ylabel('Amplitude (V)');
        xlabel('Time (s)');
        title('Raw FID');
        filename_fig = sprintf('FID_Raw_Scan_%d_of_%d_Acquisition_%d_of_%d.fig', r,
scans_amount, k, acquisitions_amount);
        saveas(h1, fullfile(experiment_directory, filename_fig));
        filename_png = sprintf('FID_Raw_Scan_%d_of_%d_Acquisition_%d_of_%d.png', r,
scans_amount, k, acquisitions_amount);
        saveas(h1, fullfile(experiment_directory, filename_png));
        close(h1);
    end
```

```
end
clear SDR_Red_Pitaya;
for r = 1:scans_amount
    for k = 1:acquisitions_amount
        h2 = openfig(fullfile(experiment_directory,
sprintf('FID_Raw_Scan_%d_of_%d_Acquisition_%d_of_%d.fig', r, scans_amount, k,
acquisitions_amount)));
        axObjs = h2.Children;
        dataObjs = axObjs.Children;
        x_t = dataObjs.XData;
        y_t = dataObjs.YData;
        close(h2);
        y_t = bandpass(y_t, [1000 (sampling_rate_samples_per_second/2)-1000],
sampling_rate_samples_per_second);
        h3 = figure;
        plot(x_t, y_t);
        grid on;
        ylabel('Amplitude (V)');
        xlabel('Time (s)');
        title('Filtered FID');
        filename_fig = sprintf('FID_Filtered_Scan_%d_of_%d_Acquisition_%d_of_%d.fig',
r, scans_amount, k, acquisitions_amount);
        saveas(h3, fullfile(experiment_directory, filename_fig));
        filename_png = sprintf('FID_Filtered_Scan_%d_of_%d_Acquisition_%d_of_%d.png',
r, scans_amount, k, acquisitions_amount);
        saveas(h3, fullfile(experiment_directory, filename_png));
        close(h3);
        if k == 1
            y_t_accumulated = y_t;
        else
            y_t_accumulated = y_t_accumulated + y_t;
        end
        y_f = fft(y_t);
        if k == 1
            y_f_accumulated = y_f;
        else
            y_f_accumulated = y_f_accumulated + y_f;
        end
        y_f_centered = fftshift(y_f);
        if k == 1
            y_f_centered_accumulated = y_f_centered;
        else
            y_f_centered_accumulated = y_f_centered_accumulated + y_f_centered;
        end
        h4 = figure;
        plot(x_axis_Hertz_shifted, abs(y_f_centered));
        grid on;
        ylabel('Spectral Magnitude (|V|)');
        xlabel('Frequency (Hz)');
        title('FFT (absolute spectral magnitude values)');
        filename_fig = sprintf('FFT_Filtered_Scan_%d_of_%d_Acquisition_%d_of_%d.fig',
r, scans_amount, k, acquisitions_amount);
        saveas(h4, fullfile(experiment_directory, filename_fig));
        filename_png = sprintf('FFT_Filtered_Scan_%d_of_%d_Acquisition_%d_of_%d.png',
r, scans_amount, k, acquisitions_amount);
        saveas(h4, fullfile(experiment_directory, filename_png));
        close(h4);
        [val, idx] = min(y_t, [], 'all');
        for i1 = idx:sample_amount
            if y_t(i1) < 0
```

```
                idx=idx+1;
            else
                idx=idx-1;
                break
            end
        end
        if abs(y_t(idx)) < abs(y_t(idx-1))
            idx=idx-1;
        end
        y_t_shifted = circshift(y_t,-idx);
        for i2 = sample_amount/2:sample_amount
            y_t_shifted(i2) = 0;
        end
        y_t_shifted(1) = 0;
        if k == 1
            y_t_shifted_accumulated = y_t_shifted;
        else
            y_t_shifted_accumulated = y_t_shifted_accumulated + y_t_shifted;
        end
        h5 = figure;
        plot(x_t, y_t_shifted);
        grid on;
        ylabel('Amplitude (V)');
        xlabel('Time (s)');
        title('Shifted FID');
        filename_fig = sprintf('FID_Shifted_Scan_%d_of_%d_Acquisition_%d_of_%d.fig',
r, scans_amount, k, acquisitions_amount);
        saveas(h5, fullfile(experiment_directory, filename_fig));
        filename_png = sprintf('FID_Shifted_Scan_%d_of_%d_Acquisition_%d_of_%d.png',
r, scans_amount, k, acquisitions_amount);
        saveas(h5, fullfile(experiment_directory, filename_png));
        close(h5);
        y_f_of_y_t_shifted = fft(y_t_shifted);
        if k == 1
            y_f_of_y_t_shifted_accumulated = y_f_of_y_t_shifted;
        else
            y_f_of_y_t_shifted_accumulated = y_f_of_y_t_shifted_accumulated +
y_f_of_y_t_shifted;
        end
        y_f_of_y_t_shifted_centered = fftshift(y_f_of_y_t_shifted);
        if k == 1
            y_f_of_y_t_shifted_centered_accumulated = y_f_of_y_t_shifted_centered;
        else
            y_f_of_y_t_shifted_centered_accumulated =
y_f_of_y_t_shifted_centered_accumulated + y_f_of_y_t_shifted_centered;
        end
        h6 = figure;
        plot(x_axis_Hertz_shifted, abs(y_f_of_y_t_shifted_centered));
        grid on;
        ylabel('Spectral Magnitude (|V|)');
        xlabel('Frequency (Hz)');
        title('FFT (shifted FID - absolute spectral magnitude values)');
        filename_fig =
sprintf('FFT_FID_Shifted_Scan_%d_of_%d_Acquisition_%d_of_%d.fig', r, scans_amount, k,
acquisitions_amount);
        saveas(h6, fullfile(experiment_directory, filename_fig));
        filename_png =
sprintf('FFT_FID_Shifted_Scan_%d_of_%d_Acquisition_%d_of_%d.png', r, scans_amount, k,
acquisitions_amount);
        saveas(h6, fullfile(experiment_directory, filename_png));
```

```
        close(h6);
        y_f_of_y_t_shifted_centered_squared =
abs(y_f_of_y_t_shifted_centered).^2/sample_amount;
        if k == 1
            y_f_of_y_t_shifted_centered_squared_accumulated =
y_f_of_y_t_shifted_centered_squared;
        else
            y_f_of_y_t_shifted_centered_squared_accumulated =
y_f_of_y_t_shifted_centered_squared_accumulated +
y_f_of_y_t_shifted_centered_squared;
        end
        h7 = figure;
        plot(x_axis_Hertz_shifted, y_f_of_y_t_shifted_centered_squared);
        grid on;
        ylabel('Squared Normalized Spectral Magnitude (|V|^2/N)');
        xlabel('Frequency (Hz)');
        title('Squared normalized FFT (shifted FID)');
        filename_fig =
sprintf('FFT_Squared_Normalized_FID_Shifted_Scan_%d_of_%d_Acquisition_%d_of_%d.fig',
r, scans_amount, k, acquisitions_amount);
        saveas(h7, fullfile(experiment_directory, filename_fig));
        filename_png =
sprintf('FFT_Squared_Normalized_FID_Shifted_Scan_%d_of_%d_Acquisition_%d_of_%d.png',
r, scans_amount, k, acquisitions_amount);
        saveas(h7, fullfile(experiment_directory, filename_png));
        close(h7);
        y_f_of_y_t_shifted_centered_squared =
medfilt1(y_f_of_y_t_shifted_centered_squared, 3);
        h8 = figure;
        plot(x_axis_ppm_shifted,
flip(y_f_of_y_t_shifted_centered_squared(minimal_displayed_ppm_value_adjuster_y_axis:
maximal_displayed_ppm_value_adjuster_y_axis)));
        grid on;
        ylabel('Squared Normalized Spectral Magnitude (|V|^2/N)');
        xlabel('Chemical Shift (ppm)');
        set (gca, 'xdir', 'reverse');
        title('NMR spectrum (shifted FID)');
        filename_fig =
sprintf('NMR_Spectrum_FID_Shifted_Scan_%d_of_%d_Acquisition_%d_of_%d.fig', r,
scans_amount, k, acquisitions_amount);
        saveas(h8, fullfile(experiment_directory, filename_fig));
        filename_png =
sprintf('NMR_Spectrum_FID_Shifted_Scan_%d_of_%d_Acquisition_%d_of_%d.png', r,
scans_amount, k, acquisitions_amount);
        saveas(h8, fullfile(experiment_directory, filename_png));
        close(h8);
    end
    y_t_accumulated;
    y_f_accumulated;
    y_f_centered_accumulated;
    y_t_shifted_accumulated;
    y_f_of_y_t_shifted_accumulated;
    y_f_of_y_t_shifted_centered_accumulated;
    y_f_of_y_t_shifted_centered_squared_accumulated;
    h10 = figure;
    tiledlayout(4,1);
    FID_not_shifted_accumulated = nexttile;
    plot(FID_not_shifted_accumulated, x_t, y_t_accumulated);
    grid on;
    ylabel('Amplitude (V) * acquisitions_amount');
```

```
    xlabel('Time (s)');
    title('Accumulated raw FIDs (no previous FID shifting)');
    y_f_of_y_t_accumulated = fft(y_t_accumulated);
    y_f_centered_of_y_t_accumulated = fftshift(y_f_of_y_t_accumulated);
    y_f_centered_squared_of_y_t_accumulated =
abs(y_f_centered_of_y_t_accumulated).^2/sample_amount;
    y_f_centered_squared_of_y_t_accumulated =
medfilt1(y_f_centered_squared_of_y_t_accumulated, 3);
    NMR_spectrum_accumulated_in_not_shifted_t = nexttile;
    plot(NMR_spectrum_accumulated_in_not_shifted_t, x_axis_ppm_shifted,
flip(y_f_centered_squared_of_y_t_accumulated(minimal_displayed_ppm_value_adjuster_y_a
xis:maximal_displayed_ppm_value_adjuster_y_axis)));
    grid on;
    ylabel('Squared Normalized Spectral Magnitude (|V|^2/N * acquisitions_amount)');
    xlabel('Chemical Shift (ppm)');
    NMR_spectrum_accumulated_in_not_shifted_t.XDir = 'reverse';
    title('NMR spectrum for (not shifted) accumulated FIDs');
    FID_shifted_accumulated = nexttile;
    plot(FID_shifted_accumulated, x_t, y_t_shifted_accumulated);
    grid on;
    ylabel('Amplitude (V) * acquisitions_amount');
    xlabel('Time (s)');
    title('Accumulated shifted FIDs');
    y_f_of_y_t_accumulated_shifted = fft(y_t_shifted_accumulated);
    y_f_centered_of_y_t_shifted_accumulated =
fftshift(y_f_of_y_t_accumulated_shifted);
    y_f_centered_squared_of_y_t_shifted_accumulated =
abs(y_f_centered_of_y_t_shifted_accumulated).^2/sample_amount;
    y_f_centered_squared_of_y_t_shifted_accumulated =
medfilt1(y_f_centered_squared_of_y_t_shifted_accumulated, 3);
    NMR_spectrum_accumulated_in_shifted_t = nexttile;
    plot(NMR_spectrum_accumulated_in_shifted_t, x_axis_ppm_shifted,
flip(y_f_centered_squared_of_y_t_shifted_accumulated(minimal_displayed_ppm_value_adju
ster_y_axis:maximal_displayed_ppm_value_adjuster_y_axis)));
    grid on;
    ylabel('Squared Normalized Spectral Magnitude (|V|^2/N * acquisitions_amount)');
    xlabel('Chemical Shift (ppm)');
    NMR_spectrum_accumulated_in_shifted_t.XDir = 'reverse';
    title('NMR spectrum for (shifted) accumulated FIDs');
    filename_fig =
sprintf('Accumulation_Results_Scan_%d_of_%d_with_%d_Acquisitions.fig', r,
scans_amount, acquisitions_amount);
    saveas(h10, fullfile(experiment_directory, filename_fig));
    filename_png =
sprintf('Accumulation_Results_Scan_%d_of_%d_with_%d_Acquisitions.png', r,
scans_amount, acquisitions_amount);
    saveas(h10, fullfile(experiment_directory, filename_png));
    close(h10);
    h11 = figure;
    plot(x_axis_ppm_shifted,
flip(y_f_centered_squared_of_y_t_accumulated(minimal_displayed_ppm_value_adjuster_y_a
xis:maximal_displayed_ppm_value_adjuster_y_axis)));
    grid on;
    ylabel('Squared Normalized Spectral Magnitude (|V|^2/N * acquisitions_amount)');
    xlabel('Chemical Shift (ppm)');
    set (gca, 'xdir', 'reverse');
    title('NMR spectrum for (not shifted) accumulated FIDs');
    filename_fig =
sprintf('Accumulation_Results_Scan_%d_of_%d_with_%d_Acquisitions_ONLY_NMR_SPECTRUM_NO
_FID_SHIFT.fig', r, scans_amount, acquisitions_amount);
```

```
    saveas(h11, fullfile(experiment_directory, filename_fig));
    filename_png =
sprintf('Accumulation_Results_Scan_%d_of_%d_with_%d_Acquisitions_ONLY_NMR_SPECTRUM_NO
_FID_SHIFT.png', r, scans_amount, acquisitions_amount);
    saveas(h11, fullfile(experiment_directory, filename_png));
    close(h11);
    h13 = figure;
    plot(x_axis_ppm_shifted,
flip(y_f_centered_squared_of_y_t_shifted_accumulated(minimal_displayed_ppm_value_adju
ster_y_axis:maximal_displayed_ppm_value_adjuster_y_axis)));
    grid on;
    ylabel('Squared Normalized Spectral Magnitude (|V|^2/N * acquisitions_amount)');
    xlabel('Chemical Shift (ppm)');
    set (gca, 'xdir', 'reverse');
    title('NMR spectrum for (shifted) accumulated FIDs');
    filename_fig =
sprintf('Accumulation_Results_Scan_%d_of_%d_with_%d_Acquisitions_ONLY_NMR_SPECTRUM_WI
TH_FID_SHIFT.fig', r, scans_amount, acquisitions_amount);
    saveas(h13, fullfile(experiment_directory, filename_fig));
    filename_png =
sprintf('Accumulation_Results_Scan_%d_of_%d_with_%d_Acquisitions_ONLY_NMR_SPECTRUM_WI
TH_FID_SHIFT.png', r, scans_amount, acquisitions_amount);
    saveas(h13, fullfile(experiment_directory, filename_png));
    close(h13);
end
```

IV. NMR Prototype electronic schematics

The custom electronics of our prototype, as indicated in Figure 76, is composed of two boards. The small one hosts the mixer ASIC, as depicted in Figure 62. The local oscillator module shown in Figure 61 as well as the passive switch and the preamplifier elements from Figure 57 are located in the big one, whose schematic diagram can be seen in Figure 106.

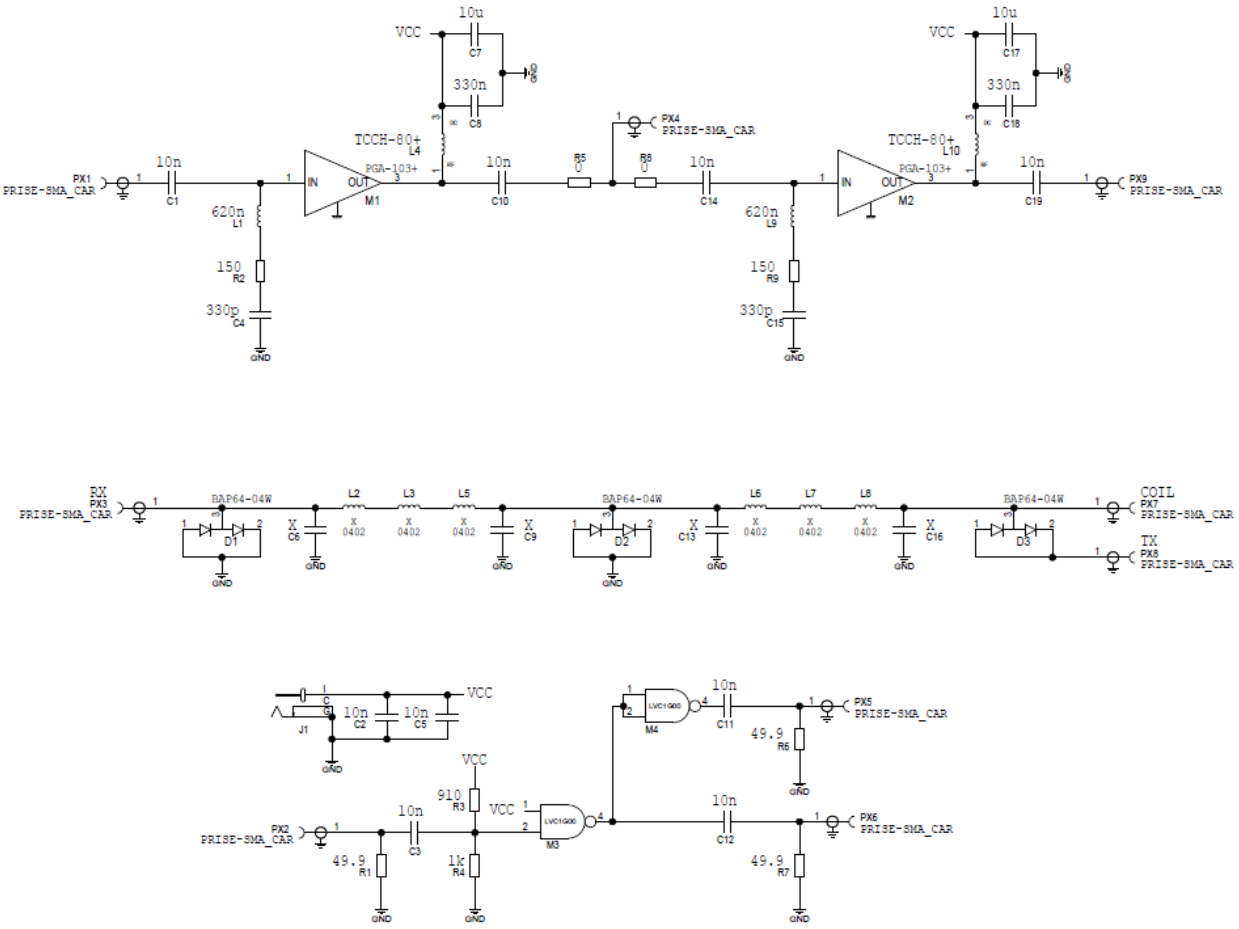

Figure 106 - Schematics of the custom electronics of our NMR Spectrometer Prototype.

Université de Strasbourg

Guilherme BAUMGARTEN

Développement et caractérisation d'une sonde RMN portable appliquée au suivi de la qualité de l'eau et à l'étude de la cinétique des réactions chimiques

Résumé

La spectroscopie de résonance magnétique nucléaire (RMN) est une technique amplement utilisée pour la détection et la quantification de composés chimiques avec un spectre d'application très large. Dans ce manuscrit, deux d'entre eux sont traités : la détection de polluants dans l'eau potable et la surveillance des réactions chimiques. Alors que les équipements de RMN de laboratoire présentent des résultats d'analyse très fiables, la RMN portable est un domaine de recherche en évolution avec de multiples défis technologiques et d'autres liés aux applications ciblées. Les dispositifs RMN portables émergents présentent cependant comme avantage évidente par rapport aux dispositifs classiques leur utilisation directe sur le terrain. Cela permet ainsi d'avoir des résultats d'analyses plus rapidement et de limiter les coûts de personnel et de consommables. Afin de concevoir des spectromètres RMN portables, on doit faire des compromis de conception, tout en étant capable de comprendre les enjeux liés à ces choix, afin que le produit final puisse toujours répondre aux exigences des applications concernées. Pour cela, nous proposons une chaîne d'outils de simulation RMN complète, capable de générer divers aboutissements correspondant à un spectromètre RMN réel. En outre, nous développons une preuve de concept de l'électronique de contrôle et d'acquisition basée sur des composants commerciaux disponibles et nous la validons sur notre prototype de spectromètre RMN portable. Finalement, ce prototype est utilisé pour évaluer le potentiel de la RMN portable pour les applications citées ci-dessus. Cette étude nous a permis d'identifier les limites du dispositif actuel et de proposer un cahier des charges visant son amélioration continue.

Mots-clés : résonance magnétique nucléaire, RMN portable, spectromètre RMN, détection de polluants, pesticides, eau potable, suivi de réactions chimiques, cinétique chimique, simulation, radio logicielle, prototypage.

Abstract

Nuclear Magnetic Reaction (NMR) spectroscopy is a widely employed technique in the detection and quantification of chemical compounds, with a wide range of applications. In this manuscript, the focus is put on two of them: the detection of pollutants in drinking water and the monitoring of chemical reactions. While laboratory NMR equipment presents highly reliable analysis results, portable miniaturized NMR is an evolving research field with multiple technological and application-related challenges. Such emerging devices present however a clear advantage when compared to the classic, stablished ones: it can be used in the field, therefore saving time and limiting staff and consumables costs. In order to design NMR spectrometers to attain the desired portability and miniaturization, one has to compromise, however being able to understand what is at stake, so that the final product still meets the demands. For that, we propose a complete NMR simulation toolchain capable of generating diverse outcomes corresponding to a real NMR spectrometer. Furthermore, we develop a proof of concept for an electronic control and acquisition unit based on commercial-off-the-shelf components and validate it on a portable NMR spectrometer prototype. Finally, we use this prototype to assess the potential of portable miniaturized NMR for the targeted applications cited above. This study allowed us to identify the limits of our current prototypical device and to provide directions for its further improvement.

Keywords: nuclear magnetic resonance, portable NMR, NMR spectrometer, pollutants detection, pesticides, drinking water, chemical reactions monitoring, chemical kinetics, simulation, software-defined radio, prototyping.

Résumé étendu

Développement et caractérisation d’une sonde RMN portable appliquée au suivi de la qualité de l’eau et à l’étude de la cinétique des réactions chimiques

Guilherme Baumgarten

Introduction, contexte et état de l’art

Le travail présenté ici a été le fruit des activités réalisées à l’Université de Strasbourg et à l’Haute Ecole Spécialisée de la Suisse du Nord-Ouest FHNW, et dans le cadre des projets WPS (Water Pollution Sensor : capteurs pour l’eau potable) et ANR Dip-NMR (spectroscope à micro-sondes RMN immergé pour l’analyse de réactions catalytiques). Ce résumé a pour objectif d’être une vue d'ensemble du travail développé et de résultats achevés pendant mes études doctorales, ainsi que de fournir un aperçu de contributions à la communauté scientifique et aux consortiums participants.

La thématique centrale de cette thèse étant la RMN (Résonance Magnétique Nucléaire) à champ faible, nous admettions l’hypothèse qu’une microsonde RMN portable serait un atout pour diverses possibles applications et promouvrait ainsi des avances scientifiques dans ce domaine, contribuant de cette manière à l’avancement de l’état de l’art des spectromètres RMN portables et miniaturisés. Les figures 1, 2 et 3 présentent des exemples the systèmes portables et miniaturisés de spectroscopie RMN faisant partie de l’état de l’art des dans ce domaine.

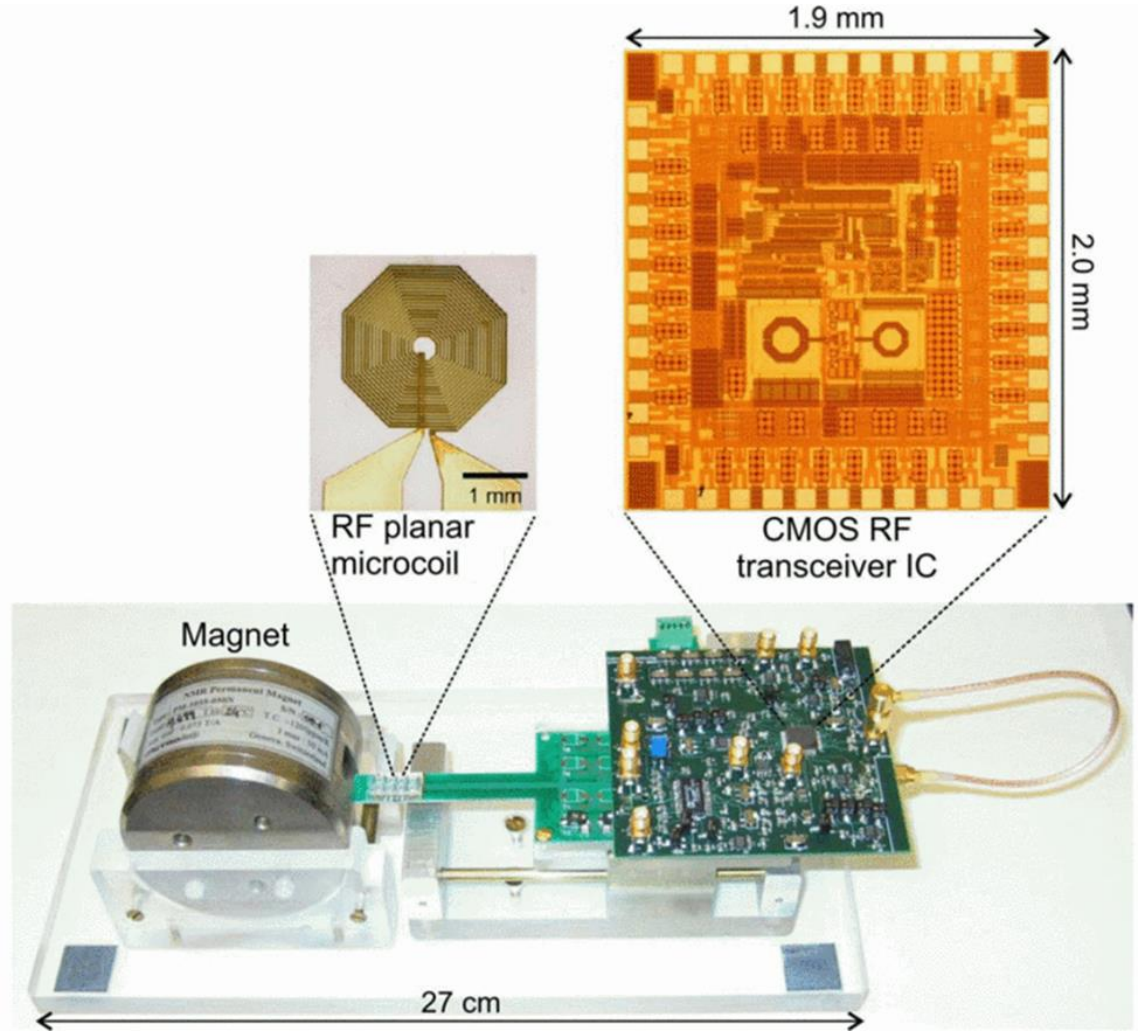

Figure 1 : Biocapteur CMOS RF utilisant RMN.

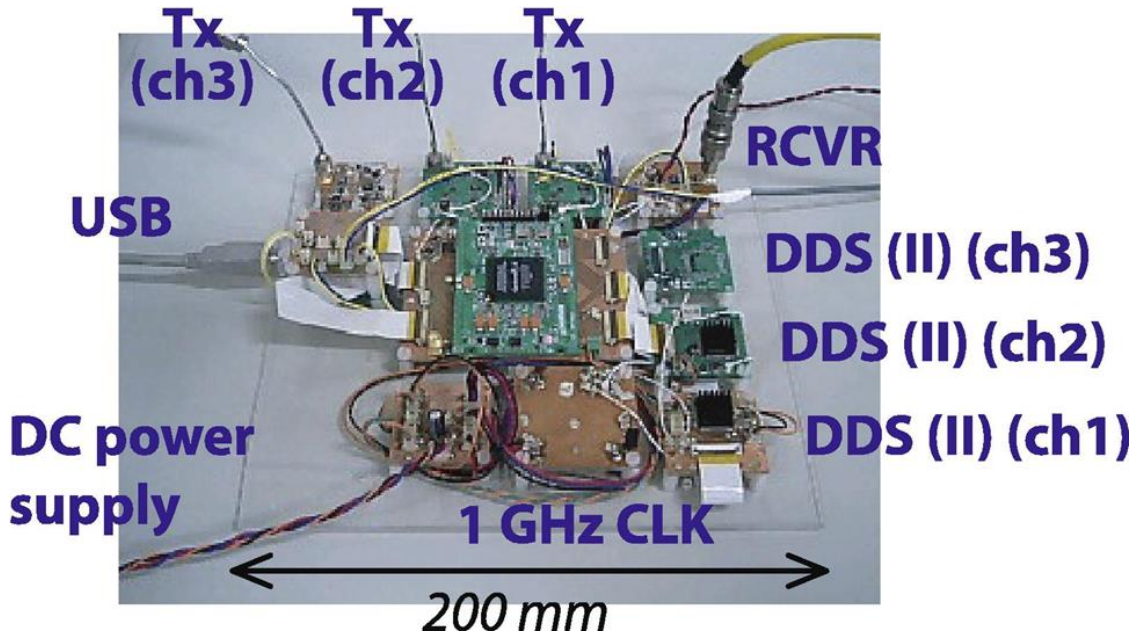

Figure 2 : Spectromètre RMN OPENCORE avec de l'électronique faite maison.

Figure 3 : Spectromètre RMN à relaxation Lab-Tools Mk3 avec un Red Pitaya STEMLab 125-14.

Bien que les techniques RMN soient principalement utilisées par les chimistes pour l'analyse et l'identification des substances contenues dans une solution, le développement d'un spectromètre RMN est en soi un sujet multidisciplinaire, où de nombreux domaines scientifiques comme la chimie, la physique et la physique quantique, les mathématiques, l'électronique, la programmation (pour n'en citer que quelques-uns) entrent en jeu, nécessitant par conséquent la compréhension concomitante de certains de leurs aspects à des degrés différents. La conception et la mise en œuvre réussies de tels systèmes ainsi que leur bon fonctionnement dépendent donc de nombreux aspects distincts qui nécessitent une large compréhension multidisciplinaire.

Ce travail a ainsi été réalisé en partant de l'idée qu'un dispositif RMN portable miniaturisé pour surveiller la qualité de l'eau et de diverses réactions chimiques serait d'un grand intérêt pour la recherche et à des fins commerciales. La détection de polluants dans l'eau potable étant un atout majeur dans ce qui concerne la préservation de la santé humaine, on cite actuellement la détection de la molécule glyphosate, partie constituante dans plusieurs pesticides, comme un sujet d'actualité dans ce qui concerne l'agriculture de précision. La figure 4 détaille l'impact des différents pesticides dans le corps humain.

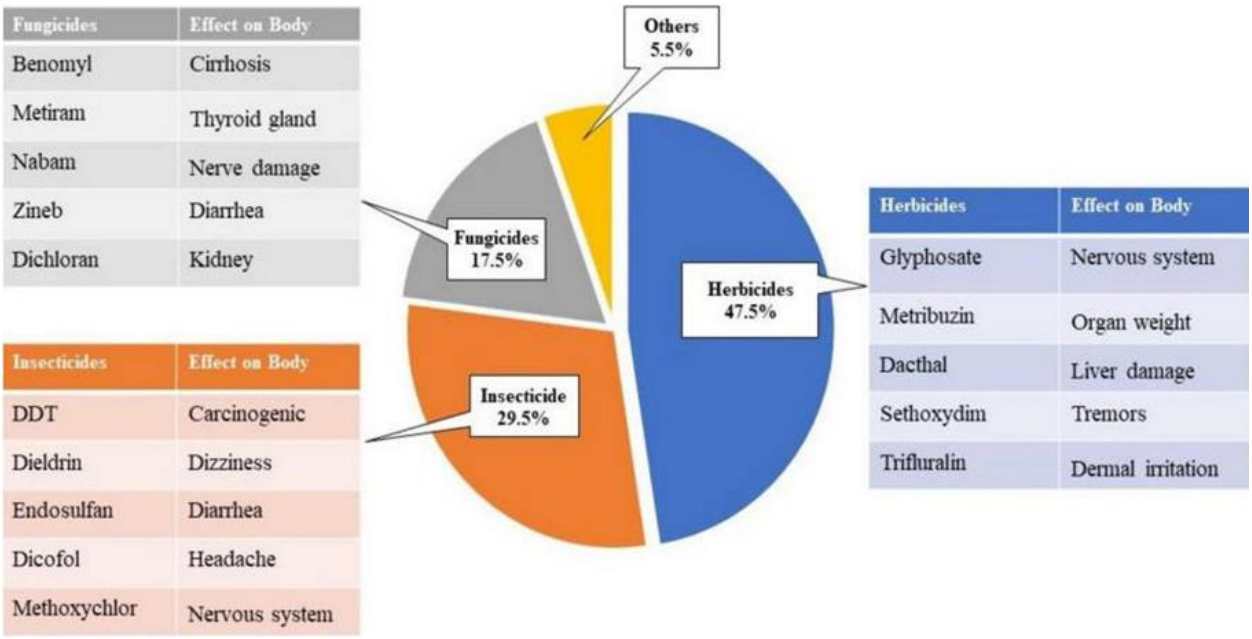

Figure 4 : Répartition des pesticides en pourcentage.

En ce qui concerne le suivi de réactions chimiques, la RMN est un outil puissant qui permet de réaliser une très fiable caractérisation de la cinétique des réactions. La figure 5 présente un exemple de suivi de réaction chimique par RMN.

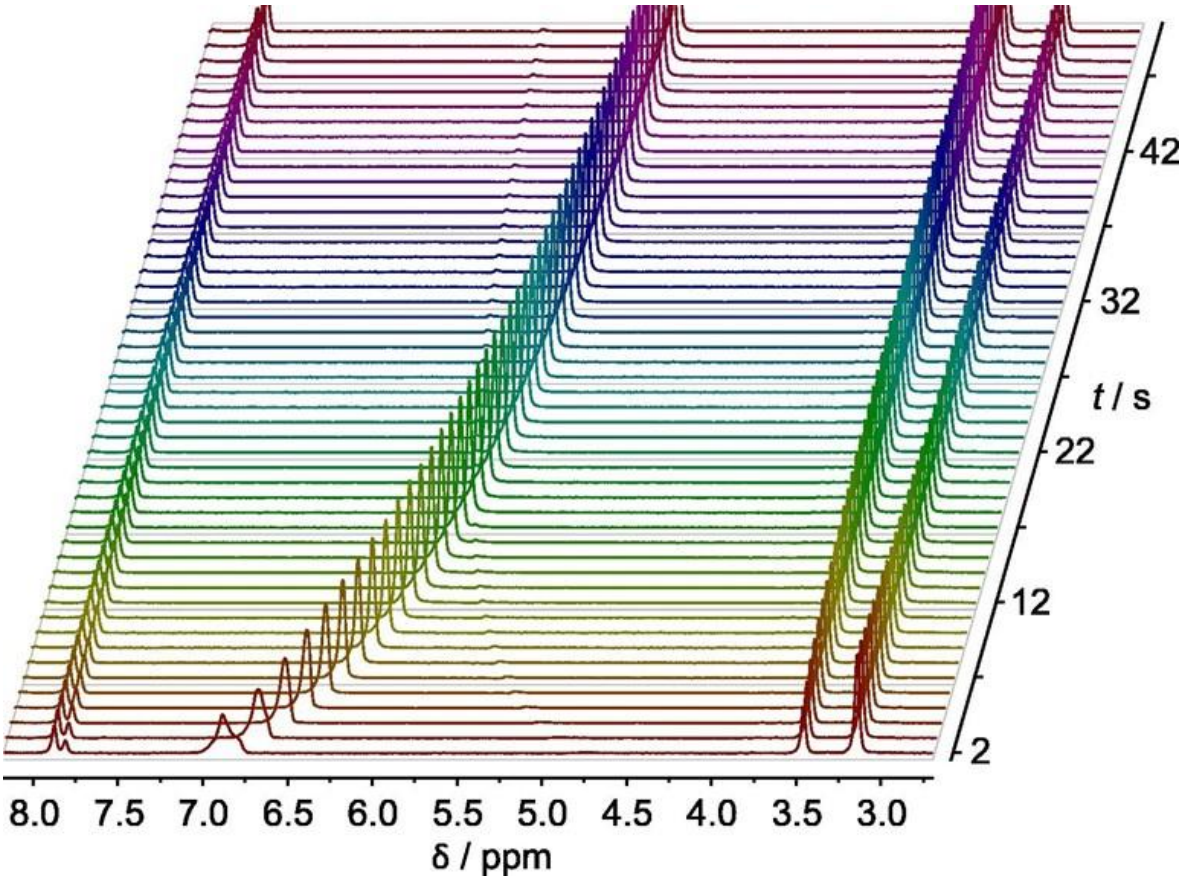

Figure 5 : Graphique empilé des spectres ^{1}H RMN en fonction du temps de réaction.

De ce fait, nous avons développé un dispositif RMN portable miniaturisé à l'aide de composants matériels à faible coût disponibles dans le commerce, ce qui avait comme objectif rendre sa mise en œuvre moins coûteuse par rapport aux alternatives actuellement disponibles sur le marché, bien que celles-là ne soient pas tout à fait des solutions portables, et encore moins miniaturisées. L'utilisation des composants électroniques disponibles dans le commerce signifiait également que le processus de production d'un tel système développé sur ces bases a pu être au moins partiellement simplifié.

Cadre théorique

La RMN est basée sur le principe de la résonance magnétique et a été décrit pour la première fois par Isidor Rabi en 1938, en conséquence des travails précédents du binôme Stern–Gerlach en 1921 et 1922.

Chaque élément chimique participant à l'expérience RMN présente un moment magnétique de par ses particules élémentaires qui s'appelle *spin*. La superposition des *spins* des molécules dans une solution chimique sous l'effet d'un champ magnétique statique (en RMN appelé $\overrightarrow{B_0}$) produit le vecteur magnétisation $\vec{M}$, comme démontré dans la figure 6.

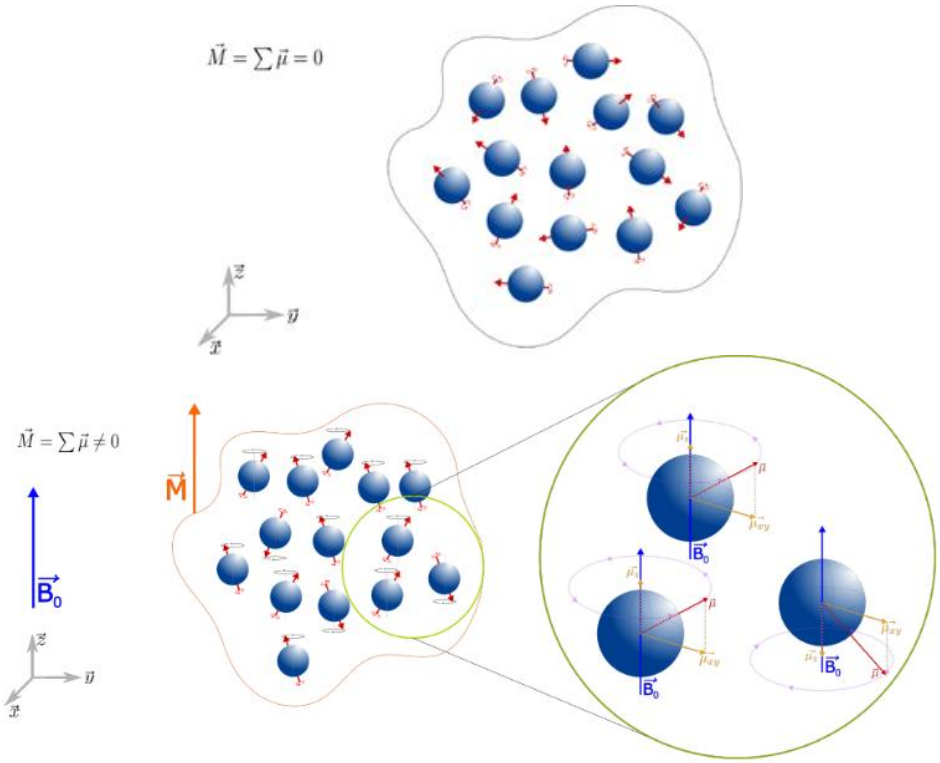

Figure 6 : Au-dessus : dans l'absence d'un champ magnétique statique, il n'y a pas de vecteur magnétisation résultant. Au-dessous : l'apparition d'un champ magnétique statique $\overrightarrow{B_0}$ fait que le vecteur magnétisation $\vec{M}$ soit.

Le mouvement tridimensionnel d'alignement de $\vec{M}$ vers la direction de $\overrightarrow{B_0}$ s'appelle précession et se produit à une fréquence spécifique appelée fréquence de Larmor, qui dépend de la nature du noyau et de l'intensité même de $\overrightarrow{B_0}$:

$$\omega_0 = \gamma B_0$$

$$f_0 = \frac{\omega_0}{2\pi}$$

$$f_0 = \frac{\gamma\, B_0}{2\pi}$$

De ce fait, pour chaque noyau diffèrent, nous avons une fréquence de Larmor différente, ce qui nous ramène à parler de ^{1}H RMN, ^{19}F RMN, ^{31}P RMN, et ainsi de suite.

L'application d'un champ magnétique temporaire $\overrightarrow{B_1}$ à la fréquence de Larmor f_0 et perpendiculaire à $\overrightarrow{B_0}$ fait que $\vec{M}$ ne soit plus aligné à $\overrightarrow{B_0}$. Dans l'exact moment où $\overrightarrow{B_1}$ cesse, $\vec{M}$ commence à s'aligner vers $\overrightarrow{B_0}$, quoiqu'à une fréquence f_{FID} un petit peu différente de la fréquence d'excitation de $\overrightarrow{B_1}$. Cette différence par rapport à la fréquence de Larmor est appelée déplacement chimique δ et caractérise le noyau, étant habituellement exprimé en termes de parties par millions (ppm), i.e., 10^{-6} de la fréquence de Larmor :

$$f_{FID} = f_0\,(1 + \delta)$$

$$\delta = \frac{f_{FID} - f_0}{f_0}$$

En mesurant le signal RMN provenant de la solution chimique avec une bobine RMN, nous obtenons un signal électrique dans la forme d'une décroissance libre de l'induction (de l'anglais : FID ou *Free Induction Decay*), comme illustré dans la figure 7.

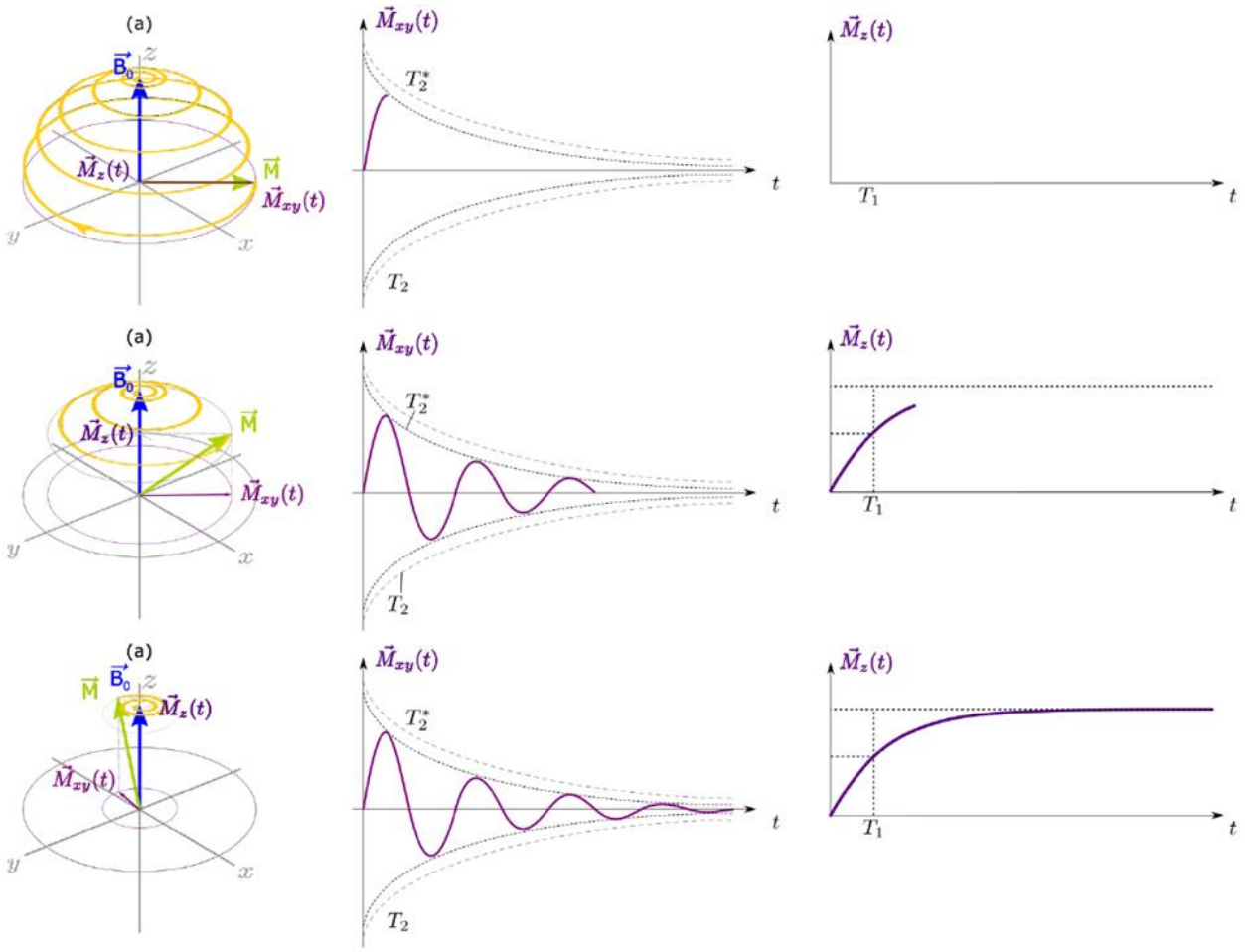

Figure 7 : L'évolution temporelle du vecteur magnétisation $\vec{M}$ dans la perspective de la bobine RMN : le signal électrique perçu est dans la forme d'une FID dont la vitesse de décroissance est définie par la constante temporelle T_2^*.

Une FID peut être décrite mathématiquement de la façon suivante :

$$\mathcal{s}_{FID}^{Q}(t) = \mathcal{s}_0[\cos(\omega_{FID}t) + i\sin(\omega_{FID}t)]e^{\frac{-t}{T_2^*}} \qquad \forall\, t \geq 0$$

En utilisant la transformation de Fourier, nous pouvons extraire l'information fréquentielle des FIDs mesurées, générant ainsi des spectres RMN avec des pics en formes de lorentziennes :

$$S_{FID}^{Q}(f) = \frac{\mathcal{s}_0}{2\pi\left(i2\pi(f_{FID} - f) - \frac{1}{T_2^*}\right)}$$

La figure 8 nous montre des exemples des spectres RMN basse et haute résolution pour la molécule d'éthanol.

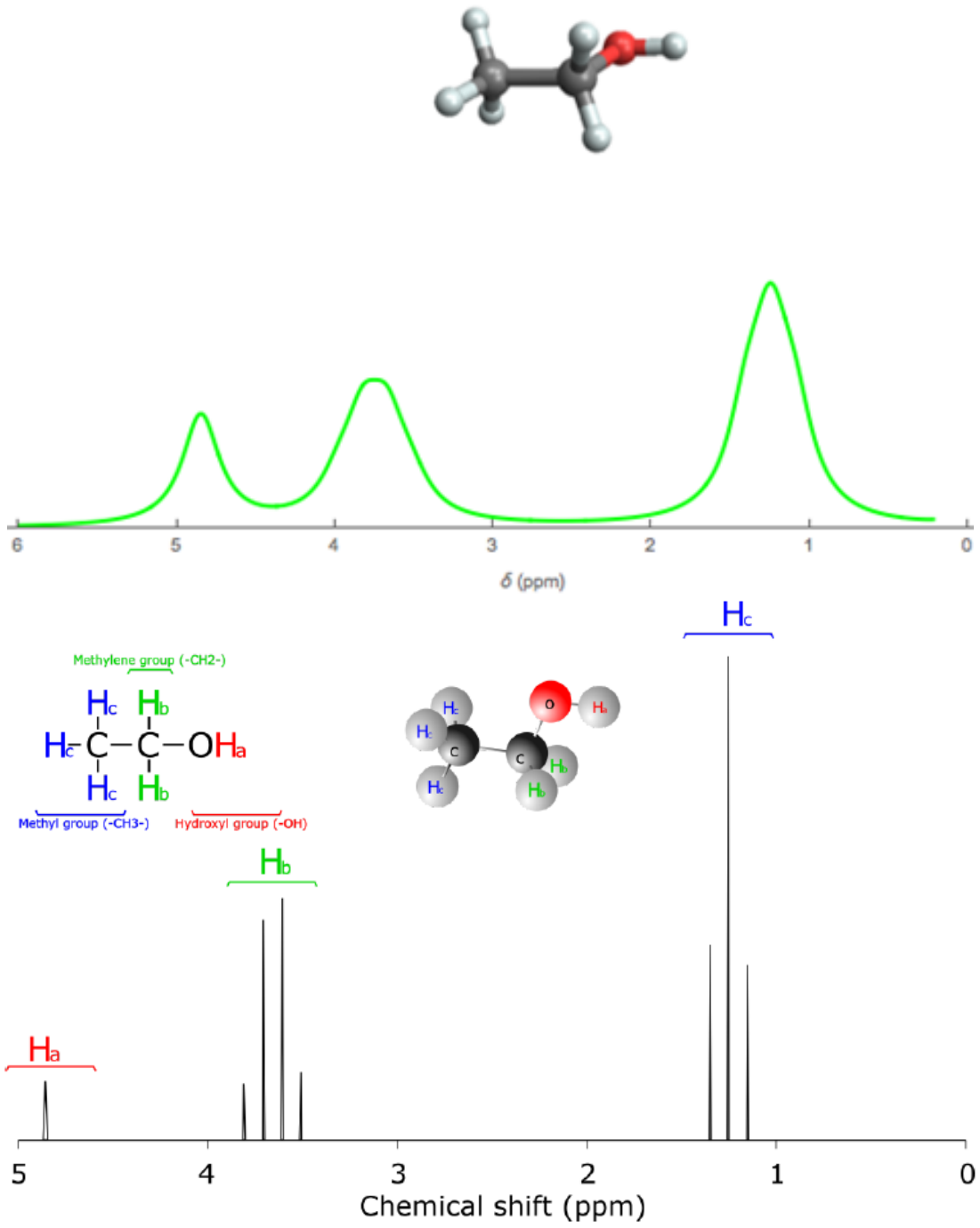

Figure 8 : Représentation spectrale des déplacements chimiques correspondant aux groupes fonctionnels de la molécule de l'éthanol. Au-dessus : résultat obtenu avec de la RMN base résolution. Au-dessous : celui pour la RMN haute résolution.

Pour pouvoir mesurer de tels spectres, un système RMN est composé normalement par un aiment permanent, une bobine d'excitation et autre pour la réception, et de l'électronique nécessaire pour générer le signal d'excitation et traiter le signal RMN mesuré. Très communément dans les systèmes RMN, les bobines d'excitation et de réception sont la même bobine, étant simplement appelée bobine RMN ou bobine réceptrice (de l'anglais : *receiving coil*). Une vue d'ensemble d'un spectromètre RMN est présentée dans la figure 9.

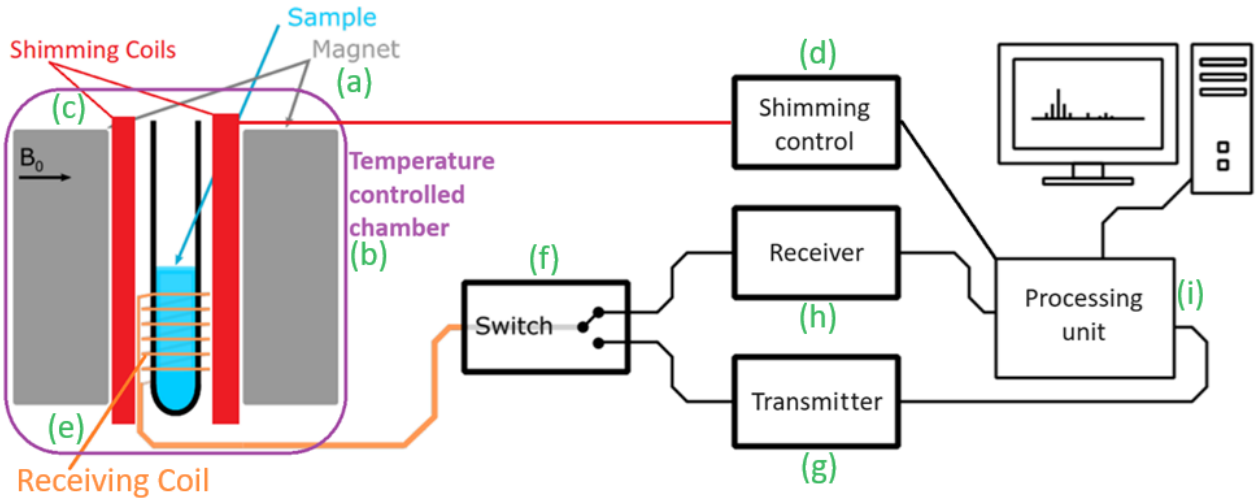

Figure 9 : Une représentation possible d'un spectromètre RMN illustrant ses différents éléments et utilisant une seule bobine pour l'excitation de l'échantillon chimique et pour la mesure ultérieure du signal RMN correspondant.

Afin de poursuivre le développement d'un prototype de spectromètre RMN, différentes activités de R&D (Recherche et Développement) ont été réalisées pendant la durée de ces études doctorales. Ces activités peuvent être formellement divisées en 3 domaines principaux : (1) le développement d'outils de simulation destinés à la compréhension et à la prédiction des performances des systèmes de spectrométrie RMN, (2) le développement d'un prototype de spectromètre RMN en tant que preuve de concept concernant les applications ciblées, et (3) la détermination des spécifications supplémentaires pour la poursuite du développement de ce prototype afin d'atteindre à terme les performances requises pour une application commerciale.

Chaîne d'outils de simulation pour la RMN

Le premier grand axe de ce travail propose des outils de simulation différents et complémentaires, modélisant une chaîne électronique de spectromètre RMN et différents aspects de l'expérience RMN. L'ensemble de cette chaîne d'outils logiciels, qui est dévoilé dans la figure 10, est, par conséquent, en mesure de fournir des informations conséquentes par rapport à la chaîne d'outils électroniques et au spectromètre RMN lui-même, étant ainsi capable d'estimer et d'évaluer certains aspects de l'utilisation de ces systèmes, et conséquemment étant capable d'éclaircir des contraintes techniques agissant dans le processus de conception d'un spectromètre RMN.

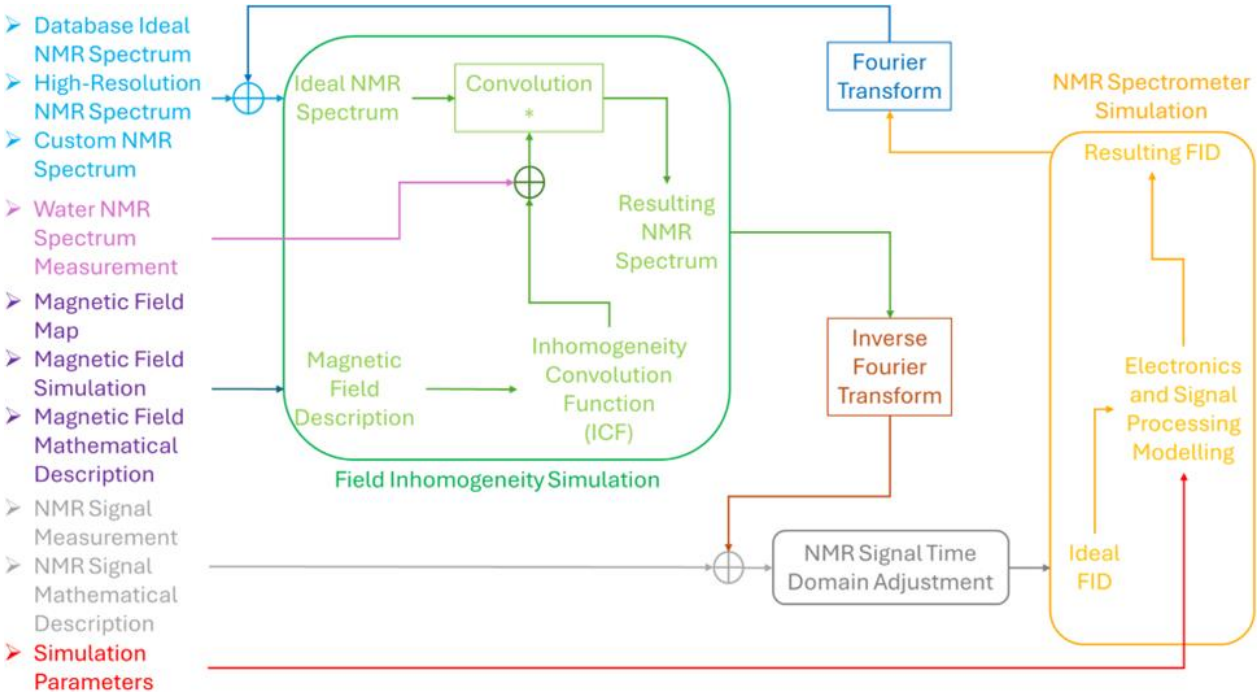

Figure 10 : Vue d'ensemble de notre chaîne d'outils de simulation pour la RMN.

Nous avons développé de cette manière les outils suivants :

- Un module de simulation capable de prédire la déformation d'un spectre RMN par rapport à l'inhomogénéité du champ magnétique statique $\overrightarrow{B_0}$, selon le diagramme de la figure 11.

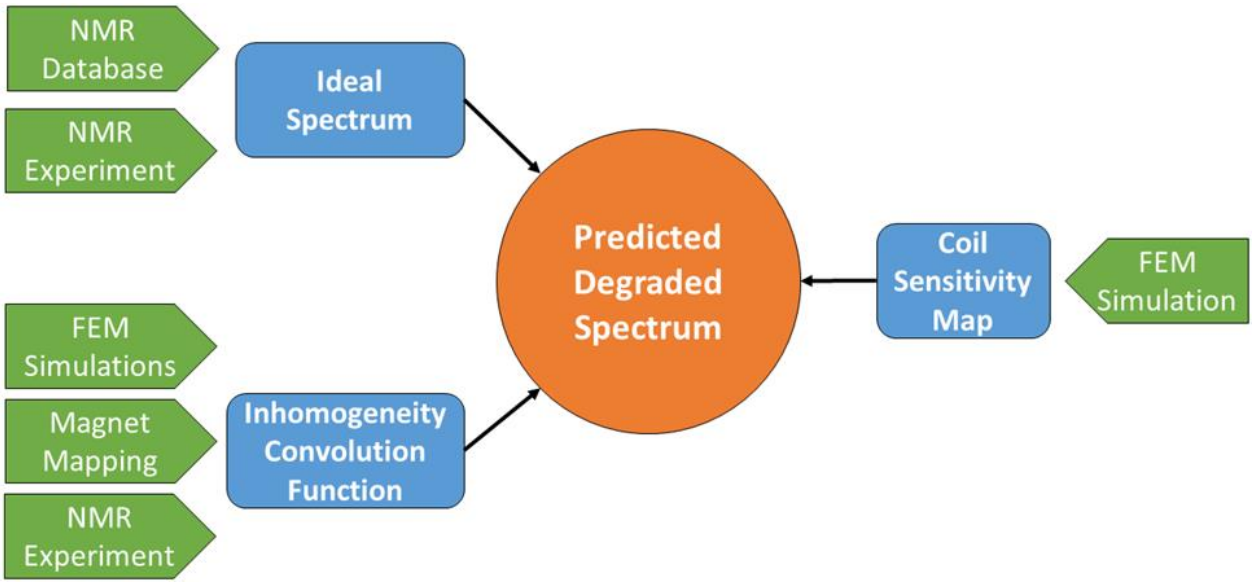

Figure 11 : La prédiction de la dégradation spectrale prend en considération trois variables : un spectre RMN idéal, la fonction de convolution d'inhomogénéité dérivée de la description du champ magnétique statique, et la sensibilité de la bobine réceptrice.

- Une application paramétrable capable de simuler toute la chaîne électronique correspondant à un spectromètre RMN (en ce qui concerne les éléments composant les modules d'émission et de réception), fournissant ainsi les signaux attendus à chacune des différentes étapes du traitement électronique. Ce programme peut nous fournir toutes les formes d'onde intermédiaires attendues dans les composants électroniques d'un spectromètre RMN. La simulation de la chaîne électronique prend en compte les éléments présentés dans la figure 12.

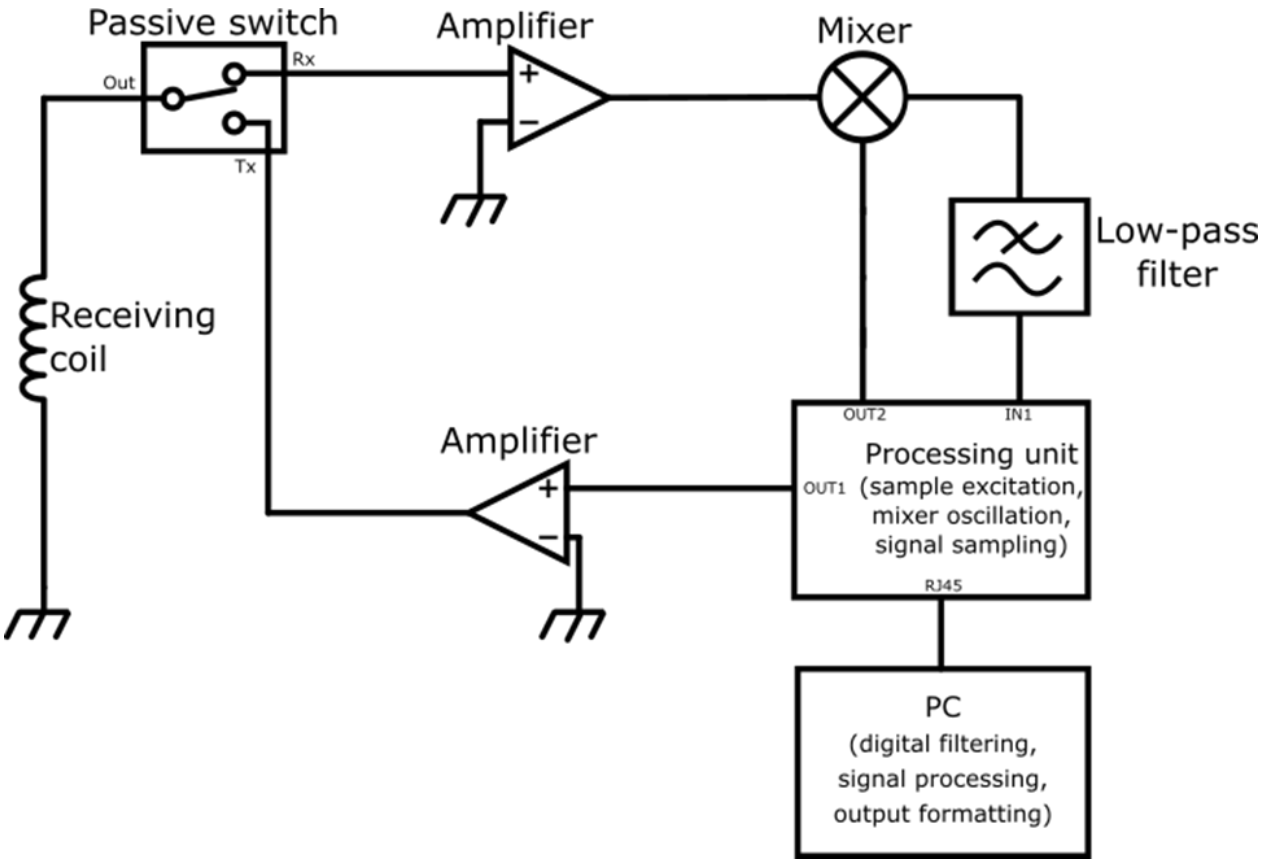

Figure 12 : Circuit de référence pour le module de simulation de la chaîne électronique.

- Un script qui permet la mise en œuvre d'une procédure d'accumulation de mesures à travers de dilatations et de déplacements temporels, à condition que les amplitudes des signaux mesurés soient au-dessus du plancher de bruit.

Prototype de spectromètre RMN

Le deuxième bloc de travail porte sur le développement d'un prototype de spectromètre RMN. Un système RMN complet est composé d'un générateur de champ magnétique très

stable et homogène (étant généralement un aimant permanent, mais aussi, par exemple, un électro-aimant), d'une bobine et de circuits électroniques de conditionnement et d'acquisition. Notre prototype est constitué d'un aimant permanent et d'un système de correction de l'homogénéité du champ magnétique $\overrightarrow{B_0}$ (*shim*) provenant d'un spectromètre RMN de type *Benchtop* de la société Pure Devices, ainsi que des éléments d'électronique commerciaux et d'autres faits par nous-mêmes. La figure 13 dépeint la composition de notre prototype de spectromètre RMN.

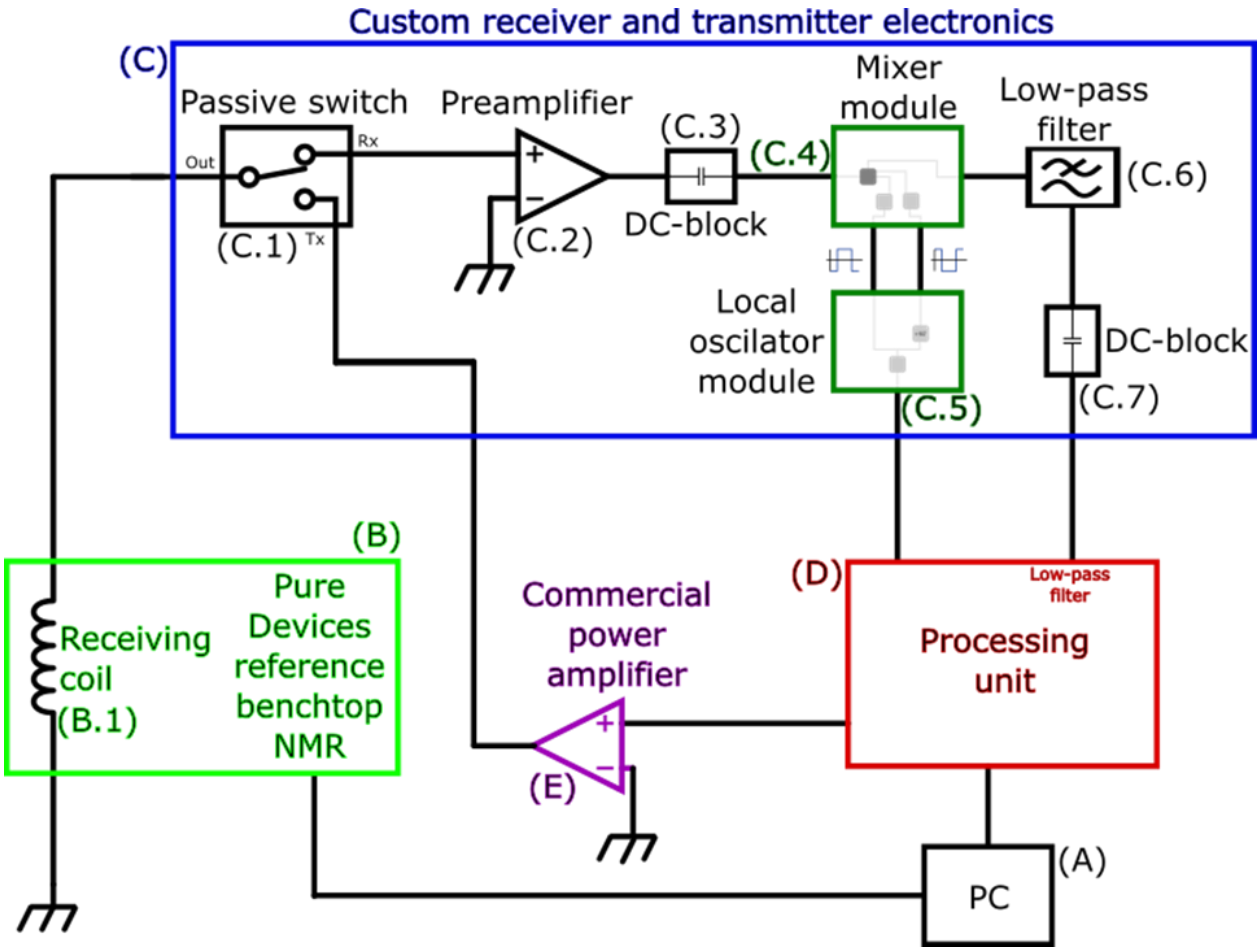

Figure 13 : Eléments électroniques composant notre prototype de spectromètre RMN.

De ce fait, dans ce travail, l'accent a été mis sur l'intégration d'une unité de contrôle dans la forme d'une carte radio logicielle de la société Red Pitaya, de même que dans la circuiterie électronique sous-jacente. Les fonctionnalités implémentées dans notre prototype incluent ainsi :

- L'excitation de l'échantillon chimique, c'est-à-dire la génération d'un signal haute fréquence égal à la fréquence de Larmor.
- La mesure et le traitement de la réponse induite de l'échantillon chimique jusqu'à son échantillonnage numérique.

- Le traitement numérique du signal induit et ensuite la mise en forme des informations mesurées.

En conséquence, parmi les éléments composant l'électronique de notre prototype, on peut citer les implémentations suivantes :

- La génération de l'excitation de base à la fréquence de Larmor.
- L'amplification et la redirection du signal d'excitation vers la bobine réceptrice.
- La réception et la pré-amplification du signal FID mesuré parvenu de l'échantillon chimique.
- Le filtrage et l'amplification supplémentaires.
- La génération du signal d'oscillateur à des fins de conversion vers le bas de la fréquence du signal mesuré pour pouvoir l'échantillonner ultérieurement.
- Le mélange des signaux mesuré et de l'oscillateur au moyen d'un mixeur électronique afin de réaliser la conversion vers le bas de la fréquence du signal mesuré.
- L'échantillonnage numérique du signal converti en fréquence vers le bas.
- Le traitement et filtrage numériques du signal échantillonné et la mise en forme des résultats obtenus afin que les spectres RMN viennent présentés dans le format correct pour les analystes RMN.

Le pilotage de la chaîne électronique étant implémenté à partir de la carte électronique commerciale de type radio logicielle présentée dans la figure 14 qui fonctionne sur un système d'exploitation basé sur Linux embarqué et qui peut être configurée et contrôlée à distance par une interface MATLAB communiquant avec cette carte via le protocole SCPI (*Standard Commands for Programmable Instruments*), nous avons décidé d'utiliser principalement MATLAB comme la plateforme logicielle de référence ainsi que pour l'environnement de traitement des signaux et des données numériques.

Figure 14 : Carte radio logicielle Red Pitaya STEMlab 125-14.

En plus de l'aiment générant le champ magnétique statique $\overrightarrow{B_0}$ et du *shim* magnétique nécessaire pour corriger son inhomogénéité au mieux, nous avons utilisé en plus la bobine réceptrice du spectromètre RMN de type *Benchtop* de la société Pure Devices, bien qu'un procédé de conception des bobines RMN ait été également développé dans le cadre de cette étude. Notre prototype avec ses parties composantes est montré dans la figure 15.

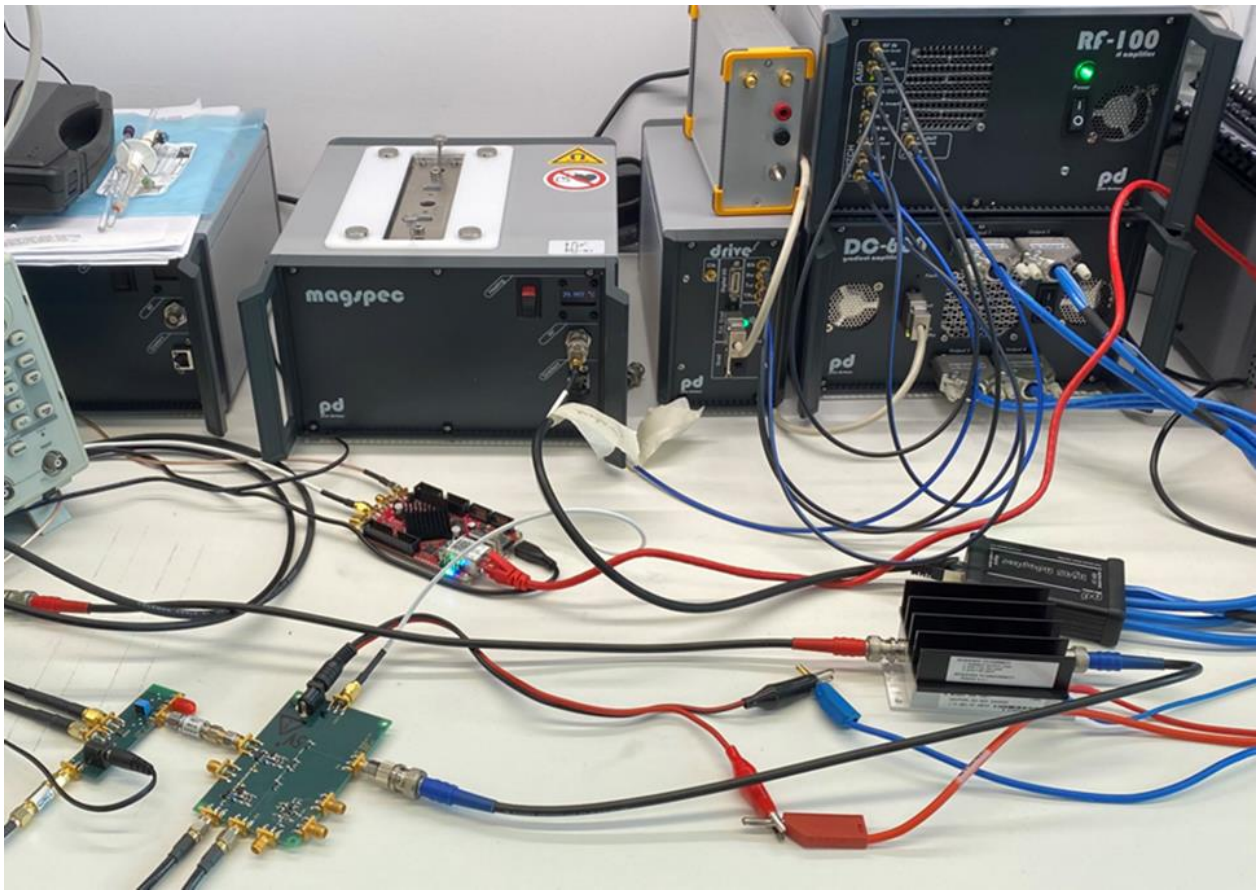

Figure 15 : Notre prototype de spectromètre RMN dans l'état actuel étant utilisé conjointement avec le spectromètre RMN de type *Benchtop* de la société Pure Devices.

Pour une validation préalable de l'usage de notre spectromètre RMN et aussi afin d'exemplifier son mode d'emploi, des mesures des substances à signal fort ont été effectuées. Les figures 16 et 17 présentent respectivement la FID et le spectre RMN de l'eau mesurés avec notre prototype.

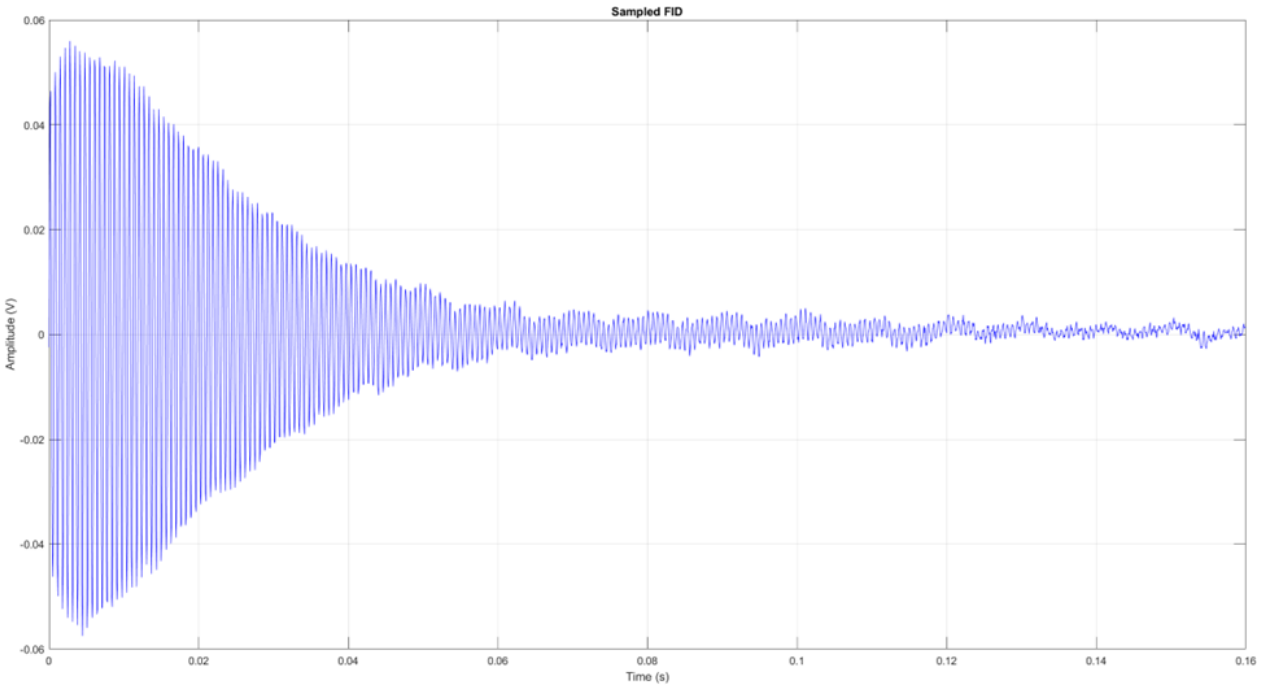

Figure 16 : FID correspondant à de l'eau pure échantillonnée par notre prototype de spectromètre RMN. (303,15 K, environ 24,35 MHz, prototype de spectromètre RMN)

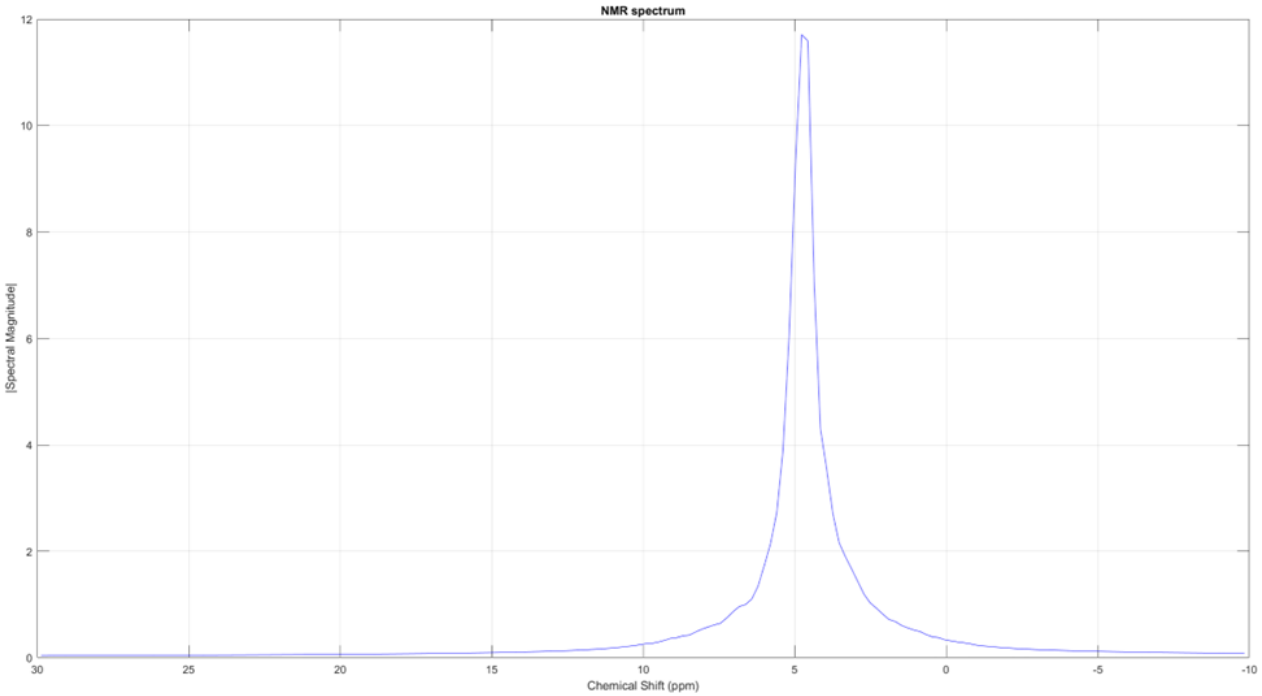

Figure 17 : Spectre ^{1}H RMN base résolution pour l'eau pure. (303,15 K, environ 24,35 MHz, prototype de spectromètre RMN)

Nous pouvions vérifier que la FID mesurée a un très haut rapport signal sur bruit, quoique la présence de bruit, surtout d'au moins avec une composante non blanche, est bien

perceptible. Ce bruit est filtré digitalement, générant ainsi un spectre RMN de base résolution assez correct.

Résultats expérimentaux

Une fois que notre prototype a été mis en fonctionnement et préalablement testé, nous avons effectué des mesures avec des solutions chimiques variées présentant des spectres RMN davantage complexes, de même qu'avec des échantillons chimiques correspondant aux applications ciblées, afin d'explorer les capacités de notre dispositif RMN.

Les figures 18 et 19 présentent respectivement la FID et le spectre RMN mesuré avec notre prototype pour l'éthanol.

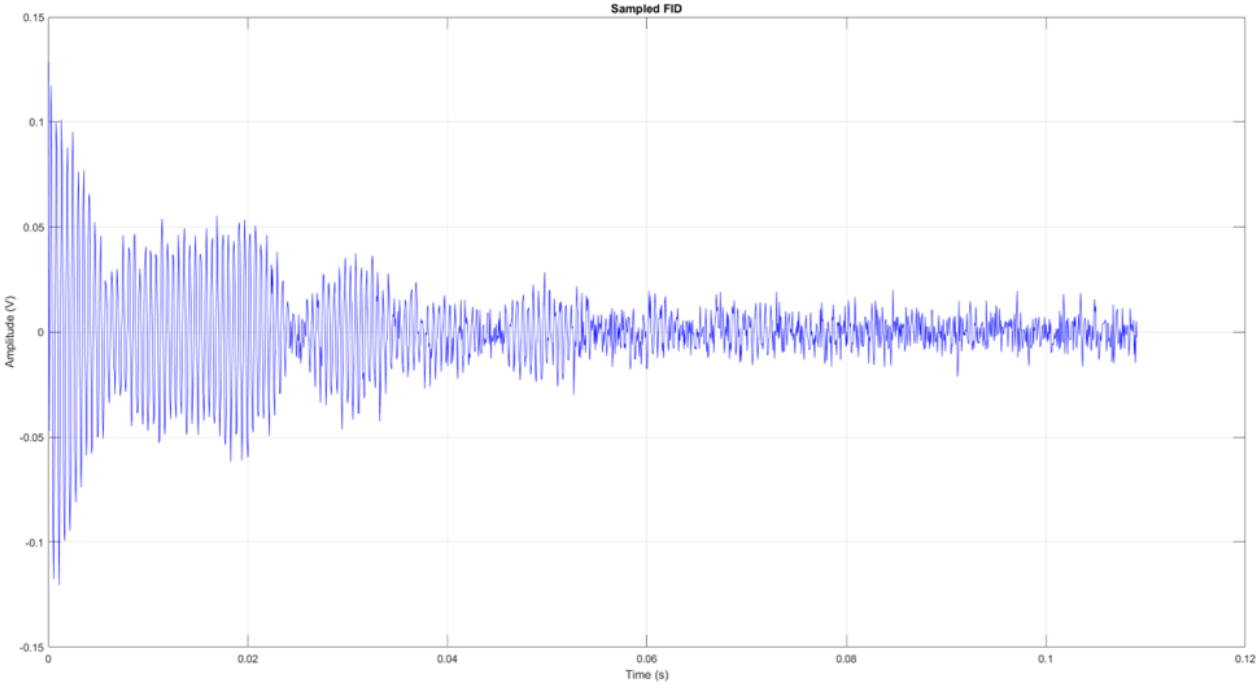

Figure 18 : FID correspondant à de l'éthanol échantillonnée par notre prototype de spectromètre RMN. (303,15 K, environ 24,35 MHz, prototype de spectromètre RMN)

La présence de bruit est évidente, cependant le rapport signal sur bruit est suffisamment grand pour qu'on puisse bien extraire les composantes fréquentielles correspondant aux trois groupes fonctionnels de la molécule d'éthanol.

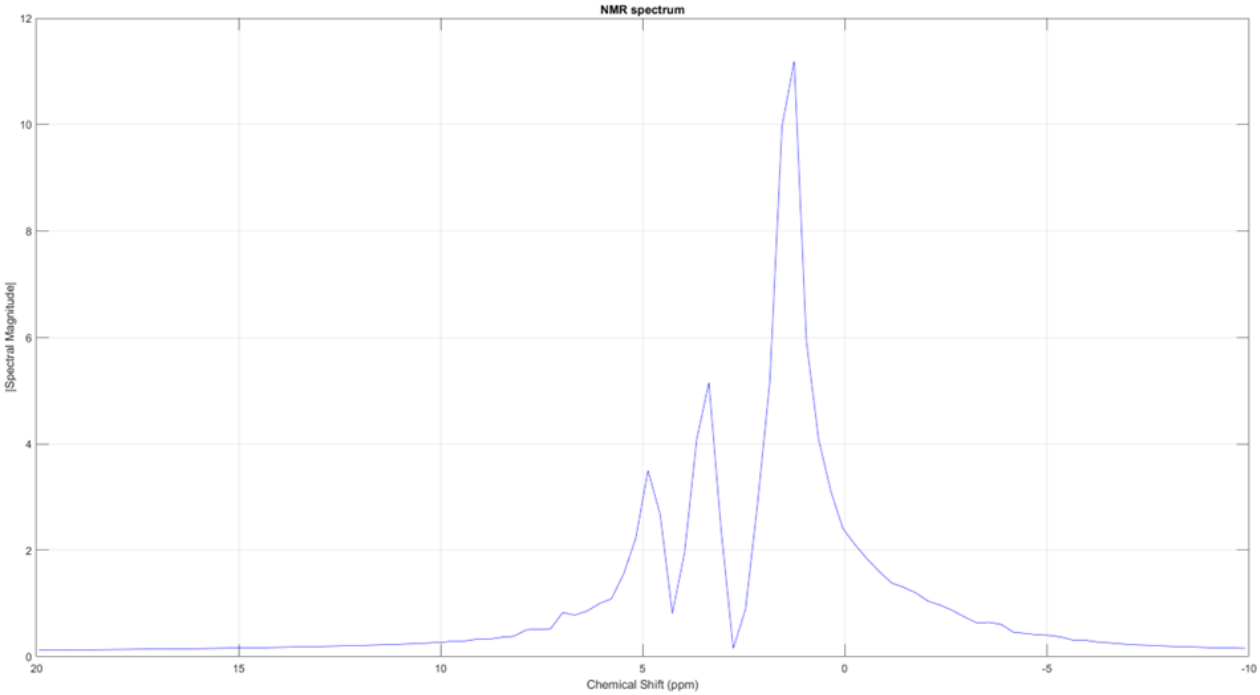

Figure 19 : Spectre ^{1}H RMN base résolution pour l'éthanol. (303,15 K, environ 24,35 MHz, prototype de spectromètre RMN)

La même expérience ayant l'éthanol comme échantillon chimique a été répétée en utilisant une de nos bobines réceptrices faites maison au lieu de la bobine réceptrice du spectromètre RMN de type *Benchtop* de la société Pure Devices, comme le montre la figure 20.

Figure 20 : Une de nos bobines réceptrices faites maison avec sa carte d'adaptation d'impédance.

Nous pouvons voir sur la figure 21 le spectre RMN résultant de cette expérience avec l'éthanol et une de nos bobines réceptrices.

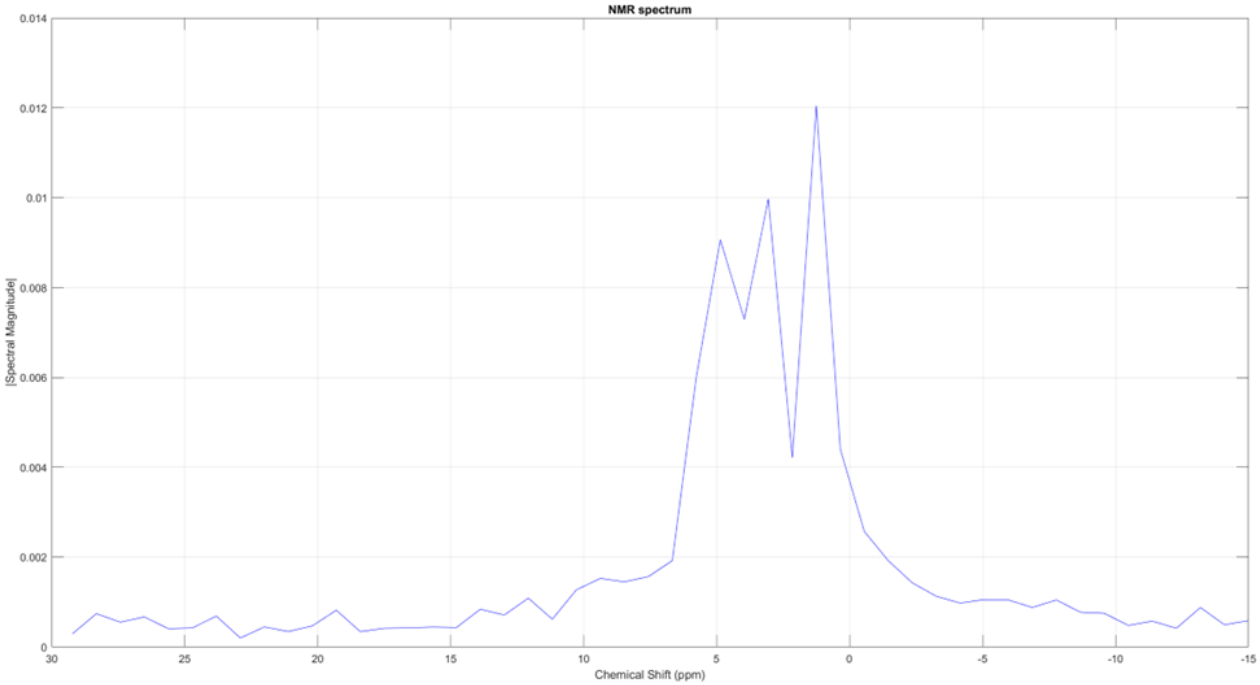

Figure 21 : Spectre ^{1}H RMN base résolution pour l'éthanol mesuré avec une de nos bobines réceptrices faites maison. (303,15 K, environ 24,35 MHz, prototype de spectromètre RMN)

Bien que la qualité du spectre RMN obtenu avec la bobine réceptrice faite maison soit bien inférieure en comparaison à celle du spectre obtenu avec la bobine réceptrice originale, nous y pouvons bien identifier les trois pics correspondants aux groupes fonctionnels de l'éthanol. Cette dégradation de la qualité spectrale a plusieurs raisons d'être : un *shim* non optimal et l'impossibilité de l'améliorer, une géométrie de la bobine et du volume de mesure de même non optimales, l'impossibilité de supprimer la bobine originale du setup, entre autres.

Ensuite, nous avons procédé avec des mesures dans des échantillons avec du glyphosate saturé dans l'eau lourde, ayant pour objectif de démontrer que ce pesticide pouvait être détecté avec l'aide de la RMN base résolution. Les figures 22 et 23 illustrent respectivement un spectre haute résolution obtenu avec un spectromètre RMN haut de gamme de la société Bruker et le spectre RMN base résolution correspondant obtenu avec notre prototype après filtrage ciblé.

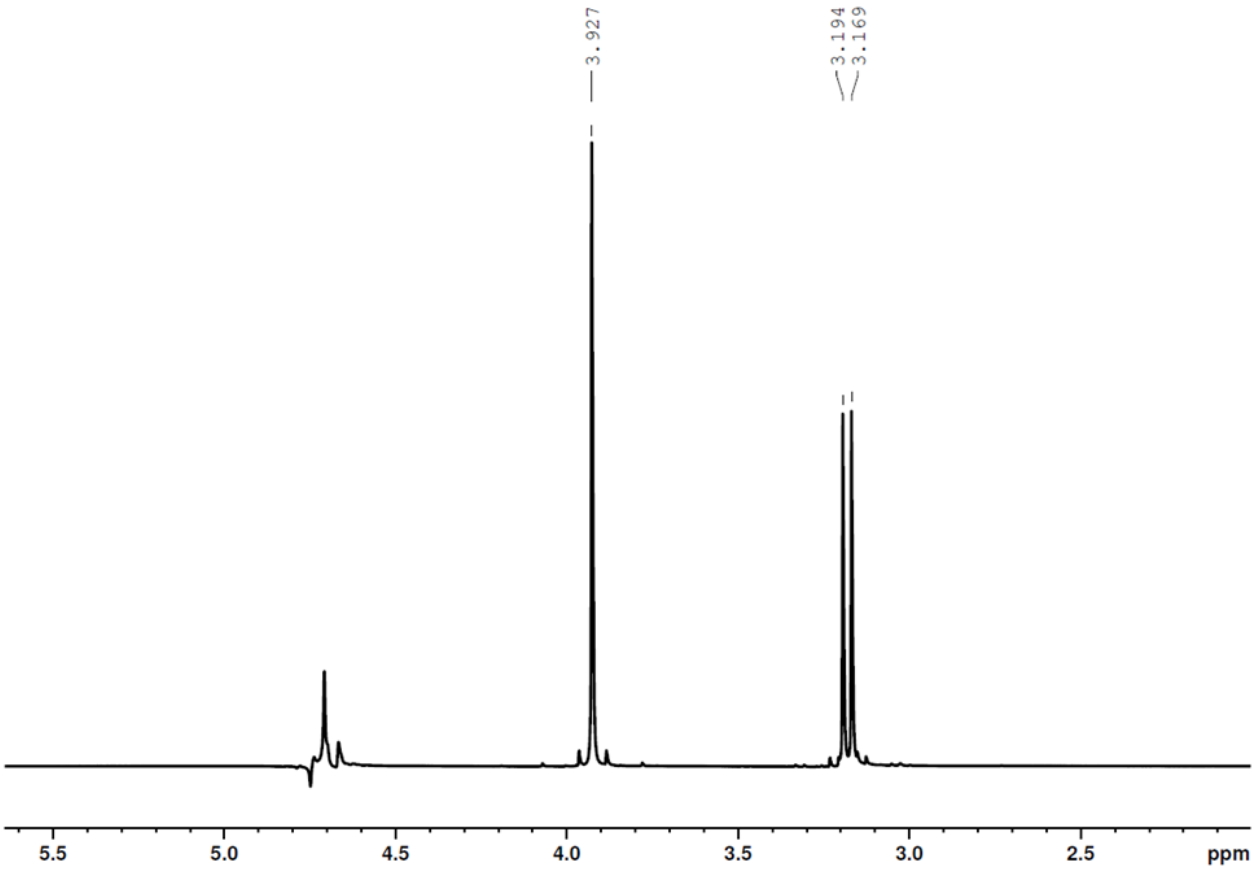

Figure 22 : Spectre ^{1}H RMN haute résolution pour une solution saturée de glyphosate dans de l'eau lourde. (298,15 K, 500 MHz, Bruker)

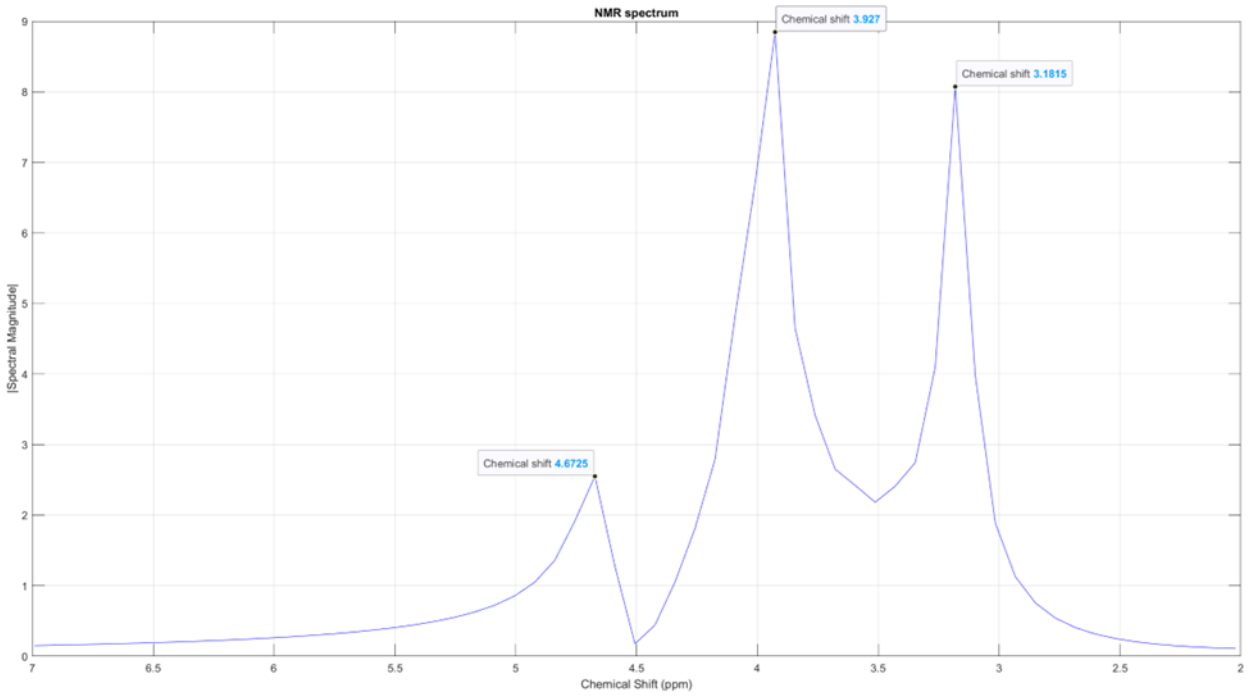

Figure 23 : Spectre ^{1}H RMN base résolution pour une solution saturée de glyphosate dans de l'eau lourde. (303,15 K, environ 24,35 MHz, prototype de spectromètre RMN)

L’apparition des trois pics dans le spectre base résolution a été possible grâce à un filtrage ciblé et celui a pu être efficacement mis en œuvre seulement parce que nous connaissions déjà le contenu de l’échantillon à être analysé. Cela montre qu’il est fondamentalement possible de détecter le glyphosate avec de la RMN base résolution. Néanmoins, pour que cette détection soit effective dans des cas réels avec des concentrations moindres dans des échantillons avec des contenus inconnus, des améliorations dans le prototype sont requises, notamment en ce qui concerne sa limite de détection.

Finalement, nous avons essayé de suivre une réaction chimique d’estérification, ayant pour but d’identifier le changement des déplacements chimiques des certains groupes fonctionnels ainsi que ses magnitudes spectrales d’un moment donné au suivant. La figure 24 illustre ce suivi de réaction effectué avec un spectromètre RMN haut champ, tandis que la figure 25 présente les résultats après ajustement obtenus avec notre prototype pour cette réaction d’estérification.

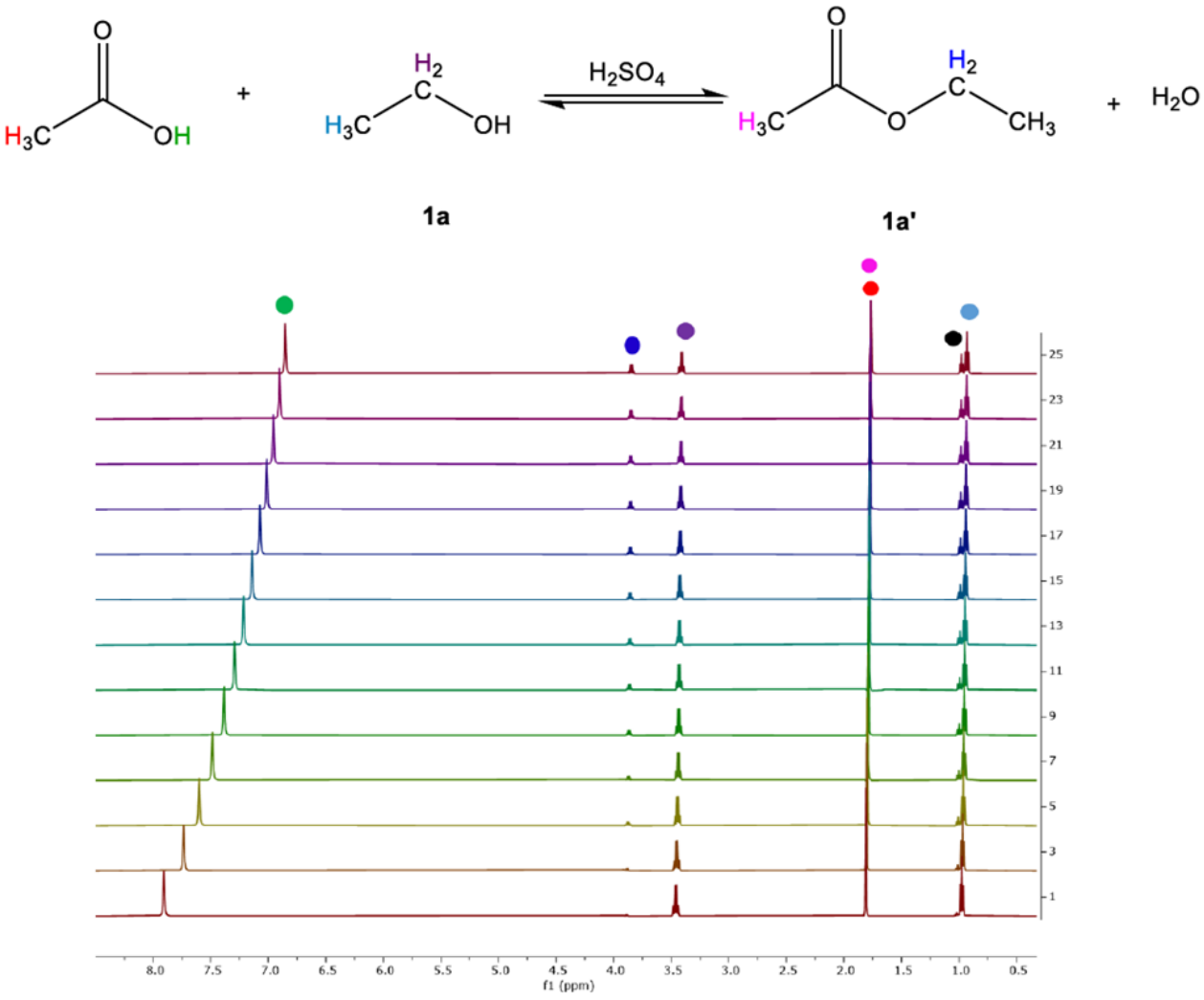

Figure 24 : Suivi de la réaction d’estérification en haut champ. (298,15 K, 500 MHz, Bruker)

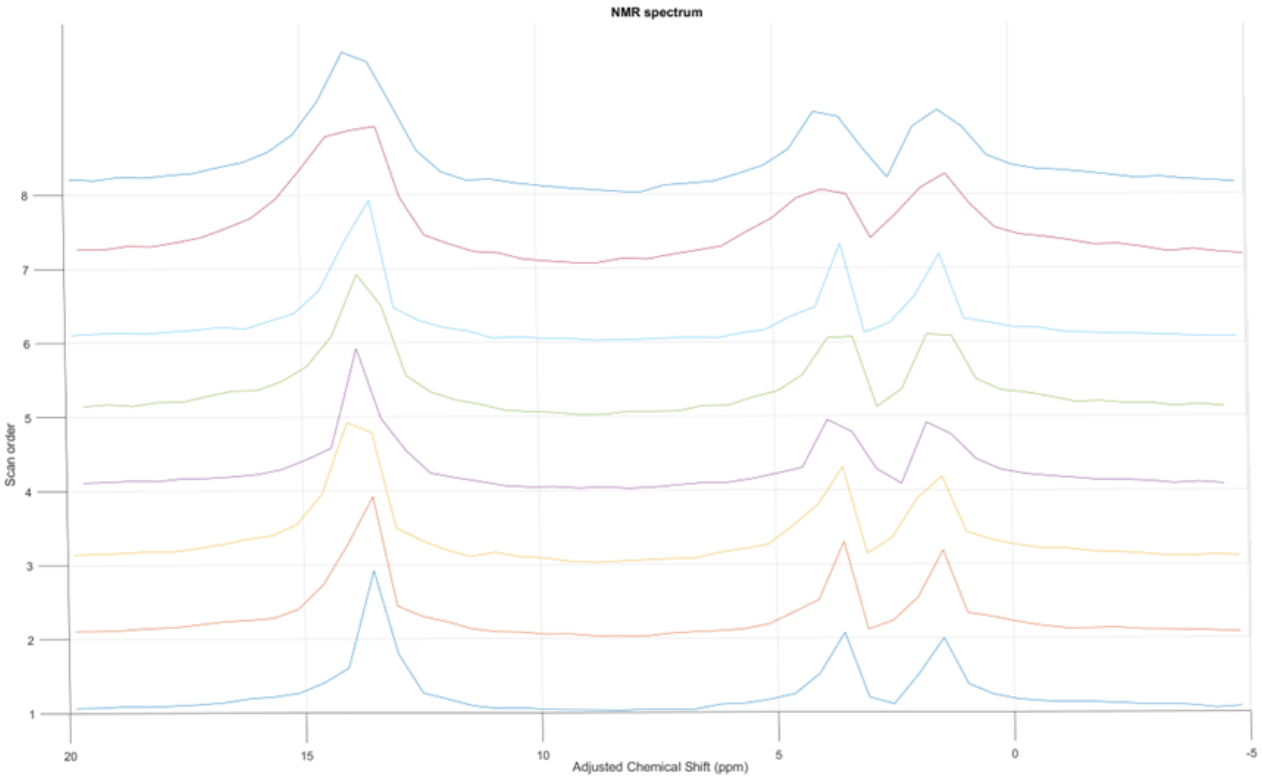

Figure 25 : Suivi de la réaction d'estérification avec notre prototype de spectromètre RMN. (303,15 K, environ 24,35 MHz, prototype de spectromètre RMN)

En raison de limitations du prototype, ce n'est pas possible de suivre cette réaction chimique, car les changements attendus des déplacements chimiques et des magnitudes spectrales sont non concluants. Néanmoins, des réactions chimiques avec des déplacements chimiques plus conséquents doivent être détectables par notre spectromètre RMN.

Discussions et conclusions

Après le déroulement de ces travaux, nous avons pu rassembler et condenser des exigences supplémentaires en termes des performances de système qui doivent être respectées afin de développer davantage un spectromètre RMN portable miniaturisé à faible champ magnétique de manière complète et entièrement fonctionnel, cela étant possible grâce aux résultats expérimentaux obtenus ainsi qu'en s'appuient sur l'utilisation de nos outils de simulation développés. Ces exigences comprennent des aspects liés à la précision du système de pilotage et de l'électronique utilisés, des estimations par rapport à l'inhomogénéité maximale acceptable pour le champ magnétique statique $\overrightarrow{B_0}$, des consignes par rapport à l'ordre de conception et la géométrie des différentes parties d'un spectromètre RMN, ainsi que des considérations par rapport à son utilisation dans des situations diverses et variées pour des applications aussi diverses. L'évaluation de l'état actuel du prototype et l'appréciation de la

problématique liée au changement de température dans le système et son impact sur les résultats obtenus, ainsi que d’autres aspects complémentaires ont été adressés, et de ce fait, des perspectives ont été présentées et des suggestions concises ont été proposées.